der Bundeswehr
Universität München

Framework for active stabilization of thermomechanical distortions in space structures

Eloi Ferrer Gil

Vollständiger Abdruck der von der
Fakultät für Luft- und Raumfahrttechnik
der Universität der Bundeswehr München
zur Erlangung des akademischen Grades eines

Doktor-Ingenieurs (Dr.-Ing.)

genehmigten Dissertation.

Vorsitzender	:	Prof. Dr.-Ing. Christian Mundt
1. Gutachter	:	Prof. Dr.-Ing. Roger Förstner
2. Gutachter	:	Prof. Dr.-Ing. Helmut Rapp

Diese Dissertation wurde am 19.09.2018 bei der Universität der Bundeswehr München eingereicht und durch die Fakultät für Luft- und Raumfahrttechnik am 19.01.2019 angenommen.

Tag der Prüfung: 08.02.2019

Kurzfassung

Der stetige Fortschritt der Technologie erlaubt es, die Umgebung mit immer höherer Genauigkeit zu erfassen. Dies führt dazu, dass die Betriebsbedingungen, um ein angemessenes Leistungsniveau dieser präzisen Instrumentierung zu gewährleisten, immer strenger werden, insbesondere für optische Nutzlasten. Im Falle von Raumfahrzeuge herrscht traditionell eine stabile und geräuschfreie Umgebung, in der hochpräzise Messungen durchgeführt werden können. Dies gilt für hochauflösende Weltraumteleskope und eine Vielzahl von Fernerkundungsmissionen.

Ein wesentlicher Faktor für die Stabilität, die hochpräzise Instrumentierung erfordert, ist eine formstabile Struktur. Traditionell wurde eine akzeptable Dimensionsstabilität nur durch passive Methoden erreicht, d.h. durch die Entwicklung einer adäquaten Konstruktion aus Materialien mit hoher Steifigkeit und niedrigen Wärmeausdehnungskoeffizienten. Mit den steigenden Anforderungen an die Stabilität stoßen die traditionellen Methoden, um den Auswirkungen von Störungen entgegenzuwirken, an ihre Grenzen. Eine besondere Art von Störungen, die zu erheblichen Maßänderungen an der Struktur führen können, sind Störungen thermischen Ursprungs. Diese verändern das Temperaturfeld in der Struktur und damit die Verschiebung zwischen verschiedenen Punkten. Aktuelle Missionen zeigen, dass das Ausmaß dieser Verformungen immer problematischer wird und daher bessere Methoden für Dimensionsstabilisierung erforderlich sind.

Diese Arbeit stellt eine Alternative zum traditionellen passiven Ansatz dar. Die vorgestellte Methode basiert auf der kontrollierten Anwendung von Wärme auf eine Struktur, um ihr Temperaturfeld und damit die entstehenden Verformungen zu verändern. Dieses Kontroll-Framework wird durch eine Frequenzbereichsformulierung des thermomechanischen Modells der Struktur ermöglicht, die wiederum durch die Finite-Elemente-Methode abgeleitet wird. Basierend auf dieser Formulierung werden die Übertragungsfunktionen zwischen Temperatur und Verschiebung ermittelt und ein Regler abgeleitet. Außerdem werden die Sensor- und Aktuatorstrategien zur Umsetzung des vorgestellten Regelungsansatzes präsentiert. Eine Simulationsumgebung wird entwickelt, um die mit dieser Methode erreichbare Dimensionsstabilität zu bewerten. Dabei werden die wichtigsten Faktoren berücksichtigt, die in der Praxis zu einer Leistungsreduzierung beitragen können, einschließlich der Sensor- und Aktuatorunsicherheiten. Die so erreichte Stabilitätsleistung unter verschiedenen Szenarien beweist, dass die vorgestellte Methode eine gegenüber den passiven Verfahren verbesserte Dimensionsstabilität erreichen kann. Es wird erwartet, dass diese Methode dazu beitragen kann, neue Arten von hochleistungsfähigen Weltraummissionen mit hohen Anforderungen an die Dimensionierung zu ermöglichen, darunter hochauflösende Teleskope, Laserkommunikationssatelliten und Formationen von Raumfahrzeugen für weltraumgestützte Interferometrie.

Abstract

The steady advance of technology allows sensing the environment at an always increasing level of accuracy. As a result, the operating conditions to guarantee an appropriate level of performance of such precise instrumentation are becoming more stringent, particularly for optical payloads. Spacecraft have traditionally granted a stable and noise-free environment from which high-precision measurements can be conducted. This has been the case for high-resolution space-based telescopes and a wide variety of remote sensing missions.

An essential factor in achieving the levels of stability that high-precision instrumentation require is to have a dimensionally stable structure. Traditionally, acceptable levels of dimensional stability have been reached based only on passive methods, i.e. by developing an adequate structural design built with materials that have high stiffness and low coefficients of thermal expansion. However, as higher levels of stability are required, traditional methods to counteract the effects of acting perturbations are approaching their limits. A particular type of perturbations that can introduce significant dimensional changes on the structure are perturbations of thermal origin. These change the temperature field in the structure and, as a result, the displacement between different points. Recent missions exemplify that the magnitude of these distortions is becoming more problematic and, thus, better methods of dimensional stabilization are required.

This work presents an alternative to the traditional passive approach. The presented method relies on the controlled application of heat on a structure in order to modify its temperature field, and as a consequence, the arising distortions. This control framework is enabled by a frequency-domain formulation of the thermomechanical model of the structure, derived in turn through the finite element method. Based on this formulation, thermomechanical transfer functions between temperature and displacement are obtained and a controller can be derived. The sensor and actuator strategies to implement the presented control approach are also presented. A simulation environment is developed to assess the dimensional stability that could be achieved with this method. This takes into account the major factors that in reality could contribute to a performance decrease, including the sensor and the actuator uncertainties. The achieved stability performance under different scenarios is assessed, which proves that the presented method can potentially provide dimensional stability beyond what is passively possible. It is expected that this method can contribute to enabling new types of high-performance space missions with stringent dimensional requirements including higher-resolution telescopes, laser communications satellites and formations of spacecraft for space-based interferometry.

Acknowledgements

The completion of this thesis would not have been possible without all the people that have helped and supported me during these last four years.

I want to thank particularly Prof. Dr.-Ing. Förstner for giving me the opportunity of working at the Institute of Space Technology and Space Applications, first in the frame of the IRASSI project and later as a researcher in the field of structural stabilization.

My thanks are also extended to all the colleagues at the institute during these years. Also, I want to thank all the members of the IRASSI team for the challenging discussions and for providing a stimulating environment.

Finally, special thanks go to my family, and particularly to Julia, for the infinite patience, support and trust during this period.

Contents

List of Figures

List of Tables

List of Abbreviations

APE	Absolute Pointing Error
BTCS	Backward Time Centered Space
CAD	Computer-Aided Design
CDM	Central Difference Method
CME	Coefficient of Moisture Expansion
CTE	Coefficient of Thermal Expansion
DLR	Deutsches Zentrum für Luft- und Raumfahrt (German Aerospace Center)
DOF	Degree of Freedom
ESA	European Space Agency
FDM	Finite Difference Method
FEM	Finite Element Method
FTCS	Forward Time Centered Space
GRACE	Gravity Recovery and Climate Experiment
HSO	Herschel Space Observatory
IRASSI	InfraRed Astronomy Satellite Swarm Interferometer
ISO	Infrared Space Observatory
JWST	James Webb Space Telescope
LPM	Lumped Parameter Method
LQR	Linear Quadratic Regulator
MIMO	Multiple-Input Multiple-Output
MLI	Multi-Layer Insulation
NASA	National Aeronautics and Space Administration

OSR	Optical Solar Reflector
PDE	Partial Differential Equation
PID	Proportional-Integral-Derivative
RPE	Relative Pointing Error
SIMO	Single-Input Multiple-Output
SISO	Single-Input Single-Output

List of Symbols

$[\Gamma]$	Actuator multiplicative factors
$[\gamma]$	Mechanical eigenvalue matrix
$[\lambda]$	Thermal eigenvalue matrix
$[\phi]$	Thermal eigenvector matrix
$[\Psi]$	Thermal expansion matrix
$[\psi]$	Mechanical eigenvector matrix
$[\varepsilon]$	Emissivity matrix
$[B]$	Derivative matrix
$[C]$	Thermal capacity matrix
$[C_u]$	Damping matrix
$[E]$	Elasticity matrix
$[F]$	View factor matrix between surfaces in the analyzed domain
$[I]$	Identity matrix
$[K]$	Conductivity matrix
$[K_u]$	Stiffness matrix
$[K_{LQR}]$	Proportional gains derived using the LQR method
$[M_K]$	Innovation gain matrix
$[M_u]$	Mass matrix
$[N]$	Shape function matrix
$[Q]$	Output weight factor matrix
$[Q_K]$	Heat perturbation noise covariance
$[R]$	Input weight factor matrix

$[R_K]$	Sensor noise covariance
$[R_r]$	Radiative surface matrix
α	Coefficient of thermal expansion
λ	Thermal conductivity
ν	Poisson's ratio
Ω	Domain of analysis
ω	Perturbation frequency
ρ	Density
σ	Stefan-Boltzmann constant
ε	Emissivity
ε_t	Thermal strain
$\{\delta\hat{T}\}$	Estimated temperature vector
$\{\delta T_c\}$	Temperature fluctuations induced by the control input
$\{\delta T_{pert}\}$	Temperature fluctuations induced by the perturbations
$\{\delta T_{sensors}\}$	Measured temperature vector
$\{\eta\}$	Mechanical modal coordinates
$\{\tau\}$	Thermal modal coordinates
$\{F_e\}$	View factor vector between the domain and the environment
$\{q\}$	Heat flux vector
$\{q_c\}$	Control heat vector
$\{q_{pert}\}$	Perturbation heat vector
$\{q_{rad}\}$	Radiation heat flux vector
$\{R_Q\}$	Heat source vector
$\{R_q\}$	Heat flux vector
$\{T\}$	Temperature vector
$\{T_s\}$	Surface temperature vector
$\{T_{eq}\}$	Temperature vector in equilibrium
$\{u\}$	Displacement vector

$\{u_{eq}\}$	Displacement vector in equilibrium
a_0	First damping parameter
a_1	Second damping parameter
$\{\varepsilon_s\}$	Sensor bias vector
$\{\varepsilon_{\Delta s}\}$	Sensor measurement error vector
A_{nm}	Cross-sectional area between nodes n and m
A_n	External area of node n
B_{nm}	Absorption factor between nodes n and m
C_n	Lumped heat capacity
c_p	Thermal capacity
E	Young's modulus
E_i	Irradiance at surface i
F	Mechanical load
F_{ie}	View factors between node i and the environment
F_{ij}	View factors between nodes i and j
H_n	Convective link parameter at node n
H_{TQ}	Transfer function between temperature and volumetric heat sources
H_{Tq}	Transfer function between temperature and heat fluxes
H_{uQ}	Transfer function between displacement and volumetric heat sources
H_{uq}	Transfer function between displacement and heat fluxes
H_{uT}	Transfer function between displacement and temperature
J_i	Radiosity at surface i
K_{nm}	Conductive link parameter between nodes n and m
l_{nm}	Distance between nodes n and m
n_e	Number of nodes in one finite element
N_i	Shape function corresponding to node i
n_n	Number of nodes in the finite element model
n_s	Number of surfaces in the domain

Q	Heat generation rate
q	Heat flux
R_{nm}	Radiative link parameter between nodes n and m
S	Surface of analysis
s	Complex frequency
T	Temperature
t	Time
T_e	Surrounding space temperature
T_f	External flow temperature
u	Displacement in the x direction
v	Displacement in the y direction
w	Displacement in the z direction

Chapter 1

Introduction

1.1 Background

One of the current challenges in the spacecraft design field consists in achieving the level of dimensional stability that new instrumentation requires to reach a certain level of performance. Given the steady advance of technology, newly developed instruments can sense the environment at unprecedented levels of precision. However, oftentimes the measurements they provide may be disturbed by external and internal perturbations in the spacecraft. Therefore, one of the limiting factors to properly operate such instrumentation are the perturbations generated and transmitted through the spacecraft itself.

This is particularly the case of spacecraft equipped with optical payloads that require stringent alignments and dimensional stability between different elements [1]. For instance, dimensional stability can be the limiting factor to the maximum pointing accuracy that can be achieved by space telescopes. Current and planned missions show that the required pointing accuracy of space telescopes is progressively becoming more stringent [2] and can only be reached with high dimensional stability. This type of stability also plays an important role in formation flying missions that have stringent navigation requirements or that perform inter-satellite distance measurements at high levels of accuracy, as in the case of space-based interferometers [3]. From these different types of missions, it becomes apparent that new missions with higher performance could be enabled by increasing the level of dimensional stability that can be reached on board spacecraft.

The perturbations that affect the dimensional stability on board the spacecraft can arise from different sources. On the one hand, there are external perturbations, which can ultimately be described as changes in the environment surrounding the spacecraft. On the other hand, there are internal perturbations, which are generated in the spacecraft itself by onboard equipment. There is also an important distinction related to the frequency of the perturbations. Low-frequency perturbations have generally only a quasi-static effect on the structure. These can mostly be described as thermal changes that induce thermomechanical distortions in the structure. At the other end of the spectrum, there are high-frequency perturbations, which include mainly mechanical vibrations.

A variety of strategies have been suggested and implemented to attenuate the impact of these different perturbations. The traditional approach has been to isolate the precise payload on board the spacecraft through passive means. This includes the construction of a secondary structure where the precise instrumentation is mounted, usually an optical bench, using materials that exhibit high stiffness and low coefficients of thermal expansion. Additionally, this secondary structure can be connected to the primary structure of the spacecraft through a statically determinate mount [4], also known as isostatic, which minimizes the mechanical interaction between both structures. By using an isostatic mount, distortions in the primary structure do not directly translate into distortions in the secondary structure. Passive methods are also implemented to insulate the onboard equipment that introduces thermal perturbations and to attenuate the thermal response of the spacecraft, which minimizes distortions induced by environmental changes. In all these passive techniques, the level of stability that can be achieved is inherently limited by the material properties and by the structural design. Furthermore, as higher levels of stability are required, the complexity and development efforts of these methods increase accordingly. Therefore, it is suggested that in order to overcome these limitations, active methods of structural control should be implemented.

Several active methods of structural control have been suggested and investigated. These include, for instance, active vibration isolation techniques such as controlled hexapod platforms [5] or active damping devices [6]. Active methods include also the field of smart structures [7], with a strong focus on piezoelectric actuation [8]. It is a fact that different types of perturbations require different active control methods. This results in approaches that can differ significantly depending on whether they are designed to counteract low-frequency or high-frequency perturbations.

The focus of this thesis is the development of a method to specifically counteract thermomechanical distortions, i.e. those distortions that result from the expansion in the materials composing the structure and that are induced by low-frequency thermal fluctuations. These thermal fluctuations are mainly induced by changes in the thermal environment of the spacecraft, which arise as the spacecraft follows its orbit, and by variations in the power dissipation of onboard equipment. These fluctuations are subsequently transmitted to the rest of the spacecraft through heat conduction and radiation.

The proposed method is based on the application of controlled heat in the structure, thereby inducing a displacement field that compensates the distortions arising due to thermal perturbations. There are three key aspects that are necessary to implement such a method and that constitute the backbone of this thesis. One aspect consists in deriving an accurate thermomechanical model of the structure that allows the estimation of the thermal and mechanical response of the structure under an uncertain environment. The other aspect is related to the formulation of a feedback control loop to derive the appropriate heat inputs that counteract distortions induced by thermal perturbations. This is directly related to the third essential aspect, which is a sensor and actuator strategy to properly measure, estimate and modify the distortion field at one given point in time. The combination of these different aspects results in a thermomechanical control framework that can be directly applied in space platforms. The same framework could be extended with minor modifications for ground applications that require also high levels of dimensional stability.

1.2 Research Objectives and Motivation

The main objective of this thesis is to develop an innovative control framework that can be directly implemented on board spacecraft to enable unprecedented levels of dimensional stability. This method must be able to compensate those distortions induced by thermal perturbations that are expected to arise in spacecraft. Thus, it is particularly important to take into account the heat exchange mechanisms describing the thermal response in space, i.e. conduction and radiation.

The first step in developing this control framework consists in establishing a thermomechanical model of the system to be controlled. Several numerical methods to develop thermomechanical models are already well established in the aerospace industry, these include finite difference [9] and finite element methods [10]. In order to facilitate the implementation of the control framework presented in this thesis, it is considered that the modeling techniques that are already established should be taken as a basis. It is necessary to account for the limitations of these current techniques and to identify novel methods to overcome them. In this sense, an objective of this thesis is to investigate the potential of a frequency-domain approach [11] to the thermomechanical problem, as well as the advantages it provides to develop a control framework.

The second step involves the derivation of control inputs that, when applied to a structure, result in a compensation of specific distortion measures. This requires the identification of a feedback controller that improves the dimensional stability level in comparison to that achieved with purely passive methods. The derivation of this feedback controller depends on the control strategy that is chosen, which includes the selection of actuators and sensors. In order to derive a control framework that could eventually be implemented, it is necessary to consider a reasonable number of both sensors and actuators. The cornerstone of the method presented in this thesis is based on controlling the structural behavior through the application of heat using heaters mounted on the structure. To achieve this, it is necessary to develop a sensor strategy based on available technologies that allows the estimation of the displacement field at each point in time.

The control framework developed in this work aims to compensate small deformations in structures that are already very stable. One of the obstacles to achieving stability at these levels is related to the uncertainty of the system. An objective of this thesis is to prove that the proposed control framework can also work under uncertain conditions. It needs to be clearly defined what these uncertain conditions include and what the sources of uncertainty are. The most significant sources of uncertainty are expected to be the uncertainty due to the randomness of thermal perturbations, the uncertainty in the behavior of both sensors and actuators, as well as the uncertainty in the thermomechanical model, mainly related to material properties. A framework to assess how these uncertainties impact the control performance must be developed.

The main motivation behind the work developed in this thesis has been to propose a possible solution to achieve the dimensional stability levels that new space missions are already requiring and are expected to require at even higher levels in the near future. The dimensional stability requirements of recent missions are close to the

limits of what is possible with only passive methods. It is expected that new missions will only be enabled if active methods of structural control are implemented. This is clearly the case of the several space-based interferometry missions that have been proposed and assessed in the last decade. One of them is IRASSI [12], the InfraRed Astronomy Satellite Swarm Interferometer, a mission study promoted by the Deustches Zentrum für Luft- und Raumfahrt (DLR, German Aerospace Center). It was in the framework of IRASSI that the work presented in this thesis started.

The motivation of this thesis is, on the one hand, to enable new kinds of space missions with stringent stability requirements. On the other hand, it is also expected that the technology presented in this thesis can represent in some cases an alternative to traditional passive approaches. In this sense, it is also a motivation to provide an active control technology that could be implemented in cases where passive methods become extremely complex, and as a consequence, expensive. This could represent a way to reduce development costs and, in some cases, it could even result in mass savings. Therefore, an additional motivation of the presented work is to reduce development efforts and minimize costs of a particular type of space missions.

1.3 Thesis Overview

This thesis begins with a review in Chapter 2 of state-of-the-art space missions that require high dimensional stability. This review illustrates why dimensional stability is a problem of growing importance by presenting the stability requirements of recent missions and of missions that have been assessed and proposed for the near future. This review has a special focus on the IRASSI mission, which is a space-based interferometer consisting of 5 satellites that plans to observe the infrared spectrum and has been the starting point for the work presented in this thesis. Chapter 2 continues with a presentation of the different perturbations that act on spacecraft and discusses possible classifications based on their properties. The available methods to counteract the structural distortions introduced by the presented perturbations are outlined. This introduces the distinction between passive and active methods of structural control and presents the most relevant active control technologies that are under investigation.

A representation of the control framework that has been developed in this thesis is illustrated in Figure 1.1. Each essential aspect of this control framework is treated and presented separately in the subsequent chapters of the thesis.

The aspects related to the thermal analysis model are presented in Chapter 3. This chapter presents the available numerical methods that are commonly used in the aerospace industry to solve thermal problems. It continues with the formulation of the finite element approach that has been selected to derive the required thermal model for the control framework. This chapter presents also a formulation of a frequency-domain approach to the transient thermal problem and its adaption for control purposes.

Chapter 4 continues with the formulation of the mechanical model, which takes as an input the temperature field calculated using the process described in Chapter 3 and outputs the displacement field. This model is also based in finite elements in order to

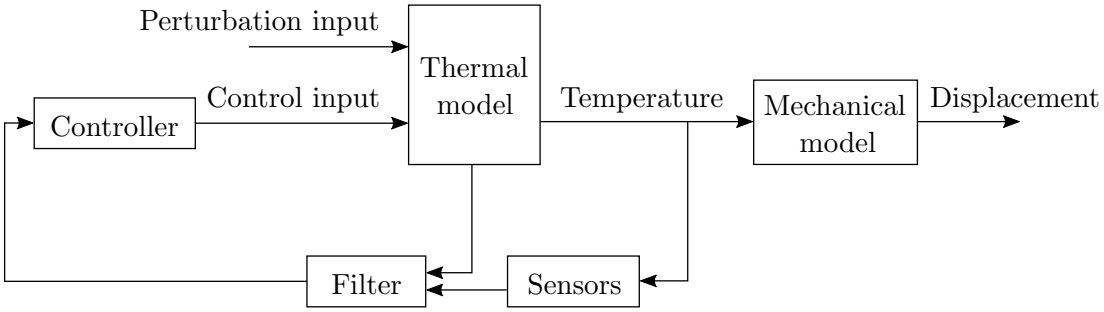

Figure 1.1: Control framework for thermomechanical distortions.

facilitate the interface between the thermal and the mechanical model. The chapter presents how the transient evolution of the displacement field can be calculated in the frequency domain, which is already a well-established type of analysis in the field of structural dynamics. It presents also the modal representation of the displacement field and its combination with the equivalent representation of the thermal problem, resulting in a modal approach to the thermomechanical problem. The chapter finishes with a presentation of the quasi-static assumption that is taken as a basis to implement the feedback controller.

Once the thermal and the mechanical formulation of the structure models have been derived, the next step has been to develop the control strategy, which is presented in Chapter 5. This chapter starts with a presentation of a simple perturbation compensation method that can be implemented when thermal perturbations can be fully characterized. The second part of the chapter presents a feedback control loop to compensate distortions that arise by random perturbations. This includes the description of the sensor strategy to estimate the displacement field based on a limited amount of temperature sensors. It also presents the possible actuation strategies to apply the control heat in the structure. The procedure to take into account the inherent uncertainties in both the sensors and actuators behavior is also presented. Subsequently, the complete formulation of the closed-loop system is presented. The chapter finishes with a step-by-step guide to implement the developed stabilization framework on any structure.

Chapter 6 evaluates the results that are obtained from applying the stabilization framework presented in the previous chapter. It first presents the most optimal performance results that can be obtained under the assumption that all the components have an ideal behavior and that no uncertainties are present. Subsequently, it presents the results under the effects of different uncertainty sources to identify which are the largest contributors to the performance decrease. The chapter presents also simulation results to validate the different assumptions that have been introduced to develop the thermomechanical model. At the end of the chapter there is a sensitivity analysis in terms of the material properties to assess how uncertainty in these variables impacts the control performance.

Finally, a thesis summary and conclusions can be found in Chapter 7. This chapter presents briefly the key aspects of the thesis and finishes with recommendations on future work.

Chapter 2

Dimensional Stability Framework

The steady advance of technology enables the development of instruments that sense the environment at an always increasing level of accuracy. When this instrumentation is operated on board a spacecraft it is often required to provide a high level of structural stability. This is necessary to achieve the quiet environment that instruments require for its proper operation and to provide the interfaces to other spacecraft elements. Thus, one of the enabling factors for more complex missions in the near future will be to achieve structural stability at the unprecedented levels that new instrumentation is requiring.

This chapter starts with a presentation of the state-of-the-art missions that require high dimensional stability. This shows why dimensional stability is a critical factor in current missions and how future missions will benefit from higher levels of stability. This stability must be achieved despite the fact that different perturbation sources act on the spacecraft. Thus, this chapter continues with a presentation of the most relevant perturbations that are expected to act on a spacecraft during its operation. Finally, the chapter gives an overview of the different control methods that have been implemented and proposed to attenuate the effects of the presented perturbations.

2.1 State-of-the-art missions

The high structural stability of spacecraft has become increasingly more problematic as the traditional passive stabilization methods based on the selection of adequate materials and mechanical decoupling have approached their limits. Problems arising from structural instabilities have become apparent in the last decade during the development phases of missions such as GAIA, launched in 2013, and LISA Pathfinder, launched in 2015. These two missions exemplify different reasons for which structural stability is becoming progressively more important. Both are single spacecraft missions. However, LISA Pathfinder is a precursor of the more complex mission known as LISA that is foreseen to consist of three spacecraft. In this regard, formation flying missions are a growing field where structural stability requirements are expected to play an important role.

GAIA is an astrometry mission [13] of the European Space Agency (ESA) designed to precisely map around 10^9 stars in the Milky Way. One of its goals is to provide precise information on the position and radial velocity of these stars, as well as of their luminosity, temperature and composition. To this purpose, the GAIA spacecraft, represented in Figure 2.1, is equipped with two identical telescopes with access to two different fields of view separated by an angle of 106.5°. It is crucial for the feasibility of the mission that the angle between these two telescopes does not change more than 7 microarcseconds over a period of 6 hours, which is the rotation period of the spacecraft [14]. Moreover, GAIA is equipped with a monitoring system that keeps track of the variations of this angle at microarcsecond level, which is arguably the most precise metrology system that has ever flown [13]. For this mission, the challenging level of structural stability has been reached using a passive approach based on a highly complex and advanced optical bench made of silicon carbide.

The most stringent structural stability requirement of the GAIA mission is expressed as an alignment between two optical elements, i.e. the two telescopes. Similar requirements exist and have existed for other single spacecraft missions, specifically in the case of space telescopes, because the alignment between optical elements directly influences the scientific performance that can be achieved. It is a logical trend that new missions, namely in the field of space telescopes, aim at reaching higher resolutions and better image quality than previous missions. This eventually translates into stringent requirements in terms of the alignment between optical elements and in terms of the spacecraft pointing, expressed as absolute pointing and pointing stability requirements.

The pointing requirements of the first space telescopes were in the range of arcseconds. This was in accordance with what could be achieved based on gyro-stellar estimation which depended on the available star catalogs that had limited accuracy. The improvements in the quality of star catalogs and in the hardware of the involved technologies have made it possible to reach attitude knowledge at subarcsecond level. Once attitude determination at a subarcsecond level has become possible, the next logical step in space telescopes technology has been to achieve also attitude control at these magnitudes. However, to achieve this performance level it is also crucial to ensure that the spacecraft structure is stable at the subarcsecond level, otherwise the measurements obtained by the attitude determination system cannot be prop-

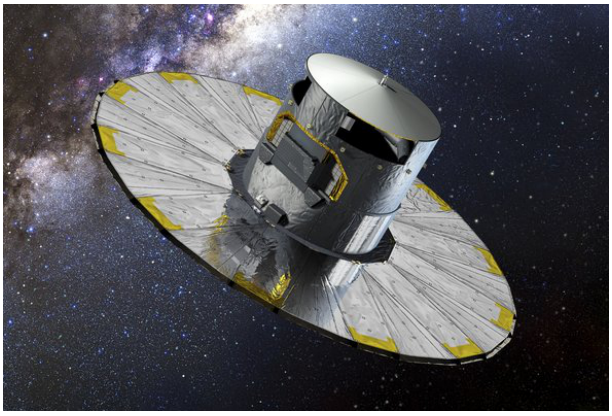

Figure 2.1: Artist's impression of GAIA (Courtesy of ESA/D. Ducros).

erly related to the pointing direction of the telescope on board the spacecraft. The coordinate system located at the attitude sensors should ideally be at a constant orientation with respect to the coordinate system centered at the telescope. However, perturbations acting on the spacecraft often introduce misalignments between these two coordinate systems.

Among the most representative examples of this tendency towards more accurate attitude control there is the Herschel Space Observatory (HSO) [15], launched in 2009 and represented in Figure 2.2. The HSO was designed following a pointing requirement of 3.7 arcsec in terms of Absolute Pointing Error (APE) and 0.3 arcsec of Relative Pointing Error (RPE), both expressed as 1σ requirements [16]. According to the ESA definitions [17], the APE is the difference between the desired pointing direction and the actual pointing direction. The RPE is defined as the difference between the instantaneous pointing direction and the average pointing direction over a time period that in the HSO case was 60 seconds. The final performance that HSO achieved after applying several corrections in the operations of its attitude and control system was slightly below 0.9 arcsec APE and 0.19 arcsec RPE [16].

More stringent requirements exist for the James Webb Space Telescope (JWST) [18], represented in Figure 2.3, which is planned to be launched in 2021 and that will observe frequencies ranging from long-wave visible light to mid-infrared. The JWST requires a pointing accuracy of 1 arcsec at 1σ level during its fine guidance mode [19] and a pointing stability of 7 milliarcseconds, also at 1σ level [20]. Achieving this stringent level of attitude accuracy is unattainable without a very advanced structural concept and the appropriate techniques to isolate the telescope from any perturbations that may arise on board the spacecraft.

Figure 2.2: Artist's impression of the Herschel Space Observatory (Courtesy of ESA/AOES Medialab).

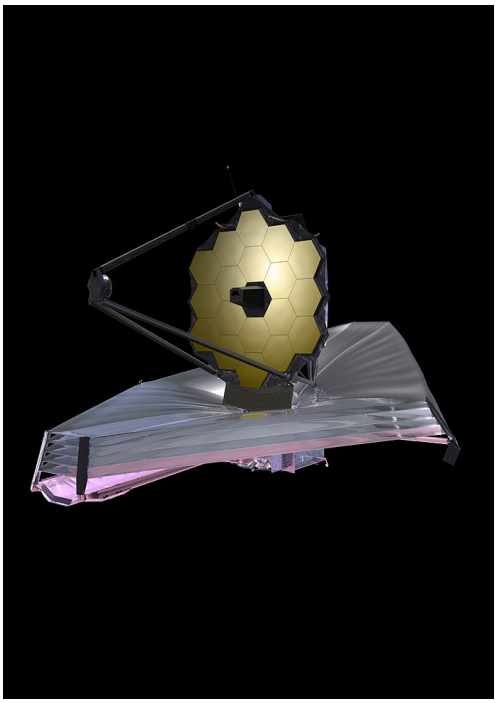

Figure 2.3: Artist's impression of the James Webb Space Telescope (Courtesy of NASA).

Another illustrative example of the importance of thermomechanical stability is the M-class type mission of the European Space Agency known as EUCLID [21], scheduled for launch in 2020. EUCLID will measure the redshift of galaxies and clusters of galaxies to better understand dark matter. The image quality that this mission is expected to achieve results also in stringent requirements on the pointing accuracy and, therefore, on the thermal and mechanical stability of the spacecraft. The pointing requirements for EUCLID are 75 milliarcseconds RPE over a period of 700 seconds and 7.5 arcsec APE, in this case expressed as 3σ requirements [22].

Also among the M-class missions of ESA there is PLATO [23], launching in 2024, which will study extrasolar planetary systems and will characterize the properties of exoplanets in habitable zones. The most stringent requirement of this mission related to its pointing is to achieve an RPE of 0.2 arcsec at 1σ [24].

To illustrate the trend towards an increase of the attitude control accuracy in new missions it is also relevant to consider missions that have been proposed and preliminarily analyzed and that could be implemented in the next decades. This includes SPICA, which has been a candidate M-class mission for ESA and developed as a collaboration between ESA and the Japan Aerospace Exploration Agency (JAXA). The first pointing requirements derived for this mission were to achieve during its standard mode of observation an APE of 0.135 arcsec and an RPE of 75 milliarcseconds over a period of 200 s, both expressed as 3σ values [25]. The spacecraft would also have a coronograph mode requiring both an APE and an RPE of 0.03 arcsec [25]. These requirements were slightly loosened in a posterior study conducted by the Concurrent Design Facility at ESA [26] which resulted in 3σ values of 0.8 arcsec APE and 0.05 RPE, also over a period of 200 s.

All these missions exemplify that there is a tendency towards an increase in the attitude accuracy demanded by new missions. It is becoming, therefore, necessary to take into account that one of the limiting factors for achieving this highly accurate attitude is the structural stability of the spacecraft itself. The structural stability requirements for these cases are often expressed as alignments between optical elements and attitude sensors and also as alignments and distances between optical elements, such as different mirrors of a telescope.

Apart from dimensional stability requirements related to attitude determination and control, there exist other reasons for which high levels of dimensional stability are required. This has been the case of the LISA Pathfinder mission [27], a precursor of the LISA gravitational wave observatory [28]. The goal of the LISA mission is to detect and measure gravitational waves. This mission is foreseen to consist of three spacecraft in a triangular formation with a side length of 2.5 million km following a heliocentric orbit. Each spacecraft will contain a pair of free falling masses that will follow a drag-free trajectory. Gravitational waves will alter the geodetic trajectories of each mass inducing distance changes between the free-falling masses from different spacecraft. Provided that the remaining perturbation sources are minimized to acceptable levels, it will be possible to detect gravitational waves by accurately measuring the distance change between free-falling masses. The range of frequencies of the gravitational waves that LISA aims at detecting requires the measurement of distance changes at picometer level [28], which will be performed using laser interferometers.

LISA Pathfinder has been a precursor mission to test some of the technologies that enable the LISA mission concept, particularly the aspects related to the distance measurement between test masses and the strategies to decouple the test masses from the spacecraft structure [27]. The mission consisted in testing only a miniaturized version of one of the arms of the full LISA interferometer. This was implemented with two free-falling masses inside the LISA Pathfinder spacecraft, which can be seen in Figure 2.4, and a laser interferometry system to track the distance changes between them [27].

There exists a large variety of physical phenomena apart from gravitational waves that can induce accelerations in the test masses present in these missions [29] and, therefore, change the distance between them. To enable the detection of gravitational waves it is crucial to minimize the acceleration noise induced by the remaining sources. These include accelerations triggered ultimately by thermomechanical distortions. Therefore, both LISA Pathfinder and LISA require an unprecedented level of thermal and mechanical stability. On the one hand, this stability is required to minimize the acceleration perturbation on the test masses. On the other hand, it is also essential to enable the laser interferometry measurements at picometer level.

The LISA mission can be seen as part of a larger class of space missions that are slowly reaching technological maturity. These are multi-spacecraft missions that aim at sensing a variety of space phenomena at unprecedented levels of precision. This type of missions are often based on taking several measurements of a particular magnitude from each spacecraft and on subsequently combining them to derive a more accurate measurement. This usually requires additional measurements of inter-satellite distances between different reference points in order to properly relate measurements taken at each spacecraft. Thus, structural stability is an essential element to ensure the feasibility of this type of missions.

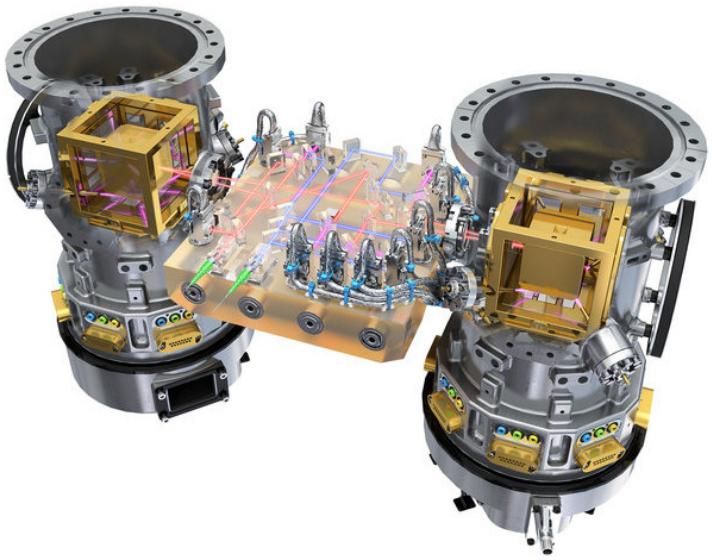

Figure 2.4: Free-falling masses inside the LISA Pathfinder spacecraft (Courtesy of ESA/ATG medialab).

One of the first such missions was GRACE [30], the Gravity Recovery and Climate Experiment, a joint partnership between NASA and DLR that was launched in 2002. The objective of GRACE has been to detect anomalies of the Earth's gravity field induced by mass fluctuations which in turn helps improve the gravity field models. GRACE consisted of two satellites that flew in a near-circular orbit at 500 km of altitude and at approximately 220 km from each other. Given that variations in the gravity field are expected to induce changes in the inter-satellite distance and relative velocity, the working principle of this mission consisted in tracking the distance change between both satellites as they orbited the Earth. The spacecraft used a K-band microwave ranging system to measure distance changes with an accuracy of 1 µm [31]. Both spacecraft were additionally equipped with a high-accurate accelerometer containing a proof mass which allowed the identification of distance changes that were not caused by variations of the gravity field [32]. Dimensional stability was crucial in such a mission to minimize shifts of the center of mass and in order to transform inter-satellite distance changes measured at the reference point of the ranging system to distance changes of the spacecraft center of mass.

To expand the measurements conducted by GRACE and improve even further the accuracy of the gravity field models, a new mission known as GRACE Follow-on [33] was launched in 2018. This mission is based on the same concept as GRACE but it has been conceived to achieve a higher resolution. GRACE Follow-on consists of two spacecraft that were inserted in an orbit at approximately 490 km of altitude, the distance between spacecraft is in the order of 200 km. In this case, the inter-satellite distance has to be measured at nanometer precision [34]. This results in even more stringent requirements in terms of the dimensional stability that is necessary between the reference point of the ranging system and the center of mass. To comply with the specified requirements it was necessary to mount both the ranging system and the high-precision accelerometers in a common high-performance optical bench that minimizes the distortions between them.

There is a specific group of multi-spacecraft missions that have stringent dimensional stability requirements, these are space-based interferometers. This type of missions aim to observe a particular range of the electromagnetic spectrum and consist of at least two spacecraft that either fly in formation or are connected through a structural boom or tethers. Space-based interferometry has been suggested as an approach to observe at high spatial resolutions those wavelengths of the electromagnetic spectrum that are blocked by the atmosphere and, therefore, cannot be observed from the ground. This concerns particularly the infrared spectrum, which has been partially observed by space telescopes such as the Infrared Space Observatory (ISO) [35], the Spitzer Space Telescope [36] and the Herschel Space Observatory [15] but never at subarcsecond resolutions. There exists a strong scientific rationale that justifies and advocates for the development of a space mission to observe the infrared spectrum at unprecedented resolutions [37]. As a consequence, several concepts have been proposed and studied to provide this level of performance.

Interferometric missions require the combination of different waves within accuracies at a higher order of magnitude than the wavelengths involved, which in the infrared case range from 0.7 µm to 1 mm. At the same time, the angular resolution that can be reached with interferometric techniques is inversely proportional to the distance

between collectors, also known as baseline. This means that longer baselines are desired to achieve a smaller value of the angular resolution, which results in more detailed images. As a consequence, space-based interferometry missions require generally the measurement of long distances at high accuracy. Performing this kind of measurements between different spacecraft inevitably requires a high level of structural stability.

Different concepts have been proposed as a solution to this challenge. One option is to connect the different spacecraft collecting infrared signals through a structural boom. This is the option that was proposed by SPIRIT [38], which consists of one beam combiner connected to two light collecting telescopes that can move through a rail. The structural boom solution gives more control over the baseline magnitude but it also limits its maximum value, which in turn limits the resolution that can be achieved. A more complex solution to overcome this limitation consists in using tethers to connect the different collectors. This approach was considered for the SPECS concept [39] in order to enable a spin-stabilized formation consisting of three light collectors and a central beam combiner. This approach theoretically reduces the effort in formation control because it forces the spacecraft to follow a specific circular trajectory. Having a tether that connects the different light collectors also helps in the estimation of the inter-spacecraft distance. However, SPECS requires this estimation to be performed at an accuracy of 1 µm and it also requires an orientation between spacecraft at subarcsecond accuracy [39]. Therefore, dimensional stability is also a critical factor for the feasibility of this mission.

Both the structural boom option and the tethered option have also been considered for the TPF mission [40] and the FIRI mission [41]. These missions have additionally assessed the option of operating the different light collectors as a free-flying formation [42, 43]. One of the advantages of the formation flying option is that it provides more flexibility with respect to the relative positions between spacecraft which can be beneficial in scientific performance terms. This has been one of the reasons why the formation flying concept has also been the core idea behind other space-based interferometry proposed missions including DARWIN [44], ESPRIT [45], PEGASE [46] and IRASSI [3].

These missions apply different interferometric techniques which result in different dimensional stability requirements for each mission. To better exemplify why this is the case, the main structural stability requirement behind the IRASSI mission is presented here in detail.

The IRASSI mission has been conceived as a space-based interferometer consisting of a free-flying formation of five spacecraft that aim to observe the infrared spectrum between 50 and 300 µm. IRASSI relies on a heterodyne detection approach to capture infrared signals, which is an alternative to the direct detection approach of other missions such as DARWIN. The idea behind the interferometry concept applied for IRASSI is to superimpose at the same wavefront the signal of one source received at the different spacecraft. In order to perform this step it is necessary to know with a certain accuracy the geometric delay d, represented in Figure 2.5, between the same signal as it reaches two different collectors.

In order to properly interfere two different signals, IRASSI requires the combination of the wavefront from different collectors with a phase error below 30°. Expressed

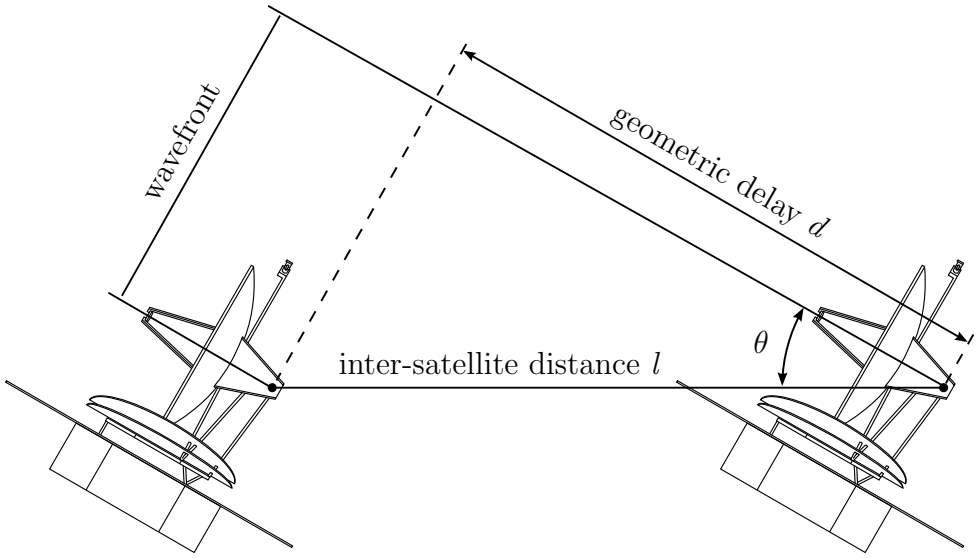

Figure 2.5: Interferometry concept for the IRASSI mission.

in terms of the wavelength this means that the geometric delay needs to be known to an accuracy of approximately $\lambda/10$. Given that the minimum wavelength that IRASSI plans to observe is 50 µm, the geometric delay represented in Figure 2.5 needs to be estimated with an accuracy of 5 µm.

The estimation of this geometric delay is based on first estimating the inter-satellite distance l and the source direction angle θ. If these two magnitudes are known and a perfect alignment is assumed between the optical elements, the geometric delay can be directly calculated using trigonometry.

The inter-satellite distance l is defined as the distance between the two reference points where the signal is detected at each spacecraft. These points correspond to the reference point of the scientific instrument. A first estimation of the inter-satellite distance can be obtained with a metrology system. However, a metrology system can only provide a measurement referred to the point of the spacecraft where this system is mounted. Therefore, it is required to subsequently transform the measured distance referred to the metrology system points to the inter-satellite distance referred to the scientific instrument points. The parameters involved in this transformation are represented in Figure 2.6.

Figure 2.6 shows that in order to apply this transformation it is necessary to know the internal distance between the scientific instrument and the metrology system. This is represented in Figure 2.6 by the vectors $\vec{r}_1$ and $\vec{r}_2$. The final distance that IRASSI requires for the scientific operations is the geometric delay represented in 2.5, which has to be known with an accuracy of 5 µm. As a consequence, all the secondary distances that are required in the process of estimating the geometric delay have to be known with even better accuracy. In terms of structural stability, it can be concluded that the internal distances r_1 and r_2 have to be stable at micrometer level and, therefore, distortions above this range are not acceptable. It is also crucial that these vectors maintain their orientation in the spacecraft reference frame.

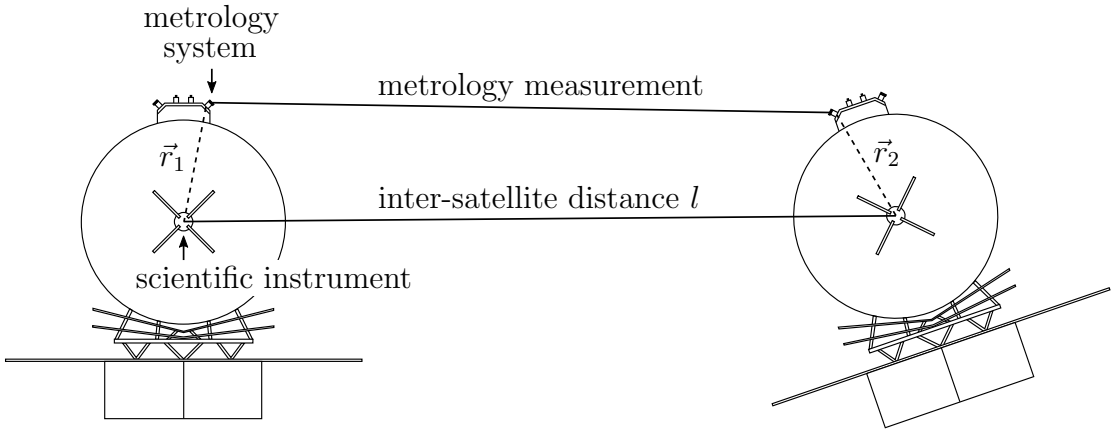

Figure 2.6: Inter-satellite distance representation of IRASSI.

Additionally, in order to perform the transformation represented in 2.6, it is also necessary to know the orientation of the metrology measurement in an inertial reference frame centered at the spacecraft and not just the one-dimensional information of its longitude. The orientation of the metrology measurement can be derived from the pointing direction of the metrology system. However, it must be guaranteed that this pointing direction of the metrology system does not change over a given threshold due to structural distortions of its platform. This additional aspect also translates into stringent requirements expressed in terms of dimensional stability.

Finally, it is also important to take into consideration that the alignment between optical elements can modify the longitude of the optical path. Figure 2.7 presents the trajectory followed by the light as it is reflected by the two main mirrors and until it reaches the scientific instrument. This trajectory is subject to changes if structural distortions change the distances between different mirrors. Eventually, this can have an impact on the geometric delay represented in Figure 2.5. Therefore, in those missions such as IRASSI where several optical elements are involved, it is often important to guarantee a certain level of structural stability between them in order to enable scientific operations.

The missions that have been cited in this section exemplify that dimensional stability is emerging as an increasingly important factor in the space industry as it

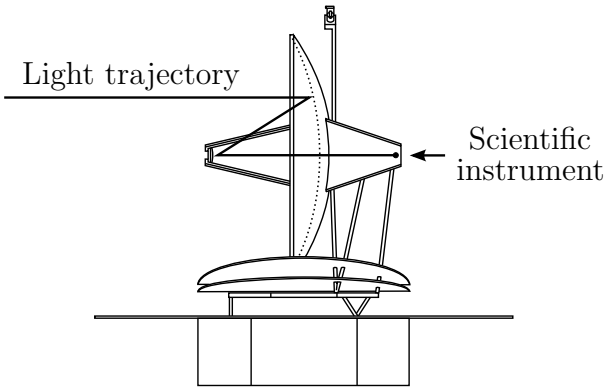

Figure 2.7: Optical path in the IRASSI spacecraft.

becomes one of the enabling factors for new types of missions. This is the case for those missions that rely on instruments that require a highly stable environment for its operations, missions that have high accuracy requirements in terms of its attitude determination and control, missions with optical elements that need to be aligned with uttermost precision as well as missions that operate several spacecraft in formation and combine data from different nodes.

An important characteristic of dimensional stability is that it must be maintained especially when perturbation sources are present. In order to develop a controlled structure that will remain stable under the effect of perturbations, it is necessary to first characterize the nature of the perturbations that are expected to arise. Therefore, the following section presents the different types of perturbations that may appear on board a spacecraft with a special focus on the low-frequency perturbations, which are the ones that can be counteracted with the method presented in this thesis.

2.2 Structural perturbations

Structural perturbations are mechanical loads acting on a structure that modify its stress and strain field, which as a consequence introduces distortions in its shape. From a spacecraft point of view, these perturbations can have an external or an internal origin. Some of them act only once during the entire operational life of the spacecraft, for instance, during its launch. In other cases, they act periodically and can overlap with phases during which high dimensional stability is required. To assess the impact such perturbations can have, it is useful to characterize them based on its frequency.

At one end of the spectrum there are low-frequency perturbations. These are perturbations with periods ranging from a few hours to several days or even years. This kind of perturbations have in its majority a thermal origin, in which case they are also known as thermomechanical perturbations. Thermomechanical perturbations are essentially perturbations on the thermal state of the structure. When these perturbations arise, the thermal field in the structure changes as a consequence. This, in turn, changes the strain field of the structure due to the thermal expansion of its materials. As a final result, the new strain field translates into dimensional distortions and misalignments between different points of the structure.

At the other end of the spectrum, there are high-frequency perturbations. These are perturbations with frequencies that can range from a few Hz to several thousand Hz. At these high frequencies, thermal perturbations have negligible effects because they are strongly attenuated. The most relevant perturbations at this range of frequencies are perturbations of mechanical origin, namely vibrations. Vibrations excite the structure at specific frequencies and as a consequence change the alignment between internal points in the structure. The location in the frequency spectrum of both thermomechanical perturbations and vibrations is represented in Figure 2.8.

The control method presented in this work is based on the application of controlled heat to counteract dimensional distortions. Due to the thermal nature of this procedure, the presented method can only be implemented to counteract low-frequency

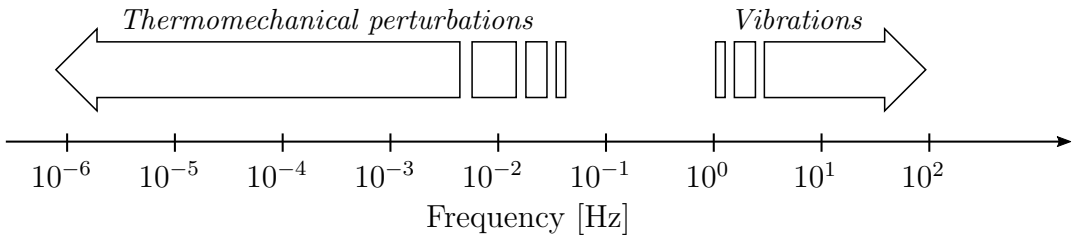

Figure 2.8: Perturbation type represented in the frequency spectrum.

perturbations, which in general have a thermal origin. Trying to apply it to counteract high-frequency perturbations is unfeasible because it would require unrealistic amounts of heat. Yet in order to clearly define the limitations of the presented method, it is sensible to present also in this chapter a description of the high-frequency perturbations that can appear on board a spacecraft.

The following subsections present more details on the origin of thermal and mechanical perturbations that are expected to act on a spacecraft during its operational life. Most of these perturbations can be and have been neglected in previous missions where stringent structural stability was not required. However, the distortion they introduce cannot be neglected at the levels of structural stability that new missions are requiring.

2.2.1 Thermal perturbations

Thermal perturbations are those perturbations that change the thermal state of a system, in this case a spacecraft. These thermal changes cause the expansion or contraction of the materials in the structure and, as a result, introduce distortions in its shape.

The first relevant thermal perturbation that acts on a spacecraft occurs when this is transferred to its operational orbit. This results in a change of the thermal environment surrounding the spacecraft. As a consequence, the structure reaches a new thermal equilibrium. The change in temperature between the two states can be significant, and thus, the introduced distortions due to thermal expansions are not negligible. These distortions are temperature dependent and, therefore, can be assumed to be permanent under the new thermal equilibrium in the operational orbit. In some cases it is possible to perform calibration procedures to estimate the extent of these distortions and to realign the critical elements in the structure by using the appropriate mechanisms. In some other cases this is not possible and it might be necessary to design the structure with the appropriate mechanical characteristics to limit the extent of these distortions.

Once the spacecraft has reached its operational orbit there continue to be thermal perturbations that can induce distortions in the structure. One first type of perturbations are related to changes in the thermal environment. This thermal perturbation arises because the spacecraft is never static at one point in space, instead it follows an orbit through different points in space with different thermal conditions. These thermal conditions can be described in terms of the radiation fluxes acting

on the spacecraft. For a generic case of a spacecraft orbiting around the Earth, the radiation fluxes acting on the spacecraft include infrared radiation emitted by the Earth, direct sunlight and sunlight reflected by the Earth, also known as albedo. The total radiation that a spacecraft receives depends on its position with respect to these radiation sources. As the spacecraft translates along its orbit the relative distance to the radiation sources changes and, as a result, the received flux also changes. For instance, a spacecraft orbiting in a highly elliptical orbit around the Earth will receive a different amount of albedo and infrared radiation when it is at the perigee than when it is at the apogee. This thermal perturbation will follow a cycle with the same period as the orbit. Given the Earth's orbit around the Sun, the spacecraft will also receive a changing solar flux as the Earth translates in its slightly elliptical orbit. In this case, the perturbation in the received solar flux will have a period of one year.

The most extreme variation in the received flux occurs if the spacecraft experiences eclipses. In that case, the spacecraft receives virtually no sunlight and, as a consequence, the change in its temperature field with respect to the illuminated condition is maximized. This results in a significant periodic distortion in the spacecraft structure that, depending on each case, can have a considerable influence on the payload operation.

Additionally, there can be changes in the presented perturbations related to variations in the sources. For instance, changes in the solar activity will translate into changes in the solar flux received at the spacecraft. Also, the temperature distribution at the surface of the Earth, or the presence and absence of clouds and continents, can induce changes in the albedo and infrared radiation received at the spacecraft.

Thermal perturbations described by changes of the received flux can also be caused by attitude changes. When the spacecraft changes its attitude, the orientation of the incident flux with respect to the spacecraft also changes. This can be understood as a change in the boundary conditions of the spacecraft, which translate into changes of its thermal state. A clear example is a space telescope that reorients itself to observe a new target. When stringent alignments are necessary to enable scientific operations it may be necessary to recalibrate and realign instruments to counteract the introduced distortions after attitude maneuvers.

Finally, the last relevant source of thermal perturbations in a spacecraft are the internal heat sources, i.e. the heat introduced by onboard instrumentation. During their operation, instruments experience power fluctuations that translate into changes of temperature and heat dissipation. These changes occur also when instruments are switched on and off. As a consequence, the heat that they transfer to the structure where they are mounted is not constant. These perturbations can have a critical impact when they originate from the same equipment that requires stability for its operation. Even though the amplitude of these perturbations is generally low, they are applied directly at the stable structure and, therefore, can introduce the largest distortions. Thus, passive methods of stabilization can only minimize to a limited extent the distortions introduced by this kind of perturbations.

2.2.2 Mechanical perturbations

Mechanical perturbations can be described as forces or pressures acting on the spacecraft structure. These loads directly change the underlying stress and strain field and, as a result, introduce distortions in the structure. The origin and characteristics of the mechanical loads acting on the spacecraft change throughout its operational life.

The mission phase during which the most severe mechanical perturbations are exerted on spacecraft is the launch phase. During this phase, spacecraft experience accelerations to orbital velocities and are excited over a wide spectrum of frequencies by high amplitude vibrations originating at the launcher. There is also a transfer of vibrations through pressure waves applied at the spacecraft surfaces caused by the acoustic noise from the engines. Additional mechanical loads transferred to the spacecraft have an aerodynamic origin caused by the turbulent flow around the launcher. There are also forces acting on the spacecraft resulting from stage and fairing separation as well as launcher maneuvers. The final result of all these mechanical loads is a permanent distortion that, in general, exceeds the stringent stability requirements of the structure. Additionally, there are also structural distortions appearing due to the gravity release, which takes place when the spacecraft transitions into microgravity conditions. For missions where the alignment between different points of the structure is an important factor it is necessary to develop the appropriate calibration and realignment procedures to compensate the distortions introduced during this phase.

The most critical perturbations in high-accuracy missions are those that arise during payload operations and that consequently can decrease the instrumentation performance. This is in particular the case of microvibrations, which are low amplitude mechanical perturbations that appear at frequencies starting at 1 Hz and that can reach several thousand Hz. Generally, in the field of spacecraft design, microvibration sources of concern have frequencies ranging from a few Hz to 1000 Hz [47, 48]. Microvibrations are produced by a variety of onboard equipment including reaction wheels, gyroscopes, cryocoolers, specific types of thrusters and, in general, devices with moving or rotating masses. One consequence of microvibrations acting on board the spacecraft is a high-frequency movement of its pointing direction, also known as jitter. This appears also at an internal level of the structure and, therefore, affects the alignment between onboard equipment. Microvibrations can generally be described as a fundamental excitation at some specific frequency together with secondary signals at several harmonics. This results in a wide spectrum of excitation, which is one of the reasons why the transfer of microvibrations to the rest of the structure is difficult to attenuate.

Another type of perturbations that can appear during payload operations are thrusting maneuvers. The force resulting from a thrusting maneuver is applied locally in the structure and only during a given time period. Considering that the amplitude of the thrusting force is low enough to preserve a certain level of stability in the structure, it can be assumed that no permanent distortions will remain once the maneuver ends. Only if a large maneuver is applied, such as to produce an orbital change, it might be necessary to calibrate or realign the onboard equipment.

There also exist other perturbations that induce a rigid body motion of the spacecraft. The most relevant perturbations included in this category are due to solar radiation pressure, gravity gradient, fuel slosh and solar array oscillations after maneuvering. Given the low amplitude of these perturbations, it can be generally assumed that they do not contribute to the structural distortion of the spacecraft. Therefore, they are relevant to develop the adequate attitude control procedures to comply with the pointing requirements but they are not expected to play a role to preserve structural stability.

2.3 Distortion minimization methods

There exist different methods that to a certain extent can minimize structural distortions on board spacecraft. These methods are usually adapted and optimized depending on the perturbation frequency. The method presented in this work aims to counteract perturbations at the low-frequency end of the spectrum. The effect of this type of perturbations can be regarded in most of the cases as quasi-static. To assess the performance of the presented method in comparison to current technologies, the presentation of distortion minimization methods included in this section is focused on those methods that have been implemented and investigated up to the moment to counteract quasi-static distortions. This type of quasi-static control is also referred to by some authors [8, 49] as shape control to differentiate it from the dynamical structural control related to the attenuation of high-frequency perturbations, namely vibrations. The methods that are used to attenuate high-frequency perturbations are based on the same physical principles as those presented here but with a stronger focus on the use of damping devices [50] and vibration isolation platforms [51, 52]. The attenuation of high-frequency perturbations is out of the scope of this work and, therefore, is not presented here in detail.

A first important distinction that can be introduced to classify structural control methods is between passive control methods and active control methods. Passive control methods do not require an energy source to attain a certain level of structural control. These methods represent the traditional approach to structural control and, therefore, have reached a high level of technological maturity. However, the inherent physical limitations of passive approaches have fostered the interest in developing higher-performance methods based on active control. The most relevant specific methods belonging to these two groups are presented in the subsections that follow.

2.3.1 Passive control methods

Passive methods of structural control are based essentially on two techniques: the construction of the structure with materials that have appropriate mechanical properties and the structural design itself. Additionally, minimization of thermomechanical distortions can also be indirectly achieved by minimizing thermal changes. Thus, passive thermal control technologies can also be regarded as methods of structural stabilization against thermomechanical perturbations.

Material selection

A basic approach to minimize the effect of thermomechanical distortions consists in using materials with specific properties so that they remain dimensionally stable when thermal conditions change. An important property to characterize the thermomechanical response of a material is the coefficient of thermal expansion (CTE), which expresses the expansion of a given material in relation to a change of its temperature. This coefficient can be expressed in terms of the linear change of the material in one dimension, in which case it is known as the linear coefficient of thermal expansion and it is mathematically defined as

$$\alpha = \frac{1}{l_0}\frac{dl}{dT} \tag{2.1}$$

where l_0 represents the initial length measurement, l is the length and T the temperature. This coefficient is usually expressed in units of µm/m/K or directly in $10^{-6}/K$. If the material is considered isotropic, the CTE defined by 2.1 can be assumed to be the same in the three spatial directions. There exists a variety of materials that have been developed to exhibit extremely low CTE values. This includes ceramic materials, such as Zerodur and silicon carbide, as well as metal alloys, such as Invar. Very small CTE values can also be achieved with composite materials. However, composite materials also experience distortions due to moisture desorption once they are transferred to space, which can be characterized by the coefficient of moisture expansion (CME). Composite materials are used to achieve high values of dimensional stability for ground applications, but whether the same level of performance can be achieved in space is still a matter of investigation [53].

Apart from the CTE, there are other material properties that determine the thermal response induced by perturbations. Two important thermal properties are thermal conductivity and heat capacity. Thermal conductivity is a measure of the heat transfer rate across a material. In materials with high thermal conductivity, heat is transferred at a higher rate. Heat capacity is related to the amount of heat required to induce a temperature change in a material. This property determines the transient behavior of a material when thermal perturbations arise. To achieve high dimensional stability different strategies in terms of material selection can be implemented. Low conductivity is beneficial to keep the temperature changes localized in the surroundings of the perturbation, whereas high conductivity is better to quickly distribute thermal changes across the entire structure and thus minimize global distortions. Similarly, there are cases for which a high or a low value of heat capacity is desirable to minimize a specific measure of the dimensional distortion. The appropriate selection of these properties depends strongly on the particular structural design and therefore has to be performed on a case-by-case basis.

There are also mechanical properties that influence the thermomechanical response of a material. These are the Young's modulus and the Poisson's ratio. The Young's modulus is a measure of the stiffness of the material. This property gives the relation between the strain and the stress in the material and thus, it is necessary to determine the displacement induced by a mechanical load. The Poisson's ratio is also a key parameter in displacement calculations because it gives the relation between transverse and axial strains.

Another aspect to take into account is that materials that have beneficial properties for dimensional stability may also exhibit other mechanical properties that are unfavorable for use in space. For instance, it is to some extent important to use lightweight materials to minimize the total spacecraft mass and it is also important to have a certain level of stiffness to withstand the shock and vibrations loads associated with the launch phase. Both are important factors when the overall spacecraft design is taken into account. Therefore, it is often not possible to select materials based only on the optimization of dimensional stability.

Structural design

The structural design is a major factor in determining the mechanical response of the structure including the induced distortions by thermal perturbations. There exist several standard techniques to improve the dimensional stability of a structure based on its design.

One first option to increase the dimensional stability of a structure is to design it based on a combination of materials with positive and negative CTE values. With the proper combination of materials and structural design it is possible to construct structures that exhibit minimal distortions in some directions [54]. With this technique, it is possible to achieve high structural stability in some particular direction but the design complexity increases substantially if distortions over several directions need to be minimized.

Another purely passive approach consists in spatially isolating the sources of perturbations. Those instruments on board the spacecraft that are expected to disturb the environment should be mounted on locations where their thermal influence can be minimized. This isolation can be achieved from a mechanical point of view by increasing the distance between perturbing instruments and the regions where stability is needed. It can also be achieved from a thermal point of view by using insulating layers and minimizing the heat transfer from perturbation sources, as explained in the next subsection. The usual practice in spacecraft design is to include a dedicated platform where the most precise instrumentation is mounted. These platforms are normally known as optical benches, they are constructed with highly stable materials and to the maximum possible extent isolated from onboard disturbances.

Misalignments between different points in the structure induced by thermal fluctuations can also be minimized if the structure is allowed to expand freely. If the structural expansion is not constrained, there appear distance changes between different points in the structure but the relative orientation between them remains constant. One approach to allow the free expansion of a stable structure, such as an optical bench, but at the same time provide some structural support to connect it to the main spacecraft structure is to use isostatic mounts. Isostatic mounts are statically determinate systems in which only the six degrees of freedom corresponding to the rigid body motion have been constrained. Rigid bodies can translate and rotate along the three spatial axes. If each of these degrees of freedom is singly constrained, the body is able to expand freely. If conversely, some of these degrees of freedom are redundantly constrained, then internal stresses arise when the struc-

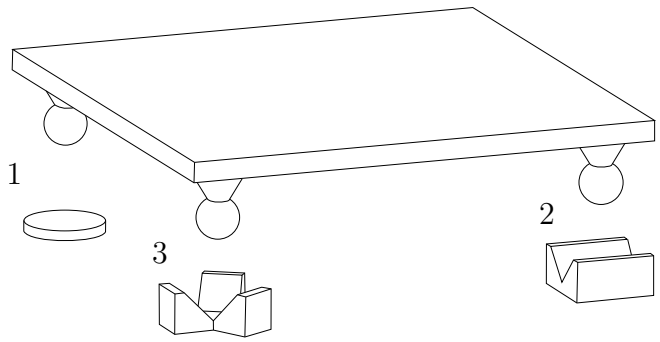

Figure 2.9: Representation of the 3-2-1 isostatic mount.

ture experiences thermal changes and its expansion is not uniform, which introduces distortions. The theoretical definition of an isostatic system can never be fully implemented due to the non-ideal behavior of real structural connections. However, it is a useful principle to minimize the mechanical interaction between two connected structures.

There exist several approaches to implement this principle. One basic approach is known as the 3-2-1 configuration [55] and it is based on mounting the structure on three contact points. In one of these contact points only the translation in the three spatial axes is constrained. The translation of the second point is constrained only in two axes, both perpendicular to the line that connects it to the first point. Finally, the third point is constrained to remain in the same plane defined by the three points, therefore, its translation is constrained in only one axis. An example of this setup is represented in Figure 2.9. This figure shows a plate that is partially constrained at three of its corners. Point 1 is only simply supported on a flat surface, point 2 can only move along the line determined by a V-groove and point 3 is supported on a sphere that can rotate in a fixed position.

The advantage of this type of systems is twofold. On the one hand the precise structure is able to expand freely and, as a result, thermal expansions have just a scaling effect on the structure. On the other hand, distortions in the supporting structure do not translate into distortions in the stable structure.

There exist alternatives to the 3-2-1 configuration that also result in an isostatic system. An approach that is frequently used in optical systems, for instance, to connect a primary and a secondary mirror, is the hexapod concept. This passive approach consists of six struts of constant length, or equivalently three bipods, that connect two structures. Variations of this hexapod mounting with adjustable lengths have also been investigated to provide active vibration control in space platforms [5].

Thermal control

An indirect strategy to increase the thermomechanical stability consists in implementing high-performance techniques of thermal control. These have the objective of minimizing temperature fluctuations, which as a result prevents the emergence of distortions induced by thermal expansions and contractions. There is an extensive variety of physical phenomena that can be exploited to provide thermal control.

This section focuses only on the most relevant passive control technologies that are used in the aerospace industry.

Passive thermal control technologies for spacecraft are based on the fact that only two basic heat exchange mechanisms exist in space: radiation and conduction. Passive thermal control methods introduce elements that modify how the heat is exchanged through these mechanisms. By properly implementing these methods it is possible to modify the temperature perturbations and gradients that arise within a structure that requires stability.

A first option of passive thermal control consists in modifying the radiation exchange between different bodies. This is mainly determined by the view factors between them, which are geometrically defined and quantify the proportion of radiation leaving one surface that can reach another surface. Therefore, a first option to modify the radiation heat exchange between different bodies is to modify the setup geometry. If it is known beforehand that a given instrument is expected to radiate a changing amount of thermal energy, it is possible to attenuate the impact of its disturbance by minimizing the view factor between the instrument and the stable structure.

Another way of modifying the radiation exchange between surfaces consists in adjusting their thermo-optical properties, namely its absorptivity and emissivity. These properties can be modified through different coatings and surface treatments depending on the intended effect. For instance, having internal surfaces with high values of emissivity can be beneficial to increase the radiation exchange between them and thus achieve a more uniform temperature field, which minimizes thermal gradients. In other cases it may be more beneficial to have a low value of emissivity in order to achieve a certain degree of insulation. Different values of absorptivity and emissivity at the external surfaces of the spacecraft also play an important role to determine the range of temperatures that is reached within the spacecraft. It is also usual to cover spacecraft surfaces with Multi-Layer Insulation (MLI) in order to achieve extremely low values of emissivity, or with Optical Solar Reflectors (OSR) to minimize the absorption of solar radiation. The spacecraft can also be equipped with radiators, which are specifically designed to maximize the amount of heat radiated to space in order to keep the spacecraft temperature within acceptable ranges.

Heat exchange between different elements in the spacecraft can also be controlled by modifying the conduction contribution. This can be adjusted by installing elements with different geometries and conductivities that modify the heat transfer paths. In some cases it may be desired to increase the heat transfer between two bodies in contact. This can be achieved through filler materials that are installed on the contact surface to increase the efficiency of the heat exchange. A similar effect can be achieved by using doublers, which are solid panels usually made of aluminum that increase the area of contact between two bodies in order to increase the amount of exchanged heat. It is also usual to install thermal straps, which are used to thermally connect two bodies that are structurally decoupled. Similar elements exist that can be tailored to specific needs but that are based on the same physical principle.

There exist also passive devices that without the use of energy can modify the heat transfer paths within spacecraft. Among these options there are heat pipes [56], which make use of capillarity and pressure differences to establish a closed loop with

a two-phase fluid in order to transport heat. These devices are often installed in spacecraft to create isothermal surfaces.

The thermal control systems presented in this section are usually implemented with the only objective of achieving thermal equilibrium and thermal stability within the requirements of a particular element. It can be considered an indirect benefit that a high level of thermal stability implies also a proportional level of thermomechanical stability. The achieved performance is nevertheless limited by material properties and design uncertainties. These thermal control methods can be combined with the other available methods of passive structural control to attenuate thermomechanical distortions up to a certain point. If higher performance is required, it is necessary to consider active structural control methods.

2.3.2 Active control methods

The field of active structural control encompasses a wide variety of techniques that can be implemented and adjusted to particular needs in different fields. A general framework to classify the different types of structures that belong to this field was proposed by Wada [57]. According to this classification, it is first possible to distinguish between those structures that are equipped with sensors, known as sensory structures, and those that are equipped with actuators, known as adaptive structures. At the intersection between these two sets of structures there are those with both sensors and actuators connected through a feedback loop. These type of structures are referred to as controlled structures. This classification framework is represented in Figure 2.10.

Within the controlled structures type it is then possible to distinguish among further subsets of structures according to more subtle characteristics. First, the subset of active structures is defined, which are those structures in which the sensors or the actuators are highly integrated into the structure to the point that they also fulfill structural functions. Within active structures it is then possible to define also the intelligent structures, which are those active structures that additionally have a distributed control architecture. In part of the literature, this type of structures are also referred to as smart structures.

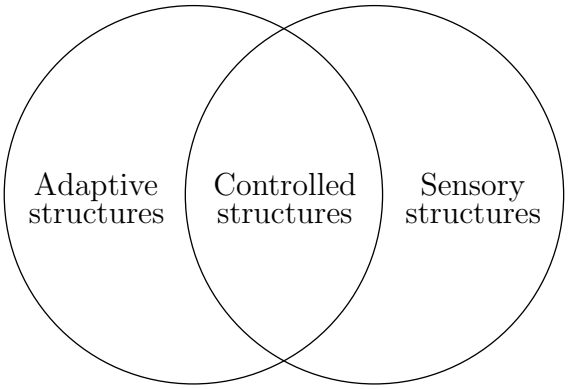

Figure 2.10: Classification of types of structures [57].

Based on these definitions, the field of controlled structures is still a very general one because there are many aspects of a structure that can be controlled. There can be controlled structures that only control specific mechanical properties, such as its stiffness or its damping. There can be controlled structures to control only its thermal properties, such as its temperature or conductivity. There is a large variety of options and this work is focused on the control of distortions, which includes only those controlled structures that ultimately control the position of some discrete points.

There exist different sensor and actuator technologies that can be used to build controlled structures for distortion control. The most relevant options that have been suggested and investigated up to date are presented here in detail.

Actuator technology

A top-level classification of actuator technologies for distortion control can be established depending on whether they act on the force or on the strain field. Force actuators are used to control the applied mechanical load at some specific points of the structure. The most common type of force actuators, particularly for applications related to vibration control in space structures, are linear voice coils [58]. Other technologies such as hydraulic actuators are used for similar purposes in civil engineering [59]. Force actuators are also implemented for static shape control. For instance, in the field of active optics, the mirror surface of a telescope is controlled with actuators in order to minimize aberrations. This technique has been applied to the JWST, in which the rigid body motion of each mirror segment is controlled to increase the optical performance [60].

Some authors distinguish between force actuators and displacement actuators, depending on whether they are commanded through displacement or force inputs [61]. Displacement actuators are usually based on machine screws driven by DC motors, but the end result is also a local mechanical load applied to the structure. They have been mostly implemented in actuated space structures where some truss members have adjustable lengths [62]. The limitation of force and displacement actuators is that they have only a local effect in the surroundings of their mounting point. A distributed actuation is more easily accomplished with strain actuators, which can be both mounted at the surface or embedded within the structure to modify the strain field.

Strain actuators based on many different physical phenomena are being considered for different applications [7]. The five most relevant mechanisms in which recent research on controlled structures has been focused are the following:

- Piezoelectric effect: Piezoelectric materials experience shape distortions as a reaction to an electrical field applied to them, the relation between the two phenomena is relatively linear. Some examples of such materials include piezoceramics and some polymers. These can be used to produce strain actuators that are controlled by the applied electric field. Several control methods, both for dynamic and quasi-static shape control, have been suggested using piezoelectric actuators [8].

- Electrostriction: This is a property similar to the piezoelectric effect. In this case, electrostrictive materials also experience deformations under the effect of an electric field. However, the relation is caused by a different physical effect to piezoelectricity and it is nonlinear. Based on materials with this property, it is possible to build strain sensors that react to changes in the electric field.
- Magnetostriction: Magnetostrictive materials are materials in which the magnetic and mechanical states are coupled. Thus, they experience deformations as a reaction to an applied magnetic field. This property can be the basis for strain actuators that are controlled through the applied magnetic field. By mounting these type of actuators at different points of the structure it is then possible to modify the strain field in the structure.
- Shape memory alloys: Shape memory alloys are alloys that experience a reversible phase change associated with a change in strain and that can be induced by heating or cooling the material. Therefore, they can be used to introduce strain loads that can be controlled through thermal inputs in the material. Given that this phenomenon relies on a thermal change, it has a large time constant and thus, it is only applicable for shape control purposes and not for strain actuation on high-frequency applications.
- Thermal strain: Thermal strain actuation is based on changing the temperature of some control elements in order to induce a strain change through material expansion. This approach was first suggested by Haftka and Adelman [49]. A similar approach based on the use of heaters was suggested by Zhang [63] to provide quasi-static shape control of thin-walled space structures such as antennae and solar arrays. This approach has also been investigated for ground applications, particularly for precise machines [64]. This is also the basis for the control method presented in this work, in which the shape of a stable structure is controlled by strategically introducing heat at some points.

Sensor technology

The same distinction that exists between force and strain actuators can also be considered to distinguish between two basic types of sensors: accelerometers and strain sensors. Accelerometers are efficient to measure the high-frequency structural distortions induced by vibrations. At the low-frequency range of perturbations, quasi-static distortions can be more efficiently measured by strain sensors. The three basic options that are available to measure strain are the following:

- Strain gauges: Strain gauges consist of a very thin conductor filament that is bonded at some point of the structure. The strain field of the structure induces a proportional deformation of the strain gauge. This results in a change in resistivity of the conductor in the gauge which can be measured and directly associated to the magnitude of the applied strain. These sensors are frequently used to measure the strain field of some structure. However, they provide only a localized measurement and, consequently, several sensors are necessary to obtain a global strain characterization of the structure, which can become unpractical.

- Piezoelectric sensors: The piezoelectric effect that can be exploited to produce strain actuators can also be the basis for piezoelectric sensors. In this case, by measuring the electrical signal at the terminals of a piezoelectric device it is possible to derive the strain acting on it. As in the case of the actuators, piezoelectric sensors can be built from piezoceramic material or polymer films. In the latter case, it is possible to embed the sensors in a composite matrix, which can be advantageous to obtain a distributed measurement of the strain field. Additionally, it is also possible to simultaneously use piezoelectric elements as both sensors and actuators, this technology is known as self-sensing piezoelectric actuation [65].
- Optical fiber sensors: Optical fiber sensors are the most recently developed type of sensors to measure strain. The working principle of this type of sensors consists in measuring changes in some property of the signal that is transmitted through an optical fiber. These changes can be directly related to a change in the strain in the structure. A specific type of optical fiber sensors that are suggested for spacecraft applications are known as Fiber Bragg Gratings (FBG) [66]. One advantage of optical fiber sensors is that, as in the case of piezoelectric sensors, they can be both mounted at the surface or embedded within a fiber-reinforced polymer.

Additionally to these technologies, when the strain in the structure is induced uniquely from thermal perturbations, it is possible to derive the displacement field based only on temperature measurements in combination with an accurate thermomechanical model. This is the selected option for this work, as presented in Section 5.3.1 of Chapter 5. If an accurate thermomechanical model is available, it becomes possible to reconstruct the global displacement field based on the measurements of relatively few thermal sensors. However, if mechanical perturbations are also present it becomes necessary to conduct additional measurements with one of the presented technologies in order to derive accurate estimations of the strain field.

Chapter 3

Thermal Analysis Framework

A crucial step in developing a method to control thermomechanical distortions is to have a model that properly describes the thermal behavior of the system. This model must be able to derive the changes in the thermal field that arise as a consequence of changes in the thermal boundary conditions. In particular, the thermal model must be able to calculate the thermal response of the system when heat control sources and heat perturbations act on the structure.

This chapter starts with a brief introduction to the thermal analysis methods that are more commonly used in the aerospace industry. This is included in Section 3.1 and presents the finite difference method, the lumped parameter method and the finite element method (FEM). Based on the characteristics of these different methods, the FEM is selected in this thesis to develop a thermal model. A detailed formulation of this approach, particularized for the specific thermal conditions considered in this thesis, is presented in Section 3.2 along with the procedure to solve steady-state and transient problems. This section includes the presentation of a method to introduce the radiation contribution into the model based on the combination of the FEM and the general problem of radiation exchange [67]. The FEM formulation includes in Subsection 3.2.4 an expansion of the known frequency-domain approach to the thermal problem [68] to enable its application on a finite element mesh. The chapter ends with the presentation of the thermal modal representation in Section 3.2.5.

3.1 Thermal Analysis Methods

Thermal analysis methods are mathematical techniques that allow the calculation of the temperature field and heat transfer within a given continuous medium. This calculation is performed under consideration of some initial and boundary conditions expressed in terms of heat fluxes or temperatures. These techniques are applied both to calculate the steady-state or the transient response of a system.

The relation between the variables involved in the thermal transfer problem can be expressed in terms of partial differential equations (PDEs). Thermal analysis methods approximate these PDEs and solve them numerically to obtain an approximation of the real solution.

Based on the conservation of energy, the basic PDE describing the heat transfer problem is expressed as [10]

$$\rho c_p \frac{\partial T}{\partial t} = -\left(\frac{\partial q_x}{\partial x} + \frac{\partial q_y}{\partial y} + \frac{\partial q_z}{\partial z}\right) + Q \tag{3.1}$$

where ρ and c_p are the density and the heat capacity of the material in the considered domain, respectively. T is the temperature, the three q terms represent the heat flux in each spatial direction and Q is the volumetric heat generation. The independent variables in the equation are the time t and the coordinates x, y and z.

The heat fluxes q can be expressed as a function of the temperature introducing Fourier's law, which relates the heat fluxes by conduction in an isotropic solid to the temperatures according to

$$\vec{q} = -\lambda \nabla T, \tag{3.2}$$

where λ is the conductivity of the material. Equation 3.2 can be expressed for each component as

$$(q_x, q_y, q_z) = \left(-\lambda \frac{\partial T}{\partial x}, -\lambda \frac{\partial T}{\partial y}, -\lambda \frac{\partial T}{\partial z}\right). \tag{3.3}$$

Introducing now the relations from 3.3 into 3.1 results in

$$\rho c_p \frac{\partial T}{\partial t} = \frac{\partial}{\partial x}\left(\lambda \frac{\partial T}{\partial x}\right) + \frac{\partial}{\partial y}\left(\lambda \frac{\partial T}{\partial y}\right) + \frac{\partial}{\partial z}\left(\lambda \frac{\partial T}{\partial z}\right) + Q. \tag{3.4}$$

This equation can be further simplified by considering constant conductivity λ throughout the material. Then,

$$\rho c_p \frac{\partial T}{\partial t} = \lambda \nabla^2 T + Q. \tag{3.5}$$

There are essentially four types of boundary conditions that can be defined at the surface of the body or domain under study. One option is to prescribe the temperature evolution at the surface

$$T(x, y, z, t) = T_s(x, y, z, t) \qquad \text{for} \qquad x, y, z \in S_1. \tag{3.6}$$

It is also an option to prescribe instead the heat flux at the surface, which can be specified in terms of a given function

$$\vec{q} \cdot \vec{n} = q_s(x, y, z, t) \qquad \text{for} \qquad x, y, z \in S_2 \tag{3.7}$$

where $\vec{n}$ is the normal vector to the surface. The heat flux can also be expressed as a convection boundary condition

$$\vec{q} \cdot \vec{n} = h(T_f - T(x, y, z, t)) \qquad \text{for} \qquad x, y, z \in S_3 \tag{3.8}$$

where h is the heat transfer coefficient and T_f the temperature of the surrounding flow. Finally, the boundary condition can be expressed for radiation exchange as

$$\vec{q} \cdot \vec{n} = \sigma \varepsilon (T_s^4 - (T(x, y, z, t))^4) \qquad \text{for} \qquad x, y, z \in S_4, \tag{3.9}$$

where σ is the Stefan-Boltzmann constant, ε is the emissivity of the surface and T_s the temperature of the surrounding space.

Additionally, it is necessary to define an initial state as

$$T(x, y, z, t_0) = T_0(x, y, z) \qquad \text{for} \qquad x, y, z \in \Omega. \tag{3.10}$$

where Ω represents the entire volume in the domain of analysis.

There exists a variety of numerical methods that solve 3.5 differing in accuracy and mathematical complexity. The discussion in this chapter is centered on the three most relevant methods that are currently used in the aerospace industry. These are the finite difference method, the lumped parameter method and the finite element method.

3.1.1 Finite Difference Method (FDM)

The Finite Difference Method (FDM) is based on approximating the continuous derivatives in 3.5 by differences between the variable values in a limited set of nodes. Mathematically, this is expressed as

$$\frac{df(x)}{dx} = \lim_{\Delta x \to 0} \frac{\Delta f}{\Delta x} = \lim_{\Delta x \to 0} \frac{f(x + \Delta x) - f(x)}{\Delta x} = \frac{f(x + \Delta x) - f(x)}{\Delta x} + \mathcal{O}(\Delta x), \tag{3.11}$$

which indicates that if the truncation error $\mathcal{O}(\Delta x)$ is negligible, then the derivative of a function $f(x)$ can be approximated from its value evaluated at two different points, x and $x + \Delta x$. As it is seen in 3.11 the magnitude of the error in the approximation is proportional to the magnitude of the step Δx.

To apply the FDM it is necessary to discretize the domain of analysis. The temporal domain is discretized in time steps of duration Δt and the spatial domain is discretized in nodes separated by distances Δx, Δy and Δz as represented in Figure 3.1.

Based on the concept of finite differences, the left-hand side of Equation 3.5 applied at node n can be approximated with a forward difference scheme using

$$\frac{\partial T_n}{\partial t} = \frac{T_n^{t+\Delta t} - T_n^t}{\Delta t} + \mathcal{O}(\Delta t) \tag{3.12}$$

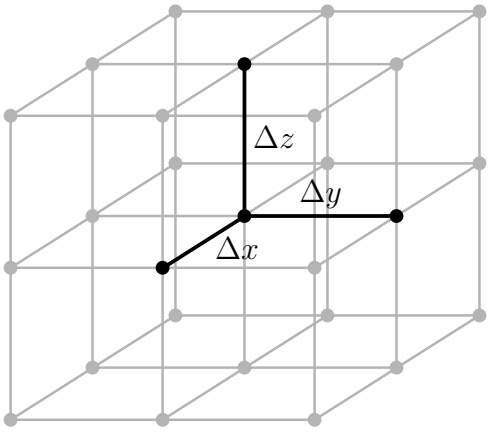

Figure 3.1: Nodal discretization in the FDM.

or with a backward difference scheme using

$$\frac{\partial T_n}{\partial t} = \frac{T_n^t - T_n^{t-\Delta t}}{\Delta t} + \mathcal{O}(\Delta t). \tag{3.13}$$

In both cases $\mathcal{O}(\Delta t)$ represents a truncation error proportional to Δt.

To approximate the right-hand side of Equation 3.5 it is necessary to approximate the second derivative of T with respect to x, y and z. The procedure is the same for the three variables and, therefore, only the approximation of the partial derivative with respect to x is presented here. The starting point is a Taylor series expansion of the temperature T as a function of x,

$$T(x_n+\Delta x, y_n, z_n) = T(x_n, y_n, z_n)+\Delta x\frac{\partial T}{\partial x}\bigg|_{x_n} +\frac{\Delta x^2}{2}\frac{\partial^2 T}{\partial x^2}\bigg|_{x_n} +\frac{\Delta x^3}{3!}\frac{\partial^3 T}{\partial x^3}\bigg|_{x_n} +... \tag{3.14}$$

In order to simplify the following expressions the notation ijk is introduced. The variable i represents the node number in the x direction, j is used for the y direction and k for the z direction. Therefore, the node n can be identified with the notation ijk and its surrounding nodes are represented in Figure 3.2. Rewritting Equation 3.14 with the ijk notation results in

$$T_{i+1,j,k} = T_{i,j,k} + \Delta x\frac{\partial T}{\partial x}\bigg|_{i,j,k} + \frac{\Delta x^2}{2}\frac{\partial^2 T}{\partial x^2}\bigg|_{i,j,k} + \frac{\Delta x^3}{3!}\frac{\partial^3 T}{\partial x^3}\bigg|_{i,j,k} + \mathcal{O}(\Delta x^4). \tag{3.15}$$

Equivalently, the Taylor series expansion at $i-1, j, k$ can be written as

$$T_{i-1,j,k} = T_{i,j,k} - \Delta x\frac{\partial T}{\partial x}\bigg|_{i,j,k} + \frac{\Delta x^2}{2}\frac{\partial^2 T}{\partial x^2}\bigg|_{i,j,k} - \frac{\Delta x^3}{3!}\frac{\partial^3 T}{\partial x^3}\bigg|_{i,j,k} + \mathcal{O}(\Delta x^4). \tag{3.16}$$

Adding Equations 3.15 and 3.16 results in

$$T_{i+1,j,k} + T_{i-1,j,k} = 2T_{i,j,k} + \Delta x^2\frac{\partial^2 T}{\partial x^2}\bigg|_{i,j,k} + \mathcal{O}(\Delta x^4), \tag{3.17}$$

and therefore,

$$\frac{\partial^2 T}{\partial x^2}\bigg|_{i,j,k} = \frac{T_{i+1,j,k} + T_{i-1,j,k} - 2T_{i,j,k}}{\Delta x^2} + \mathcal{O}(\Delta x^2). \tag{3.18}$$

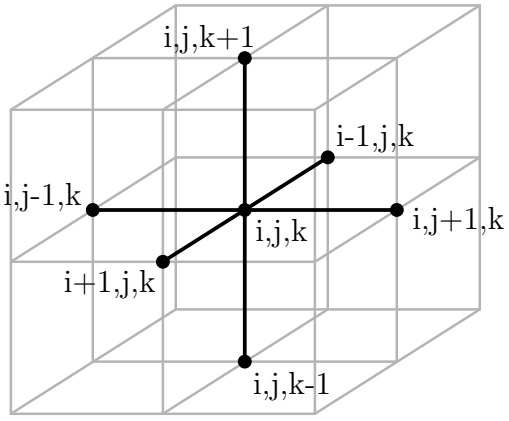

Figure 3.2: Nodal notation in the FDM.

This result is known as the second order central difference approximation because it takes into account the nodes at i as well as $i-1$ and $i+1$. This same process can be followed to approximate the derivatives with respect to y and z, resulting in

$$\left.\frac{\partial^2 T}{\partial y^2}\right|_{i,j,k} = \frac{T_{i,j+1,k} + T_{i,j-1,k} - 2T_{i,j,k}}{\Delta y^2} + \mathcal{O}(\Delta y^2) \quad \text{and} \tag{3.19}$$

$$\left.\frac{\partial^2 T}{\partial z^2}\right|_{i,j,k} = \frac{T_{i,j,k+1} + T_{i,j,k-1} - 2T_{i,j,k}}{\Delta z^2} + \mathcal{O}(\Delta z^2). \tag{3.20}$$

Neglecting the truncation errors and combining Equations 3.18, 3.19 and 3.20 with the time forward scheme from 3.12, results in what is known as a forward time centered space (FTCS) scheme of the FDM,

$$\begin{aligned} \rho c_p \left(\frac{T_{i,j,k}^{t+\Delta t} - T_{i,j,k}^{t}}{\Delta t} \right) = \; & \lambda \left(\frac{T_{i+1,j,k} + T_{i-1,j,k} - 2T_{i,j,k}}{\Delta x^2} \right) \\ & + \lambda \left(\frac{T_{i,j+1,k} + T_{i,j-1,k} - 2T_{i,j,k}}{\Delta y^2} \right) \\ & + \lambda \left(\frac{T_{i,j,k+1} + T_{i,j,k-1} - 2T_{i,j,k}}{\Delta z^2} \right) + Q_{i,j,k}. \end{aligned} \tag{3.21}$$

Equation 3.21 can now be written for all the nodes and solved to calculate the T values at $t = t + \Delta t$. This equation takes into account the heat transfer through conduction between the different nodes. To consider also heat exchange through convection and radiation it would be necessary to apply the corresponding fluxes as boundary conditions of the nodes representing external surfaces.

There exist also other integration schemes such as the backward time centered space (BTCS) or the Crank-Nicolson scheme [9]. These other procedures can differ in terms of the numerical stability they provide and the magnitude of truncation errors. However, the fundamental idea behind its implementation remains the same.

The obtained result of the FDM is an approximation of the real function T at some specific locations, corresponding to the nodes in the mesh, and for some specific time points. The main advantage of this method is that it can be quickly implemented and it results in a system of equations that can be solved using standard numerical techniques.

This method is computationally efficient and reliable when it is applied to bodies with a simple geometry. However, it is not possible to efficiently implement this method to model a complex geometry. As presented, this method requires the geometry to be meshed using a rectangular grid. Therefore, it is not prepared to mesh curved surfaces while attaining high levels of detail. Refining the mesh can help in some cases but it often results in an extremely large system of equations that is computationally expensive to solve. Given that the rectangular grid must be maintained along the entire domain, it is not possible to apply only a local mesh refinement at some regions of the geometry.

Although some finite difference approaches using irregular grids have been suggested [69], these techniques lose the mathematical simplicity on which the FDM is based and do not present a clear advantage in front other techniques such as FEM (see Section 3.1.3).

3.1.2 Lumped Parameter Method (LPM)

The Lumped Parameter Method (LPM) applied to thermal problems is based on the analogy between thermal and electrical phenomena. Heat flow can be seen as an analog to current, temperature difference as an analog to voltage difference, heat sources can be equivalent to current sources and thermal capacitance can be understood as electrical capacitance. From this perspective, the thermal and the electrical problems can be described with the same equations.

To implement the LPM the continuous medium to be analyzed is first discretized into a network of N nodes. Each node represents an isothermal volume with its thermal properties lumped in one point. It is possible to use a similar discretization scheme to the one followed for the FDM. However, it is also common to group larger volumes representing entire instruments or spacecraft parts into one single node.

These nodes are assumed to exchange heat through conduction, radiation and if necessary convection. This heat exchange is represented in the LPM through link parameters that represent conductors between nodes. Through these link parameters Equation 3.5 is rewritten into a system of equations relating the temperatures at each of the N nodes in the network. The equation for node n is

$$C_n\dot{T}_n = \sum_{m=1}^{N} K_{nm}(T_m - T_n) + \sum_{m=1}^{N} R_{nm}(T_m^4 - T_n^4) + H_n(T_f - T_n) + Q_n, \qquad (3.22)$$

where T represents temperature, C is the heat capacity and Q is a heat source. The link parameters are K_{nm}, R_{nm} and H_n. K_{nm} quantifies the heat exchange through conduction between nodes n and m, R_{nm} quantifies the nonlinear heat exchange through radiation and H_n the exchange through convection with the surrounding flow at a temperature T_f.

For structures operating in space the convection terms can be neglected. Therefore, Equation 3.22 becomes

$$C_n\dot{T}_n = \sum_{m=1}^{N} K_{nm}(T_m - T_n) + \sum_{m=1}^{N} R_{nm}(T_m^4 - T_n^4) + Q_n. \qquad (3.23)$$

The numerical values for the link parameters K_{nm} and R_{nm} can be derived from the geometrical and physical properties of the system. There exist different approaches to calculate these parameters that depend on the discretization method and differ in terms of the required computational effort and achieved accuracy. Some methods are based on experimental fitting methods and on correlations with empirical data from similar structures. Other methods derive the parameters analytically based on known properties of the structure.

One analytical possibility, resulting in the expression presented in [70], consists in deriving the conduction link parameters from a finite difference approximation and the radiation link parameters using the absorption factors [71] (see Appendix A for details). This results in the following relation:

$$C_n\dot{T}_n = \sum_{n=1}^{N} \left(\frac{\lambda_{nm} A_{nm}}{l_{nm}} (T_m - T_n) \right) + \sum_{m=1}^{N} \left(\sigma \varepsilon_n A_n B_{nm} (T_m^4 - T_n^4) \right) + Q_n, \qquad (3.24)$$

where the conduction link parameter K_{nm} from Equation 3.23 has been expressed in terms of the conductivity λ, the cross section A and the distance l between nodes n and m. The radiation link parameter R_{nm} has been expressed as a function of the Stefan-Boltzmann constant σ, the emissivity ε of node n, the external area of the node A and the absorption factor B_{nm} between nodes n and m.

Equation 3.24 still has to be integrated in time if the transient response needs to be obtained. A finite difference scheme like the one represented by 3.12 can be applied to this purpose, resulting in

$$C_n \frac{T_n^{t+\Delta t} - T_n^t}{\Delta t} = \sum_{n=1}^{N} \left(\frac{\lambda_{nm} A_{nm}}{l_{nm}} (T_m - T_n) \right) + \sum_{m=1}^{N} \left(\sigma \varepsilon_n A_n B_{nm} (T_m^4 - T_n^4) \right) + Q_n. \tag{3.25}$$

This equation can be written for the N nodes in the network resulting in a system of equations that can be solved to calculate the thermal evolution of the system.

Lumped parameter methods have been traditionally used in several industries and are particularly popular in the field of electrical machine design [72]. In the aerospace industry it is the standard approach for software tools such as ESATAN[1] and SINDA[2].

The main advantage of the LPM is that it can be very fast to implement and it allows the setup of a thermal model for analysis at the initial stages of the design. In other words, LPM can be applied with a coarse level of discretization when little details about a structure are known. The achieved accuracy is proportional to the level of spatial discretization and can be sufficient for preliminary estimations.

The LPM is particularly suited when the focus of the thermal analysis is on the heat transfer between different parts of the domain and not in the thermal field itself. The accuracy achieved by the LPM is directly dependent on the accuracy of the link parameter estimation. Therefore, if there is uncertainty in the link parameters, this will directly translate into uncertainty in the results. The precise determination of the link parameters is, therefore, crucial to apply this method but can become very complex and prone to errors if high accuracy needs to be achieved, as it is the case for the problem presented in this thesis.

3.1.3 Finite Element Method (FEM)

The Finite Element Method (FEM) applied to thermal problems is a numerical method that approximates the thermal field described by the PDE 3.5 by dividing the domain into finite elements. Each of these elements has a specific geometrical shape and at least one node at each of its vertices and possibly more along its edges. A representation of some of the different geometrical shapes that can be used to construct finite elements in the FEM can be seen in Figure 3.3. It is also possible to combine different types of elements to mesh a single domain.

The thermal field inside one finite element is then defined by the values at each node of the element and a set of shape functions, which are functions with an

[1] https://www.esatan-tms.com

[2] https://www.mscsoftware.com/product/sinda

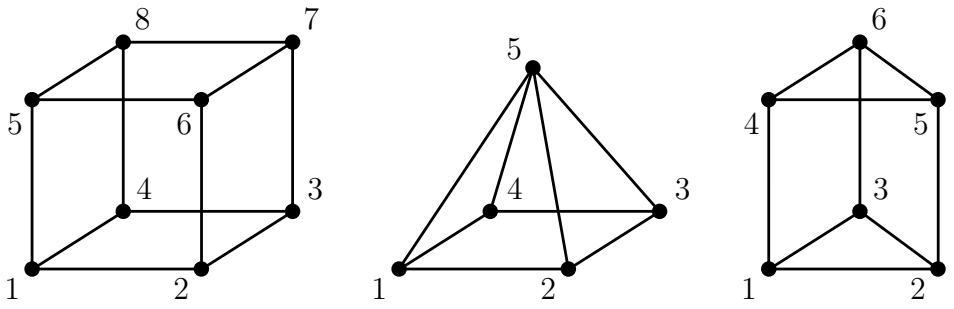

Figure 3.3: Different geometrical shapes to generate a mesh using the FEM.

assumed shape that interpolate the values obtained at each node. There exist several possibilities that can be chosen as shape functions but the most usual choice is to use a low order polynomial function. Then, the thermal field within one finite element is described with

$$\overline{T}(x, y, z, t) = \sum_{i=1}^{n_e} T_i(t) N_i(x, y, z), \tag{3.26}$$

where n_e is the number of nodes in one element, T_i is the temperature at each node and N_i is the shape function, which can be evaluated at any point defined by x, y and z. There are as many shape functions as nodes per element.

Once the shape functions have been defined, there exist several approaches to formulate the FEM. A frequent approach used in the thermal domain is known as the Galerkin method [10]. Instead of solving the heat transfer PDE 3.5, the Galerkin method solves its integration at each element multiplied by the shape function which acts as a weight factor. This is expressed as

$$\int_\Omega N_i \left(\rho c_p \frac{\partial \overline{T}}{\partial t} - \lambda \nabla^2 \overline{T} - Q \right) d\Omega = 0 \quad \text{for} \quad i = 1, 2, \ldots, n_e \tag{3.27}$$

Applying this expression, one equation for each shape function in each finite element is obtained. Once the equations have been derived for all the elements they can be combined to form the system of equations

$$[C]\{\dot{T}\} + [K]\{T\} = \{R_q\} + \{R_Q\}, \tag{3.28}$$

where $[C]$ is the thermal capacity matrix, $[K]$ is the conductivity matrix, $\{T\}$ is the vector that contains the temperature at each node, $\{R_q\}$ is the heat flux vector and $\{R_Q\}$ is the heat source vector. The details on the calculation of these matrices as well as the introduction of radiation terms can be found in Section 3.2.1.

The finite difference scheme described by Equation 3.12 can be introduced in Equation 3.28 in order to obtain the time evolution of the termal field. This results in

$$[C] \left(\frac{\{T\}^{t+\Delta t} - \{T\}^t}{\Delta t} \right) + [K]\{T\}^t = \{R_q\} + \{R_Q\}. \tag{3.29}$$

Additional vectors and matrices can be calculated to account for boundary conditions such as convection, radiation or applied heat fluxes at the surface of some elements.

The FEM is used in a wide variety of domains and is particularly popular in the field of mechanical and structural dynamics analysis. The increase in computational power in the last years has also facilitated the shift towards FEM in fields where traditionally the LPM or the FDM had been used.

The main advantage of the FEM in front of the FDM or the LPM is that it can easily handle complex geometries. The geometric shapes of the finite elements can be adapted to the shape of the entire domain and, therefore, there is no added complexity in analyzing curved geometries. The basic form of the FDM, instead, is limited to modeling the geometry with rectangular grids which can be a major disadvantage to model complex shapes.

One aspect that limits the implementation of the FEM in the thermal domain, and particularly in the aerospace industry, is the computation of the factors related to the radiation exchange [73]. This requires the computation of view factors between all the external surfaces of the elements in the domain. This is normally done using a ray tracing algorithm in combination with a Monte Carlo simulation [74] but the required computational effort can become prohibitive when the domain is meshed with a large number of finite elements. Recent research has been focused on reducing this computational effort using finite element reduction techniques [75] with the goal of fostering a transition from LPM towards FEM in the thermal domain.

On the other hand, the LPM can be a good choice when the only needed result is in the thermal domain, i.e. temperature distributions or heat fluxes. However, inefficiencies may arise if the thermal results obtained by the LPM are used as an input for a mechanical analysis based on another technique, usually the FEM. In this case it is necessary to use mapping tools that can consistently translate the results obtained in an LPM mesh into an input for a different FEM mesh.

The work presented in this thesis is focused on achieving thermomechanical control at high levels of accuracy, which means that a full thermomechanical model of the system needs to be developed. Therefore, it is decided that the optimal choice is to use the same numerical method for both the thermal and the mechanical analysis. In the presented case, this means using the FEM for both thermal and mechanical modeling. Even if this entails an additional computational effort in the thermal side, it is considered to be compensated by the benefits of not having to implement mapping tools between different numerical methods and the higher level of accuracy that can be achieved in the results.

3.2 Thermal Analysis in FEM

The FEM is the selected numerical method to derive the thermomechanical model of the structure that is subsequently used to develop a control strategy. Essentially, the thermomechanical FEM model consists of a thermal model in combination with a mechanical model. In order to clarify the notation used throughout this thesis, this section includes a brief presentation of the basic FEM formulation applied to the thermal problem. This formulation can be found in reference bibliography that presents the fundamentals of FEM [76] but it is particularized here for a baseline case used throughout the thesis to exemplify the application of the presented control

framework. This fundamental FEM formulation is then expanded to consider also the radiation exchange between elements. In addition to the standard ways of solving the steady-state and transient problems, presented in subsections 3.2.2 and 3.2.3, this section presents the development of a new approach to apply a frequency-domain technique [11, 68] on a thermal model in combination with the FEM.

3.2.1 Thermal FEM formulation

This section provides a short overview of the derivation of the FEM equations related to the thermal problem taking into account radiation exchange, external fluxes and internal heat generation. The detailed presentation on all the equations that have been followed to derive the thermal model for this thesis can be found in Appendix B.

The first step in formulating a FEM approach is to write the matrix form of Equations 3.26 and 3.27. Thus, the temperature in the domain is expressed as

$$\overline{T}(x,y,z,t) = \sum_{i=1}^{n_e} T_i(t) N_i(x,y,z) = [N]\{T\}, \tag{3.30}$$

where $[N]$ is a row vector containing the shape functions evaluated at (x,y,z) and $\{T\}$ is a column vector with the nodal temperatures. Similarly, the heat flux can be expressed as

$$q(x,y,z,t) = \{q\} = -\lambda[B]\{T\}, \tag{3.31}$$

where $[B]$ is the derivative matrix built with the gradient of the shape functions as

$$[B] = \nabla[N] = \begin{bmatrix} \dfrac{\partial N_1}{\partial x} & \dfrac{\partial N_2}{\partial x} & \cdots & \dfrac{\partial N_{n_e}}{\partial x} \\ \dfrac{\partial N_1}{\partial y} & \dfrac{\partial N_2}{\partial y} & \cdots & \dfrac{\partial N_{n_e}}{\partial y} \\ \dfrac{\partial N_1}{\partial z} & \dfrac{\partial N_2}{\partial z} & \cdots & \dfrac{\partial N_{n_e}}{\partial z} \end{bmatrix}. \tag{3.32}$$

As presented in Section 3.1.3, the Galerkin method is based on calculating the nodal temperatures $\{T\}$ that satisfy the condition

$$\int_\Omega N_i \left(\rho c_p \frac{\partial \overline{T}}{\partial t} - \lambda \nabla^2 \overline{T} - Q \right) d\Omega = 0 \quad \text{for} \quad i = 1, 2, \ldots, n_e \tag{3.33}$$

Introducing the expression 3.30 and 3.31 into 3.33 results in a system of equations expressed as (see Appendix B for details)

$$\begin{aligned} \left(\int_\Omega \rho c_p [N]^T [N] d\Omega \right) \{\dot{T}\} = &- \left(\int_\Omega \lambda [B]^T [B] d\Omega \right) \{T\} \\ &- \int_S [N]^T \{q\}^T \{n\} ds \\ &+ \int_\Omega [N]^T Q d\Omega, \end{aligned} \tag{3.34}$$

which can equivalently be written as

$$[C]\{\dot{T}\} + [K]\{T\} = \{R_q\} + \{R_Q\}, \tag{3.35}$$

with

$$[C] = \int_{\Omega} \rho c_p [N]^T [N] d\Omega, \tag{3.36}$$

$$[K] = \int_{\Omega} \lambda [B]^T [B] d\Omega, \tag{3.37}$$

$$\{R_q\} = -\int_{S} [N]^T \{q\}^T \{n\} ds \tag{3.38}$$

$$\text{and} \quad \{R_Q\} = \int_{\Omega} [N]^T Q d\Omega. \tag{3.39}$$

In the previous expressions $[C]$ is known as the heat capacity matrix, $[K]$ is the thermal conductivity matrix, $\{R_q\}$ is the heat flux vector and $\{R_Q\}$ is the heat source vector. These matrices and vectors are expressed for one finite element. They can be calculated for all the elements in the domain and assembled to build global matrices that take into account all the nodes in the mesh.

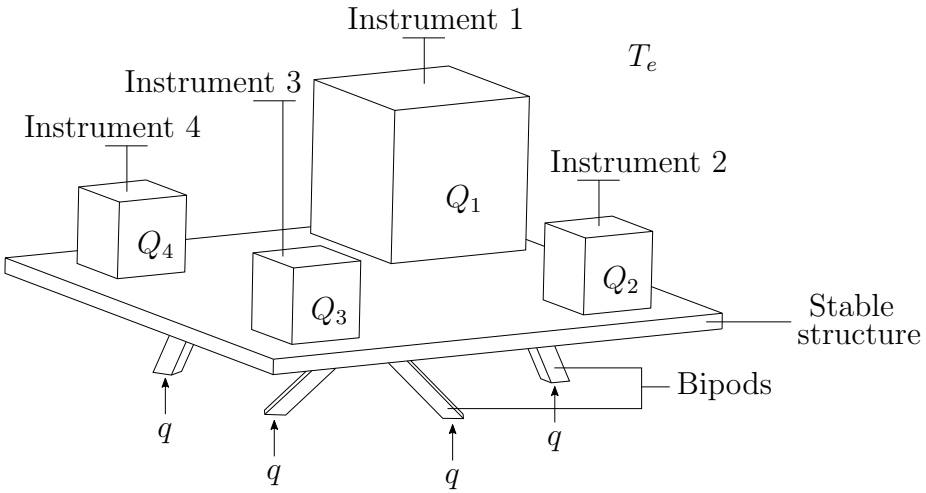

Figure 3.4: Baseline concept with boundary conditions.

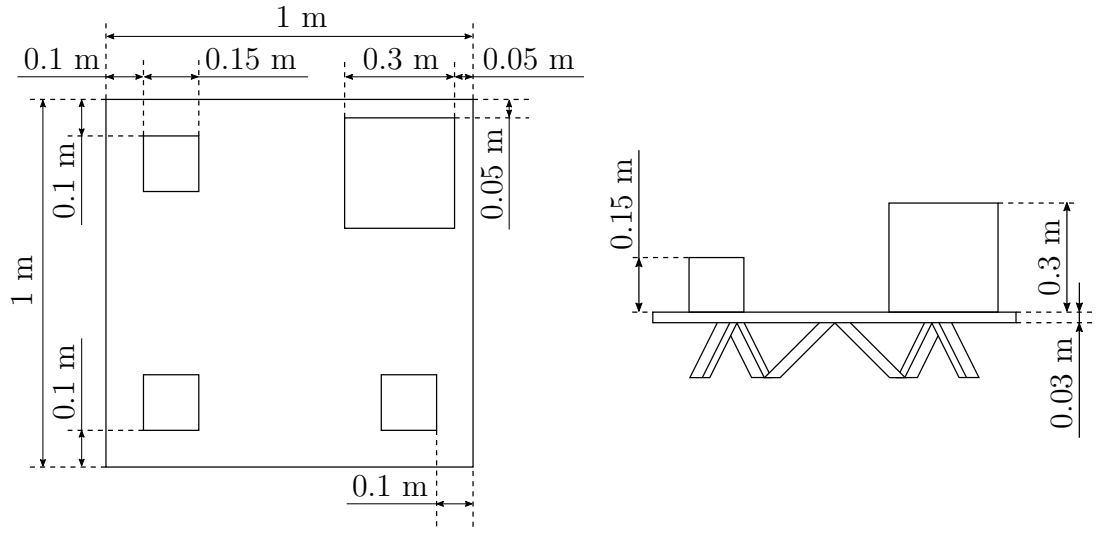

Figure 3.5: Main dimensions of the baseline concept.

Material properties						
Material	λ	c_p	ρ	E	ν	α
Silicon carbide	$190\,\frac{\mathrm{W}}{\mathrm{m\,K}}$	$400\,\frac{\mathrm{J}}{\mathrm{kg\,K}}$	$3150\,\frac{\mathrm{kg}}{\mathrm{m}^3}$	420 GPa	0.14	$2.00\,\frac{\mu\mathrm{m}}{\mathrm{m\,K}}$
Aluminum alloy	$120\,\frac{\mathrm{W}}{\mathrm{m\,K}}$	$900\,\frac{\mathrm{J}}{\mathrm{kg\,K}}$	$2750\,\frac{\mathrm{kg}}{\mathrm{m}^3}$	73 GPa	0.33	$23.1\,\frac{\mu\mathrm{m}}{\mathrm{m\,K}}$
Titanium alloy	$7\,\frac{\mathrm{W}}{\mathrm{m\,K}}$	$560\,\frac{\mathrm{J}}{\mathrm{kg\,K}}$	$4420\,\frac{\mathrm{kg}}{\mathrm{m}^3}$	114 GPa	0.34	$8.60\,\frac{\mu\mathrm{m}}{\mathrm{m\,K}}$

Table 3.1: Material properties for the considered baseline concept.

A baseline case that will be used throughout this thesis to exemplify the different steps of the control framework is presented here. This consists of a structural plate with four instruments that is supported by three bipods. This baseline concept is represented in Figure 3.4. Additionally, its main dimensions are indicated in Figure 3.5. In this baseline case, the structural plate is assumed to be made of silicon carbide and supported by bipods made of a generic titanium alloy. The four boxes represent different instruments and at this stage they are assumed to be made of an aluminum alloy. The material properties that need to be defined in order to analyze the thermomechanical behavior of the structure are the thermal conductivity (λ), the heat capacity (c_p), the density (ρ), the Young's modulus (E), the Poisson's ratio (ν) and the coefficient of thermal expansion (α). The assumed properties for the three considered materials are included in Table 3.1.

It is also necessary to define the emissivity at each surface, which depends on the applied surface treatments. In this case, it is assumed that the structural plate has an emissivity equal to $\varepsilon = 0.7$, which results in a relatively high radiation link with its surroundings. The bipods and the instrument boxes are assumed to be insulated to a higher degree, which is modeled with an emissivity of $\varepsilon = 0.2$.

As illustrated in Figure 3.4, the considered boundary conditions can include radiation exchange with an environment assumed to be at temperature T_e, applied heat fluxes at the base of the bipods (q) and internal heat sources at the instruments (Q). The representation of the meshed domain using hexahedrons that has been used to implement the FEM is included in Figure 3.6.

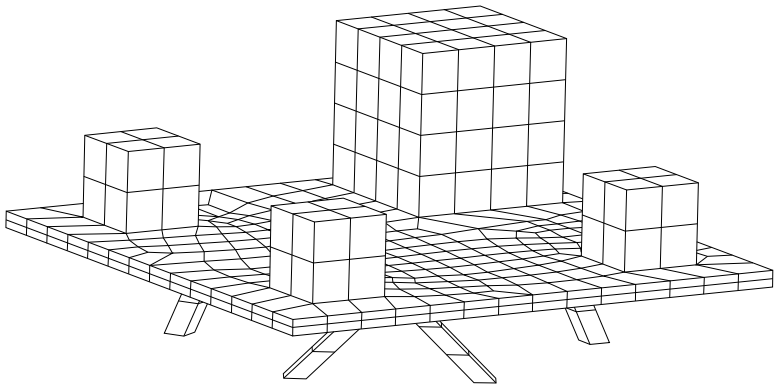

Figure 3.6: Meshed domain of the baseline concept.

The next mathematical step consists in introducing the radiation exchange terms to Equation 3.35, which can be modeled as boundary conditions. Physically, the radiation exchange can be described as an external flux applied to the surfaces of the domain. The magnitude of this flux is in turn dependent on the temperature of these surfaces.

To model the radiation exchange it is necessary to divide the external surfaces of the domain into smaller units. The approach presented in this work uses the same division that has been used to create the finite element mesh. Therefore, each radiation exchange area corresponds to one external area of one finite element as represented in Figure 3.7.

The first approximation in the presented approach consists in assuming that each of these external surfaces is isothermal. This is in general not true because the temperature at these surfaces is defined by the shape functions $[N]$, which are not constant along an external surface. However, the error can be negligible if the surfaces are small enough, i.e. if the domain is discretized with enough detail.

The radiation leaving each surface, which includes an emitted, a transmitted as well as a reflected component, is known as radiosity and is represented here by J. It can be calculated at surface i by the equation

$$J_i = \varepsilon_i \sigma T_i^4 + (1 - \varepsilon_i) \sum_{j=1}^{n_s} F_{ij} J_j + (1 - \varepsilon_i) F_{ie} \sigma T_e^4, \tag{3.40}$$

where n_s is the total number of surfaces in the domain that exchange radiation and F_{ij} is the view factor between surfaces i and j. The last term at the right-hand side represents the radiation from the environment that is reflected by surface i, therefore, F_{ie} is the view factor between surface i and the environment, whereas T_e is the environmental temperature.

Equation 3.40 can be written in matrix form for all the surfaces in the domain as

$$\left([I] - \left([I] - [\varepsilon]\right)[F]\right)\{J\} = \sigma[\varepsilon]\{T_s\}^4 + \left([I] - [\varepsilon]\right)\{F_e\}\sigma T_e^4 \tag{3.41}$$

where $[I]$ is an identity matrix of dimension n_s; $[\varepsilon]$ is the emissivity matrix, built with the emissivity of each surface in its diagonal; $[F]$ is the view factor matrix, which contains a view factor F_{ij} at each cell (i, j); $\{J\}$ is a column vector with the radiosity value at each surface, $\{T_s\}$ is the column vector with the temperature at each surface and $\{F_e\}$ is the column vector with the view factor between each surface and the environment.

Using the abbreviation

$$[A] = \left([I] - \left([I] - [\varepsilon]\right)[F]\right)^{-1}, \tag{3.42}$$

Equation 3.41 can be written as

$$\{J\} = \sigma[A][\varepsilon]\{T_s\}^4 + [A]\left([I] - [\varepsilon]\right)\{F_e\}\sigma T_e^4. \tag{3.43}$$

The next step is to define the received radiation at each surface, this is known as irradiance and can be quantified as

$$E_i = \sum_{j=1}^{n_s} F_{ij} J_j + F_{ie} \sigma T_e^4. \tag{3.44}$$

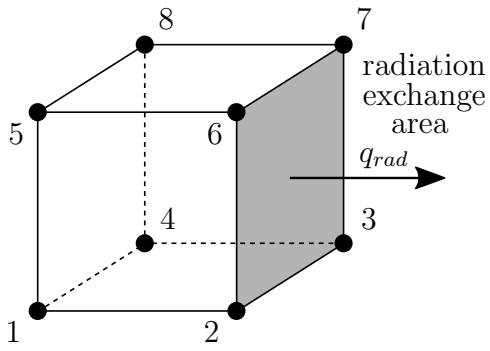

Figure 3.7: Representation of a radiation exchange area in one finite element.

The heat flux at each surface is the difference between the radiosity, expressed by 3.40, and the irradiance, expressed by 3.44. Thus,

$$q_{rad,i} = J_i - E_i, \tag{3.45}$$

which in matrix form, combining 3.44 and 3.45, can be expressed as

$$\{q_{rad}\} = ([I] - [F])\{J\} - \{F_e\}\sigma T_e^4. \tag{3.46}$$

Introducing now $\{J\}$, calculated according to 3.43, the flux vector can be expressed as

$$\{q_{rad}\} = [D_s]\{T_s\}^4 + \{S\}T_e^4 \tag{3.47}$$

with

$$[D_s] = \sigma\left([I] - [F]\right)[A][\varepsilon] \tag{3.48}$$

and

$$\{S\} = \sigma\left(([I] - [F])[A]([I] - [\varepsilon])\{F_e\} - \{F_e\}\right). \tag{3.49}$$

The only remaining step to incorporate the flux function 3.47 into the FEM system of equations expressed by 3.35 is to express it as a function of the nodal temperatures $\{T\}$ and not of the surface temperatures $\{T_s\}$. This can be achieved with a relation such as

$$\{T_s\} = [\Lambda]\{T\} \tag{3.50}$$

where $[\Lambda]$ is a matrix with as many rows as surfaces and as many columns as nodes. Since the domain has been meshed using hexahedron elements there are 4 nodes at each surface, one at each corner. The approach used in this work is to consider that the isothermal temperature of each surface is equal to the average of the four nodal temperatures in the surface. Under this assumption, it is possible to build the $[\Lambda]$ matrix accordingly.

Introducing now

$$[D] = [D_s][\Lambda], \tag{3.51}$$

the radiation flux at each surface expressed as a function of the nodal temperature vector is finally expressed as

$$\{q_{rad}\} = [D]\{T\}^4 + \{S\}T_e^4. \tag{3.52}$$

This radiation flux vector, which contains the radiation heat load at each external surface, can now be introduced into the FEM system of equations 3.35 using expression 3.38. Since the radiation flux q_{rad} is spatially constant at surface i due to the isothermal assumption, the heat flux vector at element i can be calculated with

$$\{R_{q,i}\} = -\int_{S_i} [N]^T \{q\}^T \{n\} ds = q_{rad,i} \int_{S_i} [N]^T ds \tag{3.53}$$

where

$$q_{rad,i} = -\{q\}^T \{n\} \tag{3.54}$$

because $\{q\}$ is an incident flux perpendicular to the surface and in the opposite direction to the normal vector $\{n\}$. Vector $\{R_{q,i}\}$ can be calculated at each radiating surface and assembled to produce the heat flux vector $\{R_{q,rad}\}$ for the global system, which can be expressed as

$$\{R_{q,rad}\} = [R_r]\{q_{rad}\} \tag{3.55}$$

where $[R_r]$ is a matrix based on the surface integration at each radiating surface according to 3.53.

This relation can be now introduced to the system of equations expressed in 3.35 resulting in

$$[C]\{\dot{T}\} + [K]\{T\} = \{R_q\} + \{R_Q\} + [R_r]\{q_{rad}\}. \tag{3.56}$$

This system takes into account applied heat fluxes from external conditions (e.g. solar flux) and due to the radiation exchange. The solution to this system must be calculated in combination with Equation 3.52 to take into account also the relation between radiation fluxes and nodal temperatures. Therefore, the complete system of equations to solve the thermal field in the domain of analysis is expressed as

$$\begin{cases} [C]\{\dot{T}\} + [K]\{T\} = \{R_q\} + \{R_Q\} + [R_r]\{q_{rad}\} \\ \{q_{rad}\} = [D]\{T\}^4 + \{S\}T_e^4 \end{cases} \tag{3.57}$$

3.2.2 Steady-state analysis

The first basic condition that can be analyzed with the system presented in the previous section is the steady-state analysis. This is the condition that is reached when the temperature in the system is in equilibrium and does not change with time. This means that $\dot{T} = 0$ and, therefore, system 3.57 can be simplified to

$$\begin{cases} [K]\{T\} - [R_r]\{q_{rad}\} = \{R_q\} + \{R_Q\} \\ -[D]\{T\}^4 + \{q_{rad}\} = \{S\}T_e^4 \end{cases} \tag{3.58}$$

This nonlinear system can be solved using the Newton method following a similar approach to the one outlined in reference [77]. The first step is to write system 3.58 in matrix form, i.e.,

$$\begin{bmatrix} [K] & -[R_r] \\ -[D]\{T\}^3 & [I] \end{bmatrix} \begin{Bmatrix} T \\ q_{rad} \end{Bmatrix} = \begin{Bmatrix} \{R_q\} + \{R_Q\} \\ \{S\}T_e^4 \end{Bmatrix} \tag{3.59}$$

This system of equations can be solved iteratively based on the Newton method using the expression

$$\begin{bmatrix} [K] & -[R_r] \\ -4[D]\{T_k\}^3 & [I] \end{bmatrix} \begin{Bmatrix} \Delta T \\ \Delta q \end{Bmatrix} = \\ = \begin{Bmatrix} -[K]\{T_k\} + [R_r]\{q_{rad,k}\} + \{R_q\} + \{R_Q\} \\ -\{q_{rad,k}\} + [D]\{T_k\}^4 + \{S\}T_e^4 \end{Bmatrix} \quad (3.60)$$

where

$$\begin{Bmatrix} \Delta T \\ \Delta q \end{Bmatrix} = \begin{Bmatrix} T_{k+1} - T_k \\ q_{rad,k+1} - q_{rad,k} \end{Bmatrix}. \quad (3.61)$$

Specifying a tolerance value for ΔT and Δq it is possible to iteratively solve system 3.60 until the desired accuracy of the solution is reached.

The steady-state solution for a particular set of boundary conditions of the baseline case included in this work is calculated and presented here. These boundary conditions include an environmental temperature of $T_e = 290\,\mathrm{K}$, a heat flux of $q = 2\,\mathrm{W}$ applied at the base of each bipod and an internal heat generation of $Q_1 = 10\,\mathrm{W}$ at instrument 1. These environmental conditions are represented in Figure 3.8. The equilibrium thermal field that the structure reaches under these conditions is represented in Figure 3.9.

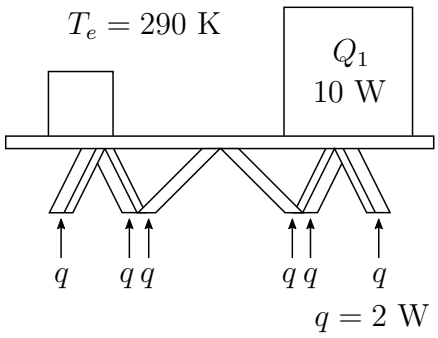

Figure 3.8: Steady-state boundary conditions of the baseline concept.

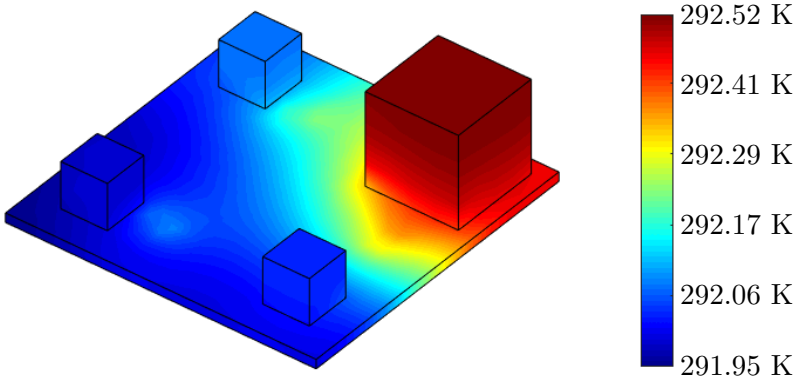

Figure 3.9: Steady-state thermal field of the baseline concept.

3.2.3 Transient analysis in the time domain

A more elaborate approach is necessary to calculate the transient response of the system triggered by changes in the boundary conditions. The traditional approach to solve the transient problem is to use an integration scheme in the time domain. Using the Crank-Nicolson method [9] the system of equations 3.57 is expressed as

$$\begin{cases} [C]\left\{\dfrac{T^{t+\Delta t}-T^t}{\Delta t}\right\} = -[K]\left\{\dfrac{T^{t+\Delta t}+T^t}{2}\right\} + \left\{\dfrac{R_q^{t+\Delta t}+R_q^t}{2}\right\} \\ \qquad\qquad + \left\{\dfrac{R_Q^{t+\Delta t}+R_Q^t}{2}\right\} + [R_r]\left\{\dfrac{q_{rad}^{t+\Delta t}+q_{rad}^t}{2}\right\} \\ \left\{\dfrac{q_{rad}^{t+\Delta t}+q_{rad}^t}{2}\right\} = [D]\left\{\dfrac{T^{t+\Delta t}+T^t}{2}\right\}^4 + \{S\}T_e^4 \end{cases} \tag{3.62}$$

where the environmental temperature T_e has been assumed to be constant in time and, therefore, does not change at each time step. This system of equations can be rearranged and written in matrix form so that it can be solved for the temperature and flux values at $t' = t + \Delta t$. This results in

$$\begin{bmatrix} [C] + \dfrac{[K]\Delta t}{2} & -\dfrac{[R_r]\Delta t}{2} \\ -\dfrac{1}{2}\left[D\left(\dfrac{T^{t+\Delta t}+T^t}{2}\right)^3\right] & \dfrac{1}{2}[I] \end{bmatrix} \begin{Bmatrix} T^{t+\Delta t} \\ q_{rad}^{t+\Delta t} \end{Bmatrix} = \\ \begin{Bmatrix} [C]\{T^t\} - \frac{[K]\Delta t}{2}\{T^t\} + \frac{[R_r]\Delta t}{2}\{q_{rad}^t\} + \left\{\frac{R_q^{t+\Delta t}+R_q^t}{2}\right\}\Delta t + \left\{\frac{R_Q^{t+\Delta t}+R_Q^t}{2}\right\}\Delta t \\ -\frac{\{q_{rad}\}}{2} + \left[D\left(\frac{T^{t+\Delta t}+T^t}{2}\right)^3\right]\frac{\{T^t\}}{2} + \{S\}T_e^4 \end{Bmatrix} \tag{3.63}$$

This nonlinear system can be solved using the Newton method as it has been done to solve the steady-state solution in Section 3.2.2. This requires an iterative process to solve the solution at each time step, which can be expressed as

$$\begin{bmatrix} [C] + \dfrac{[K]\Delta t}{2} & -\dfrac{[R_r]\Delta t}{2} \\ -2\left[D\left(\dfrac{T_k^{t+\Delta t}+T^t}{2}\right)^3\right] & \dfrac{1}{2}[I] \end{bmatrix} \begin{Bmatrix} \Delta T^{t+\Delta t} \\ \Delta q_{rad}^{t+\Delta t} \end{Bmatrix} = \begin{Bmatrix} F_1 \\ F_2 \end{Bmatrix} \tag{3.64}$$

with

$$F_1 = -[C]\{T_k^{t+\Delta t} - T^t\} - [K]\Delta t\left\{\frac{T_k^{t+\Delta t}+T^t}{2}\right\} + [R_r]\Delta t\left\{\frac{q_{rad,k}^{t+\Delta t}+q_{rad}^t}{2}\right\} \\ + \left\{\frac{R_q^{t+\Delta t}+R_q^t}{2}\right\}\Delta t + \left\{\frac{R_Q^{t+\Delta t}+R_Q^t}{2}\right\}\Delta t \tag{3.65}$$

and

$$F_2 = -\left\{\frac{q_{rad,k}^{t+\Delta t}+q_{rad}^t}{2}\right\} + [D]\left\{\frac{T_k^{t+\Delta t}+T^t}{2}\right\}^4 + \{S\}T_e^4. \tag{3.66}$$

The temperature and radiation flux at $t' = t + \Delta t$ is obtained from

$$\begin{Bmatrix} \Delta T^{t+\Delta t} \\ \Delta q_{rad}^{t+\Delta t} \end{Bmatrix} = \begin{Bmatrix} T_{k+1}^{t+\Delta t} - T_k^{t+\Delta t} \\ q_{rad,k+1}^{t+\Delta t} - q_{rad,k}^{t+\Delta t} \end{Bmatrix}. \tag{3.67}$$

This allows the calculation of the temperature and radiation heat flux evolution in time when the changes in the applied heat flux q or in the internal heat sources Q are known. These changes are introduced in system 3.63 for each time step using the corresponding time functions

$$q = q(t) \qquad \text{and} \qquad Q = Q(t).$$

The process that has been presented here describes the traditional approach to calculate the transient response of a thermal system. This approach is reliable and can be implemented for any varying conditions that can be described in the time domain.

However, it is important to note that for some kind of problems this method is mathematically inefficient. To calculate the response at some particular point in time, i.e. at $t = t_i$, it is still necessary to perform the numerical integration from the initial state at $t = 0$ to the time step $t = t_i$. Also, if an analysis has been performed under some assumed functions $q(t)$ and $Q(t)$ and some new information arises, which provides a better characterization of these functions, it is necessary to recalculate all the analysis in order to obtain the updated values of the thermal response.

The limitations of the time integration approach can be overcome in some cases using an alternative approach based on a transformation of the involved equations into the frequency domain. This approach offers some advantages over the traditional time integration approach and it also sets the foundations to implement a feedback loop that ultimately allows the control of thermomechanical distortions. The details of this approach are presented in the following section.

3.2.4 Transient analysis in the frequency domain

The frequency domain approach to the transient analysis problem is an alternative method to the traditional time integration approach. The approaches based on the frequency domain have gained popularity in recent years to analyze the thermal behavior of structures subjected to different types of perturbations that act on a spectrum of frequencies [11, 78, 79]. This is particularly useful to assess the thermal stability within a specific range of frequencies. Therefore, it has been used to perform thermal analysis in high-precision space missions such as LISA [70, 79].

The main characteristic of these methods lies in calculating thermal transfer functions obtained from a linearization of the thermal equations, which basically concerns the radiation terms. Given that it is required to linearize the equations, the method presented here is only valid for cases in which only small changes in the thermal state are expected. This is generally always the case when the method is implemented to analyze highly stable structures because they are inherently designed for stability and insulated from large thermal variations.

The frequency-based method outlined in this section follows the linearization approach as presented in references [11] and [68] in combination with a modal representation of the thermal field. This approach has been generally applied on thermal models described using the LPM. Here, the approach is modified and expanded to apply it in a FEM model, which ultimately allows the calculation of transfer functions between heat flux and nodal temperatures evaluated at a given frequency and also the calculation of thermal modes, as described in Subsection 3.2.5.

First, the system of equations 3.57 is written just in terms of the temperature by combining its two expressions. This results in

$$[C]\{\dot{T}\} + [K]\{T\} - [R_r][D]\{T\}^4 = \{R_q\} + \{R_Q\} + [R_r]\{S\}T_e^4. \tag{3.68}$$

At this point it is useful to write the heat flux vector $\{R_q\}$ and the heat source vector $\{R_Q\}$ as a product of a matrix and a load vector. This is expressed as

$$\{R_q\} = [R_q^1]\{q\} \tag{3.69}$$

$$\{R_Q\} = [R_Q^1]\{Q\} \tag{3.70}$$

where each column in the matrices $[R_q^1]$ and $[R_Q^1]$ is calculated using 3.38 and 3.39, respectively, considering a heat load equal to one. These matrices are then multiplied by the column vectors $\{q\}$ and $\{Q\}$ where each cell contains the heat load value in a different surface or element volume, respectively. Introducing these expressions into Equation 3.68 results in

$$[C]\{\dot{T}\} + [K]\{T\} - [R_r][D]\{T\}^4 = [R_q^1]\{q\} + [R_Q^1]\{Q\} + [R_r]\{S\}T_e^4. \tag{3.71}$$

The temperature and heat values can be linearized around equilibrium using

$$T = T_{eq} + \delta T, \tag{3.72}$$

$$q = q_{eq} + \delta q \tag{3.73}$$

$$\text{and} \quad Q = Q_{eq} + \delta Q. \tag{3.74}$$

Thus, from 3.72,

$$T^4 = (T_{eq} + \delta T)^4 = T_{eq}^4 + 4T_{eq}^3\delta T + \mathcal{O}(\delta T^2). \tag{3.75}$$

If the changes in temperature are small, the truncation error proportional to δT^2 can be neglected. Introducing these identities into Equation 3.71 results in

$$\begin{aligned}[C]\{\dot{T}_{eq}\} + [C]\{\delta\dot{T}\} + [K]\{T_{eq}\} + [K]\{\delta T\} - [R_r][D]\{T_{eq}\}^4 - 4[R_r][D][T_{eq}^3]\{\delta T\} = \\ [R_q^1]\{q_{eq}\} + [R_q^1]\{\delta q\} + [R_Q^1]\{Q_{eq}\} + [R_Q^1]\{\delta Q\} + [R_r]\{S\}T_e^4\end{aligned} \tag{3.76}$$

where $[T_{eq}^3]$ is obtained by expressing the vector $\{T_{eq}^3\}$ as a diagonal matrix. Taking now into account that due to the equilibrium condition

$$\{\dot{T}_{eq}\} = 0 \tag{3.77}$$

$$\text{and} \quad [K]\{T_{eq}\} - [R_r][D]\{T_{eq}\}^4 = [R_q^1]\{q_{eq}\} + [R_Q^1]\{Q_{eq}\} + [R_r]\{S\}T_e^4 \tag{3.78}$$

it is possible to simplify Equation 3.76 to

$$[C]\{\delta\dot{T}\} + [K]\{\delta T\} - 4[R_r][D][T_{eq}^3]\{\delta T\} = [R_q^1]\{\delta q\} + [R_Q^1]\{\delta Q\}. \tag{3.79}$$

Premultiplying by $[C]^{-1}$ and introducing the following abbreviations

$$[H_T] = [C]^{-1}\left([K] - 4[R_r][D][T_{eq}^3]\right), \tag{3.80}$$

$$[H_q] = [C]^{-1}[R_q^1], \tag{3.81}$$

$$[H_Q] = [C]^{-1}[R_Q^1], \tag{3.82}$$

Equation 3.78 can be written as

$$\{\delta\dot{T}\} + [H_T]\{\delta T\} = [H_q]\{\delta q\} + [H_Q]\{\delta Q\}. \tag{3.83}$$

This equation gives now the linear relation between the changes in temperature and the changes in heat fluxes or heat sources applied to the structure. The next step in order to calculate the transfer functions between these variables as a function of the frequency consists in diagonalizing the matrix $[H_T]$ which can be achieved through the introduction of modal coordinates. The modal coordinate representation is a common approach in the structural dynamics field. In this section, an equivalent approach is applied in the linearized thermal domain to characterize the thermal field. First, the eigenvectors and eigenvalues of matrix $[H_T]$ are calculated

$[\phi]$: Eigenvector matrix
$[\lambda]$: Eigenvalue diagonal matrix

The transformation from the physical coordinates of temperature $\{\delta T\}$ to the modal coordinates $\{\tau\}$ is implemented using

$$\{\delta T\} = [\phi]\{\tau\}. \tag{3.84}$$

Introducing the coordinate transformation 3.84 into 3.83 yields

$$[\phi]\{\dot{\tau}\} + [H_T][\phi]\{\tau\} = [H_q]\{\delta q\} + [H_Q]\{\delta Q\}. \tag{3.85}$$

And premultiplying now by $[\phi]^{-1}$

$$[\phi]^{-1}[\phi]\{\dot{\tau}\} + [\phi]^{-1}[H_T][\phi]\{\tau\} = [\phi]^{-1}[H_q]\{\delta q\} + [\phi]^{-1}[H_Q]\{\delta Q\}. \tag{3.86}$$

It is important to notice that

$$[\phi]^{-1}[\phi] = [I] \tag{3.87}$$

$$[\phi]^{-1}[H_T][\phi] = [\lambda] \tag{3.88}$$

which are both diagonal. Therefore, Equation 3.86 can be rewritten as

$$[I]\{\dot{\tau}\} + [\lambda]\{\tau\} = [\phi]^{-1}[H_q]\{\delta q\} + [\phi]^{-1}[H_Q]\{\delta Q\}. \tag{3.89}$$

Equation 3.89 expresses the relation between the different variables in the time domain. By taking the Laplace transform of the dependent variables, it is possible to express this relation in the frequency domain and to calculate transfer functions between the modal coordinates $\{\tau\}$ and the heat inputs $\{\delta q\}$ and $\{\delta Q\}$. The applied Laplace transforms are

$$\mathcal{L}\{\dot{\tau}(t)\} = s\tau(s) \tag{3.90}$$

$$\mathcal{L}\{\tau(t)\} = \tau(s) \tag{3.91}$$

$$\mathcal{L}\{\delta q(t)\} = \delta q(s) \tag{3.92}$$

$$\mathcal{L}\{\delta Q(t)\} = \delta Q(s) \tag{3.93}$$

where $s = j\omega$ is the complex frequency parameter. Introducing these relations into Equation 3.89 yields

$$s[I]\{\tau(s)\} + [\lambda]\{\tau(s)\} = [\phi]^{-1}[H_q]\{\delta q(s)\} + [\phi]^{-1}[H_Q]\{\delta Q(s)\} \tag{3.94}$$

which solving for $\{\tau(s)\}$ results in

$$\{\tau(s)\} = (s[I] + [\lambda])^{-1}\,[\phi]^{-1}[H_q]\{\delta q(s)\} + (s[I] + [\lambda])^{-1}\,[\phi]^{-1}[H_Q]\{\delta Q(s)\}. \tag{3.95}$$

This equation provides a linear relation between the modal coordinates $\{\tau\}$ and the heat input, which includes heat fluxes and volumetric heat sources. The inverse matrix at the right-hand side can be directly calculated by taking into account that both $[I]$ and $[\lambda]$ are diagonal matrices. The temperature values can be calculated from the modal coordinates in Equation 3.95 using the transformation expressed in 3.84. Therefore, the transfer function between the temperature change at node i and the heat flux change at surface k can be finally calculated as

$$H_{Tq}(s) = \frac{\delta T_i}{\delta q_k} = \sum_{j=1}^{n_n} \phi_{ij} \frac{A_{jk}}{s + \lambda_j} \tag{3.96}$$

where A_{jk} is the value at cell jk of matrix $[\phi]^{-1}[H_q]$ and n_n is the total number of nodes in the model. Equivalently, the transfer function between the temperature change at node i and the heat source change at element k can be calculated as

$$H_{TQ}(s) = \frac{\delta T_i}{\delta Q_k} = \sum_{j=1}^{n_n} \phi_{ij} \frac{B_{jk}}{s + \lambda_j} \tag{3.97}$$

with B_{jk} being the value at cell jk of matrix $[\phi]^{-1}[H_Q]$.

The transfer functions 3.96 and 3.97 can be evaluated at a given frequency s to calculate the relation between the temperature change and the heat input change. These transfer functions can be calculated between any combination of nodes and elements in the structure, i.e., it is possible to know the thermal change at any node in the structure induced by a given heat input at any element.

This analysis is very powerful to analyze the heat transfer and temperature dependencies in the structure. These insights are obtained purely from the magnitude and phase of the transfer functions between different nodes without the need to integrate in time. If the magnitude and frequency of a given perturbation are known, the temperature response at any point in the structure can be obtained by simply multiplying the magnitude of the perturbation by the transfer functions 3.96 or 3.97, depending on whether the perturbation is expressed in terms of heat flux or heat source.

With this approach it is possible to calculate the thermal evolution of the baseline concept presented in Section 3.2.1 and represented in Figure 3.4 when a thermal perturbation arises. A generic example is included here to illustrate how the approach works. In this example a thermal perturbation δQ_1 arising in the instrument 1 is assumed. This perturbation is modeled as a sinusoidal wave with a frequency of 10^{-5} Hz and an amplitude of 5 W. Using Equation 3.97 it is possible to calculate

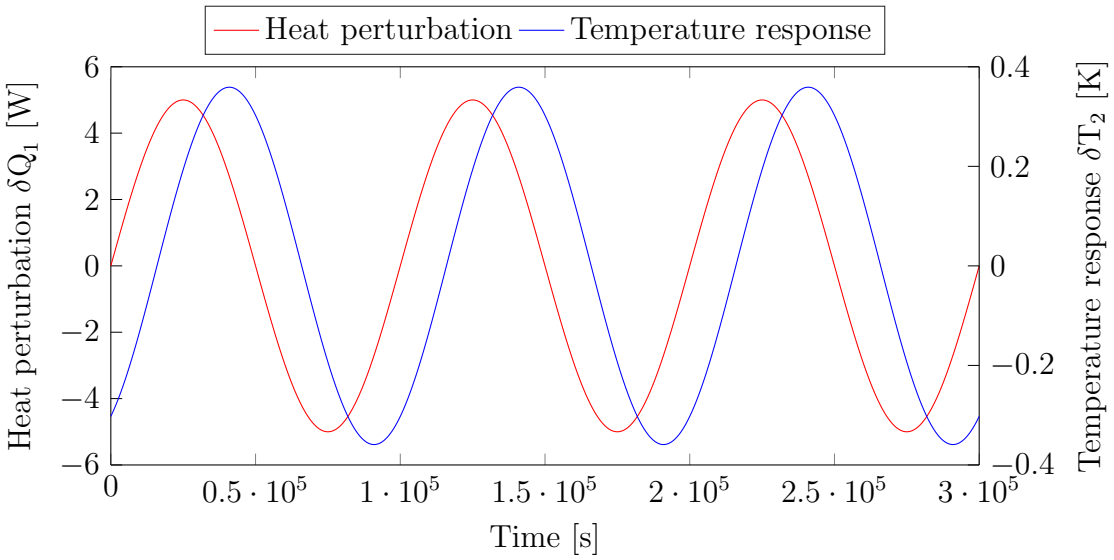

Figure 3.10: Perturbation input and corresponding temperature response.

the temperature change at one representative node of instrument 2, indicated here as δT_2. It results in

$$H_{TQ}\left(j\frac{2\pi}{10^5}\right) = \frac{\delta T_2}{\delta Q_1} = 0.039 - j0.061 = 0.072\angle -57.39^\circ \tag{3.98}$$

The complex result indicates that there is a phase delay between the perturbation δQ_1 and the temperature change at instrument 2, δT_2. Taking into account that the perturbation can be expressed in polar form as

$$\delta Q_1 = 5\angle 0^\circ \text{ W} \tag{3.99}$$

it is possible to calculate the thermal response by multiplying the transfer function 3.98 by the perturbation 3.99. This gives as a result

$$\delta T_2 = 0.194 - j0.303 = 0.359\angle -57.39^\circ \text{ K} \tag{3.100}$$

These two magnitudes, δQ_1 and δT_2, are represented in Figure 3.10.

An important advantage of having linearized the thermal equations is that the thermal response under several perturbations can be obtained by superimposing the individual responses to each perturbation. Thus, if additionally to δQ_1 there are perturbations arising from other instruments, it is possible to calculate the global response by adding the responses induced by each instrument.

One limitation of the frequency-domain approach is that it only provides the solution of the non-homogeneous differential equation expressed by 3.85. However, the complete solution of an ordinary differential equation is always the combination of the non-homogeneous and the homogeneous solution. The solution of the homogeneous equation corresponds to transient terms that converge to zero with time. These transient terms are not captured by this approach and, as a result, the frequency-domain approach only provides a portion of the total response. The time domain and the frequency domain approach converge to the same result but show

some initial discrepancy that is progressively attenuated to zero. This behavior can be seen in Figure 3.11.

These transient terms can be analytically calculated by applying the inverse Laplace transform of the response function expressed in the frequency domain. First, the Laplace transform of the perturbation is calculated in this case as

$$\delta Q_1 = 5\sin\omega t \rightarrow \mathcal{L}\{5\sin\omega t\} = \frac{5\omega}{s^2+\omega^2}. \tag{3.101}$$

The temperature response in the frequency domain is obtained by multiplying the previous expression by the transfer function expressed by 3.97. Thus, the response function calculated in the frequency domain is

$$\delta T_2(s) = \sum_{j=1}^{n_n} \frac{C_j}{s+\lambda_j}\frac{5\omega}{s^2+\omega^2} \tag{3.102}$$

where for the sake of clarity, the factors $\phi_{ij}B_{jk}$ from Equation 3.97 have been substituted for C_j. The analytical expression of the response in the time domain can be obtained by applying the inverse Laplace transform, thus

$$\begin{aligned}\delta T_2(t) &= \mathcal{L}^{-1}\left(\sum_{j=1}^{n_n} \frac{C_j}{s+\lambda_j}\frac{5\omega}{s^2+\omega^2}\right) \\ &= \sum_{j=1}^{n_n}\left(\frac{5C_j\omega e^{-\lambda_j t}}{\lambda_j^2+\omega^2} + \frac{5C_j\lambda_j\sin\omega t - 5C_j\omega\cos\omega t}{\lambda_j^2+\omega^2}\right).\end{aligned} \tag{3.103}$$

The second term inside the summation is a periodic function and it corresponds to the response that is obtained when the transfer function evaluated at some given frequency is multiplied by the perturbation, as done in 3.100. The first term inside the summation is exponentially converging to zero. It is a transient term that can only be obtained in the time domain by directly calculating the inverse Laplace transform.

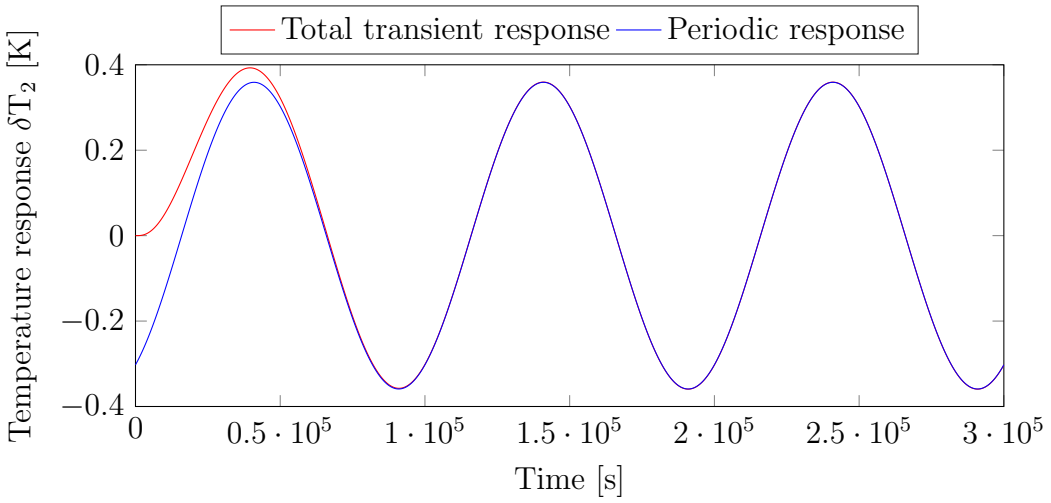

Figure 3.11: Temperature response obtained using the time domain approach and the frequency domain approach.

3.2.5 Modal representation

The previous section has introduced the transformation into modal coordinates to calculate an expression of the transfer functions, resulting in Equations 3.96 and 3.97. By using these transfer functions, the temperature response of the system is obtained according to Equation 3.84, which is repeated here for clarity,

$$\{\delta T\} = [\phi]\{\tau\}.$$

Considering that each column in the eigenvector matrix $[\phi]$ represents a linearized thermal mode, it can be interpreted that the solution is expressed as a linear combination of all the thermal modes. In other words, the thermal response is obtained by assigning a different weight to each column of the matrix $[\phi]$. The weight of each column is determined by vector $\{\tau\}$.

Each thermal mode, corresponding to each column vector of matrix $[\phi]$, represents a normalized fundamental shape in which the temperature fluctuates within the structure. Given a finite element model of the structure, there are as many modes as degrees of freedom have been considered. Different thermal modes are excited depending on the origin and frequency of the perturbation. Figure 3.12 shows the first 8 modes of the baseline case that are excited when the perturbation comes from instrument 1 at a frequency of 10^{-5} Hz.

The weight of each mode depends on the frequency of the perturbation. At lower frequencies, the weight is more concentrated over a small number of thermal modes, whereas at higher frequencies, the total response tends to be more distributed over a larger number of modes. This behavior can be seen in Figure 3.13, which represents the weight of each of the first 8 modes that determine the response at different frequencies. As it can be observed, the weight difference between different modes is much smaller at higher frequencies.

The advantage of using the modal representation is that under some circumstances it is acceptable to neglect a large number of modes and describe the response using only those that carry the largest weight. This procedure is known as modal truncation and it implies that instead of calculating the transfer functions with the summation up to n_n, only the terms up to N are considered, with $N < n_n$, i.e.,

$$H_{Tq}(s) = \frac{\delta T_i}{\delta q_k} = \sum_{j=1}^{N} \phi_{ij} \frac{A_{jk}}{s + \lambda_j} \tag{3.104}$$

$$H_{TQ}(s) = \frac{\delta T_i}{\delta Q_k} = \sum_{j=1}^{N} \phi_{ij} \frac{B_{jk}}{s + \lambda_j} \tag{3.105}$$

Based on the modal truncation procedure it is possible to develop a feasible sensor strategy that relies only on a limited number of sensors. This is a crucial step to implement a feedback control loop, and therefore, it is presented in detail in Section 5.3.1 of Chapter 5.

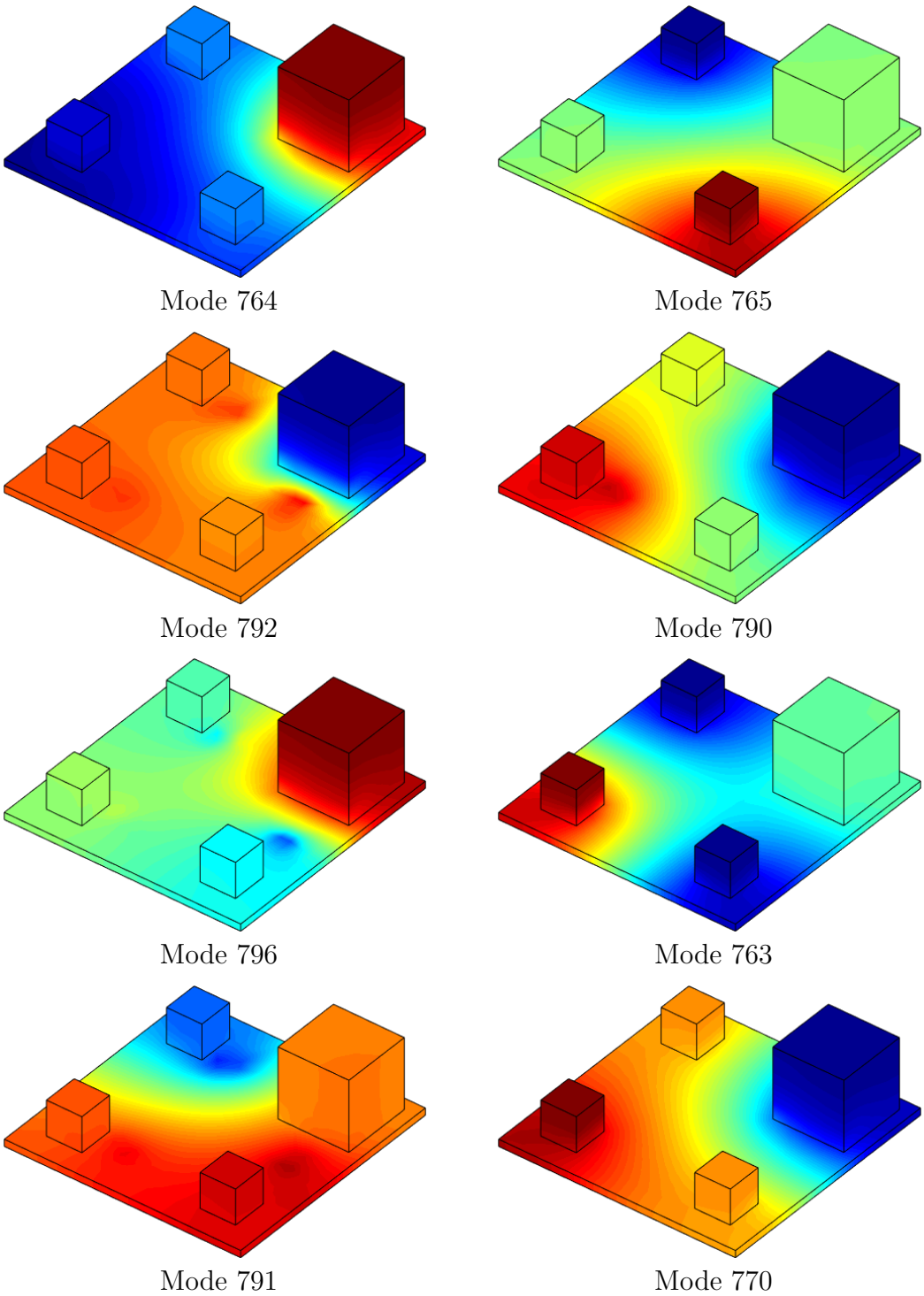

Figure 3.12: First linearized thermal modes that describe the response to perturbations from Instrument 1 at $f = 10^{-5}$ Hz.

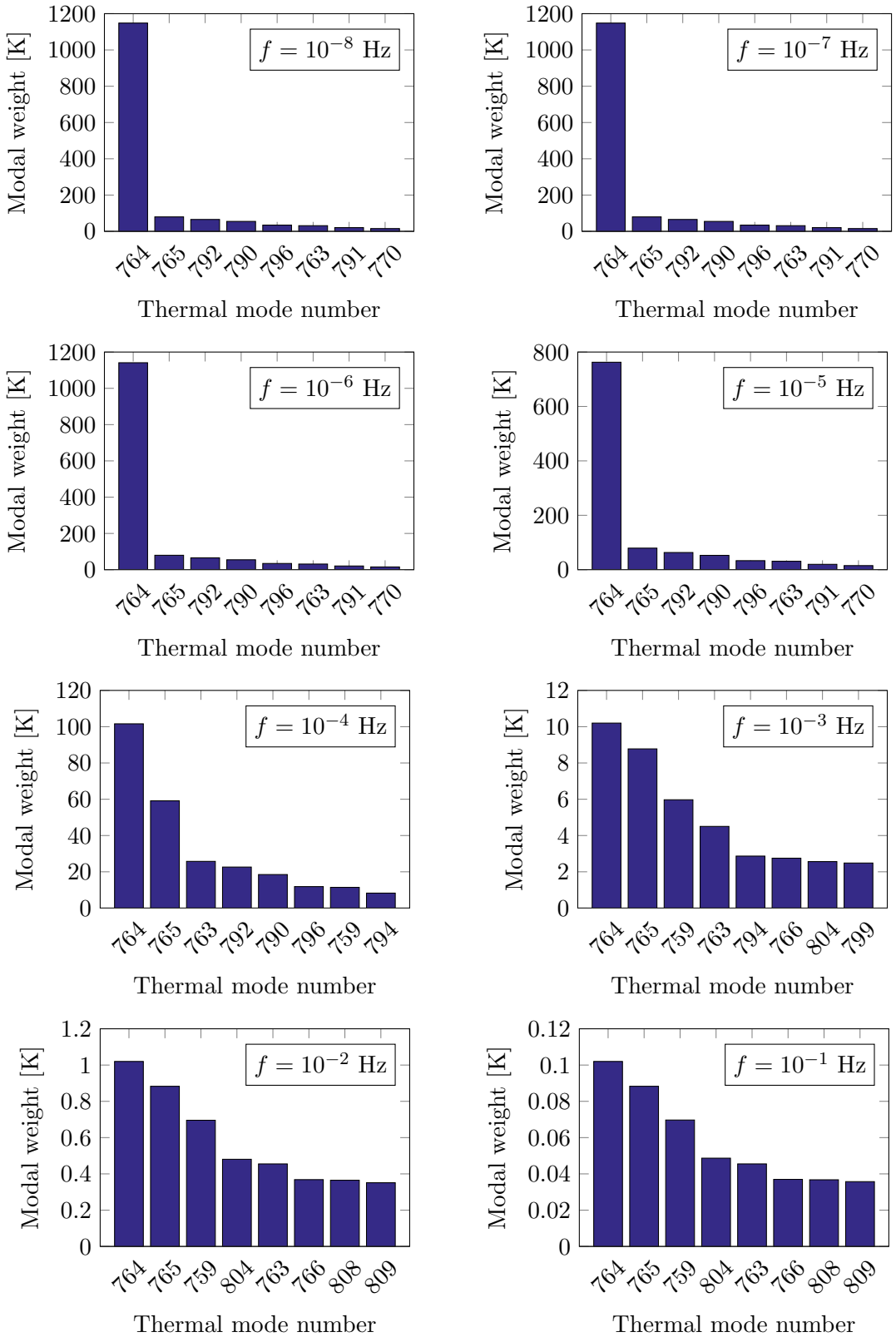

Figure 3.13: Modal weight of the first 8 linearized thermal modes that describe the response to perturbations of 1 W from Instrument 1 at frequencies between 10^{-8} Hz and 10^{-1} Hz.

Chapter 4

Structural Analysis Framework

Once the thermal FEM model has been established, the next step is to formulate the mechanical counterpart in order to obtain a complete thermomechanical model. The mechanical model calculates the displacement in each spatial direction at each node caused by a given mechanical load, which in this case is the thermal stress induced by temperature fluctuations. Based on the obtained displacement field it is possible to calculate distortions between specific points in the structure.

This chapter starts with a presentation in Section 4.1 of the FEM formulation for mechanical problems, with a special emphasis on the modeling of thermal stress. This formulation is briefly presented with the purpose of clarifying the notation that is used in the subsequent chapters. This first section includes also a short explanation of the mathematical procedure that has been followed to solve the steady-state condition. For completeness, a standard procedure to solve the transient problem is also included to discuss its limitations over the alternative approach, presented in Subsection 4.1.3, based on a frequency domain transformation.

The frequency domain analysis is already a well-established technique in the field of structural dynamics [80]. This approach is presented in Subsection 4.1.3 and it is expanded to combine it with the thermal formulation presented in Chapter 3, which results in the derivation of the thermomechanical transfer functions presented in Section 4.2. These functions give the relation between displacement and applied heat changes as a function of the frequency and are the basis to develop a control loop to stabilize distortions of thermal origin. Finally, the chapter finishes with the presentation and analysis of the quasi-static assumption, which simplifies the formulation of the control framework presented in Chapter 5.

4.1 Thermomechanical FEM formulation

The FEM formulation for thermal problems presented in Section 3.2.1 considers that each node in the mesh has one degree of freedom, the temperature. In the mechanical case, the ultimate variables obtained by the FEM are the displacements at each node in each spatial direction. This implies that there are three degrees of freedom for each node in the mesh.

As presented in Section 3.2.1 for the thermal case, the displacement field within a finite element can be calculated based on assumed shape functions. This relation can be expressed as

$$\{\overline{u}(x, y, z, t)\} = [N]\{u\}, \tag{4.1}$$

where $\overline{u}$ is the displacement vector containing the displacements in each direction at coordinates x, y and z. Vector $\{u\}$ is the nodal displacement vector and it contains the displacements in each direction at each node expressed as u_n, v_n and w_n. It can be written as

$$\{u\} = \{u_1 \quad v_1 \quad w_1 \quad u_2 \quad v_2 \quad w_2 \quad \dots\}^T. \tag{4.2}$$

According to this definition, the dimension of the $\{u\}$ vector is three times the total number of nodes in the mesh. The $[N]$ matrix has to take also into account this 3 DOF representation and, therefore, it is expressed as

$$[N] = \begin{bmatrix} N_1 & 0 & 0 & N_2 & 0 & 0 & \dots \\ 0 & N_1 & 0 & 0 & N_2 & 0 & \dots \\ 0 & 0 & N_1 & 0 & 0 & N_2 & \dots \end{bmatrix}. \tag{4.3}$$

The nodal displacement vector $\{u\}$ can be obtained by solving the equations of motion of the structure. These equations of motion can be derived from Newton's second law and can be expressed in matrix form as [80]

$$[M_u]\{\ddot{u}\} + [C_u]\{\dot{u}\} + [K_u]\{u\} = \{F(t)\} \tag{4.4}$$

where $[M_u]$ is called the mass matrix, $[C_u]$ is the damping matrix, $[K_u]$ is the stiffness matrix and $\{F(t)\}$ is the applied mechanical load, which generally varies with time. The mass matrix can be calculated as

$$[M_u] = \int_\Omega \rho [N]^T [N] d\Omega \tag{4.5}$$

where ρ is the material density and $[N]$ is the shape function matrix assembled for each element in the domain Ω. Similarly, the stiffness matrix $[K_u]$ is calculated as

$$[K_u] = \int_\Omega [B]^T [E] [B] d\Omega \tag{4.6}$$

where $[B]$ is the displacement differentiation matrix which is defined as

$$[B] = \begin{bmatrix} \frac{\partial N_1}{\partial x} & 0 & 0 & \frac{\partial N_2}{\partial x} & 0 & 0 & \dots \\ 0 & \frac{\partial N_1}{\partial y} & 0 & 0 & \frac{\partial N_2}{\partial y} & 0 & \dots \\ 0 & 0 & \frac{\partial N_1}{\partial z} & 0 & 0 & \frac{\partial N_2}{\partial z} & \dots \\ \frac{\partial N_1}{\partial y} & \frac{\partial N_1}{\partial x} & 0 & \frac{\partial N_2}{\partial y} & \frac{\partial N_2}{\partial x} & 0 & \dots \\ 0 & \frac{\partial N_1}{\partial z} & \frac{\partial N_1}{\partial y} & 0 & \frac{\partial N_2}{\partial z} & \frac{\partial N_2}{\partial y} & \dots \\ \frac{\partial N_1}{\partial z} & 0 & \frac{\partial N_1}{\partial x} & \frac{\partial N_2}{\partial z} & 0 & \frac{\partial N_2}{\partial x} & \dots \end{bmatrix} \tag{4.7}$$

and $[E]$ is the elasticity matrix

$$[E] = \frac{E}{(1+\nu)(1-2\nu)} \begin{bmatrix} 1-\nu & \nu & \nu & 0 & 0 & 0 \\ \nu & 1-\nu & \nu & 0 & 0 & 0 \\ \nu & \nu & 1-\nu & 0 & 0 & 0 \\ 0 & 0 & 0 & \frac{1-2\nu}{2} & 0 & 0 \\ 0 & 0 & 0 & 0 & \frac{1-2\nu}{2} & 0 \\ 0 & 0 & 0 & 0 & 0 & \frac{1-2\nu}{2} \end{bmatrix} \tag{4.8}$$

with E being the Young's modulus and ν the Poisson's ratio.

The calculation of the damping matrix $[C_u]$ depends on the damping model that is considered. There exist several mathematical models to derive this matrix. One option, known as proportional damping [81], consists in defining the damping matrix as a linear combination of the mass and the stiffness matrix, i.e.

$$[C_u] = a_0[M_u] + a_1[K_u] \tag{4.9}$$

where a_0 and a_1 are two parameters that can be adjusted based on experimental data or on mathematical estimations of the damping level.

The vector at the right-hand side of the equation of motion expressed by 4.4 represents the mechanical loads applied to the structure. It includes the necessary external forces that constrain the structure and that are represented in this chapter by the vector $\{F_d\}$. It also includes the mechanical loads resulting from external forces and pressures as well as from internal stress. The thermomechanical stress is a specific type of internal stress and it arises due to the material expansion and contraction induced by thermal fluctuations. In order to calculate the mechanical load associated with this thermal expansion, it is necessary to choose a mathematical model of this effect. Here, it is assumed that the materials are isotropic. Thus, the thermal strain that arises at a given temperature can be calculated as

$$\{\varepsilon_t\} = \begin{Bmatrix} \alpha T \\ \alpha T \\ \alpha T \\ 0 \\ 0 \\ 0 \end{Bmatrix} \tag{4.10}$$

where α is the coefficient of thermal expansion and T the temperature. This vector contains six components because in the three-dimensional case the strain vector is described by three normal strains (ε_x, ε_y and ε_z) and three shear strains (γ_{xy}, γ_{yz} and γ_{zx}). Based on the thermal strain described by 4.10 it is possible to calculate the mechanical load applied to the structure as

$$\{F_t\} = \int_\Omega [B]^T [E]\{\varepsilon_t\} d\Omega. \tag{4.11}$$

Considering the relation between thermal strain and temperature expressed by Equation 4.10, it is also possible to express the mechanical load in matrix form as a function of the temperature vector, i.e.

$$\{F_t\} = [F_T]\{T\}. \tag{4.12}$$

Based on this notation it is possible to rewrite the equation of motion 4.4 as

$$[M_u]\{\ddot{u}\} + [C_u]\{\dot{u}\} + [K_u]\{u\} = [F_T]\{T\} + \{F_d\} \tag{4.13}$$

which gives the relation between temperature and displacement field in the structure.

4.1.1 Steady-state analysis

The first basic analysis that can be performed is to calculate the displacement field when only static forces are present, this is the steady-state condition. Under steady-state conditions both the acceleration $\ddot{u}$ and the velocity $\dot{u}$ are equal to zero and, therefore, Equation 4.13 can be written as

$$[K_u]\{u\} = [F_T]\{T\} + \{F_d\} \tag{4.14}$$

The first necessary step to solve the previous system of equations it to define the mechanical boundary conditions. Boundary conditions in structural analyses are usually expressed as displacement constraints at some specific nodes in the structure. In the application presented in this work, the focus is on the distortions arising due to the thermal expansion in a body that is free-floating in space, i.e. a satellite.

The free-floating condition is equivalent to constraining only the 6 DOF corresponding to the rigid body motion and allowing the free thermal expansion of the structure. In mathematical terms, this condition can be simulated with an artificial isostatic constraint, i.e. following the same principle of the isostatic mount that has been presented in Section 2.3.1 and that is known as 3-2-1 constraint. This condition can be implemented by constraining the displacement at three different nodes. In one node, the displacements in all three directions are forced to be zero. In a second node, only the displacements in those two directions perpendicular to the line that connects it to the first node are constrained. The third node is forced to remain in the same plane defined by the three points at $t = 0$. This isostatic condition with the mentioned constraints is represented for the baseline case presented in this thesis in Figure 4.1.

The mathematical implication of this condition is that there are 6 components in the $\{u\}$ vector of Equation 4.14 that are forced to be zero. Conversely, the $\{F_d\}$ vector containing the constraint loads is empty except in those cells that correspond to a displacement constraint. Therefore, there are only 6 unknowns in the $\{F_d\}$ vector. The global system defined by 4.14 can be directly solved for the displacement vector by removing these 6 unknowns from the system. To this purpose, the 6 equations that contain these unknowns are removed from the system. Additionally, the columns of matrix $[K_u]$ that are multiplied by a null displacement can also be removed. As a result, the global system of equations can be reduced to the following expression

$$[K_u^r]\{u^r\} = [F_T^r]\{T\} \tag{4.15}$$

where the superscript r indicates that the matrix or vector has been reduced and the $\{F_d^r\}$ vector is not written because all its cells are zero. This system of equations can now be solved to obtain the displacement field that arises due to the thermal state calculated as indicated in Section 3.2.2. This is considered to be the equilibrium state with respect to which distortions arise when thermal boundary conditions change.

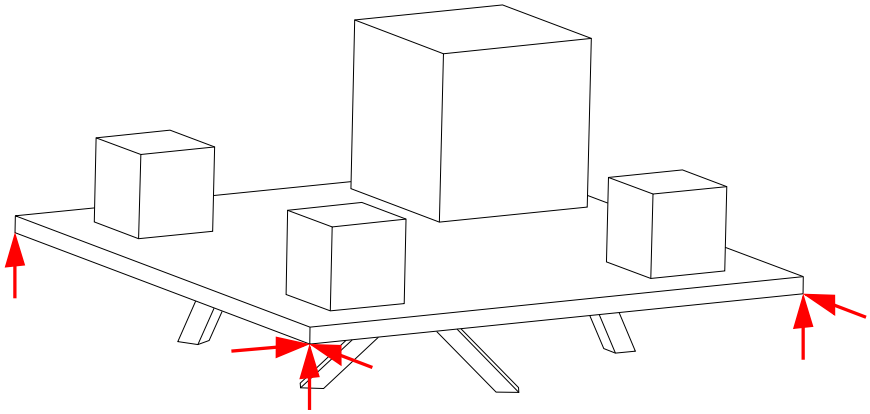

Figure 4.1: Artificial isostatic constraint for the baseline concept.

4.1.2 Transient analysis in the time domain

The traditional approach to solving the system of equations expressed by 4.13 when transient mechanical loads are present is to implement a time integration scheme. The integration scheme presented here is equivalent to the one presented for the thermal problem in Section 3.2.3.

First, the examined time period is subdivided into time steps. Then, given some initial conditions, a system of equations is solved to calculate the displacement, velocity and acceleration at the following time step. The procedure is repeated until the entire time period of interest is covered.

There exist several algorithms to perform this integration that differ in their complexity, accuracy and stability. Some of the algorithms that can be applied to integrate structural dynamics equations are the Central Difference Method (CDM), the Houbolt method, the Park method, the Wilson-θ method and the Newmark method, which for some choice of its parameters is known as the average acceleration method [80]. This last one is arguably the most frequently used in the field of structural dynamics and, therefore, it is outlined here to exemplify how time-integration schemes are applied in this domain.

The assumption behind the average acceleration method is that the acceleration is constant during an integration step. The average value of the acceleration at each integration step is assumed to be

$$\{\ddot{u}\}_{avg} = \frac{\{\ddot{u}\}^t + \{\ddot{u}\}^{t+\Delta t}}{2}. \tag{4.16}$$

Based on this assumption and using the kinematic equations, the velocity at each time step can be calculated using

$$\{\dot{u}\}^{t+\Delta t} = \{\dot{u}\}^t + \left(\{\ddot{u}\}^t + \{\ddot{u}\}^{t+\Delta t}\right)\frac{\Delta t}{2}. \tag{4.17}$$

Similarly, the displacement vector at $t + \Delta t$ can be written as a function of the displacement at t, the velocity and the acceleration as

$$\{u\}^{t+\Delta t} = \{u\}^t + \{\dot{u}\}^t \Delta t + \left(\{\ddot{u}\}^t + \{\ddot{u}\}^{t+\Delta t}\right)\frac{\Delta t^2}{4}. \tag{4.18}$$

Equation 4.18 can be solved for the acceleration at $t + \Delta t$ resulting in

$$\{\ddot{u}\}^{t+\Delta t} = \frac{4}{\Delta t^2}\left(\{u\}^{t+\Delta t} - \{u\}^t\right) - \frac{4}{\Delta t}\{\dot{u}\}^t - \{\ddot{u}\}^t. \tag{4.19}$$

Substituting the previous expression into Equation 4.17 it is possible to express the velocity at $t + \Delta t$ as

$$\{\dot{u}\}^{t+\Delta t} = \frac{2}{\Delta t}\left(\{u\}^{t+\Delta t} - \{u\}^t\right) - \{\dot{u}\}^t. \tag{4.20}$$

The average acceleration method calculates the displacement at $t + \Delta t$ by solving the equations of motion expressed by the system

$$[M_u]\{\ddot{u}\}^{t+\Delta t} + [C_u]\{\dot{u}\}^{t+\Delta t} + [K_u]\{u\}^{t+\Delta t} = \{F(t + \Delta t)\} \tag{4.21}$$

in which the acceleration and the velocity can be calculated from the values at the previous time step by using 4.19 and 4.20, respectively. Introducing these expressions into Equation 4.21 results in

$$\begin{aligned}[\hat{K}]\{u\}^{t+\Delta t} = \{F(t + \Delta t)\} \\ + [M_u]\left(\{\ddot{u}\}^t + \frac{4}{\Delta t}\{\dot{u}\}^t + \frac{4}{\Delta t^2}\{u\}^t\right) \\ + [C_u]\left(\{\dot{u}\}^t + \frac{2}{\Delta t}\{u\}^t\right)\end{aligned} \tag{4.22}$$

where

$$[\hat{K}] = \frac{4}{\Delta t^2}[M_u] + \frac{2}{\Delta t}[C_u] + [K_u]. \tag{4.23}$$

Equation 4.22 can be solved to obtain the displacement values at $t' = t + \Delta t$. The solution can be introduced in 4.19 and 4.20 to obtain the acceleration and velocity values at the same time step. These can then be taken as the initial values to calculate the solution at the following time step.

The results obtained by this method are directly related to the particular function that models the perturbation load. If the response needs to be evaluated under a different perturbation function it is necessary to perform a new time integration in its entirety. This limits the field of application of this method because it becomes computationally expensive when the response needs to be calculated for a wide variety of perturbations at different amplitudes and frequencies.

Structures are often excited at very different frequencies during its lifetime and, therefore, alternative methods based on solving the problem in the frequency domain can be more efficient for structural dynamics analyses. In the framework of this work, the frequency domain approach to the mechanical problem has been combined with the thermal transfer functions obtained in Section 3.2.5 to derive the thermomechanical transfer functions that are subsequently used to develop a controller. The following section presents the frequency domain approach to calculate the mechanical response of the system.

4.1.3 Transient analysis in the frequency domain

The transient response described by the equations of motion in 4.13 can also be calculated by transforming the equations into the frequency domain. This approach has been extensively implemented in the structural dynamics field because it ultimately allows the calculation of transfer functions between applied loads and displacements. Based on these transfer functions it is possible to calculate the displacement response induced by a given mechanical load at a specific frequency. Thus, it is useful to calculate the structural response to high-frequency vibrations and it can also be implemented to obtain the response to low-frequency oscillations induced by thermal perturbations.

In the work presented in this thesis, the focus is on calculating the structural distortions with respect to an equilibrium state. Therefore, the first step consists in rewriting the equations of motion to take into account only changes around the considered equilibrium condition. This can be achieved by introducing the identities

$$T = T_{eq} + \delta T \tag{4.24}$$

and

$$u = u_{eq} + \delta u. \tag{4.25}$$

Thus, the equations of motion can be expressed as

$$\begin{aligned}[M_u]\{\delta\ddot{u}\} + [C_u]\{\delta\dot{u}\} + [K_u]\{u_{eq}\} + [K_u]\{\delta u\} \\ = [F_T]\{T_{eq}\} + [F_T]\{\delta T\} + \{F_d\} + \{\delta F_d\}.\end{aligned} \tag{4.26}$$

where the $\{\delta F_d\}$ term represents the change in the reaction forces that constrain the structure under displacement variations. Taking the equilibrium condition into account, as explained in Section 4.1.1,

$$[K_u]\{u_{eq}\} = [F_T]\{T_{eq}\} + \{F_d\} \tag{4.27}$$

it is possible to write Equation 4.26 as

$$[M_u]\{\delta\ddot{u}\} + [C_u]\{\delta\dot{u}\} + [K_u]\{\delta u\} = [F_T]\{\delta T\} + \{\delta F_d\}. \tag{4.28}$$

As it has been done in Section 4.1.1 to solve the steady-state problem, it is necessary to reduce the previous system of equations in order to calculate the solution of the displacement vector $\{\delta u\}$. Introducing an artificial isostatic constraint to prevent the rigid body motion of the structure it is possible to remove six rows and six columns of the previous system. These rows correspond to the unknowns in the $\{\delta F_d\}$ vector which, thus, disappears from the previous expression. This yields

$$[M_u^r]\{\delta\ddot{u}^r\} + [C_u^r]\{\delta\dot{u}^r\} + [K_u^r]\{\delta u^r\} = [F_T^r]\{\delta T\}. \tag{4.29}$$

Premultiplying now by $[M_u^r]^{-1}$

$$\{\delta\ddot{u}^r\} + [C_M]\{\delta\dot{u}^r\} + [K_M]\{\delta u^r\} = [R_T]\{\delta T\} \tag{4.30}$$

with

$$[C_M] = [M_u^r]^{-1}[C_u^r], \tag{4.31}$$

$$[K_M] = [M_u^r]^{-1}[K_u^r] \tag{4.32}$$

$$\text{and } [R_T] = [M_u^r]^{-1}[F_T^r]. \tag{4.33}$$

The system of equations expressed by 4.30 gives the relation between displacement and temperature changes. The transfer functions between these two variables can be calculated based on this system using a modal representation obtained from a transformation into the frequency domain. The modal representation is implemented following a similar approach to that presented in Section 3.2.4 for the thermal problem. This requires the calculation of the eigenvectors and eigenvalues of matrix $[K_M]$, i.e.

$$[\psi] \ : \text{Eigenvector matrix}$$
$$[\gamma] \ : \text{Eigenvalue diagonal matrix}$$

The modal coordinates are now introduced, which are related to the displacement coordinates according to

$$\{\delta u^r\} = [\psi]\{\eta\}. \tag{4.34}$$

Introducing the previous identity into Equation 4.30 and premultiplying by $[\psi]^{-1}$ results in

$$[\psi]^{-1}[\psi]\{\ddot{\eta}\} + [\psi]^{-1}[C_M][\psi]\{\dot{\eta}\} + [\psi]^{-1}[K_M][\psi]\{\eta\} = [\psi]^{-1}[R_T]\{\delta T\}. \tag{4.35}$$

In this previous equation

$$[\psi]^{-1}[\psi] = [I] \tag{4.36}$$

and

$$[\psi]^{-1}[K_M][\psi] = [\gamma] \tag{4.37}$$

which are both diagonal. Additionally, considering that the damping matrix $[C_u]$ is built as a linear combination of $[M_u]$ and $[K_u]$, as expressed by Equation 4.9, the operation $[\psi]^{-1}[C_M][\psi]$ also results in a diagonal matrix that can be expressed as

$$[\psi]^{-1}[C_M][\psi] = [\xi]. \tag{4.38}$$

Thus, Equation 4.35 can finally be written as

$$\{\ddot{\eta}\} + [\xi]\{\dot{\eta}\} + [\gamma]\{\eta\} = [\psi]^{-1}[R_T]\{\delta T\}. \tag{4.39}$$

At this point, the Laplace transform of the independent variables in the previous equation is introduced to calculate the transfer functions between displacement and temperature. The necessary Laplace transforms are

$$\mathcal{L}\{\ddot{\eta}(t)\} = s^2\eta(s) \tag{4.40}$$
$$\mathcal{L}\{\dot{\eta}(t)\} = s\eta(s) \tag{4.41}$$
$$\mathcal{L}\{\eta(t)\} = \eta(s) \tag{4.42}$$
$$\mathcal{L}\{\delta T(t)\} = \delta T(s) \tag{4.43}$$

which after being introduced in Equation 4.39 result in

$$s^2\{\eta(s)\} + s[\xi]\{\eta(s)\} + [\gamma]\{\eta(s)\} = [\psi]^{-1}[R_T]\{\delta T(s)\}. \tag{4.44}$$

Solving the previous expression for $\{\eta(s)\}$ results in

$$\{\eta(s)\} = \left(s^2[I] + s[\xi] + [\gamma]\right)^{-1}[\psi]^{-1}[R_T]\{\delta T(s)\}. \tag{4.45}$$

The first inverse matrix at the right-hand side can be directly calculated given that its components are all diagonal. Once the vector $\{\eta(s)\}$ has been calculated for a given input $\{\delta T(s)\}$, it is possible to calculate the displacement change vector $\{\delta u^r\}$ using Equation 4.34. Thus, considering only row i in Equation 4.34 and expressing the result as a summation of all the columns in matrix $[\psi]$ multiplied by the corresponding component in $\{\eta(s)\}$, the transfer function with respect to a temperature change at node k at a frequency s can be calculated using

$$H_{uT}(s) = \frac{\delta u_i}{\delta T_k} = \sum_{j=1}^{3n_n} \psi_{ij} \frac{C_{jk}}{s^2 + \xi_j s + \gamma_j} \tag{4.46}$$

where ψ_{ij} represents the ij cell of matrix $[\psi]$ and C_{ij} is the jk cell of matrix $[\psi]^{-1}[R_T]$. The summation ranges from $j = 1$ to $j = 3n_n$ because each of the n_n nodes in the mesh has three degrees of freedom. This transfer function enables the calculation of the displacement at any point in the structure given some temperature change at any other point. These transfer functions can be combined with the thermal transfer equations calculated in Section 3.2.4 to produce thermomechanical transfer functions that give a direct relation between displacement and applied heat.

4.2 Thermomechanical transfer functions

Thermomechanical transfer functions are mathematical expressions that can be evaluated at a given frequency to provide the relation between displacement and heat input. These functions can be derived by combining the mechanical transfer functions, which relate displacement and temperature (see Section 4.1.3), with the thermal transfer functions, which relate temperature and applied heat (see Section 3.2.4). Thus, thermomechanical transfer functions between the displacement at node i and the heat load l can be expressed as

$$H_{uq}(s) = \frac{\delta u_i}{\delta q_l} = \sum_{k=1}^{n_n} \frac{\delta u_i}{\delta T_k} \frac{\delta T_k}{\delta q_l}. \tag{4.47}$$

The combination of the thermal transfer function according to expression 3.96 presented in Section 3.2.4 and the mechanical transfer function according to the expression 4.46 presented in Section 4.1.3 results in

$$H_{uq}(s) = \frac{\delta u_i}{\delta q_l} = \sum_{j=1}^{3n_n} \sum_{k=1}^{n_n} \psi_{ij} \frac{\mathcal{C}_{jk}}{s^2 + \xi_j s + \gamma_j} \frac{A_{kl}}{s + \lambda_k}, \tag{4.48}$$

which defines the displacement change at node i given some heat flux change δq at surface l. In this expression, the value C_{jk} from 4.46 has been substituted for $\mathcal{C}_{jk}$, which is the jk cell of the $[\psi]^{-1}[R_T][\phi]$ matrix that takes into account the thermal modes represented by $[\phi]$.

Similarly, it is possible to calculate the response to an applied heat source change δQ at element l by using the thermal transfer function 3.97, which results in

$$H_{uQ}(s) = \frac{\delta u_i}{\delta Q_l} = \sum_{j=1}^{3n_n} \sum_{k=1}^{n_n} \psi_{ij} \frac{\mathcal{C}_{jk}}{s^2 + \xi_j s + \gamma_j} \frac{B_{kl}}{s + \lambda_k}. \tag{4.49}$$

Considering again the baseline case presented in Section 3.2.4 it is possible to apply now these transfer functions to calculate the introduced distortion given a thermal change. The same case is illustrated here to exemplify the calculation of the distance change between points A and B of the structure, which are reference points of two different instruments, as represented in Figure 4.2.

Assuming an internal heat change at instrument 1 equal to $\delta Q_1 = 5\,\mathrm{W}$ at a frequency of $10^{-5}\,\mathrm{Hz}$ and applying Equation 4.49 it is possible to calculate the displacement variation at point A and at point B in each spatial direction. The difference between the two values gives the distance change between A and B, which can thus be calculated by

$$\delta u_{AB} = \left(\frac{\delta u_A}{\delta Q_1}\left(10^{-5}\,\mathrm{Hz}\right) - \frac{\delta u_B}{\delta Q_1}\left(10^{-5}\,\mathrm{Hz}\right) \right) \delta Q_1 = 0.139\,\mu\mathrm{m}\ \angle -36.55^\circ \tag{4.50}$$

$$\delta v_{AB} = \left(\frac{\delta v_A}{\delta Q_1}\left(10^{-5}\,\mathrm{Hz}\right) - \frac{\delta v_B}{\delta Q_1}\left(10^{-5}\,\mathrm{Hz}\right) \right) \delta Q_1 = 0.204\,\mu\mathrm{m}\ \angle -54.97^\circ \tag{4.51}$$

$$\delta w_{AB} = \left(\frac{\delta w_A}{\delta Q_1}\left(10^{-5}\,\mathrm{Hz}\right) - \frac{\delta w_B}{\delta Q_1}\left(10^{-5}\,\mathrm{Hz}\right) \right) \delta Q_1 = 0.403\,\mu\mathrm{m}\ \angle -41.05^\circ \tag{4.52}$$

This displacement response is illustrated in Figure 4.3. It shows that the phase delay with respect to the perturbation is different in each direction and that the largest distortion appears in the z-direction.

The same procedure can be applied to calculate the displacement response under a perturbation with a different location, magnitude or frequency. Also, given that the equations have been linearized, the total response under different perturbations can be calculated by superimposing each individual response from each perturbation. Assuming that there are n different heat sources from n different points, each acting at a different frequency, the resulting displacement response can be calculated as

$$\delta u = \sum_{i=1}^{n} \left(H_{uQ_i}(s_i) \right) \delta Q_i \tag{4.53}$$

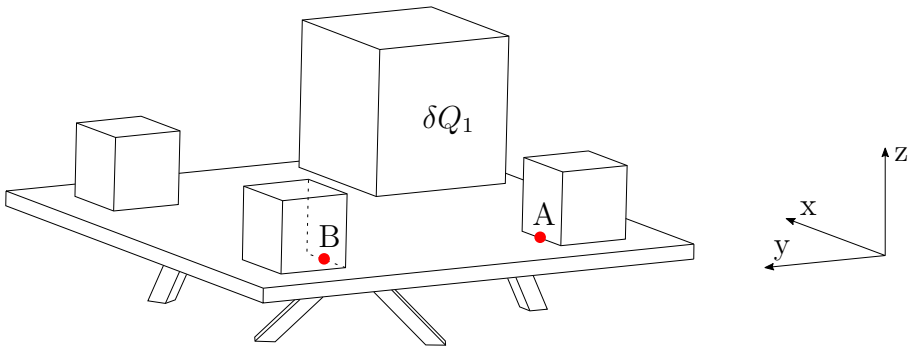

Figure 4.2: Representation of points A and B in the baseline concept.

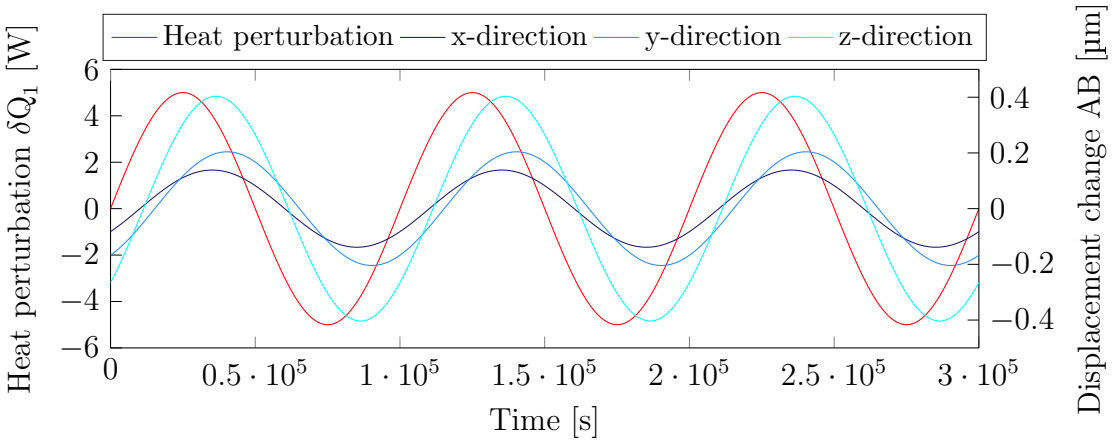

Figure 4.3: Displacement change between points A and B induced by a perturbation of 5 W at $f = 10^{-5}$ Hz from Instrument 1.

4.2.1 Modal representation and truncation

The previous transfer functions are based on a modal representation of both the thermal and the mechanical problem. The details on the thermal modal representation have been presented in Section 3.2.5. Based on the same approach, the mechanical response of the system can be expressed as a linear combination of several mechanical modes. In this case, each mode represents a fundamental possible shape that the structure can take as it oscillates. Each shape mode can be expressed as a normalized vector that corresponds to a column in the $[\psi]$ matrix and that contains the displacement of each degree of freedom. Figure 4.4 illustrates the first eight mechanical modes that describe the structural response of the baseline case.

Each mode has a different weight in the total response, which implies a different contribution to the distortion field. Most of the weight is often distributed among a small number of modes relative to the total number of modes. This weight distribution depends on the location, magnitude and frequency of the applied load. The calculation of the response can be simplified by considering only a subset of mechanical and thermal modes, those with the greatest weights. This introduces a certain error in the calculation but reduces the number of terms that must be taken into account. In mathematical terms, this implies considering only N out of the total n_n thermal modes and M out of the $3n_n$ mechanical modes. In that case, the thermomechanical transfer functions can be expressed as

$$H_{uq}(s) = \frac{\delta u_i}{\delta q_l} = \sum_{j=1}^{M} \sum_{k=1}^{N} \psi_{ij} \frac{\mathcal{C}_{jk}}{s^2 + \xi_j s + \gamma_j} \frac{A_{kl}}{s + \lambda_k} \tag{4.54}$$

$$\text{and} \quad H_{uQ}(s) = \frac{\delta u_i}{\delta Q_l} = \sum_{j=1}^{M} \sum_{k=1}^{N} \psi_{ij} \frac{\mathcal{C}_{jk}}{s^2 + \xi_j s + \gamma_j} \frac{B_{kl}}{s + \lambda_k}. \tag{4.55}$$

This reduction of the number of terms included in the transfer functions can be understood as a simplification of the thermomechanical model. The magnitude of the error that this procedure introduces is proportional to the overall weight of the neglected nodes. The error can be marginally decreased by considering additional modes, but each additional mode introduces a lower decrease of the error.

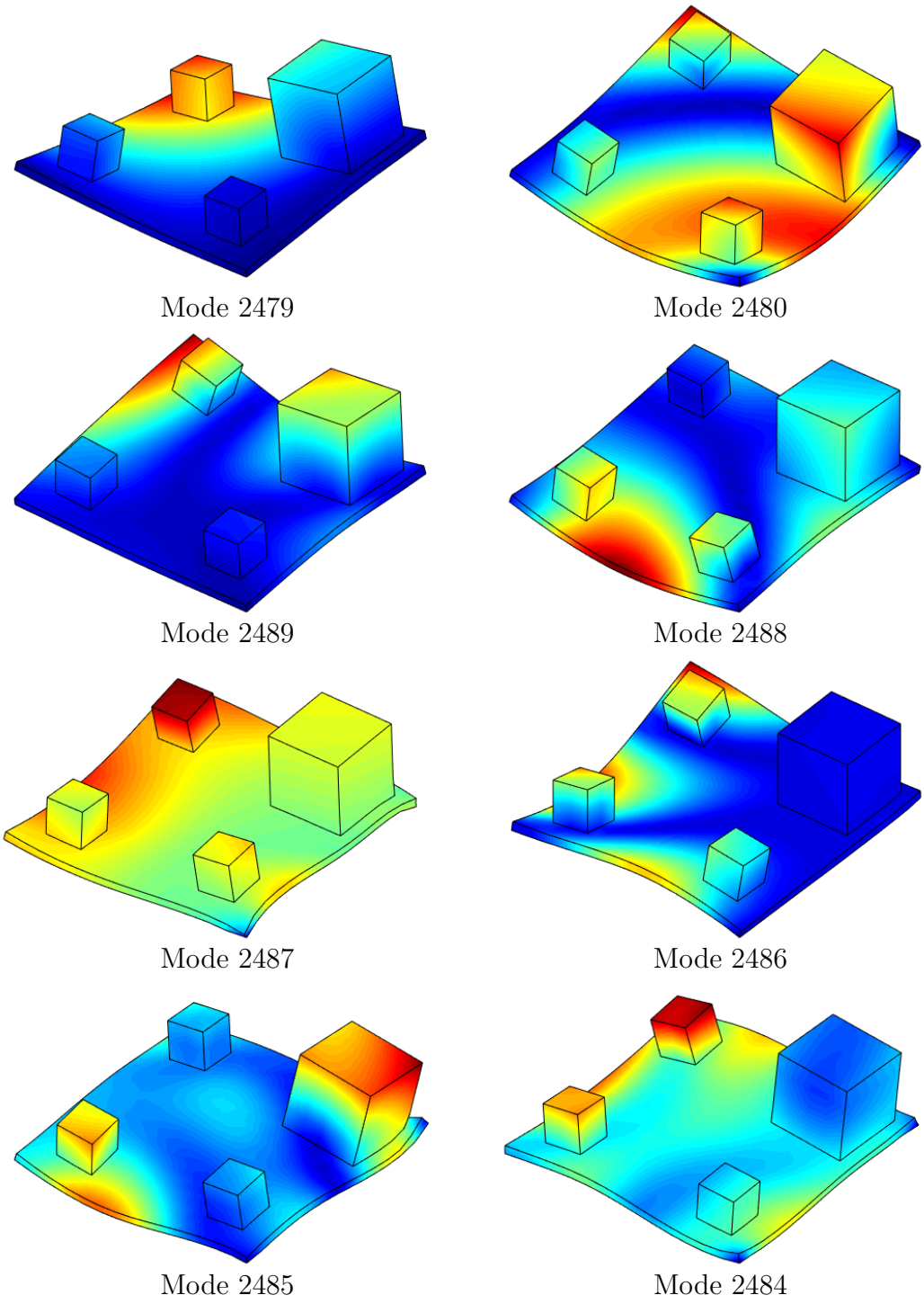

Figure 4.4: First 8 mechanical modes that describe the displacement response.

4.2.2 Quasi-static assumption

The thermomechanical transfer functions derived in the previous sections can be evaluated as a function of the frequency. The result is illustrated in Figures 4.5 and 4.6 for the thermal and the mechanical case, respectively.

It can be observed that the thermal transfer function, expressed as the temperature change at point A given a heat input at instrument 1 at frequencies ranging from 10^{-8} Hz to 10^{-2} Hz, behaves as a low-pass filter. Figure 4.5 shows that the transfer gain is constant up to approximately 10^{-5} Hz and that it decreases afterwards. The mechanical transfer function illustrated in Figure 4.6 represents the displacement change in the x-direction of point A given a temperature change at the same point. In this case, the introduced distortion is almost constant at frequencies below 10 Hz and it shows an attenuated resonant behavior above this threshold.

Based on the data represented by these two figures it can be concluded that throughout the frequency regime at which thermal perturbations are relevant, the mechanical behavior can be described as quasi-static. Figure 4.5 proves that for the baseline case, thermal perturbations above 10^{-5} Hz are quickly attenuated. At frequencies above 10^{-2} Hz, any low-amplitude heat perturbation can only have a negligible effect. Throughout all this range, the mechanical transfer function has a flat gain because the contributions arising due to damping and inertia effects are negligible. In this case, they only influence significantly the response at frequencies above 10 Hz.

Assuming that the inertia and damping contributions are negligible is equivalent to treating the mechanical problem as quasi-static, i.e. each instantaneous state can be considered to be in mechanical equilibrium and can be solved using the steady-state Equation 4.15. When this assumption is implemented, the thermomechanical transfer functions can be simplified if the inertia and damping terms are removed. This results in

$$H_{uq}(s) = \frac{\delta u_i}{\delta q_l} = \sum_{j=1}^{3n_n} \sum_{k=1}^{n_n} \psi_{ij} \frac{\mathcal{C}_{jk}}{\gamma_j} \frac{A_{kl}}{s+\lambda_k} \tag{4.56}$$

$$\text{and} \quad H_{uQ}(s) = \frac{\delta u_i}{\delta Q_l} = \sum_{j=1}^{3n_n} \sum_{k=1}^{n_n} \psi_{ij} \frac{\mathcal{C}_{jk}}{\gamma_j} \frac{B_{kl}}{s+\lambda_k}, \tag{4.57}$$

which considering the abbreviations

$$\mathcal{A}_{kl} = A_{kl} \left(\sum_{j=1}^{3n_n} \psi_{ij} \frac{\mathcal{C}_{jk}}{\gamma_j} \right) \tag{4.58}$$

$$\text{and} \quad \mathcal{B}_{kl} = B_{kl} \left(\sum_{j=1}^{3n_n} \psi_{ij} \frac{\mathcal{C}_{jk}}{\gamma_j} \right), \tag{4.59}$$

can be finally written as

$$H_{uq}(s) = \frac{\delta u_i}{\delta q_l} = \sum_{k=1}^{n_n} \frac{\mathcal{A}_{kl}}{s+\lambda_k} \tag{4.60}$$

$$\text{and} \quad H_{uQ}(s) = \frac{\delta u_i}{\delta Q_l} = \sum_{k=1}^{n_n} \frac{\mathcal{B}_{kl}}{s+\lambda_k}. \tag{4.61}$$

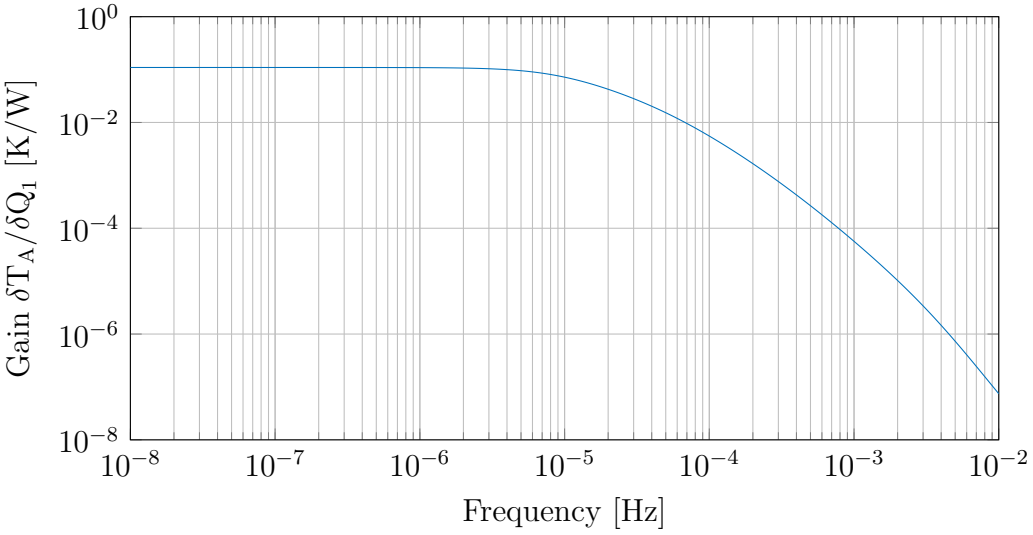

Figure 4.5: Transfer gain between temperature fluctuation at point A and heat perturbation in Instrument 1.

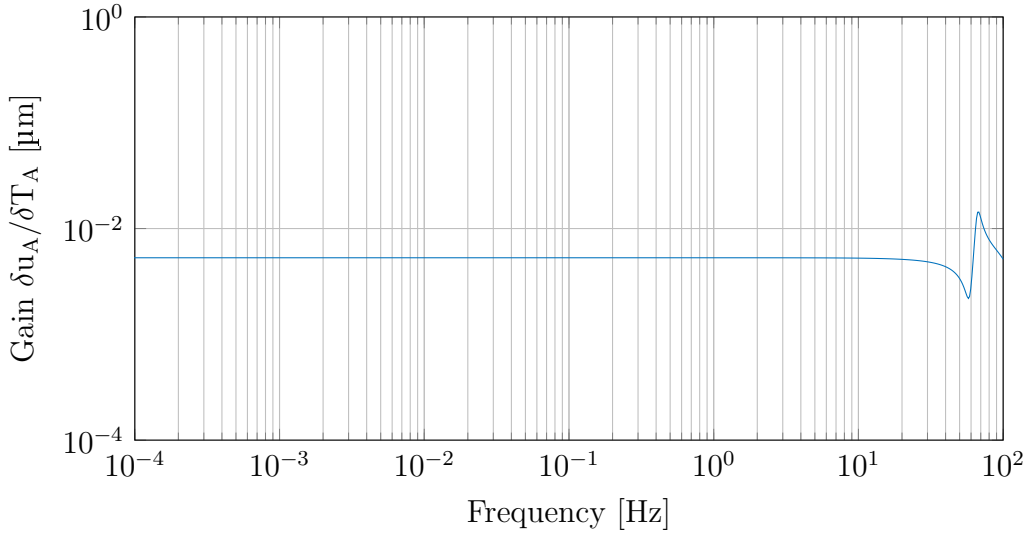

Figure 4.6: Transfer gain between displacement change and temperature fluctuation at point A.

Chapter 5

Control Framework

The previous chapters have presented the FEM derivation of a thermomechanical model. Based on this model it has been possible to derive thermomechanical transfer functions that relate heat input and structural displacements as a function of the frequency. This formulation is the first step in developing a control framework that enables the distortion minimization at some points based on the applied heat.

A direct approach to displacement control can be implemented if the expected heat perturbations can be thoroughly characterized. When perturbations are predictable and it is feasible to characterize them, it becomes possible to calculate the displacements they introduce to the structure and to determine the heat input that is necessary to compensate them. This approach is referred to in this chapter as the perturbation compensation method and is presented in detail in Section 5.1. The more general case is that in which the heat perturbations acting on the structure have a random component. Under this condition it is necessary to install sensors to estimate the displacement state of the structure and to implement a control loop to calculate the heat inputs that can minimize the introduced distortions. The approach developed in this thesis is presented in detail in Section 5.2.

The possible sensor and actuator strategies as well as the modeling of their behavior to simulate the performance of the described control loop are presented in detail in Sections 5.3 and 5.4. This includes the implementation of a Kalman filter, as presented in Section 5.5, in order to mitigate the impact of noise affecting the control. The complete formulation of the control loop with all the aspects presented in this chapter is included in Section 5.6. Finally, the chapter ends with a list of necessary steps in Section 5.7 to implement the presented framework in a real structure.

5.1 Perturbation compensation method

The perturbation compensation method is a direct approach to calculate the necessary heat input that cancels the distortion effects of a particular heat perturbation acting on a structure. From a mathematical point of view, this approach consists in solving a linear system of equations where the unknown variables are the heat inputs applied by the control heat sources.

Considering that a mathematical function of the applied heat perturbation δQ_n expressed in the frequency domain is known, it is possible to calculate the induced displacement response by using the corresponding transfer function, as expressed by Equation 4.61, thus

$$\delta u_i = \left[H_{u_i Q_n}\right]_s \delta Q_n = \left[\frac{\delta u_i}{\delta Q_n}(s)\right] \delta Q_n. \tag{5.1}$$

The previous equation describes a single-input and single-output (SISO) system, in which the displacement in the x-direction at node i is calculated as a function of the heat perturbation at source n. If more output variables are considered, such as the displacement at node i in the three spatial directions, the problem becomes a single-input and multiple-output (SIMO) system, which in this case can be expressed as

$$\begin{Bmatrix} \delta u_i \\ \delta v_i \\ \delta w_i \end{Bmatrix} = \begin{bmatrix} H_{u_i Q_n} \\ H_{v_i Q_n} \\ H_{w_i Q_n} \end{bmatrix}_s \left\{\delta Q_n\right\}. \tag{5.2}$$

This system can be further extended to consider several heat sources which results in a multiple-input and multiple-output (MIMO) system,

$$\begin{Bmatrix} \delta u_i \\ \delta v_i \\ \delta w_i \end{Bmatrix} = \begin{bmatrix} H_{u_i Q_n} & \dots & H_{u_i Q_m} \\ H_{v_i Q_n} & \dots & H_{v_i Q_m} \\ H_{w_i Q_n} & \dots & H_{w_i Q_m} \end{bmatrix}_s \begin{Bmatrix} \delta Q_n \\ \dots \\ \delta Q_m \end{Bmatrix}. \tag{5.3}$$

The previous MIMO system has three outputs corresponding to the displacement in each direction at node i. These displacements can be forced to be zero by introducing three further variables in the system. These new variables describe the controlled heat added to the system by additional heat sources. Considering that these three control heat sources are δQ_1, δQ_2 and δQ_3 it is possible to express the system response as

$$\begin{aligned} \begin{Bmatrix} \delta u_i \\ \delta v_i \\ \delta w_i \end{Bmatrix} = & \begin{bmatrix} H_{u_i Q_n} & \dots & H_{u_i Q_m} \\ H_{v_i Q_n} & \dots & H_{v_i Q_m} \\ H_{w_i Q_n} & \dots & H_{w_i Q_m} \end{bmatrix}_s \begin{Bmatrix} \delta Q_n \\ \dots \\ \delta Q_m \end{Bmatrix} \\ & + \begin{bmatrix} H_{u_i Q_1} & H_{u_i Q_2} & H_{u_i Q_3} \\ H_{v_i Q_1} & H_{v_i Q_2} & H_{v_i Q_3} \\ H_{w_i Q_1} & H_{w_i Q_2} & H_{w_i Q_3} \end{bmatrix}_s \begin{Bmatrix} \delta Q_1 \\ \delta Q_2 \\ \delta Q_3 \end{Bmatrix}. \end{aligned} \tag{5.4}$$

The control heat vector that cancels the displacement vector at node i can be derived from the previous system of equations as

$$\begin{Bmatrix} \delta Q_1 \\ \delta Q_2 \\ \delta Q_3 \end{Bmatrix} = - \begin{bmatrix} H_{u_i Q_1} & H_{u_i Q_2} & H_{u_i Q_3} \\ H_{v_i Q_1} & H_{v_i Q_2} & H_{v_i Q_3} \\ H_{w_i Q_1} & H_{w_i Q_2} & H_{w_i Q_3} \end{bmatrix}_s^{-1} \begin{bmatrix} H_{u_i Q_n} & \dots & H_{u_i Q_m} \\ H_{v_i Q_n} & \dots & H_{v_i Q_m} \\ H_{w_i Q_n} & \dots & H_{w_i Q_m} \end{bmatrix}_s \begin{Bmatrix} \delta Q_n \\ \dots \\ \delta Q_m \end{Bmatrix}. \tag{5.5}$$

An essential requirement to apply this method is to have a mathematical expression of the heat perturbations acting on the structure, which correspond to the heat vector at the right-hand side of the previous system. This system is solved in the frequency domain and thus, it is necessary to have an expression of the corresponding perturbation functions also in this domain. If instead a time domain function is available, the most straightforward procedure to obtain the frequency representation is to calculate it in terms of the Fourier series. This transformation provides an equivalent expression of a given time function expressed as a summation of several sinusoidal terms, i.e.

$$\delta Q_n(t) = \delta Q_{n,0} + \sum_{k=1}^{N} \delta Q_{n,k} \sin(\omega_k t + \varphi_{n,k}) \tag{5.6}$$

where the necessary coefficients can be calculated using standard Fourier series transformation techniques. In those cases in which there are several perturbation sources, each of them with several components at different frequencies, it becomes necessary to solve system 5.5 at different frequencies to obtain the components of δQ_1, δQ_2 and δQ_3, which in turn are also expressed using Equation 5.6. Each component k is thus calculated using

$$\begin{Bmatrix} \delta Q_1 \\ \delta Q_2 \\ \delta Q_3 \end{Bmatrix}_k = - \begin{bmatrix} H_{u_i Q_1} & H_{u_i Q_2} & H_{u_i Q_3} \\ H_{v_i Q_1} & H_{v_i Q_2} & H_{v_i Q_3} \\ H_{w_i Q_1} & H_{w_i Q_2} & H_{w_i Q_3} \end{bmatrix}^{-1}_{\omega_k} \begin{bmatrix} H_{u_i Q_n} & \dots & H_{u_i Q_m} \\ H_{v_i Q_n} & \dots & H_{v_i Q_m} \\ H_{w_i Q_n} & \dots & H_{w_i Q_m} \end{bmatrix}_{\omega_k} \begin{Bmatrix} \delta Q_n \angle \varphi_n \\ \dots \\ \delta Q_m \angle \varphi_m \end{Bmatrix}_k . \tag{5.7}$$

By solving the previous system at all the required frequencies ω_k it is possible to calculate the Fourier series of the heat control sources. When this calculated control heat acts on the structure in conjunction with the known perturbations, the thermal field that arises cancels the distortions at node i.

The number of heat control sources is always equal to the number of degrees of freedom that are controlled. In the previous case, this number is three because only the displacements of node i in the three spatial directions are controlled. If further points in the structure were to be controlled it would be necessary to consider additional control sources.

In general, it cannot be assumed that heat perturbations acting on the structure are known and can be fully characterized. While some information about the level of expected perturbations can be known beforehand, it must be expected that a random component will always be present. Therefore, the perturbation compensation method presented in this section is only useful in those cases where any random perturbation acting on the structure is nonexistent or can be neglected. Since this is not normally the case it is required to implement a feedback control loop that provides in real time the necessary heat input based on the estimation of the present distortions from a set of sensors. The approach that has been followed in this thesis is presented in the next section.

5.2 Optimal control method

The control strategy behind the method presented in this thesis consists in controlling the temperature distribution within a structure in order to minimize its displacement at some specific locations. The key aspect is not to minimize temperature fluctuations, which would also be a way to reduce distortions induced by thermomechanical effects, but rather to generate the temperature field that cancels the distortions at some points introduced by an external perturbation.

In mathematical terms this implies that the system which is ultimately controlled corresponds to the thermal model of the structure, which has been derived in Section 3.2.4 and can be described by the equation

$$\{\delta\dot{T}\} + [H_T]\{\delta T\} = [H_q]\{\delta q\} + [H_Q]\{\delta Q\}. \tag{5.8}$$

In order to simplify the following mathematical formulation the applied heat terms at the right-hand side of the previous equation are grouped into a single term, $[H]\{\delta q\}$, which is assumed hereafter to represent both heat fluxes and heat sources. Thus, Equation 5.8 becomes

$$\{\delta\dot{T}\} + [H_T]\{\delta T\} = [H]\{\delta q\}. \tag{5.9}$$

However, it is important to make a distinction between heat inputs associated to control, $\{\delta q_c\}$, and heat inputs associated to perturbations, $\{\delta q_{pert}\}$. Therefore, Equation 5.9 is rewritten into

$$\{\delta\dot{T}\} + [H_T]\{\delta T\} = [H_c]\{\delta q_c\} + [H_{pert}]\{\delta q_{pert}\}. \tag{5.10}$$

where the $[H_c]$ and $[H_{pert}]$ matrices are built from the specific columns of $[H]$ that represent the corresponding control or perturbation elements. This equation describes a MIMO system where the inputs are a finite number of heat fluxes or sources and the outputs are the temperatures at the nodes in the mesh. One possibility is to directly implement a controller to the continuous-time system described by Equation 5.10. However, taking into account that in reality the control inputs have a discrete nature and that, additionally, they are estimated from sensor readings that are also obtained at discrete time steps, it is necessary to discretize the equations before developing the control loop. The continuous system of equations described by 5.10 can be approximated using a forward difference scheme as

$$\begin{aligned}\frac{\{\delta T\}^{t+\Delta t} - \{\delta T\}^t}{\Delta t} = &- [H_T]\left(\theta\{\delta T\}^{t+\Delta t} + (1-\theta)\{\delta T\}^t\right) \\ &+ [H_c]\left(\theta\{\delta q_c\}^{t+\Delta t} + (1-\theta)\{\delta q_c\}^t\right) \\ &+ [H_{pert}]\left(\theta\{\delta q_{pert}\}^{t+\Delta t} + (1-\theta)\{\delta q_{pert}\}^t\right)\end{aligned} \tag{5.11}$$

where θ is an approximation parameter that can take values between 0 and 1. For $\theta = 0$ the previous equation results in an explicit scheme, $\theta = 1$ results in an implicit scheme and for values in between the scheme is considered semi-implicit. Here, the equations are solved for $\theta = 0.5$, which results in the Crank-Nicolson method and

can be written as

$$\begin{aligned}\frac{\{\delta T\}^{t+\Delta t}-\{\delta T\}^{t}}{\Delta t} =& -[H_T]\frac{\{\delta T\}^{t+\Delta t}+\{\delta T\}^{t}}{2}\\ &+[H_c]\frac{\{\delta q_c\}^{t+\Delta t}+\{\delta q_c\}^{t}}{2}\\ &+[H_{pert}]\frac{\{\delta q_{pert}\}^{t+\Delta t}+\{\delta q_{pert}\}^{t}}{2}.\end{aligned} \tag{5.12}$$

Rearranging the terms in the previous equation it is possible to write

$$\begin{aligned}\{\delta T\}^{t+\Delta t} =& \left([I]+\frac{[H_T]\Delta t}{2}\right)^{-1}\left([I]-\frac{[H_T]\Delta t}{2}\right)\{\delta T\}^{t}\\ &+\left([I]+\frac{[H_T]\Delta t}{2}\right)^{-1}([H_c]\Delta t)\,\frac{\{\delta q_c\}^{t+\Delta t}+\{\delta q_c\}^{t}}{2}\\ &+\left([I]+\frac{[H_T]\Delta t}{2}\right)^{-1}([H_{pert}]\Delta t)\,\frac{\{\delta q_{pert}\}^{t+\Delta t}+\{\delta q_{pert}\}^{t}}{2}\end{aligned} \tag{5.13}$$

which can be abbreviated to

$$\begin{aligned}\{\delta T\}^{t+\Delta t} =& [\mathcal{H}_T]\{\delta T\}^{t}\\ &+[\mathcal{H}_c]\frac{\{\delta q_c\}^{t+\Delta t}+\{\delta q_c\}^{t}}{2}\\ &+[\mathcal{H}_{pert}]\frac{\{\delta q_{pert}\}^{t+\Delta t}+\{\delta q_{pert}\}^{t}}{2}.\end{aligned} \tag{5.14}$$

This system of equations can now be taken as the basis to develop a discretized control loop. One possibility is to calculate the optimal control law that minimizes a defined cost function, which is a common approach in the field of smart structures both using thermal strain [63, 64] or piezoactuators [82, 83]. If this approach is implemented on a linear system the controller is known as linear quadratic regulator (LQR), which is one of the most widely used control methods in the aerospace field [84]. The LQR provides a particular solution to the optimal control problem in which the control inputs are calculated to optimize a quadratic function of both inputs and outputs. This quadratic function is defined as

$$J=\int_0^{\infty}\left(Y^2(t)+\rho U^2(t)\right)dt \tag{5.15}$$

where Y represents the output, U represents the control input and ρ is a relative weight factor between them. Thus, for low values of ρ the function gives more weight to the output values whereas for large values of ρ the opposite is true. The previous expression assumes that there exists a control input for which the integrand converges to zero and thus the integral is finite.

According to expression 5.14 the control inputs are described by the heat vector $\{\delta q_c\}$ and, therefore, the second term inside the integrand of the cost function can be expressed in matrix form as

$$\rho U^2(t)=\{\delta q_c\}^T[R]\{\delta q_c\} \tag{5.16}$$

where $[R]$ is a weight matrix that specifies the relative weight of each heat control input with respect to the output variables. Considering that the same weight is assigned to each input source it is possible to build the $[R]$ matrix as a multiple of the identity matrix.

Additionally, it is necessary to define the outputs of the system and their corresponding weight in order to calculate the cost function 5.15. Previous approaches of shape control based on the LQR controller and thermal strain have been based on directly canceling specific thermal modes in order to minimize the effect of thermal perturbations on the displacement field [64, 85]. The approach developed here differs from previous strategies because the output that is being controlled corresponds directly to the displacement at some specific positions. Thus, the output that is considered in the cost function is the displacement variation at the controlled locations and not the intermediate temperature fluctuations.

The displacement variations are indirectly related to Equation 5.14 because they depend on the temperature fluctuations. The relation between these two variables has been derived in Chapter 4 and it is expressed by Equation 4.28, which is repeated here for clarity

$$[M_u]\{\delta\ddot{u}\} + [C_u]\{\delta\dot{u}\} + [K_u]\{\delta u\} = [F_T]\{\delta T\} + \{\delta F_d\}. \tag{5.17}$$

Chapter 4 has also shown in Section 4.2.2 that when the internal stress arising in the structure has a thermal origin it can be generally assumed that the behavior is quasi-static. This implies that the contribution to the deformation field induced by inertia and damping effects can be neglected and thus, the previous equation can be simplified to

$$[K_u]\{\delta u\} = [F_T]\{\delta T\} + \{\delta F_d\}. \tag{5.18}$$

This system of equations can be reduced by removing the unknown variables in the $\{\delta F_d\}$ vector that correspond to the reaction forces that constrain the structure. This process is explained in detail in Section 4.1.1 and if applied to this case results in the equation

$$[K_u^r]\{\delta u^r\} = [F_T^r]\{\delta T\} \tag{5.19}$$

or equivalently,

$$\{\delta u^r\} = [K_u^r]^{-1}[F_T^r]\{\delta T\} = [\mathcal{F}_T]\{\delta T\}. \tag{5.20}$$

In general, only some points in the structure will be controlled and, as a consequence, the outputs of the system correspond to only some specific cells of the $\{\delta u^r\}$ vector. This can be expressed by further reducing Equation 5.20 and thereby expressing the outputs of the system as

$$\{\delta u\}_{out} = [\mathcal{F}_T]_{out}\{\delta T\} \tag{5.21}$$

where $[\mathcal{F}_T]_{out}$ is built from only the relevant rows of the $[\mathcal{F}_T]$ matrix or evaluating the mechanical transfer functions at the corresponding frequency, which is 0 Hz for the static case. Based on this expression it is possible to define now the output of the system included in the cost function 5.15, which can be calculated as

$$Y^2(t) = \{\delta u\}_{out}^T\{\delta u\}_{out} = \{\delta T\}^T[\mathcal{F}_T]_{out}^T[\mathcal{F}_T]_{out}\{\delta T\} = \{\delta T\}^T[Q]\{\delta T\} \tag{5.22}$$

where $[Q]$ is the weight matrix assigning different relative weights among the different cells of vector $\{\delta T\}$ and as indicated is calculated from $[\mathcal{F}_T]_{out}$. By inserting now

Equations 5.16 and 5.22 into the cost function 5.15 it is possible to express it as

$$\begin{aligned} J &= \int_0^\infty \left(\{\delta u\}_{out}^T \{\delta u\}_{out} + \{\delta q_c\}^T [R] \{\delta q_c\} \right) dt \\ &= \int_0^\infty \left(\{\delta T\}^T [Q] \{\delta T\} + \{\delta q_c\}^T [R] \{\delta q_c\} \right) dt. \end{aligned} \tag{5.23}$$

Based on the LQR method, the input $\{\delta q_c\}$ that minimizes J is defined considering a feedback loop that applies a proportional gain to the output, i.e.

$$\{\delta q_c\}^t = -[K_{LQR}] \{\delta T\}^t \tag{5.24}$$

where the gain matrix $[K_{LQR}]$ is in turn calculated in the discrete-time case as

$$[K_{LQR}] = \left([R] + [\mathcal{H}_c]^T [P] [\mathcal{H}_c] \right)^{-1} [\mathcal{H}_c]^T [P] [\mathcal{H}_T] \tag{5.25}$$

and $[P]$ is obtained from the expression

$$\begin{aligned} [P] = {} & [\mathcal{H}_T]^T [P] [\mathcal{H}_T] + [Q] \\ & - \left([\mathcal{H}_T]^T [P] [\mathcal{H}_c] \right) \left([R] + [\mathcal{H}_c]^T [P] [\mathcal{H}_c] \right)^{-1} \left([\mathcal{H}_c]^T [P] [\mathcal{H}_T] \right) \end{aligned} \tag{5.26}$$

which is known as the discrete-time algebraic Riccati equation and can be solved for $[P]$ using a Newton-type iterative method [86]. Taking now into account the definition of the control input expressed by 5.24, it is possible to write the closed-loop system of equations based on 5.14, which results in

$$\begin{cases} \{\delta T\}^{t+\Delta t} + \dfrac{[\mathcal{H}_c][K_{LQR}]}{2} \{\delta T\}^{t+\Delta t} = \left([\mathcal{H}_T] - \dfrac{[\mathcal{H}_c][K_{LQR}]}{2} \right) \{\delta T\}^t \\ \qquad\qquad + [\mathcal{H}_{pert}] \dfrac{\{\delta q_{pert}\}^{t+\Delta t} + \{\delta q_{pert}\}^t}{2} \\ \{\delta u\}^{t+\Delta t} = [\mathcal{F}_T] \{\delta T\}^{t+\Delta t} \end{cases} \tag{5.27}$$

The system described by the previous equation can only be implemented under the assumption that all the nodal temperatures are known. This is mathematically consistent but currently unfeasible from a technical point of view given that it would require a temperature sensor for each node in the mesh. Thus, it is necessary to develop a strategy that enables the implementation of the presented system when only partial information about the thermal or distortion state of the structure is available.

Additionally, the uncertainty in the behavior of sensors and actuators must be taken into account. Sensors provide noisy measurements with limited accuracy and it cannot be assumed that actuators behave exactly as commanded. The strategies to mitigate the control performance decrease induced by these factors are presented in sections 5.3 and 5.4. The LQR method previously presented must be modified accordingly to integrate these strategies which results in the closed-loop formulation presented in Section 5.6.

5.3 Sensor model framework

Sensors are crucial to estimate the state of the variables that are being controlled. The control strategy presented in this thesis aims to stabilize the displacement changes at some specific points based on the modification of the thermal field. In other words, the temperature distribution is controlled in such a way that some specific distortion metrics in the structure remain at approximately constant values. Thus, as presented in the previous section, the necessary heat inputs to ultimately control the distortion field are not directly calculated as a function of the underlying displacements but as a function of the temperature field, which is modified at each instant to induce a displacement field where distortions are stabilized.

This section starts with a presentation of the possible sensor strategies that could be implemented to estimate the thermal state of the structure, which is necessary to derive the control heat inputs. The formulation for the chosen strategy is then described along with the sensor model to take into account the sensor uncertainties.

5.3.1 Sensor strategies

The objective of the sensor strategy is to estimate the full temperature vector $\{\delta T\}$ to enable the calculation of the control heat inputs using Equation 5.24.

The most straightforward option to perform this estimation would be to equip the structure with as many temperature sensors as considered nodes in the FEM model and to mount each of them at a position corresponding to one node. This would involve a large number of sensors and it would also require embedding them at internal positions of the structure which could deteriorate its mechanical properties. Given the current state of technology concerning temperature sensors, it is regarded as unfeasible to implement such an option.

Assuming that it is not an option to directly measure each cell of the $\{\delta T\}$ vector, an alternative consists in measuring only the temperature of the structure at some specific points and implementing afterwards a mathematical procedure to reconstruct the full thermal field while minimizing the estimation error. The mathematical technique that has been implemented in this thesis is described as a thermal modal expansion and is presented in detail in Section 5.3.2.

Apart from the technical challenge associated with the limited amount of measurements, it must also be taken into account that each individual sensor does not provide an ideal measurement. Instead, errors arising from uncertainties and an intrinsic level of noise are always present. Even high-accuracy temperature sensors rarely provide accuracies below $\pm 0.1\,\mathrm{K}$ at a wide range of temperatures. The procedure followed to model this source of errors is presented in Section 5.3.3.

A promising sensor option, in opposition to the traditional approach of directly mounted sensors in the structure, is to use infrared cameras. These could take several temperature measurements at different points of the structure simultaneously. In principle, this would allow the measurement at more points than with mounted sensors and it would not compromise the mechanical properties of the structure. If

combined with actuators external to the structure, which is a possible option presented in Section 5.4.1, it would result in a completely non-intrusive control strategy that would not require mounting any equipment directly in the stable structure.

It should also be noted that displacement sensors could also be implemented to improve the temperature estimation. This could be performed based on Equation 5.20 presented in Section 5.2. This equation gives a relation between temperature and displacement. As in the case of the temperature sensors, it is not feasible to equip the structure with sensors to measure the entire $\{\delta u\}$ vector. However, if some of its cells are known, either through direct measurements of the displacement or through estimations based on strain sensors, it is possible to use Equation 5.20 to reduce the error in the estimation of the $\{\delta T\}$ vector obtained purely from temperature sensors.

5.3.2 Thermal modal expansion

A mathematical procedure is necessary to estimate the entire $\{\delta T\}$ vector based on the measurement of only some of its values. A very similar problem exists in the structural dynamics field where, also for shape control purposes, the displacement or strain field needs to be reconstructed based on a limited number of measurements.

A possible solution to this problem is based on the modal representation of the involved variables. This has been applied in the structural dynamics field [87] but the same principle can be applied in the thermal case, as presented in reference [88], to estimate the thermal field of a structure from the measurements of only some sensors. This principle is presented here in detail as it enables the control loop expressed by Equation 5.27.

The enabling idea behind the field reconstruction as presented in [87] and [88] is the modal representation. This procedure has been presented in this thesis in Section 3.2.5 for the linearized thermal problem and in Section 4.2.1 for the mechanical problem. The modal representation of the thermal problem results in the thermal field being expressed as

$$\{\delta T\} = [\phi]\{\tau\} \tag{5.28}$$

where each column in the $[\phi]$ matrix represents a thermal mode and the $\{\tau\}$ vector assigns a different weight to each mode to express the resulting response. The important property of this representation is that, at the expense of introducing an error, it allows the calculation of vector $\{\delta T\}$ based only on a subset of modes. This is known as modal truncation and is presented in detail for the linearized thermal case in Section 3.2.5.

Considering that there are n degrees of freedom in the model, all the variables in the Equation 5.28 have a dimension equal to n. However, if the model is truncated and only m out of the n modes are considered, then the dimensions of each of these variables become

$$\{\delta T\}_n = [\phi]_{n\times m}\{\tau\}_m. \tag{5.29}$$

If the previous equation is written only for the s positions where the temperature is

directly measured with a sensor, with always $s < n$, it can be expressed as

$$\{\delta T_{sensors}\}_s = [\phi]_{s\times m}\{\tau\}_m. \tag{5.30}$$

In general, s is different than m and, therefore, the reduced $[\phi]$ matrix in the previous equation is not square, and thus, not directly invertible. However, if the number of sensors exceeds the number of considered modes, i.e. if $s > m$, the pseudoinverse $[\phi]^+_{m\times s}$ of the reduced $[\phi]_{s\times m}$ matrix can be obtained which allows the calculation of the least squares solution of the reduced vector $\{\tau\}_m$, which is expressed as $\{\bar{\tau}\}_m$. This operation can be expressed in matrix form as

$$\{\bar{\tau}\}_m = [\phi]^+_{m\times s}\{\delta T_{sensors}\}_s\,. \tag{5.31}$$

Combining now Equation 5.31 with 5.29 results in an estimation of the full temperature vector which can be expressed as

$$\{\delta\overline{T}\}_n = [\phi]_{n\times m}[\phi]^+_{m\times s}\{\delta T_{sensors}\}_s \tag{5.32}$$

and abbreviated to

$$\{\delta\overline{T}\}_n = [\Psi]\{\delta T_{sensors}\}_s \tag{5.33}$$

with

$$[\Psi] = [\phi]_{n\times m}[\phi]^+_{m\times s}. \tag{5.34}$$

This estimation combines the expected shape of the thermal field described by the thermal modes with the actual temperature measurements provided by the sensors. A critical aspect to minimize the estimation error of this procedure concerns the selection of the subset of modes that are considered to construct the reduced $[\phi]_{s\times m}$ matrix.

As presented in Section 3.2.5, the thermal response is dominated by a few modes. This weight distribution in which the influence of particular thermal modes is reinforced is more accentuated at lower frequencies. In order to identify which are the relevant modes that should be considered in the $[\phi]_{s\times m}$ matrix it is necessary to know the spatial origin of the expected perturbations. Specific thermal modes are associated with perturbations arising from particular points. Thus, if the spatial origin of a perturbation is known, even if its behavior is not, it is possible to know which thermal modes will have the largest weight in the response.

The first step in selecting the modes that should be taken into account in matrix $[\phi]_{s\times m}$ is to identify the possible perturbation sources in the stable structure. Once these have been identified it is possible to determine which are the thermal modes that carry the highest weight in the system response. Based on this information it is possible to select the locations where sensors should be placed. There should always be at least as many sensors as considered modes, otherwise, it is not possible to properly invert the matrix in Equation 5.32. Additionally, sensors should be placed at locations where the modal amplitudes take the maximum values and, consequently, can be more easily detected by the sensors. If conversely, sensors are placed at points where the modal amplitudes are minimal, the measured signal will be more easily covered by noise.

This procedure can be implemented to estimate the thermal response triggered by heat perturbations. However, in the controlled cases it must be taken into account

that part of the thermal response is induced by heat control sources. Thus, the presented approach must be expanded to consider also the contribution of the control sources. The total thermal response can be expressed as

$$\{\delta T\} = \{\delta T_{pert}\} + \{\delta T_c\} \tag{5.35}$$

where $\{\delta T_{pert}\}$ represents the thermal fluctuations induced by perturbations and $\{\delta T_c\}$ the fluctuations induced by control heat sources. In order to estimate the total thermal response under the effect of both perturbation and control heat sources one option is to install additional sensors to estimate the weight of those thermal modes associated to the control heat sources. This is a viable option that introduces an estimation error proportional to the errors from the measurements and to the magnitude of the modal truncation. An alternative option is to calculate the thermal response contribution induced by the heat control sources through the thermal model of the structure. This can be calculated by adapting Equation 5.10 to consider only the heat control contribution, i.e.

$$\{\dot{\delta T_c}\} + [H_T]\{\delta T_c\} = [H_c]\{\delta q_c\}. \tag{5.36}$$

This step can be performed because, in contrast to the heat related to perturbation sources, the heat applied by the control sources is known. It is important to consider that when the sensors measure the temperature, they measure the entire response resulting from both control and perturbation sources. Thus, before applying the thermal modal expansion expressed by Equation 5.33 it is first necessary to subtract the control contribution from the sensor measurement, hence

$$\{\delta\overline{T}\}_n = [\Psi]\left(\{\delta T_{sensors}\}_s - \{\delta T_c\}_s\right) + \{\delta T_c\}. \tag{5.37}$$

This expression applies the thermal modal expansion to a vector that represents only the thermal response induced by the perturbations. Afterwards, the thermal response induced by the control sources is added to the initial thermal response estimation to obtain the global estimation that considers both perturbation and control sources.

Considering that the $\{\delta T_{sensors}\}$ vector is a subset of the entire $\{\delta T\}$ vector it is possible to relate both vectors with a mapping matrix of dimensions $s \times n$ that selects the corresponding cells from $\{\delta T\}$, thus

$$\{\delta T_{sensors}\} = [\Pi]\{\delta T\}. \tag{5.38}$$

Based on this relation, Equation 5.37 can be written in terms of the $\{\delta T\}$ vector as

$$\{\delta\overline{T}\}_n = [\Psi][\Pi]\left(\{\delta T\} - \{\delta T_c\}\right) + \{\delta T_c\} \tag{5.39}$$

an rearranged as

$$\{\delta\overline{T}\}_n = \begin{bmatrix}[I] - [\Psi][\Pi] & [\Psi][\Pi]\end{bmatrix} \begin{Bmatrix}\{\delta T_c\} \\ \{\delta T\}\end{Bmatrix} \tag{5.40}$$

which expresses the temperature estimation based on a combination of the temperature induced by the control sources and the thermal expansion performed through the sensor measurements. Equation 5.40 can be introduced into the controlled system 5.27 to calculate the heat control inputs that stabilize the structure. However, as presented in the following subsections, it is also necessary to take into account that there exist inaccuracies in the measurements provided by the sensors, and thus, further errors are introduced in the estimation $\{\delta\overline{T}\}$.

5.3.3 Sensor model and uncertainty

The main limitation of current temperature sensors is the accuracy of their measurements. Apart from the inherent inaccuracy of each sensor, which can be understood as a bias from the real measurement, there is also a certain level of noise at the measurements. Thus, the temperature values provided by the sensors can be modeled as

$$\{\delta T_{sensors}\} = [\Pi]\left(\{\delta T_{actual}\} + \{\varepsilon_s\} + \{\varepsilon_{\Delta s}\}\right) \tag{5.41}$$

where $\{\varepsilon_s\}$ is a random vector that is assumed to be constant in time, representing the measurement bias at each sensor, and $\{\varepsilon_{\Delta s}\}$ is a random vector that changes for each retrieved measurement and represents the sensor noise.

In this work, each individual value in both the $\{\varepsilon_s\}$ and the $\{\varepsilon_{\Delta s}\}$ vectors is assumed to follow a Gaussian distribution. A simulation is set up to allow for different values in the variance of these variables in order to assess the impact of these inaccuracies in the achieved stability performance. The values of $\{\varepsilon_s\}$ are established at the beginning of the simulation and are assumed to remain constant because they are inherent to each sensor. The values of $\{\varepsilon_{\Delta s}\}$ are updated for each retrieved measurement from the sensors.

The measurement errors described in this section are directly transmitted to the temperature estimation that has been presented in Section 5.3.2. Thus, based on the model expressed by Equation 5.40 the temperature field estimation is calculated to be

$$\{\delta\overline{T}\}_n = \begin{bmatrix}[I] - [\Psi][\Pi] & [\Psi][\Pi]\end{bmatrix} \begin{Bmatrix} \{\delta T_c\} \\ \{\delta T\} + \{\varepsilon_s\} + \{\varepsilon_{\Delta s}\} \end{Bmatrix} \tag{5.42}$$

As a result, the estimation error increases and, therefore, the applied control heat inputs calculated through Equation 5.24 are not optimal. These errors can be partially mitigated if adequate filters to improve the temperature estimation are implemented. This filter should take also into account that there are other sources of uncertainties in the model, including the acting perturbations and the uncertainties in the actuator behavior, which depend on the actuator strategy and are presented in Section 5.4. All these factors are taken into account in this work by implementing a Kalman filter, which is presented in detail in Section 5.5.

5.4 Actuator model framework

Another set of elements that are essential to implement the control loop presented in Section 5.2 are the actuators. The function of the actuators is to apply the heat load described by Equation 5.24. There exist different technical options to apply a change in heat load on a structure. These different options, and particularly the ones that are regarded as more viable and thus taken into account in the subsequent steps of this work, are presented in Section 5.4.1. Additionally, it must be taken into account that the behavior of real actuators is not ideal and, therefore, the heat load they apply does not exactly correspond to the commanded heat load derived by the control laws. This non-ideal effect is modeled as presented in Section 5.4.2.

5.4.1 Actuator strategies

According to the thermal system as described by 5.10, the heat control sources are represented by the vector $\{\delta q_c\}$. This vector can contain heat loads expressed as flux, understood as heat power per unit area, or as heat generation, understood as heat power per unit volume. The different physical options that vector $\{\delta q_c\}$ can represent are indicated in Figure 5.1.

If the control heat is applied as heat generation, the implementation can only consist of heating elements embedded inside the structure that are controlled through its power per unit volume. This option provides a uniform heat load around the location where the heater is mounted but affects also the mechanical integrity of the structure.

If the control is instead applied as heat flux, two options exist. One option is to use a heater element directly mounted at some surface of the structure. This can be achieved with film heaters, which apply the commanded heating power distributed along its surface. The other option is to use external radiation sources. These sources could consist of radiating elements within the field of view of the structure. By controlling the radiated power of these elements the radiating flux acting on the structure is accordingly changed and its distortion state can be controlled. It is important to note that in this case the radiated power on the structure could be controlled not only through changes in temperature of the radiating elements but also through changes of its thermo-optical properties. This would enable distortion control only by changing the surface properties, for instance through louvers.

When the heat flux is applied through film heaters mounted in the structure, its action has a more localized effect that is then distributed to other regions of the structure through conduction. If instead radiation sources are used, all those parts of the structure that have a radiative link with the radiating element are immediately affected. This is expected to result in some performance difference between both cases. Additionally, nonlinear effects due to radiation terms can become an additional source of errors if distortions are controlled through radiation heat. Despite these fundamental differences, both options are physically possible.

It is also possible to base the control actuation on a completely opposed approach relying on cooling power instead of heat. This would imply mounting cooling devices on the structure that are able to extract heat from some specific locations. Technically, this could be implemented using thermoelectric coolers or some type of cryocooler based on a cycle of a cooling fluid. However, it is uncertain whether current cooling devices could perform at changing levels of power with the performance required to apply precise distortion control. The technical difficulties associated

$$\{\delta q_c\} \begin{cases} \text{Heat generation } \delta Q_v \left[\dfrac{W}{m^3}\right] : \text{ Internal source} \\ \text{Heat flux } \delta q_s \left[\dfrac{W}{m^2}\right] \begin{cases} \text{Conduction source} \\ \text{Radiation source} \end{cases} \end{cases}$$

Figure 5.1: Classification of possible heat control sources.

with this option appear to have a higher degree of complexity than a purely heat based approach. However, it should be kept in mind that distortion control using cooling devices or through a combination of both cooling and heating devices is theoretically a possible option.

The heat control inputs described by $\{\delta q_c\}$ can take positive and negative values. This does not imply that the control heaters should be capable of applying negative heat power, i.e. cooling power. The heat control inputs always represent changes from a reference state which is taken as the average condition around which the thermal equations are linearized. Thus, it should only be ensured that the power applied by the actuators in the reference state is higher than the amplitude of the expected heat control inputs. This initial power level applied by the actuators determines the maximum amplitude of the distortions that can be stabilized without changing the equilibrium condition of the structure around which the stabilization takes place.

Part of the actuator strategy includes also the identification of the locations where the control heat should be applied. Based exclusively on the thermomechanical model derived in Chapters 3 and 4 it is theoretically possible to control a particular distortion metric from any other point of the structure. In reality, the possible locations where heaters can be placed will be more restricted due to the presence of support equipment and other practical matters. Nonetheless, it is still possible to identify those locations that minimize a given cost function. This cost function must be defined and assessed on a case-by-case basis but a sensible option is to identify the locations that minimize the required control power. Other options could be to minimize the global distortion at the remaining parts of the structure that are not stabilized or the temperature fluctuations around some specific part of the structure.

The heater locations that minimize the required control heat power can be identified based on the gain of the thermomechanical transfer functions expressed by Equations 4.56 and 4.57. These functions express the distortion at node i given a heat input at position k. If evaluated for all the possible k positions, it is possible to calculate the gain field distribution in the structure. The distortion at node i should be controlled from those regions where the gain is maximum because these are the spots where a given value of input power has a larger effect at node i. The gain field is a function of the frequency and, therefore, optimal positions are in general frequency-dependent.

To exemplify this procedure the gain field for the baseline case included in this thesis is presented here. The distance change between points A and B, as illustrated in Figure 4.2 of Section 4.2, induced by a given control source at position k can be determined in each spatial direction x, y and z based on the thermomechanical transfer functions calculated at A and B, i.e.

$$\frac{\delta u_{AB}}{\delta Q_k} = \frac{\delta u_A}{\delta Q_k}(s) - \frac{\delta u_B}{\delta Q_k}(s) \tag{5.43}$$

$$\frac{\delta v_{AB}}{\delta Q_k} = \frac{\delta v_A}{\delta Q_k}(s) - \frac{\delta v_B}{\delta Q_k}(s) \tag{5.44}$$

$$\frac{\delta w_{AB}}{\delta Q_k} = \frac{\delta w_A}{\delta Q_k}(s) - \frac{\delta w_B}{\delta Q_k}(s) \tag{5.45}$$

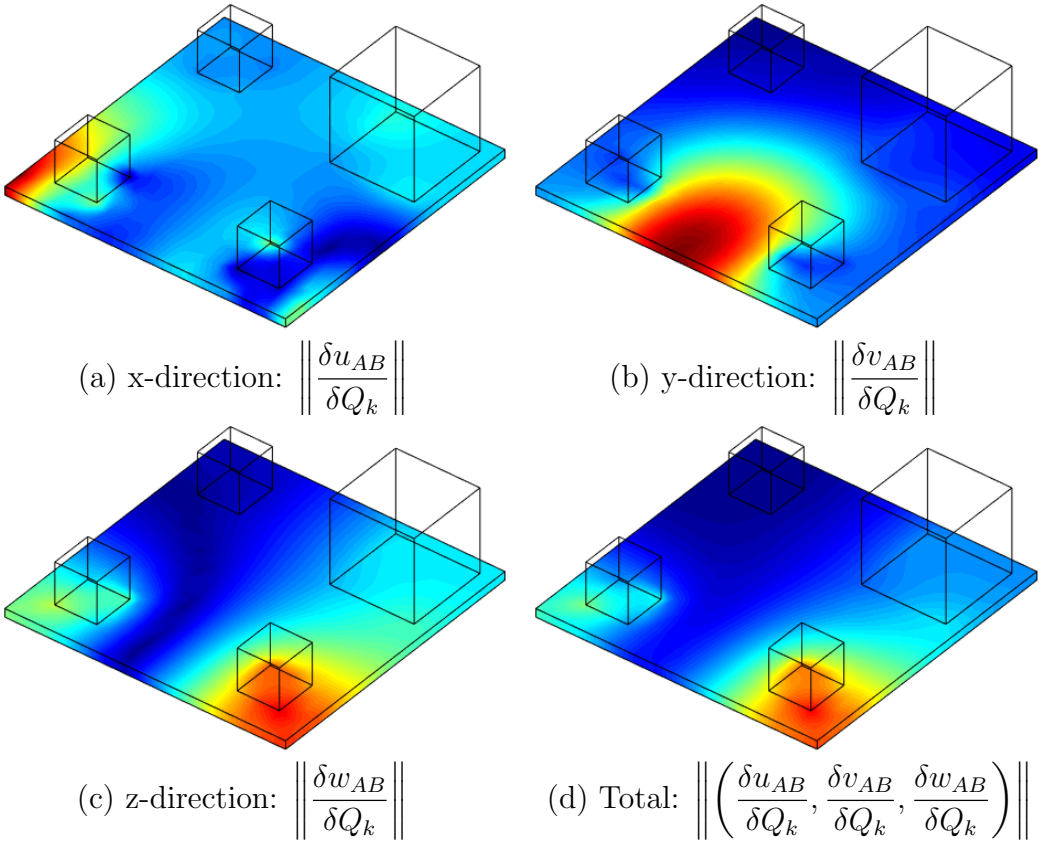

(a) x-direction: $\left\| \frac{\delta u_{AB}}{\delta Q_k} \right\|$ (b) y-direction: $\left\| \frac{\delta v_{AB}}{\delta Q_k} \right\|$

(c) z-direction: $\left\| \frac{\delta w_{AB}}{\delta Q_k} \right\|$ (d) Total: $\left\| \left(\frac{\delta u_{AB}}{\delta Q_k}, \frac{\delta v_{AB}}{\delta Q_k}, \frac{\delta w_{AB}}{\delta Q_k} \right) \right\|$

Figure 5.2: Thermomechanical gains related to to the distance change between points A and B under static conditions. (Red regions correspond to maximum gain and blue regions to minimum gain).

If the perturbation frequency is known, the gain of each of these functions can be evaluated at the same frequency to identify the locations from which the distortion AB can be controlled with minimum input power. If the perturbation frequency is unknown it is also possible to evaluate the transfer functions for the static case, i.e. at $f = 0\,\text{Hz}$ to qualitatively assess the gain distribution. The gain field in the static case considering that heaters can only be mounted in the structural plate are represented for each direction and for the total distortion in Figure 5.2.

This type of analysis increases in complexity as more degrees of freedom need to be controlled, which requires more heaters. If only the absolute distance between points A and B needs to be controlled, only one heater is required and its optimal location can be directly derived from Figure 5.2 (d). If instead it is required to stabilize the distortion AB in each spatial direction, it is necessary to use three heaters, each one partially contributing to the stabilization of each degree of freedom. Thus, in order to identify the optimal locations, it is necessary to take into account the gain field represented by Figures 5.2 (a), (b) and (c) as well as the expected magnitude of the distortions in each direction. In a scenario with multiple perturbation sources and multiple degrees of freedom to be controlled, the optimal heater locations depend eventually on the distortion field that arises in the structure. Thus, in those cases, the optimization can only be performed based on the probability of the expected level of perturbations.

5.4.2 Actuator model and uncertainty

Amongst the multiple sources of uncertainty that exist when the presented control framework is implemented there is the uncertainty in the actuators' behavior. It cannot be assumed that the heat power applied by the actuators in the structure, $\{\delta q_{applied}\}$, matches exactly the commanded heat power, $\{\delta q_{commanded}\}$, calculated through the control law expressed by Equation 5.24. The relation between these two variables can be modeled according to

$$\{\delta q_{applied}\} = ([I] + [\Gamma])\{\delta q_{commanded}\} + \{q_{offset}\} \tag{5.46}$$

where $[\Gamma]$ is a diagonal matrix with multiplicative factors and $\{q_{offset}\}$ is a vector with additive factors. The multiplicative factors Γ_j in the diagonal of $[\Gamma]$ are assumed to be a characteristic value of each actuator. It is assumed that these factors follow a Gaussian distribution centered at 0 and that they remain constant throughout the lifetime of the actuators. For negative values of Γ_j the model indicates an underperformance of the actuator. Conversely, for positive values of Γ_j the actuator overperforms with respect to the commanded signal.

The additive factors in $\{q_{offset}\}$ indicate a constant offset from the commanded signal. This effect can arise in actuators that experience hysteresis. In case electric heaters are used as actuators, it can be assumed that these factors are negligible because the applied heat is in direct relation to the commanded power. Consequently, if no power is applied there is no physical effect that can induce an offset. Thus, this factor is not included in the presented simulations on Chapter 6 but should be taken into account in case heat control based on other technologies is considered.

5.5 Kalman filter

As presented in Section 5.3.1, the temperature field estimation performed through the modal transformation and the sensor measurements will be partially inaccurate due to the modal truncation and the sensor uncertainties, including noise. Additionally, the structure cannot be exactly controlled as desired due to the uncertainty in the actuators' behavior, which may not react exactly as commanded. This situation is generally worsened by the fact that random perturbations will be acting on the structure and thus, it is not possible to predict the evolution of the system based purely on the thermomechanical model.

Despite all these technical obstacles, an accurate estimation of the thermomechanical state of the structure in real time is essential, not only to calculate the heat control inputs but to assess whether the distortions are being stabilized at all. The estimation of the thermal state presented in Section 5.3.2 is based on the thermal modal representation in combination with sensor measurements. It is also possible to conduct a parallel estimation of the thermal state based on the expected dynamics of the system described by the thermal model, i.e. by expression 5.13. An improved estimation of the thermal state can be achieved by adequately combining the results from both estimations.

A frequently used procedure to implement this additional step in the estimation process is the Kalman filter. The standard formulation of the Kalman filter produces an estimation of a given variable following a two-step process. First, the variable is estimated using the system dynamics model. Then, this initial estimation is updated with the data provided by sensors. The final estimated value results from a weighted average of these two inputs, model and sensors, in which the values with higher certainty have more weight. In turn, this relative weight is inferred from the expected noise level at the sensors and the expected magnitude of perturbations acting on the model.

The initial estimation of the temperature field is obtained from the known variables in the system of equations 5.13, which describes the thermal behavior of the structure. This system is rewritten here to introduce the distinction between known and unknown random variables. The discrete-time form of the system is

$$\begin{aligned}\{\delta T\}^{t+\Delta t} = &\left([I] + \frac{[H_T]\Delta t}{2}\right)^{-1}\left([I] - \frac{[H_T]\Delta t}{2}\right)\{\delta T\}^t \\ &+ \left([I] + \frac{[H_T]\Delta t}{2}\right)^{-1}([H_c]\Delta t)\,\frac{\{\delta q_c\}^{t+\Delta t} + \{\delta q_c\}^t}{2} \\ &+ \left([I] + \frac{[H_T]\Delta t}{2}\right)^{-1}([H_{pert}]\Delta t)\,\frac{\{\delta q_{pert}\}^{t+\Delta t} + \{\delta q_{pert}\}^t}{2}.\end{aligned} \tag{5.47}$$

It is first important to take into account that the control heat input $\{\delta q_c\}$ cannot be calculated from the actual temperature vector, as expressed in Equation 5.24, as this information is unknown. Instead, the heat control input has to be calculated from the estimated temperature vector. Additionally, considering that the actuator behavior is not ideal, as expressed by Equation 5.46, it is possible to express the actual control heat input as

$$\{\delta q_c\} = -\left([I] + [\Gamma]\right)[K_{LQR}]\{\delta \hat{T}\}. \tag{5.48}$$

Introducing this control heat input into Equation 5.47 results in

$$\begin{aligned}\{\delta T\}^{t+\Delta t} = &\left([I] + \frac{[H_T]\Delta t}{2}\right)^{-1}\left([I] - \frac{[H_T]\Delta t}{2}\right)\{\delta T\}^t \\ &- \left([I] + \frac{[H_T]\Delta t}{2}\right)^{-1}([H_c]\Delta t)\,[K_{LQR}]\frac{\{\delta \hat{T}\}^{t+\Delta t} + \{\delta \hat{T}\}^t}{2} \\ &- \left([I] + \frac{[H_T]\Delta t}{2}\right)^{-1}([H_c]\Delta t)\,[\Gamma][K_{LQR}]\frac{\{\delta \hat{T}\}^{t+\Delta t} + \{\delta \hat{T}\}^t}{2} \\ &+ \left([I] + \frac{[H_T]\Delta t}{2}\right)^{-1}([H_{pert}]\Delta t)\,\frac{\{\delta q_{pert}\}^{t+\Delta t} + \{\delta q_{pert}\}^t}{2}.\end{aligned} \tag{5.49}$$

This expression defines the temperature dynamics of the model and can also be used to define the dynamics of the estimated temperature.

Substituting $\{\delta T\}^t$ in the previous expression for its estimation, represented as $\{\delta\hat{T}\}^t$, and applying the same substitution at $t = t + \Delta t$, results after rearranging the terms in

$$\begin{aligned}
&\{\delta\hat{T}\}^{t+\Delta t} = \\
&\left([I] + \frac{[H_T]\Delta t}{2} + \frac{[H_c][K_{LQR}]\Delta t}{2}\right)^{-1}\left([I] - \frac{[H_T]\Delta t}{2} - \frac{[H_c][K_{LQR}]\Delta t}{2}\right)\{\delta\hat{T}\}^t \\
&- \left([I] + \frac{[H_T]\Delta t}{2} + \frac{[H_c][K_{LQR}]\Delta t}{2}\right)^{-1}\frac{[H_c]\Delta t}{2}[\Gamma][K_{LQR}]\left(\{\delta\hat{T}\}^{t+\Delta t} + \{\delta\hat{T}\}^t\right) \\
&+ \left([I] + \frac{[H_T]\Delta t}{2} + \frac{[H_c][K_{LQR}]\Delta t}{2}\right)^{-1}\frac{[H_{pert}]\Delta t}{2}\left(\{\delta q_{pert}\}^{t+\Delta t} + \{\delta q_{pert}\}^t\right).
\end{aligned} \tag{5.50}$$

Only the first term at the right-hand side of the previous expression consists of known variables. The two remaining terms contain random variables, namely $[\Gamma]$ and $\{\delta q_{pert}\}$, and thus cannot be taken into account to obtain an initial estimation of $\{\delta T\}^{t+\Delta t}$. Introducing the abbreviations

$$\begin{aligned}
&[A^*] = \\
&\left([I] + \frac{[H_T]\Delta t}{2} + \frac{[H_c][K_{LQR}]\Delta t}{2}\right)^{-1}\left([I] - \frac{[H_T]\Delta t}{2} - \frac{[H_c][K_{LQR}]\Delta t}{2}\right),
\end{aligned} \tag{5.51}$$

$$[B_1^*] = -\left([I] + \frac{[H_T]\Delta t}{2} + \frac{[H_c][K_{LQR}]\Delta t}{2}\right)^{-1}\frac{[H_c]\Delta t}{2}, \tag{5.52}$$

$$\text{and} \quad [B_2^*] = \left([I] + \frac{[H_T]\Delta t}{2} + \frac{[H_c][K_{LQR}]\Delta t}{2}\right)^{-1}\frac{[H_{pert}]\Delta t}{2} \tag{5.53}$$

it is possible to rewrite Equation 5.50 as

$$\{\delta\hat{T}\}^{t+\Delta t} = [A^*]\{\delta\hat{T}\}^t + [B_1^* \quad B_2^*]\begin{Bmatrix}[\Gamma][K_{LQR}]\left(\{\delta\hat{T}\}^{t+\Delta t} + \{\delta\hat{T}\}^t\right) \\ \{\delta q_{pert}\}^{t+\Delta t} + \{\delta q_{pert}\}^t\end{Bmatrix}. \tag{5.54}$$

Based only on the known terms of Equation 5.54, the initial estimation of $\{\delta T\}^{t+\Delta t}$, represented as $\{\delta\hat{T}\}_*^{t+\Delta t}$, can be calculated as

$$\{\delta\hat{T}\}_*^{t+\Delta t} = [A^*]\{\delta\hat{T}\}^t. \tag{5.55}$$

The second step of the Kalman filter performs an update of this first estimation based on the measurements provided by the sensors. This update is expressed as

$$\{\delta\hat{T}\}^{t+\Delta t} = \{\delta\hat{T}\}_*^{t+\Delta t} + [M_K]\left(\{\delta\overline{T}\}_n^{t+\Delta t} - \{\delta\hat{T}\}_*^{t+\Delta t}\right), \tag{5.56}$$

where $[M_K]$ is a matrix known as the innovation gain and $\{\delta\overline{T}\}_n^{t+\Delta t}$ is the thermal estimation at $t+\Delta t$ obtained from the temperature sensors in combination with the thermal modal expansion process described in Section 5.3.2. Introducing the thermal estimation expressed by the expression 5.42 it is possible to write the previous expression as

$$\begin{aligned}
&\{\delta\hat{T}\}^{t+\Delta t} = \{\delta\hat{T}\}_*^{t+\Delta t} + \\
&[M_K]\left([[I] - [\Psi][\Pi] \quad [\Psi][\Pi]]\begin{Bmatrix}\{\delta T_{control}\}^{t+\Delta t} \\ \{\delta T\}^{t+\Delta t} + \{\varepsilon_s\} + \{\varepsilon_{\Delta s}\}^{t+\Delta t}\end{Bmatrix} - \{\delta\hat{T}\}_*^{t+\Delta t}\right)
\end{aligned} \tag{5.57}$$

The innovation gain matrix $[M_K]$ is calculated as a function of the expected noise acting as heat input in the model and in the sensor measurements. This noise level is quantified through the covariance matrices $[Q_K]$ and $[R_K]$.

The $[Q_K]$ matrix represents the covariance of the second term in the right-hand side of Equation 5.54. This can be calculated as

$$[Q_K] = [B_1^* \quad B_2^*] \begin{pmatrix} \sigma_1^2 & & & & & & \\ & \ddots & & & & & \\ & & \sigma_n^2 & & & & \\ & & & \sigma_a^2 & & & \\ & & & & \ddots & & \\ & & & & & \sigma_m^2 \end{pmatrix} [B_1^* \quad B_2^*]^T \tag{5.58}$$

where σ_1^2 to σ_n^2 are the variances of the uncertainty in the heat control sources and σ_a^2 to σ_m^2 are the variances of the perturbation heat sources acting on the spacecraft. The performance obtained by the Kalman filter ultimately depends on the accuracy to which these variables are known. A better characterization of the expected level of random perturbations, as well as of the uncertainty in the actuators, results consequently in better estimations.

The other covariance matrix, $[R_K]$, represents the variance in the estimated temperature vector. Assuming that all the sensors have the same level of noise described by a variance σ_s^2, the $[R_K]$ matrix can be built as

$$[R_K] = \sigma_s^2[I], \tag{5.59}$$

where $[I]$ is the identity matrix with a dimension equal to the number of nodes.

Based on these definitions, the innovation gain matrix is calculated as

$$[M_K] = [P_K] \left([P_K] + [R_K]\right)^{-1}, \tag{5.60}$$

where $[P_K]$ is obtained from the equation

$$[P_K] = [A^*][P_K][A^*]^T - [A^*][P_K] \left([P_K] + [R_K]\right)^{-1} [P_K][A^*]^T + [Q_K] \tag{5.61}$$

which considering the change of notation

$$[\mathcal{A}] = [A^*]^T \tag{5.62}$$

can be written in the form

$$[P_K] = [\mathcal{A}]^T[P_K][\mathcal{A}] - [\mathcal{A}]^T[P_K] \left([P_K] + [R_K]\right)^{-1} [P_K][\mathcal{A}] + [Q_K]. \tag{5.63}$$

This is known as the algebraic Riccati equation and can be solved numerically for $[P_K]$ following a Newton-type iterative procedure [86].

5.6 Closed-loop system formulation

The equations that have been presented in this chapter can be finally combined into a full system that describes the closed-loop dynamics of the system together with the sensor and actuator models.

Section 5.2 has ended with the closed-loop formulation of an ideal system where the temperatures at all nodes are known and there are no sensor or actuator uncertainties. This system can be expanded to take into account the uncertainties of both the sensors and the actuators as well as the methods to counteract the errors they introduce, i.e. the thermal modal expansion and the Kalman filter. The most important variables in the closed-loop system are the temperature values contained in vector $\{\delta T\}$. However, the control is in reality based on the best available knowledge of this vector, which corresponds to the estimated vector $\{\delta\hat{T}\}$, derived by the Kalman filter as explained in Section 5.5. In turn, the Kalman filter requires an estimation of the temperature based purely on the thermal model of the system which includes a thermal field expansion presented in Section 5.3.2. The thermal modal expansion process includes a superposition of the thermal field induced from the perturbation sources and the thermal field induced by the control sources, which is expressed as $\{\delta T_c\}$.

These three vectors, $\{\delta T_c\}$, $\{\delta T\}$ and $\{\delta\hat{T}\}$, are coupled to each other and thus they must be solved simultaneously to simulate the evolution of the entire system. The system describing the evolution of the $\{\delta T_c\}$ vector has been presented in Section 5.3.2 and can be expressed in discrete-time form based on Equation 5.36 as

$$\begin{aligned}\left([I]+\frac{[H_T]\Delta t}{2}\right)\{\delta T_c\}^{t+\Delta t} = &\left([I]-\frac{[H_T]\Delta t}{2}\right)\{\delta T_c\}^{t} \\ &-\left(\frac{[H_c][K_{LQR}]\Delta t}{2}\right)\left(\{\delta\hat{T}\}^{t+\Delta t}+\{\delta\hat{T}\}^{t}\right).\end{aligned} \tag{5.64}$$

The evolution of the actual temperature field arising in the structure is described by the $\{\delta T\}$ vector and can be described by equation 5.13 with the addition of the uncertainties introduced by the actuators and the random perturbation terms, i.e.

$$\begin{aligned}\left([I]+\frac{[H_T]\Delta t}{2}\right)\{\delta T\}^{t+\Delta t} = &\left([I]-\frac{[H_T]\Delta t}{2}\right)\{\delta T\}^{t} \\ &-\left(\frac{[H_c][K_{LQR}]\Delta t}{2}\right)\left(\{\delta\hat{T}\}^{t+\Delta t}+\{\delta\hat{T}\}^{t}\right) \\ &-\left(\frac{[H_c][\Gamma][K_{LQR}]\Delta t}{2}\right)\left(\{\delta\hat{T}\}^{t+\Delta t}+\{\delta\hat{T}\}^{t}\right) \\ &+\left(\frac{[H_{pert}]\Delta t}{2}\right)\left(\{\delta q_{pert}\}^{t+\Delta t}+\{\delta q_{pert}\}^{t}\right).\end{aligned} \tag{5.65}$$

Finally, the evolution of the estimated temperature vector $\{\delta\hat{T}\}$ is calculated following the Kalman filter framework presented in Section 5.5. This can be expressed

based on the combination of Equation 5.55 and 5.57 as

$$\{\delta\hat{T}\}^{t+\Delta t} = [M_K]\left(\left[[I]-[\Psi][\Pi] \quad [\Psi][\Pi]\right]\left\{\begin{matrix}\{\delta T_c\}^{t+\Delta t}\\ \{\delta T\}^{t+\Delta t}+\{\varepsilon_s\}+\{\varepsilon_{\Delta s}\}^{t+\Delta t}\end{matrix}\right\}\right) + \left([A^*]-[M_K][A^*]\right)\{\delta\hat{T}\}^t. \tag{5.66}$$

The systems of equations 5.64, 5.65 and 5.66 describing the evolution of $\{\delta T_c\}$, $\{\delta T\}$ and $\{\delta\hat{T}\}$ respectively, can be combined into a full closed-loop system of equations expressed as

$$\begin{bmatrix} [I]+\frac{[H_T]\Delta t}{2} & 0 & \frac{[H_c][K_{LQR}]\Delta t}{2} \\ 0 & [I]+\frac{[H_T]\Delta t}{2} & \frac{[H_c]\left([I]+[\Gamma]\right)[K_{LQR}]\Delta t}{2} \\ [M_K][\Psi][\Pi]-[M_K] & -[M_K][\Psi][\Pi] & [I] \end{bmatrix}\begin{Bmatrix}\delta T_c\\ \delta T\\ \delta\hat{T}\end{Bmatrix}^{t+\Delta t} =$$

$$\begin{bmatrix} [I]-\frac{[H_T]\Delta t}{2} & 0 & -\frac{[H_c][K_{LQR}]\Delta t}{2} \\ 0 & [I]-\frac{[H_T]\Delta t}{2} & -\frac{[H_c]\left([I]+[\Gamma]\right)[K_{LQR}]\Delta t}{2} \\ 0 & 0 & [A^*]-[M_K][A^*] \end{bmatrix}\begin{Bmatrix}\delta T_c\\ \delta T\\ \delta\hat{T}\end{Bmatrix}^{t}$$

$$+\begin{bmatrix}0\\ \frac{[H_{pert}]\Delta t}{2}\\ 0\end{bmatrix}\left(\{\delta q_{pert}\}^{t+\Delta t}+\{\delta q_{pert}\}^t\right)+\begin{bmatrix}0\\ 0\\ [M_K][\Psi][\Pi]\end{bmatrix}\left(\{\varepsilon_s\}+\{\varepsilon_{\Delta s}\}^{t+\Delta t}\right) \tag{5.67}$$

This system of equations completely describes the control framework presented in this work. It describes the closed-loop dynamics of the thermal system derived in Chapter 3 using a proportional gain based on a linear quadratic regulator. Additionally, it takes into account that the temperature field can only be estimated through a limited set of noisy sensors and that the actuators do not exactly behave as commanded. To partially mitigate the uncertainties resulting from sensor noise and from the perturbations acting on the spacecraft the system includes a Kalman filter. This system of equations can be complemented with equation 5.19 to obtain the displacement field in the structure.

The stability performance that can be achieved through the implementation of this system is assessed in the next chapter, where also the contribution of each error source to the performance decrease is analyzed in detail. To finalize this chapter a step-by-step guideline to implement this control framework to any structure is presented. This guideline serves also as a summary of the most relevant aspects that have been presented in the previous chapters and that should be taken into account to simulate or practically implement the presented framework.

5.7 Implementation guidelines

This section presents the specific steps that have been followed to simulate the developed control framework and to obtain the results presented in Chapter 6. The same procedure described here could be applied to simulate the stability performance that could be reached on any other structure and to apply the presented stabilization framework on a real structure.

1. The first step, assuming that the structure that has to be stabilized has been defined, is to obtain a finite element representation of it. To perform this step, it is first required to develop a geometric model of the structure, which can easily be accomplished with currently available CAD software. Once the geometry has been defined, it is necessary to generate a mesh of finite elements. The presented framework has been developed assuming that the geometry is divided in hexahedrons. This step can be performed manually for simple geometries but it is recommended to use available FEM software to ease the process and avoid errors. The finite element model for the examples presented in this thesis has been developed using ANSYS Workbench, which incorporates both a design modeler to define the geometry and tools to obtain a finite element mesh with the desired characteristics. The result of this step should be a list of all the nodes in the model with their corresponding coordinates and a list of all the elements in the model, each defined by a set of nodes.

2. The second step consists in assigning to each finite element a set of physical properties, which are defined by its material. The necessary properties that need to be defined for each element are the thermal conductivity, the heat capacity, the density, the Young's modulus, the Poisson's ratio and the coefficient of thermal expansion. In case the element has an external surface, i.e. it is not completely surrounded by other finite elements, it is also necessary to define its emissivity. This step has been conducted for the presented thesis within the specific MATLAB code developed to simulate this control framework. The code assigns the corresponding physical properties depending on the element number and the body to which it belongs.

3. The radiation surfaces need to be defined. Given that the geometry has been divided in hexahedrons, each radiation surface corresponds to one surface from a hexahedron. Thus, each radiation surface can be fully defined by the four nodes at its corners. Once the radiation surfaces have been defined it is necessary to calculate the view factors between them. These are purely geometrical factors and can be numerically calculated through a ray tracing algorithm. In the presented examples these have been calculated using ANSYS mechanical. Through this software it is possible to calculate view factors between specific surfaces and output them as a `txt` file.

4. Similarly, it is necessary to identify external surfaces to which heat fluxes can potentially be applied. This step is only necessary in case applied heat fluxes to the structure are considered to be a possible boundary condition. Each of these surfaces must belong also to a hexahedron in the mesh and thus, as in the case of the radiation surfaces, can be defined by the four nodes at the corners.

5. After completing the four previous steps, the definition of the finite element model is concluded and it becomes possible to calculate the necessary matrices to solve the required problems. To perform these calculations it is first required to select some shape functions that describe the thermal and displacement field within the finite elements. The assumed shaped functions for the presented examples are included in Appendix B.

6. The next step consists in solving the thermal equilibrium condition of the structure given some boundary conditions. This requires the calculation of the thermal matrices and vectors (which include $[K]$, $[R_q]$, $[R_Q]$, $[R_r]$, $[D]$ and $\{S\}$) according to the expressions presented in Chapter 3. Once this set of matrices and vectors have been built it is possible to calculate the temperature field of the structure under steady-state conditions, as presented in Section 3.2.2. In the presented examples this has been performed using the MATLAB tool developed for this thesis.

7. Based on the calculated steady-state solution, the next step consists in calculating the thermal transfer functions that are linearized around this steady-state of equilibrium. This requires the calculation of further finite element matrices as described in Section 3.2.4. After this step, a full characterization of the thermal behavior through transfer functions is obtained.

8. The next step consists in calculating the finite element matrices that are necessary to describe the mechanical response of the structure. This process is described in detail in Section 4.1. It requires the calculation of the stiffness matrix $[K_u^r]$ and the mechanical load matrix $[F_T^r]$. These equations can then be combined with the thermal transfer functions calculated in the previous step to obtain the thermomechanical transfer functions.

9. Evaluating the thermomechanical transfer functions at different frequencies it is possible to identify optimal locations where control heaters should be placed. If the goal is to minimize control heat power, heaters should be placed at those locations where thermomechanical transfer functions reach maximum gains. If the optimization of a variable other than the control heat power is desired, such as global temperature fluctuation, a more detailed assessment to fulfill the given requirements must be performed.

10. The temperature sensor locations should be identified based on the location of perturbation sources. Thus, it is required to identify the possible perturbation sources that are expected to act on the structure. These may be, among others, instruments mounted on the structure or external perturbations that have a radiation link to the structure. Once these have been identified, it is possible to select the thermal modes (calculated from matrix $[K]$ as explained in Section 3.2.5) that better characterize the thermal response under the effect of the considered perturbations. Sensors should be placed at those locations where the selected thermal modes reach maximum amplitudes.

11. Based also on the selected thermal modes, the next step consists in calculating the modal expansion matrix (represented by $[\Psi]$ in Section 5.3.2) that allows the estimation of the entire temperature field in the structure based on a limited set of sensor measurements.

12. To implement the control loop it is necessary to clearly define the variables that need to be controlled. Thus, it is necessary to express the stability requirements in terms of displacements at specific nodes in the finite element model. These definitions must identify which specific nodes and in which spatial directions must be stabilized. Generally, these nodes will correspond to some reference points of precise instruments mounted on the structure.

13. After calculating the thermomechanical transfer functions that relate displacement field with applied heat and after defining the stability requirements in correspondence with the finite element model, it is possible to calculate the proportional control gains following the procedure presented in Section 5.2.

14. Based on the expected level of noise in the sensor measurements, the uncertainty in the control heaters and the expected magnitude of heat perturbations it is possible to calculate the innovation gain $[M_K]$ of the Kalman filter, following the procedure explained in Section 5.5.

15. After applying the previous steps, the structure is ready to be controlled. The sensors measurements can be filtered using the Kalman filter developed in step 14. The entire temperature field can be estimated from the filtered measurements using the expansion matrix calculated in step 11. This estimated temperature field expressed as a vector can be multiplied by the proportional gains calculated in step 13. Subsequently, the heaters mounted in the structure after step 9 apply the control heat input that stabilizes the structure according to the requirements derived in step 12. The obtained behavior can be simulated through the implementation of Equation 5.67. Several examples are included in Chapter 6.

16. Finally, validation procedures can be performed to ensure that an acceptable level of performance can be reached. These include the validation of the radiation linearization and the quasi-static assumption. Also, it is possible to simulate the achieved performance under different levels of uncertainty in the sensors and the actuators. All these procedures are exemplified for a baseline case in Chapter 6.

Chapter 6

Control Results

Based on the thermomechanical model and the control loop that have been presented in the previous sections it is possible to simulate the behavior of the baseline case presented in this thesis to assess the dimensional stability that can be achieved with such a system. The enhancement in dimensional stability that this system provides is ultimately dependent on a variety of parameters that define the structure, its environment and the inherent uncertainty in the control equipment.

In this chapter, these different parameters are identified and its influence on the achieved performance is evaluated. First, the results from stabilizing one point in the structure assuming ideal conditions are presented in Section 6.1. This includes the achieved performance using the perturbation compensation method presented in Section 5.1 and the feedback control based on the linear quadratic regulator presented in Section 5.2 considering ideal sensors and actuators. Section 6.2 evaluates the impact of the different inaccuracy sources in the control feedback loop, namely the sensor and the actuator contributions to the performance decrease. The chapter continues with Section 6.3, where the errors introduced due to the approximations included in the model are assessed. Section 6.4 presents the results for a case in which the relative distance between two points in the structure are stabilized. Finally, the chapter ends with Section 6.5, where the influence of eventual uncertainties in the material properties to the achieved performance is evaluated.

The dimensions and characteristics of the baseline structure assumed in this section have been presented in Section 3.2. An illustration of this structure is included also in Figure 6.1 for clarification purposes. Figure 6.1 shows also the location of points A and B which appear throughout the different results included in this chapter.

Taking into account the actuator strategy presented in Section 5.4 it is possible to qualitatively identify the heater locations that minimize the control input power required to stabilize the distortions in the surroundings of points A and B. Based on this approach it is decided to place three heat actuators as represented in Figure 6.2. These locations could be changed to optimize for specific perturbation conditions. However, throughout the examples presented in this chapter the actuator locations are assumed to be the same in order to simplify the performance comparison between different scenarios. This implies that for particular cases there is still a certain margin of improvement in terms of the input power required for control.

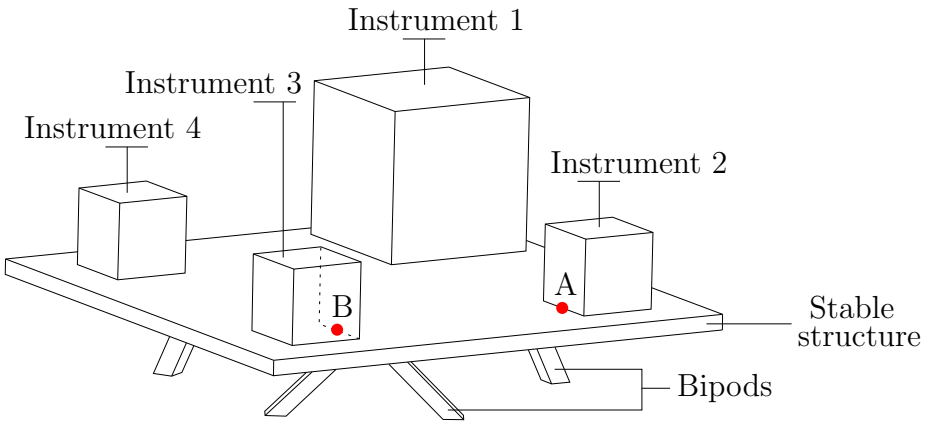

Figure 6.1: Representation of the baseline concept with instruments and reference points.

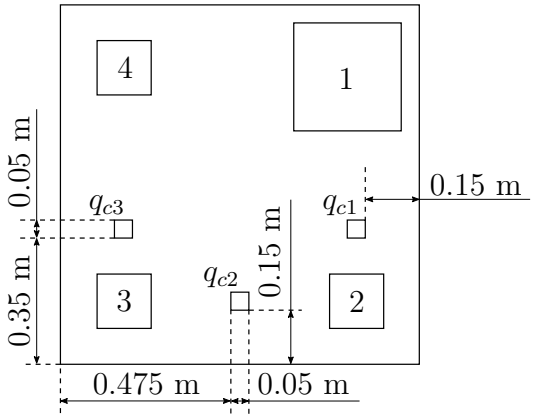

Figure 6.2: Baseline concept with control sources.

6.1 Ideal control performance

The most ideal condition under which the presented thermomechanical stabilization framework can be applied is that in which the perturbations are predictable. In this case, it is possible to calculate the exact heat input that is necessary to compensate the distortions introduced by a given perturbation. This can be achieved following the procedure presented in Section 5.1. A basic example is presented here to illustrate the magnitude of expected distortions in the baseline case.

In this first example it is assumed that the only acting perturbation arises in Instrument 1 and that the objective of the stabilization is to cancel the displacements at point A. The perturbation follows a sinusoidal signal with a frequency of 10^{-5} Hz and an amplitude of 10 W, as represented in Figure 6.3. This could be a perturbation arising from the operational cycle of the instrument which in turn could depend on the orbital period of the spacecraft orbiting around the Earth. Given that orbital periods around the Earth can range from approximately 90 minutes to several hours and that these same spacecraft also orbit around the Sun with an orbital period of one year, it is not uncommon to experience thermal perturbations at frequencies below 10^{-5} Hz on board spacecraft.

Based on Equation 5.5 presented in Section 5.1 it is possible to calculate the heat inputs that need to be applied at the three heat actuators represented in Figure 6.2 in order to cancel the distortions at point A. The resulting displacements in the three spatial directions of point A when the heat inputs represented by Figure 6.3 and Figure 6.4 act simultaneously on the structure are theoretically zero.

Figure 6.5 illustrates the comparison between the uncontrolled and the controlled case in terms of the displacement at point A. In this case the structure is made of silicon carbide, which as indicated by the material properties in Table 3.1 on page 40 remains very stable under thermal perturbations. Thus, even in the uncontrolled case the distortions only exceed the 1 µm range in the z-direction. Figure 6.5 shows that if perturbations are known, distortions can be virtually forced to be zero (the controlled response corresponds to values in the order of magnitude of 10^{-22} m). In absolute terms, this might not make a great difference in this case but it could also be applied in structures that are not particularly stable. For instance, if the same structure were made of aluminum, the distortions would exceed 1 µm in all three directions but they could still be stabilized to virtually 0 µm using the same system (see Appendix C for more details on the aluminum case).

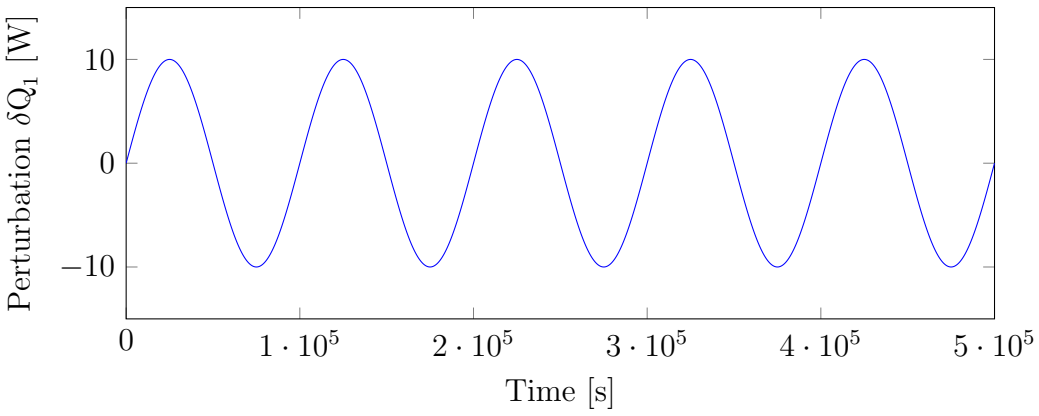

Figure 6.3: Assumed sinusoidal perturbation arising in Instrument 1.

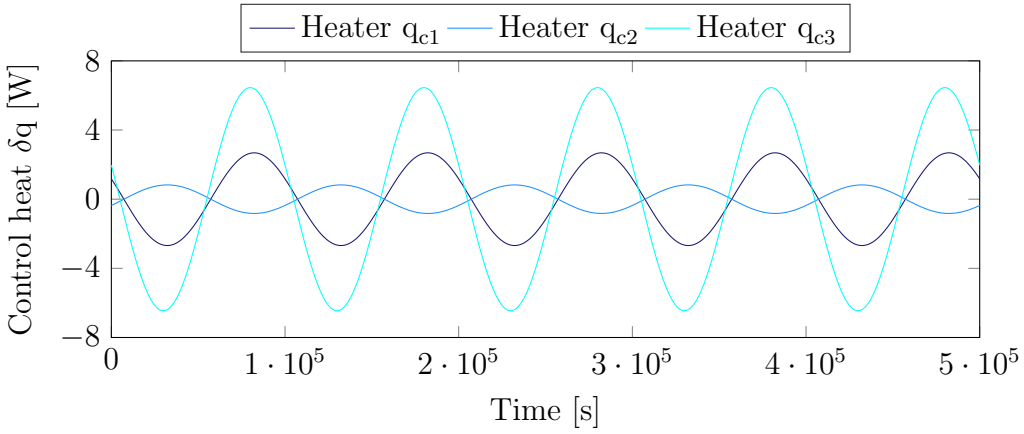

Figure 6.4: Required control heat inputs at the actuators to compensate the distortion induced by Instrument 1.

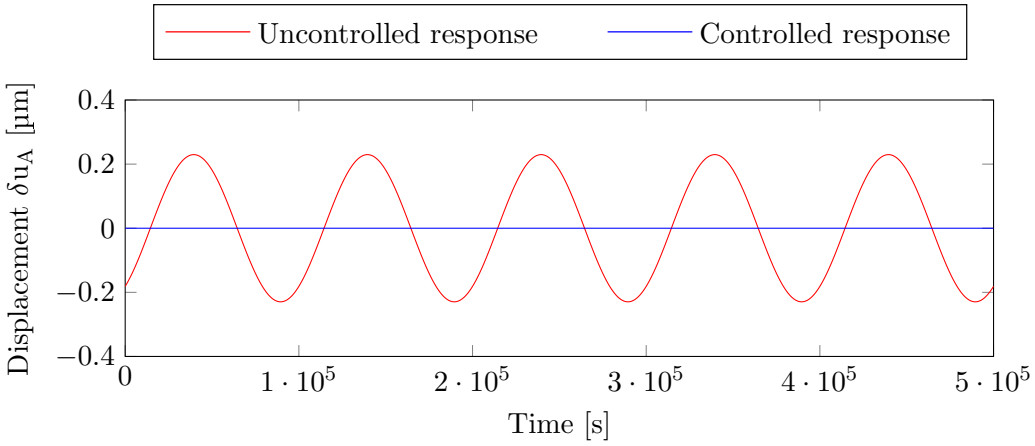

(a) Displacement in the x-direction.

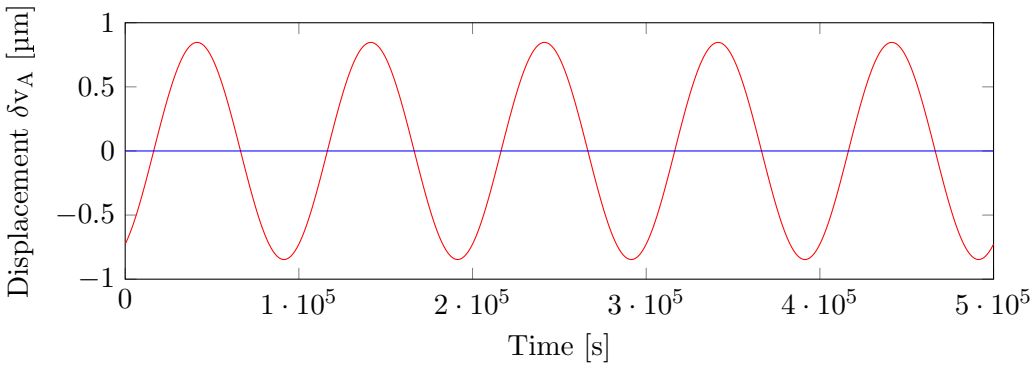

(b) Displacement in the y-direction.

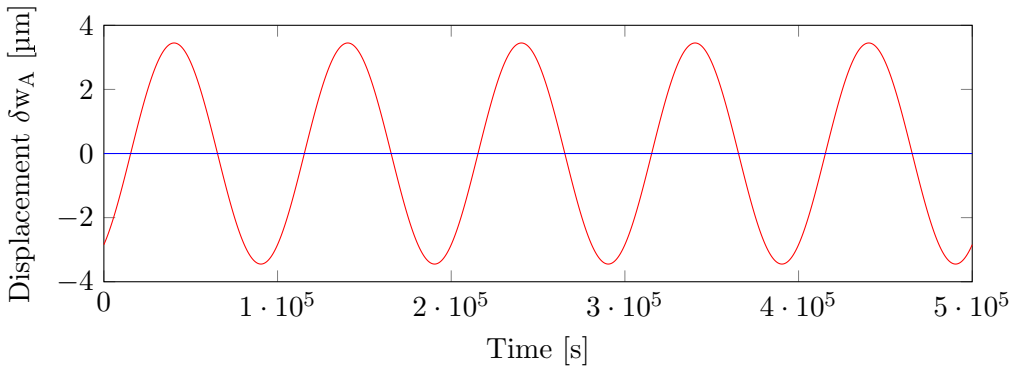

(c) Displacement in the z-direction.

Figure 6.5: Displacements at point A induced by perturbations in Instrument 1.

In general, it cannot be assumed that the perturbation arising in Instrument 1 is known beforehand. Therefore, the control method based on sensor measurements presented in Section 5.2 has been developed. The ideal conditions for the implementation of this second method are to consider that there is no uncertainty in the behavior of sensors and actuators. This means that sensors are assumed to provide exact temperature measurements corresponding to the actual temperature in the structure and that actuators behave exactly as commanded. Additionally, it is assumed that the structure is equipped with as many sensors as nodes considered in the thermomechanical model. Under these assumptions it is possible to simulate the best ideal performance that could theoretically be achieved, even when perturbations are random.

The response under these conditions is simulated assuming that the perturbation from Instrument 1 follows a random function that is obtained by adding several sinusoidal signals with a random amplitude, at a random frequency between 10^{-7} Hz and 10^{-3} Hz and with random phases. The total amplitude of the resulting signal is constrained to be always below 10 W, which corresponds to the assumed power level of the Instrument 1 under steady-state conditions. A sample of this random signal generated adding six random sinusoidal waves is presented in Figure 6.6.

The displacement response, both for the uncontrolled and the controlled case, is presented in Figure 6.7. This figure illustrates that it is possible to strongly counteract the distortion effects of perturbations even when the perturbation function is unknown but as long as the temperature field can be properly measured. In this case, the controlled response does not exceed 10^{-9} m, i.e. 0.001 µm, in any direction. In the framework of this thesis, this is considered to be the highest theoretical level of stabilization that can be achieved with this method. Numerical results beyond this value of precision can be obtained, but it would be questionable whether the thermal and mechanical models used in the derivation of the FEM are valid at these magnitudes. In reality, there is a number of non-idealities that significantly undermine this high degree of stability. The most important factors are expected to be related to sensor and actuator uncertainties and thus, several countermeasures have been devised, as presented in sections 5.3 and 5.4. Their individual contribution to the performance decrease as well as the expected performance that can be achieved when all these factors are considered are presented in the following section.

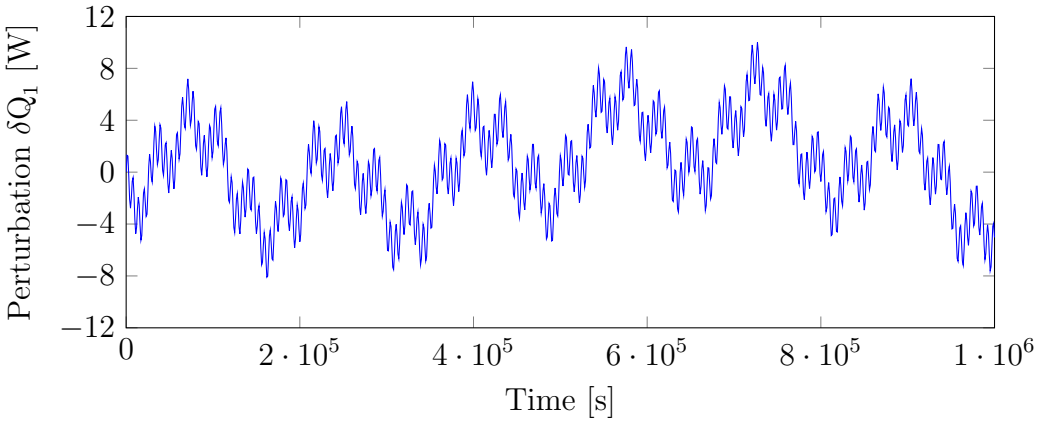

Figure 6.6: Assumed random perturbation arising in Instrument 1.

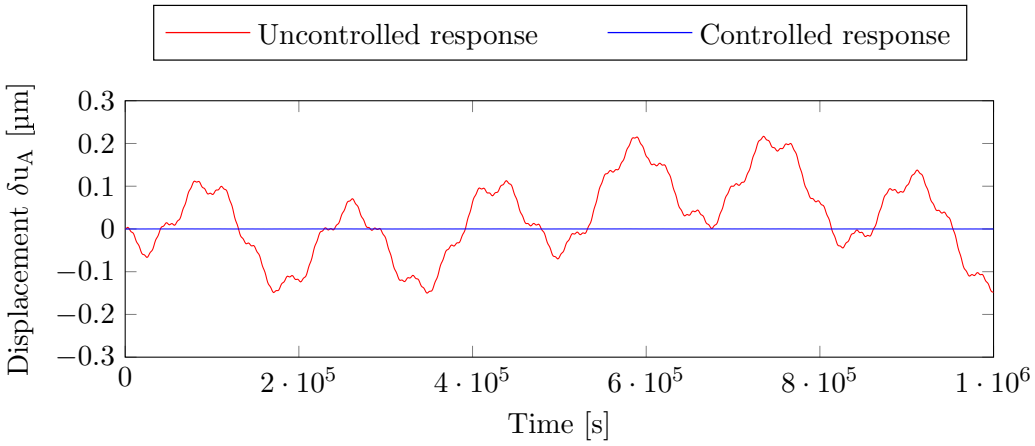

(a) Displacement in the x-direction.

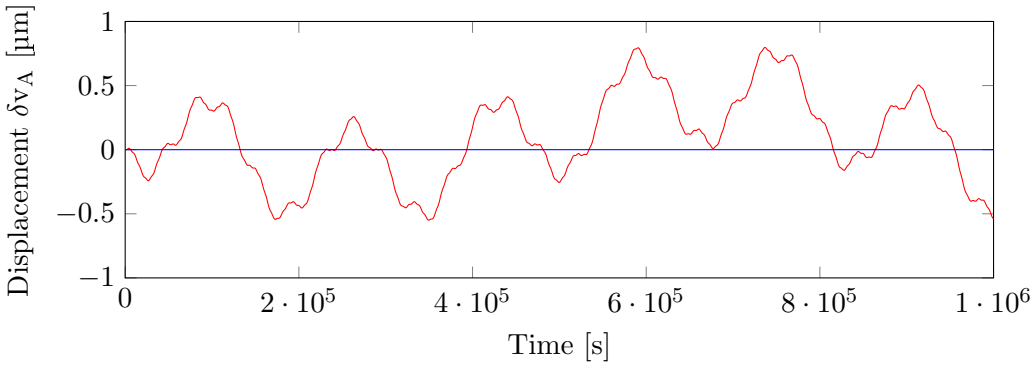

(b) Displacement in the y-direction.

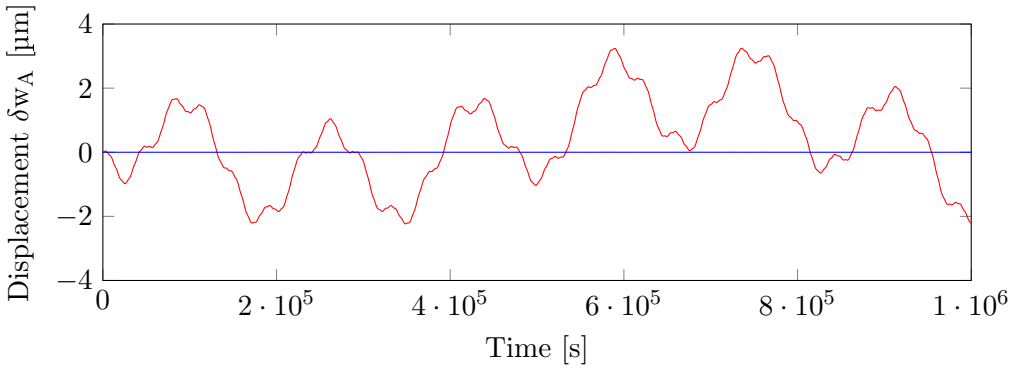

(c) Displacement in the z-direction.

Figure 6.7: Uncontrolled displacements at point A induced by random perturbations arising in Instrument 1 and controlled displacements considering ideal conditions.

6.2 Non-ideal control performance

The high level of stability that can be achieved according to the simulation examples presented in the previous section cannot be achieved in reality because of non-ideal conditions. The two main sources that contribute to the performance decrease arise from the uncertainties related to the sensor and the actuator behavior. These two sources of uncertainty are first analyzed separately in Section 6.2.1 and Section 6.2.2, respectively. Subsequently, the performance that can be achieved when both uncertainty sources are considered is presented in Section 6.2.3.

6.2.1 Sensor contribution

The magnitude of the performance decrease introduced by sensors is dependent on two factors. The first factor is related to the fact that the number of sensors is limited and thus, only some particular nodes of the thermal model can be measured. The second factor is related to the inherent noise of the sensor measurements, modeled as presented in Section 5.3.3, which further increases the errors in the temperature estimation. These two factors are first assessed separately for the same baseline case presented in the previous section. Subsequently, the total performance decrease resulting only from sensor uncertainties is presented.

Contribution related to the number of sensors

The thermal model of the baseline case considered in this thesis includes 1063 DOF. Based on the current state of the art in temperature sensors it is considered unfeasible to equip the structure with such a large number of sensors. Here, the achieved performance when only a portion of the DOF can be measured is presented. It is assumed that only 20 sensors are mounted on the structure. To isolate the effect related to the sensor number it is considered that these 20 sensors are ideal, i.e. they provide a noise-free measurement. The thermal modal expansion procedure presented in Section 5.3.2 is implemented based only on the first 10 thermal modes.

From the 20 sensors that are mounted in the structure, 10 are located at the positions where the 10 considered thermal modes reach its maximum amplitude. From the remaining 10 sensors, 6 are located at each of the bipod struts, which correspond to the most external parts of the structure, and the other 4 are distributed randomly at different locations in the structural plate.

In the presented results, the structure is controlled through ideal heaters that are located at those positions indicated in Figure 6.2. The comparison between the uncontrolled and the controlled displacements at point A is represented in Figure 6.8. These graphs illustrate that the limitation of the number of sensors does not introduce a large performance decrease as long as the temperature measurements are ideal. A more detailed view of the controlled response is included in Figure 6.10 on page 104, which shows that only in the z-direction an amplitude above 0.001 µm is achieved. These graphs prove that the achieved stability is extremely better than in the uncontrolled case even if only a limited number of measurements is available.

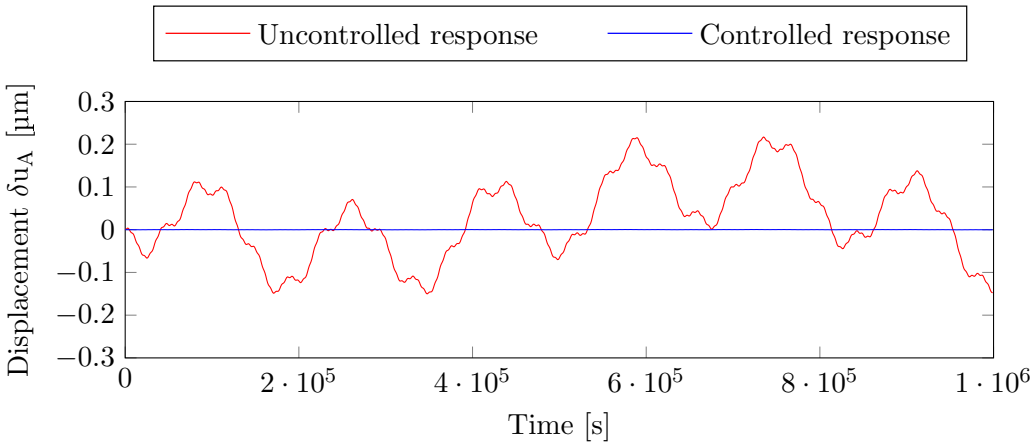

(a) Displacement in the x-direction.

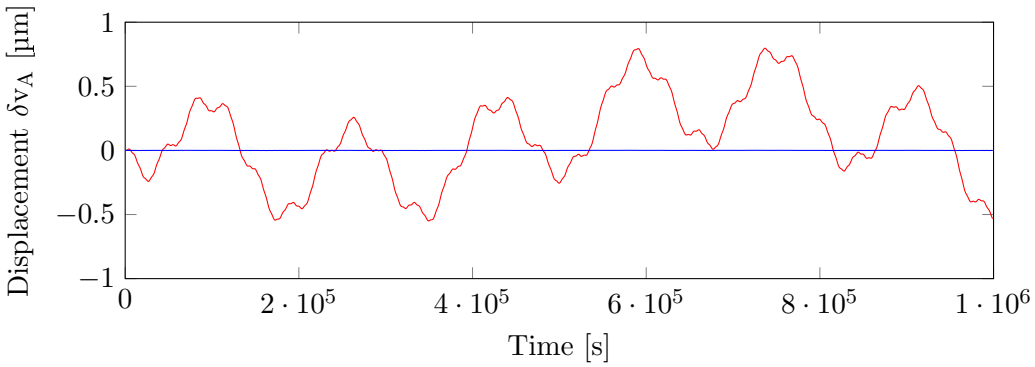

(b) Displacement in the y-direction.

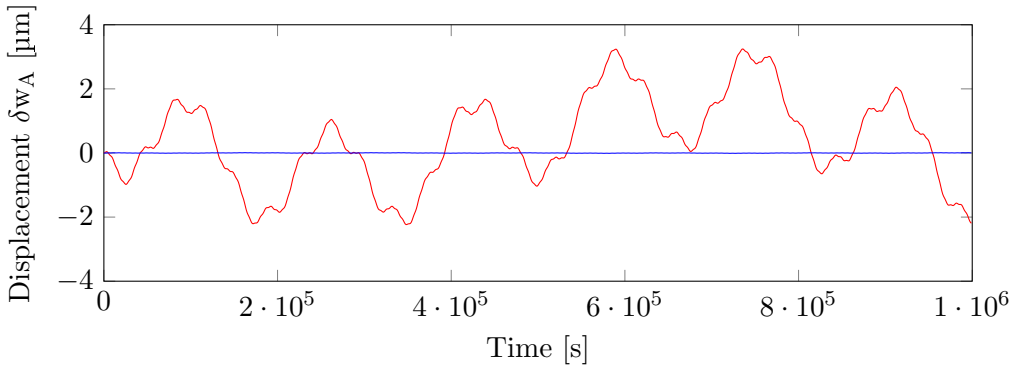

(c) Displacement in the z-direction.

Figure 6.8: Uncontrolled displacements at point A induced by random perturbations arising in Instrument 1 and controlled displacements considering only 20 ideal sensors.

Contribution related to the sensor noise

The second sensor contribution to the performance decrease is a consequence of the measurement noise. To analyze the impact of sensor noise a best case scenario is assessed in which the temperature is measured at all DOF but with noisy sensors. The noise is modeled according to Equation 5.41 in Section 5.3.3. It is assumed that both the bias at each sensor and the noise of each retrieved measurement have a standard deviation equal to $\sigma = 0.05$ K.

The comparison between the uncontrolled case and the controlled case under these assumptions is represented in Figure 6.9. A detailed view of the controlled response is additionally included in Figure 6.10 on page 104. Figure 6.9 illustrates that there is a significant improvement of the stabilization in the controlled case. However, in comparison to the previously presented case where only a few sensors were providing exact temperature measurements, the achieved performance is up to 10 times worse. In the case where only 20 ideal sensors are available, the maximum stabilization amplitude appears in the z-direction, reaching approximately 0.01 µm. In this case with 1063 noisy sensors, however, the maximum stabilization amplitude exceeds 0.001 µm in all directions, and the worse performance takes place also in the z-direction, where it reaches a maximum of approximately 0.07 µm. The exact values in terms of the amplitude and standard deviation in each direction are included in Table 6.2 and Table 6.3, respectively. These illustrate that for both measures the achieved performance is approximately an order of magnitude worse than in the previously presented case.

It can also be observed in Figure 6.9, particularly in the z-direction displacement, that distortions at the highest frequencies are only partially attenuated. This effect is related to the nature of the high-frequency perturbations, which have a lower gain than low-frequency perturbations. As a result, temperature changes induced by high-frequency perturbations have a lower amplitude. This explains why these temperature changes are the first to be masked under a given level of sensor noise. Given that these high-frequency low-amplitude temperature changes cannot be properly measured with noisy sensors they cannot be fully compensated and, as a result, they still appear in the controlled case.

Figure 6.9, and more clearly Figure 6.10, illustrate also that the decrease in performance introduced by sensor noise is more severe than the one introduced due to the limitation in number of sensors. In reality, both contributions are present, which results in an even worse performance than when both factors are assessed separately. The next section presents the performance that is achieved in this worst-case scenario that considers only a limited number of noisy sensors. Subsequently, the performance between the three cases is compared.

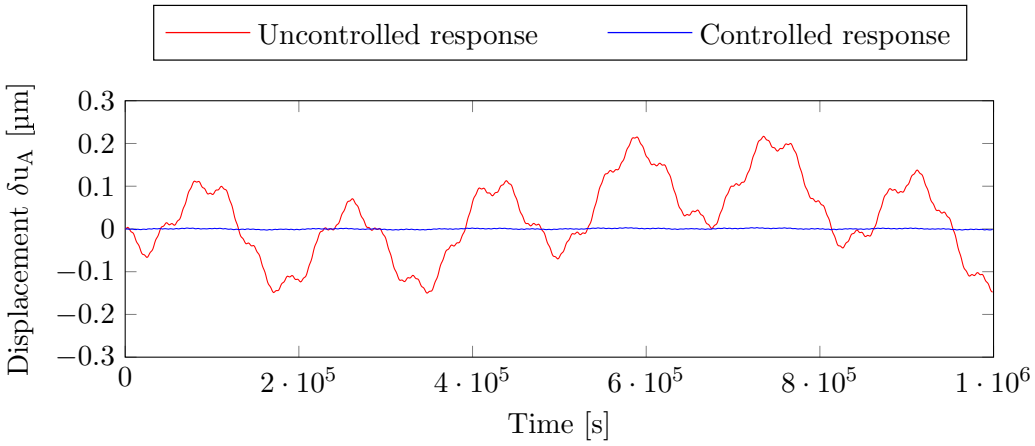

(a) Displacement in the x-direction.

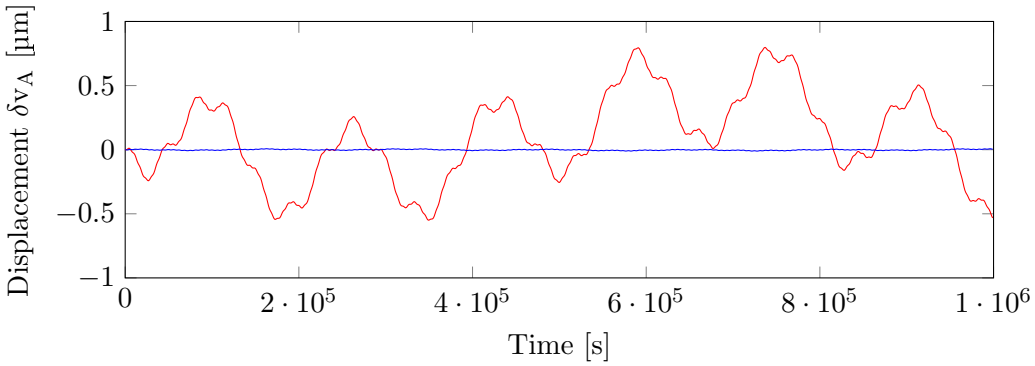

(b) Displacement in the y-direction.

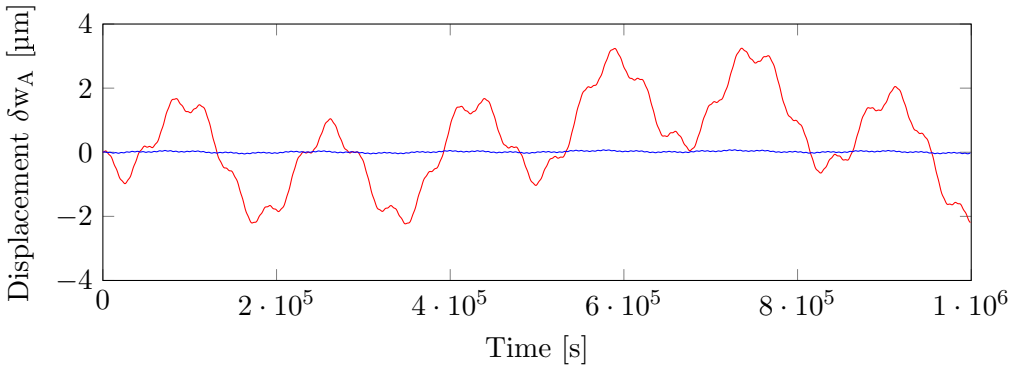

(c) Displacement in the z-direction.

Figure 6.9: Uncontrolled displacements at point A induced by random perturbations arising in Instrument 1 and controlled displacements considering 1063 noisy sensors.

Total contribution of the sensors

The real implementation of the proposed control strategy can only consist of a limited number of sensors that provide noisy measurements, which is the combination of the two previously presented cases. This situation is simulated to assess the total impact that sensor uncertainties have on the achieved performance. For completeness, this case is presented in comparison with the two previous cases. Thus, the result in Figure 6.10 presents the controlled performance in the three simulated cases, i.e. with 20 ideal sensors, with 1063 noisy sensors and the combination presented here with 20 noisy sensors.

Figure 6.10 illustrates that the largest contributor to the performance decrease is the noise in the sensors and not the fact that only a few measurements are available. Thus, one conclusion of this study is that if and when more accurate temperature sensors become available, it will be possible to improve the achieved performance.

The condition in which there are only 20 noisy sensors is by definition the more adverse among the three options presented here. Logically, it results in the worst result, which can be seen by the fluctuations with the largest amplitude in Figure 6.10. This figure illustrates that the achieved performance in this case is worse than in the previously presented cases but that it still represents a major improvement with respect to the uncontrolled case.

An important characteristic of this stabilization result is that the fluctuation does not take place around 0 µm, which can be clearly seen in Subfigure 6.10b. This is a consequence of the combined effect of having only a limited number of sensors and the fact that each provides a biased measurement. As mentioned in Section 5.3.3, it is assumed that each sensor has an inherent constant bias that takes a random value with a standard deviation of $\sigma = 0.05$ K. When the measurements are limited but exact, as in the 20 ideal sensor case, it is possible to clearly measure the thermal state around which the structure is fluctuating. This is not possible when each measurement is biased, but the error averages around 0 if a large number of sensors is available. Thus, the bias is more severe for the 20 sensor case than for the 1063 sensor case. The value of the bias is different in each direction and it changes for each realization of the simulation. The corresponding values for the case presented in this section are included in Table 6.1. The relevance of this bias is always dependent on the stabilization application. For applications where only the stabilization of one point in relative terms is required, the fact that there is a bias around which the stabilization takes places is not important. In cases where it is required to absolutely stabilize one or more points, then it is essential to ensure that the expected magnitude of this bias does not exceed the stability requirements.

Despite the fact that the combined effect of both the limitation in number of sensors and their noise increases the amplitude of the stabilized signal, the achieved performance is still more than one order of magnitude better than in the uncontrolled case. The precise values in terms of the amplitude and standard deviations for each of these three presented cases are included in Table 6.2 and Table 6.3, respectively. It is important to note that the presented maximum amplitudes are not measured around zero but around the value at which the displacement is stabilized, i.e. without considering the bias. This can be added from the values included in Table 6.1.

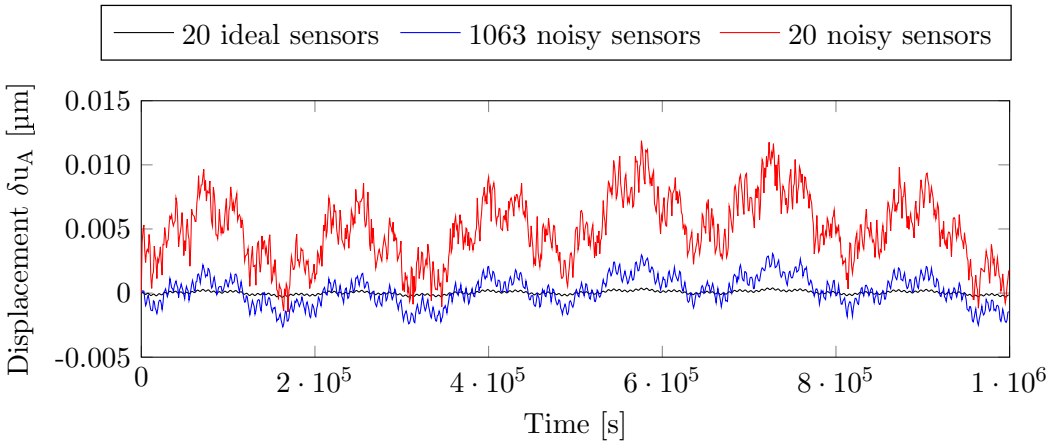

(a) Displacement in the x-direction.

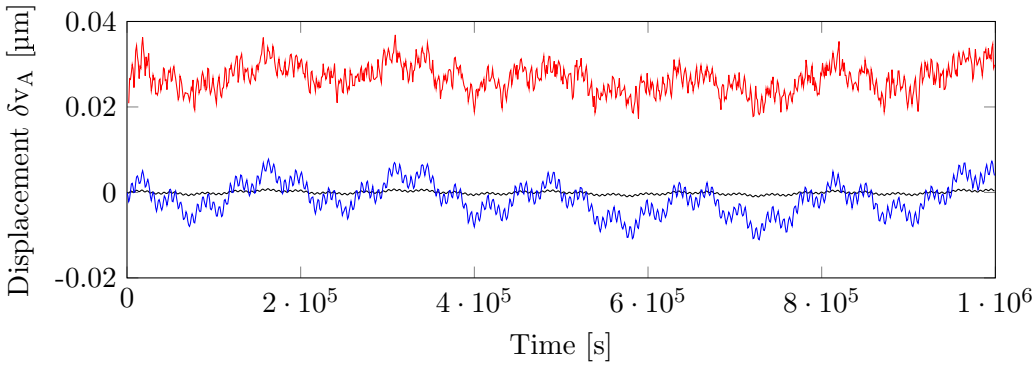

(b) Displacement in the y-direction.

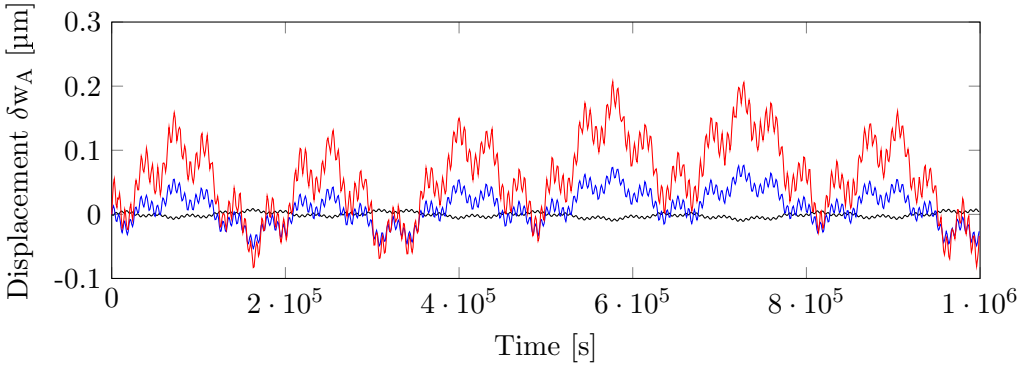

(c) Displacement in the z-direction.

Figure 6.10: Performance achieved under 3 different situations modeling the sensor uncertainty.

Stabilization bias	
Direction	Bias
x	$4.940{\cdot}10^{-3}$ µm
y	$2.670{\cdot}10^{-2}$ µm
z	$5.779{\cdot}10^{-2}$ µm

Table 6.1: Stabilization bias in each direction for the case with 20 noisy sensors.

Maximum amplitude				
Direction	Uncontrolled response	20 ideal sensors	1063 noisy sensors	20 noisy sensors
x	0.217 µm	$3.727{\cdot}10^{-4}$ µm	$2.925{\cdot}10^{-3}$ µm	$6.935{\cdot}10^{-3}$ µm
y	0.798 µm	$9.827{\cdot}10^{-4}$ µm	$9.664{\cdot}10^{-3}$ µm	$1.012{\cdot}10^{-2}$ µm
z	3.245 µm	$1.023{\cdot}10^{-2}$ µm	$6.619{\cdot}10^{-2}$ µm	0.149 µm

Table 6.2: Maximum amplitude of displacements at point A achieved in each of the considered cases modeling the sensor behavior.

Standard deviation				
Direction	Uncontrolled response	20 ideal sensors	1063 noisy sensors	20 noisy sensors
x	0.091 µm	$1.428{\cdot}10^{-4}$ µm	$1.119{\cdot}10^{-3}$ µm	$2.568{\cdot}10^{-3}$ µm
y	0.336 µm	$3.753{\cdot}10^{-4}$ µm	$3.784{\cdot}10^{-3}$ µm	$3.323{\cdot}10^{-3}$ µm
z	1.371 µm	$3.929{\cdot}10^{-3}$ µm	$2.595{\cdot}10^{-2}$ µm	$5.904{\cdot}10^{-2}$ µm

Table 6.3: Standard deviation of displacements at point A achieved in each of the considered cases modeling the sensor behavior.

6.2.2 Actuator contribution

The other important factor that can potentially affect the achieved performance of the presented framework is the uncertainty in the actuator behavior. As explained in detail in Section 5.4.2, the actuators do not apply exactly the signal that is commanded. In the presented simulations it is assumed that heaters are used as actuators and that there exists a linear relation between the commanded signal and the applied signal. The factor relating both signals is taken as a random value with an average value of 1 and a standard deviation of $\sigma = 5\%$.

Based on this approach, the sample used in the presented simulation considers three heaters that apply the heat control according to

$$\begin{aligned} q_{applied,1} &= 1.016 \cdot q_{commanded,1} \\ q_{applied,2} &= 0.977 \cdot q_{commanded,2} \\ q_{applied,3} &= 0.921 \cdot q_{commanded,3} \end{aligned} \tag{6.1}$$

In order to assess the impact that this uncertainty factor has on the achieved performance, the simulation is conducted assuming that the remaining uncertainty sources,

namely related to the sensor behavior, are not present. The comparison between the uncontrolled case and the controlled case with non-ideal actuators is represented in Figure 6.11. The results appear to be very similar to those obtained under ideal conditions, as represented in Figure 6.7 on page 98. A more thorough analysis shows that to a certain extent there is a performance decrease due to the non-ideal behavior of the actuators. However, the achieved performance is still several orders of magnitude better than in the uncontrolled case. A numerical comparison between these two cases in terms of the maximum reached amplitude and the standard deviation is included in Tables 6.4 and 6.5.

It is also important to evaluate the difference between the applied heat under ideal conditions and the actual heat that the non-ideal actuators apply to the structure. The evolution of these two signals for each actuator is represented in Figure 6.12.

Figure 6.12 illustrates that, despite the slight differences in the actuator behavior, the control signals follow the same pattern and thus, the required control power remains at the same order of magnitude. A detailed view of the difference between the ideal control heat and the actual applied heat for each actuator is included in Figure 6.13. This figure shows that the overperformance of heater 1 is mostly compensated by the underperformance of heater 2. The difference between ideal and actual heat is in this case smaller for heater 3.

It is also important to note that the non-ideal behavior of heaters does not destabilize the system and that their contribution to the performance decrease is negligible in comparison to the magnitude of the stabilized distortions. In order to fully assess the impact of using non-ideal actuators it is necessary to evaluate the achieved performance considering also non-ideal sensors. This results in the most realistic scenario in which both sensors and actuators are non-ideal. The achieved performance under these adverse conditions is presented in the next subsection.

Maximum amplitude			
Direction	Uncontrolled response	Ideal control	Non-ideal actuators
x	0.217 µm	$1.267{\cdot}10^{-4}$ µm	$1.712{\cdot}10^{-3}$ µm
y	0.798 µm	$5.036{\cdot}10^{-6}$ µm	$2.203{\cdot}10^{-3}$ µm
z	3.245 µm	$6.838{\cdot}10^{-4}$ µm	$6.643{\cdot}10^{-3}$ µm

Table 6.4: Maximum amplitude of displacements at point A achieved in each of the considered cases modeling the actuator behavior.

Standard deviation			
Direction	Uncontrolled response	Ideal control	Non-ideal actuators
x	0.091 µm	$4.860{\cdot}10^{-5}$ µm	$7.103{\cdot}10^{-4}$ µm
y	0.336 µm	$1.953{\cdot}10^{-6}$ µm	$8.348{\cdot}10^{-4}$ µm
z	1.371 µm	$2.624{\cdot}10^{-4}$ µm	$2.853{\cdot}10^{-3}$ µm

Table 6.5: Standard deviation of displacements at point A achieved in each of the considered cases modeling the actuator behavior.

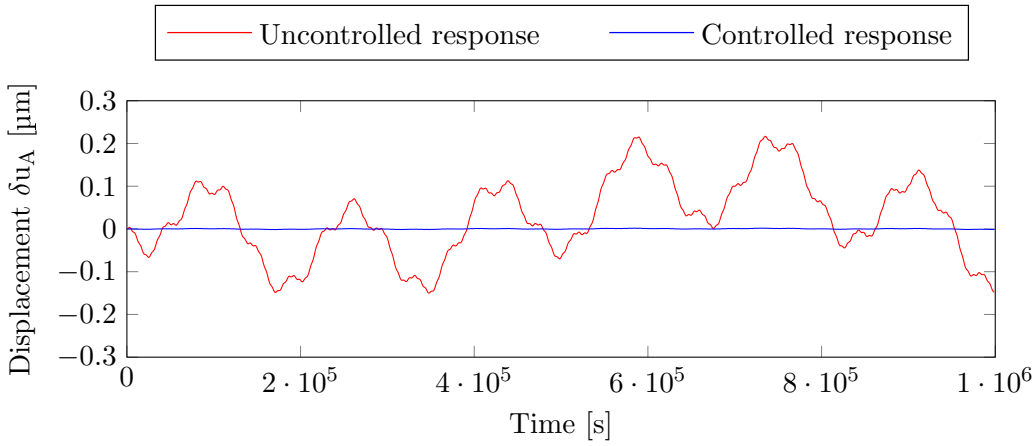

(a) Displacement in the x-direction.

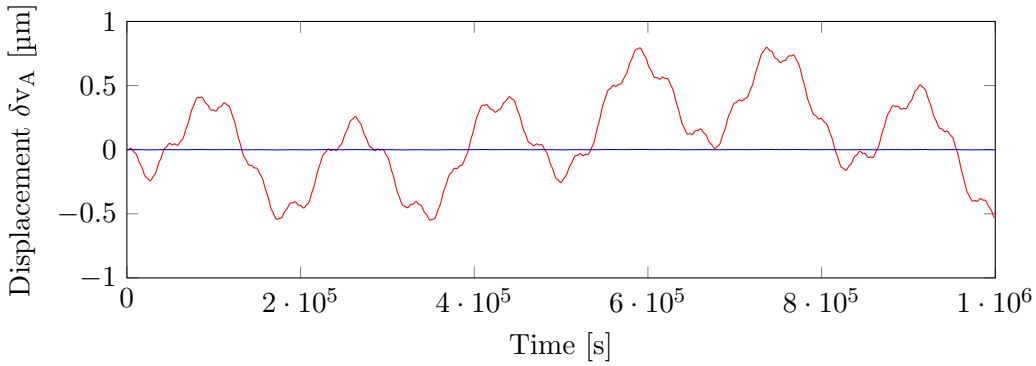

(b) Displacement in the y-direction.

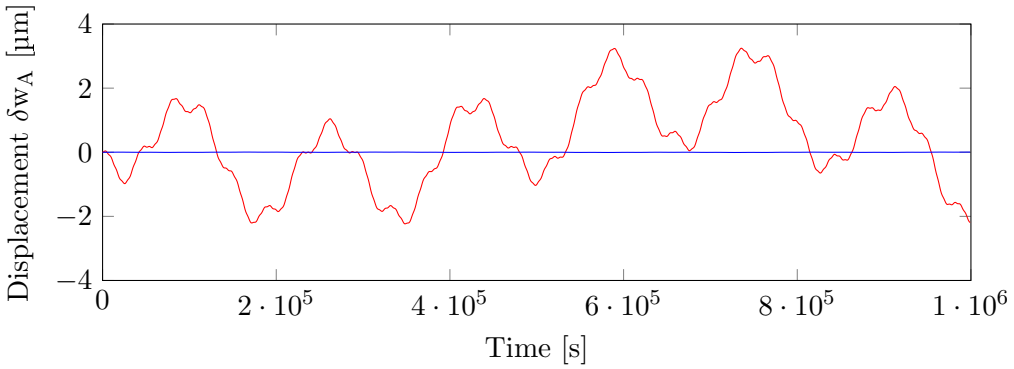

(c) Displacement in the z-direction.

Figure 6.11: Displacements at point A induced by random perturbations arising in Instrument 1 considering ideal sensors and non-ideal actuators.

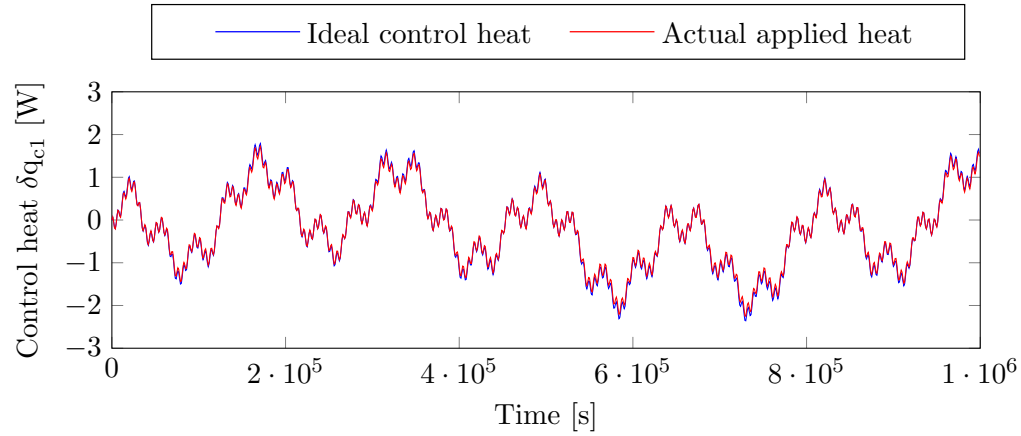

(a) Applied control heat at source 1.

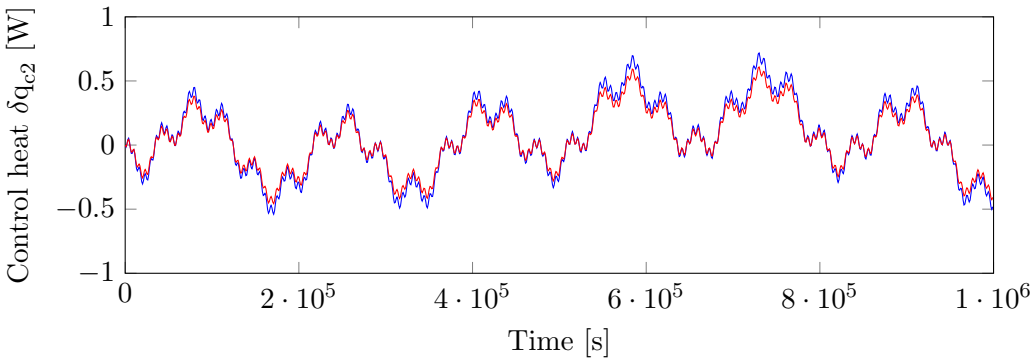

(b) Applied control heat at source 2.

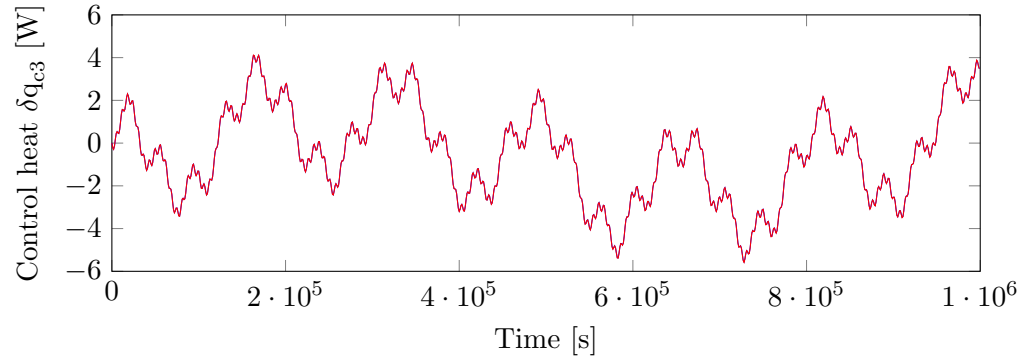

(c) Applied control heat at source 3.

Figure 6.12: Comparison in terms of the applied heat control between the ideal actuator case and the non-ideal actuator case.

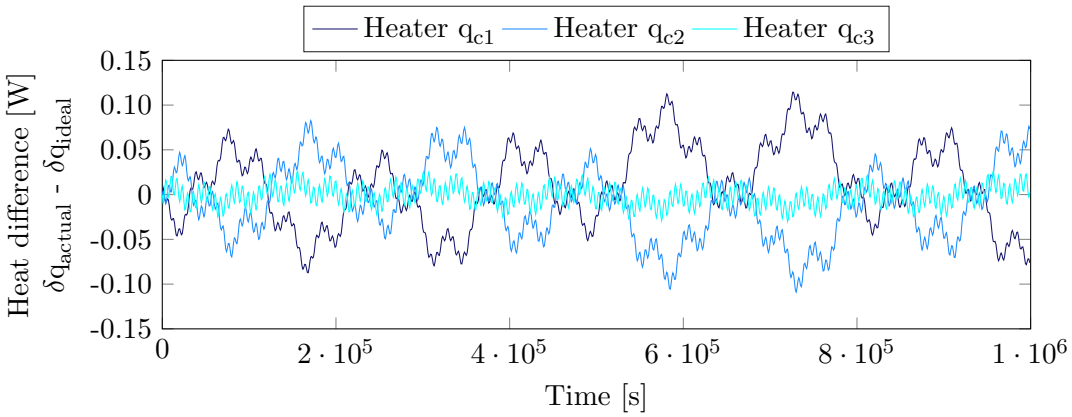

Figure 6.13: Heat difference between ideal and actual control heat at each heater.

6.2.3 Achieved performance

The presented control framework can only be implemented in reality with sensors and actuators that are inherently non-ideal. Thus, in order to simulate the performance that could be achieved with the presented system it is necessary to combine the effects of sensor uncertainties, as presented in Section 6.2.1, with the effects of actuator uncertainties, as presented in Section 6.2.2. This combination includes, on the one hand, the fact that there is only a limited number of noisy sensors and, on the other hand, the fact that actuators do not exactly apply the commanded signal.

The results presented in this section assume that the structure is equipped with 20 noisy sensors and that the actuators follow the non-ideal behavior as described by Equation 6.1 in Section 6.2.2. The comparison between the uncontrolled response and the controlled response under the mentioned assumptions is illustrated in Figure 6.14. This figure proves that even under the adverse conditions that include using non-ideal sensors and actuators, it is still possible to increase the achieved structural stabilization by more than one order of magnitude. Figure 6.14 illustrates also that the remaining displacements correspond to the response induced by the high-frequency perturbations. This effect has been shown to appear due to the noise in the sensors, as presented in detail in Section 6.2.1.

A numerical comparison between the uncontrolled response, the theoretical controlled response that could be achieved under ideal conditions and the simulated response that is achieved with non-ideal sensors and actuators is presented in Tables 6.6 and 6.7. Table 6.6 presents the maximum amplitude that is reached in each case and Table 6.7 the standard deviation. The last column in both tables presents the achieved improvement between the uncontrolled and the non-ideal controlled case.

The impact that non-ideal actuators have on the performance can be analyzed in more detail by comparing the performance results of two cases, both with non-ideal sensors but one considering ideal actuators and the other non-ideal actuators. The displacement evolution of point A for these two cases is represented in Figure 6.15, which illustrates that the achieved performance is slightly worsened when the actuators do not behave exactly as commanded. In turn, a comparison of heat input for these two cases is included in Figure 6.16.

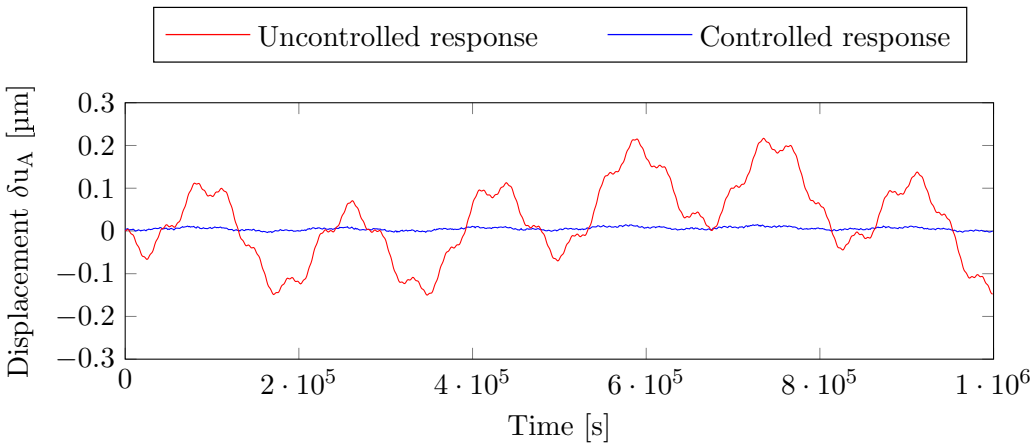

(a) Displacement in the x-direction.

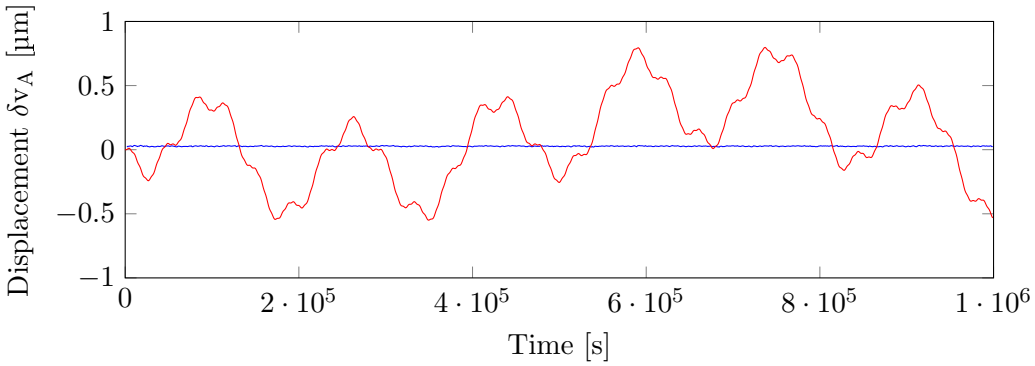

(b) Displacement in the y-direction.

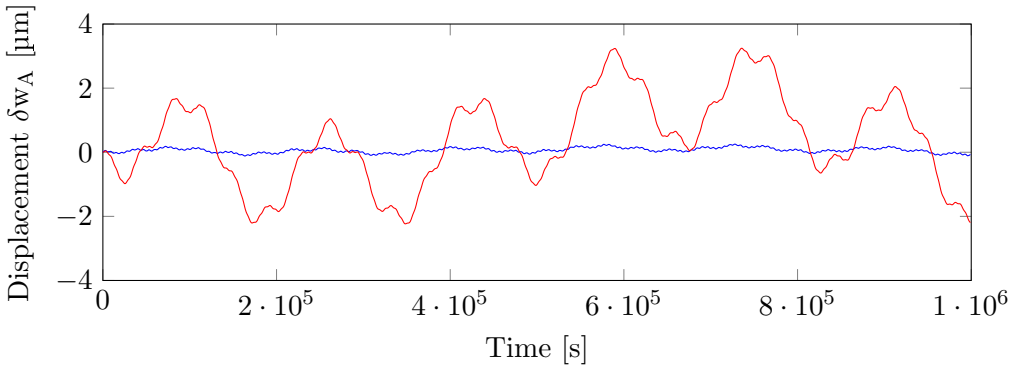

(c) Displacement in the z-direction.

Figure 6.14: Displacements at point A induced by random perturbations arising in Instrument 1 considering 20 noisy sensors and non-ideal actuators.

Maximum amplitude				
Direction	Uncontrolled response	Ideal controlled response	Non-ideal controlled response	Reduction factor
x	0.217 µm	$1.267 \cdot 10^{-4}$ µm	$9.669 \cdot 10^{-3}$ µm	22.4
y	0.798 µm	$5.036 \cdot 10^{-6}$ µm	$7.069 \cdot 10^{-3}$ µm	112.8
z	3.245 µm	$6.838 \cdot 10^{-4}$ µm	0.190 µm	17.1

Table 6.6: Comparison in terms of the maximum amplitude of displacements at point A for the uncontrolled and controlled cases.

Standard deviation				
Direction	Uncontrolled response	Ideal controlled response	Non-ideal controlled response	Reduction factor
x	0.091 µm	$4.860 \cdot 10^{-5}$ µm	$3.798 \cdot 10^{-3}$ µm	24.0
y	0.336 µm	$1.953 \cdot 10^{-6}$ µm	$2.365 \cdot 10^{-3}$ µm	141.9
z	1.371 µm	$2.624 \cdot 10^{-4}$ µm	$7.626 \cdot 10^{-2}$ µm	18.0

Table 6.7: Comparison in terms of the standard deviation of displacements at point A for the uncontrolled and controlled cases.

The contribution to the performance decrease induced by the uncertainty in the actuators is ultimately a consequence of the estimation error of the temperature field. The temperature field estimation is performed by combining the sensor measurements with the estimated temperature changes introduced by the actuators. If the actuators are ideal it is possible to calculate exactly the temperature change they introduce based on the thermomechanical model. However, if their behavior is partially uncertain the temperature field variation they introduce can only be estimated within some level of accuracy. This inaccuracy in the temperature field estimation affects the calculation of the required control inputs, which eventually translates into a decrease in the achieved level of stability. A detailed view of the stability decrease due to this phenomenon is included in Figure 6.17, which illustrates how the achieved performance partially decreases due to this inaccuracy in the applied heat.

The variation in the control inputs that is ultimately introduced by the actuator uncertainty is presented in Figure 6.16. This figure presents the required control inputs that would be applied through ideal actuators compared to the control inputs as calculated when sensors and actuators are not ideal. The noise that is introduced by sensor measurements can only be partially attenuated by the Kalman filter in the temperature estimation process. Thus, the control inputs that are calculated incorporate also part of this noise. A detailed view of the difference between this two cases is represented in Figure 6.18.

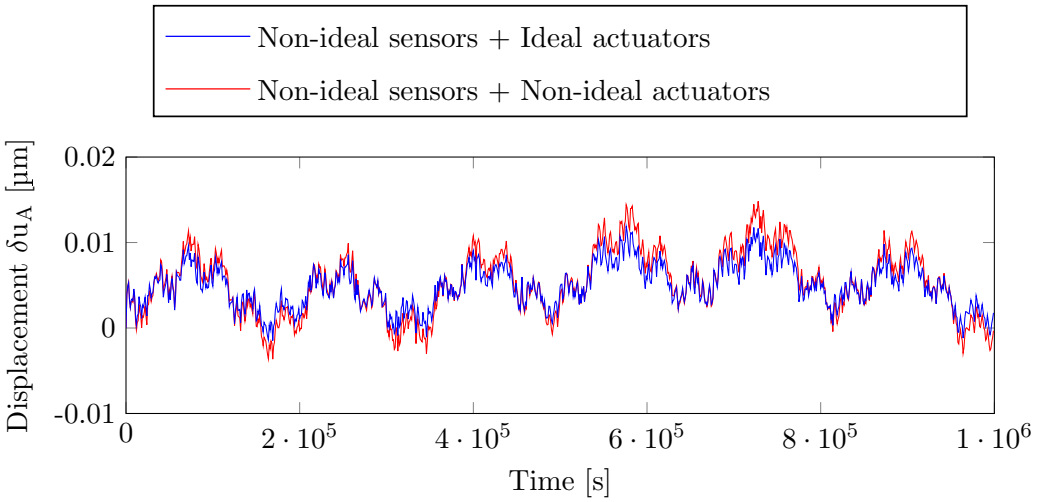

(a) Displacement in the x-direction.

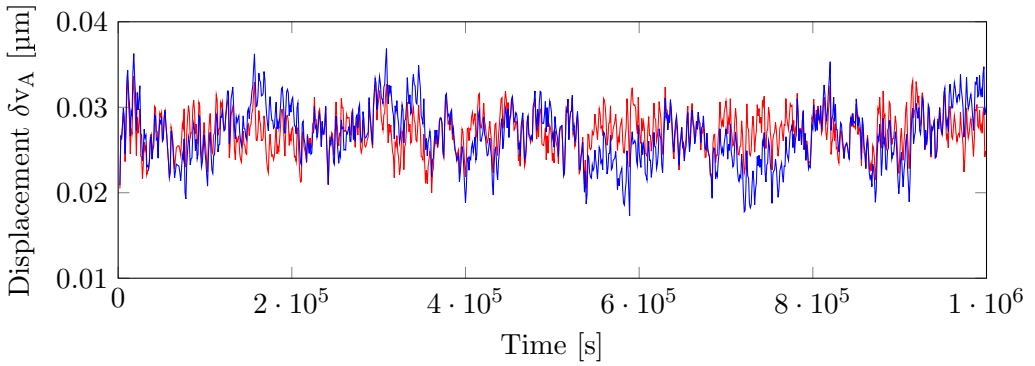

(b) Displacement in the y-direction.

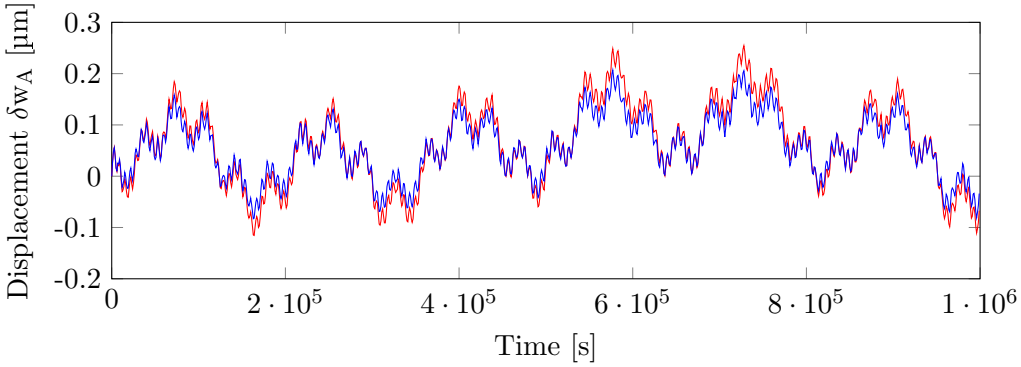

(c) Displacement in the z-direction.

Figure 6.15: Comparison of displacements at point A induced by random perturbations arising in Instrument 1 with non-ideal sensors and considering the ideal and the non-ideal actuator cases.

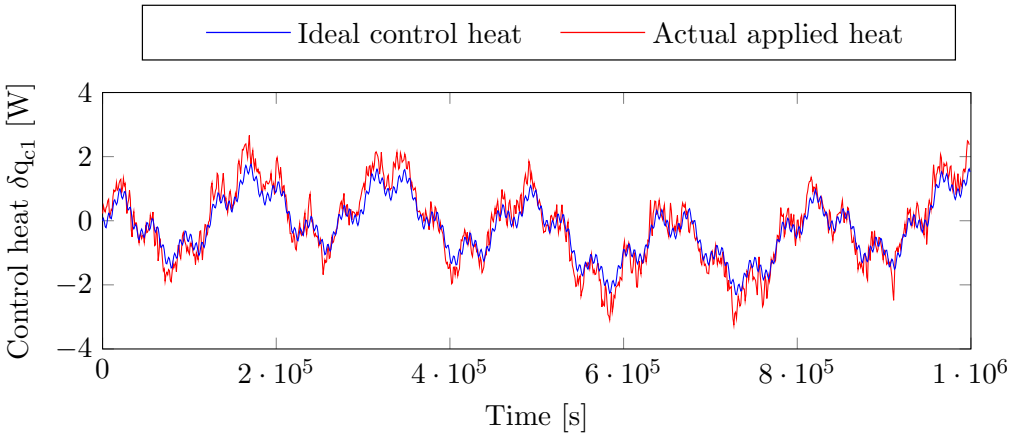

(a) Applied control heat at source 1.

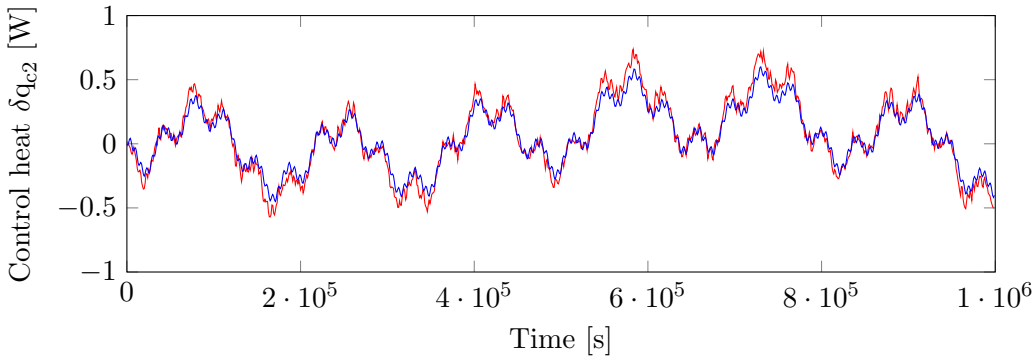

(b) Applied control heat at source 2.

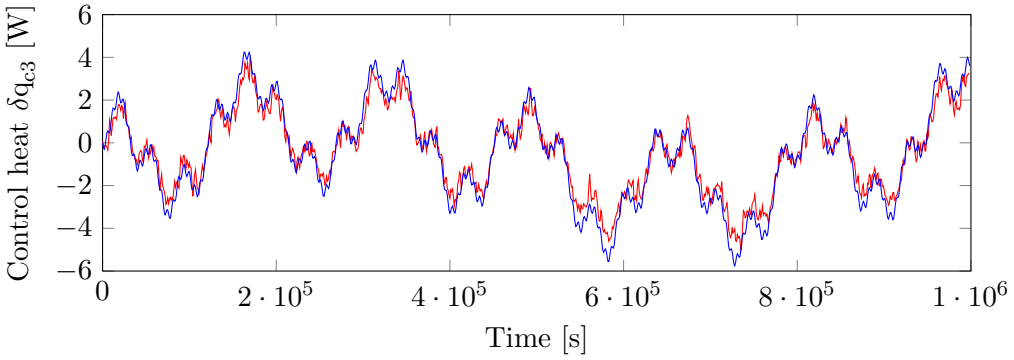

(c) Applied control heat at source 3.

Figure 6.16: Comparison in terms of the applied control heat between the ideal case with only sensor uncertainties and the non-ideal case with sensor and actuator uncertainties.

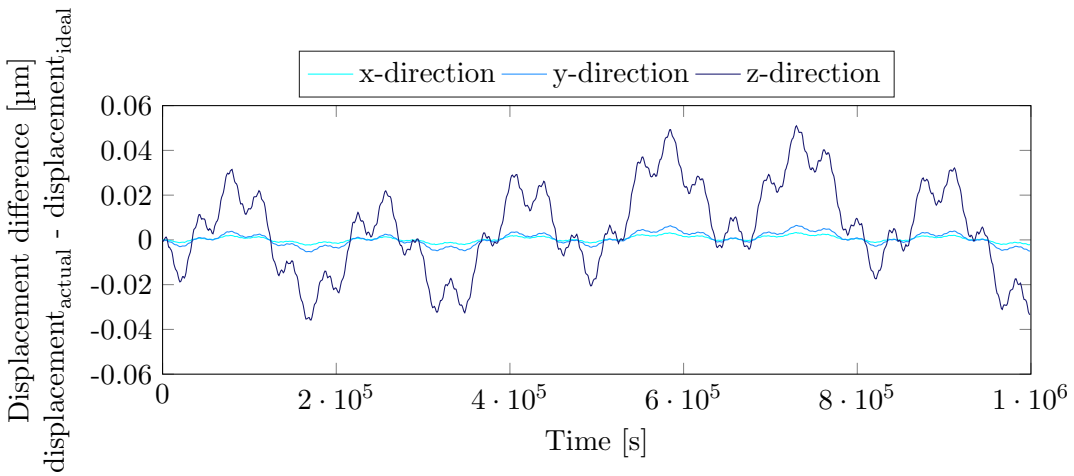

Figure 6.17: Stabilized displacement difference between the case with ideal actuators and the case with non-ideal actuators. In both cases, sensor behavior is non-ideal.

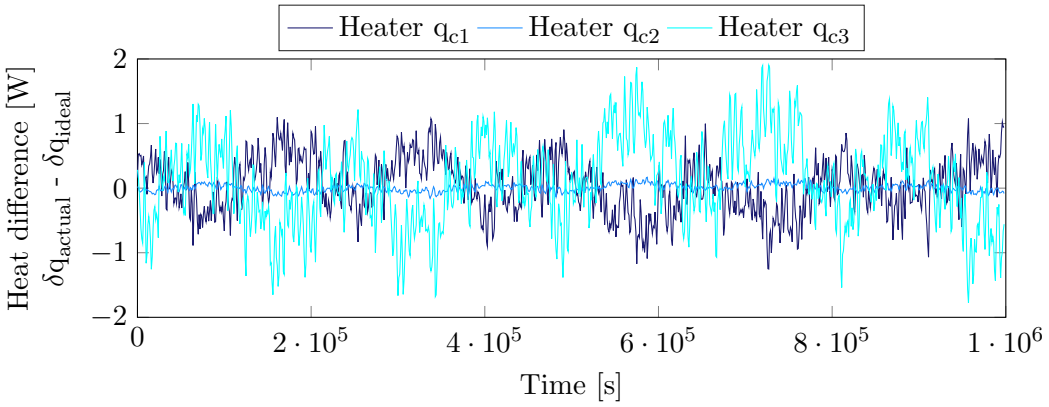

Figure 6.18: Heat difference between the ideal control heat and the actual control heat at each heater when sensor behavior is non-ideal.

6.3 Errors introduced by approximations

The previous section has evaluated the impact that uncertainties in the equipment performance, namely in the sensors and in the actuators, can have on the achieved stability. This section evaluates the decrease in performance that could potentially arise due to the mathematical approximations introduced to develop the control framework. There are two potential sources of errors related to the derivation of the thermomechanical model that represents the studied structure. The first one is the linearization of the radiation terms, as presented in Section 3.2.4, which is necessary to derive the transfer functions of the thermal problem. The second possible source of errors is the assumption that the structure has a quasi-static behavior when affected by low-frequency thermal perturbations. This step is necessary, as presented in Section 5.2, in order to calculate the control gains of the feedback loop.

The possible impact of the linearization of the radiation terms is subsequently evaluated and presented in Subsection 6.3.1. This is followed by the evaluation of the influence that the quasi-static assumption can have on the stability performance, presented in Subsection 6.3.2. The presented results are valid for the baseline case

considered in this thesis but they cannot be extrapolated to all the possible cases. The validation of these approximations should be verified in a case-by-case basis to ensure that an acceptable level of performance can be reached.

6.3.1 Linearization of radiation terms

According to the Stefan-Boltzmann law the power radiated from a black body follows a fourth power law in terms of the temperature. This relation has been linearized following the procedure presented in Section 3.2.4 in order to obtain a linear relation between temperature and heat flux. If under some circumstances there is a strong discrepancy between the values provided by the Stefan-Boltzmann law and the linearized model, this will translate into an error in the temperature estimation obtained from the thermal model. In turn, it will result in an inaccuracy on the calculated control heat inputs which will decrease the final stability performance.

The simulations that have been presented in the previous sections of this chapter have been performed following the model expressed by Equation 5.67 on page 89, which is based on the assumption that the thermal behavior is linear. If this is not the case, the actual thermal evolution of the system will differ from that obtained from the linear model. In order to assess the magnitude of this potential difference, a time integration of the model considering the nonlinear terms, as expressed in Equation 3.63 of Section 3.2.3, is performed. Afterwards, the temperature evolution obtained through the nonlinear model is compared to that obtained from the linear model.

The nonlinear model is executed considering as heat inputs a random perturbation from instrument 1 and the heat control inputs that are obtained from the linear control model. The comparison between the nonlinear and the linear evolution results in a difference that is several orders of magnitude below the amplitude of the fluctuation at each node. As an example, Figure 6.19 shows the temperature evolution of one specific node in the model both according to the linear and the nonlinear model. Both lines appear superimposed which proves that the difference between both models is negligible in this case. For the sake of clarity, the difference in temperature between these two cases is included in Figure 6.20, which illustrates that for the presented case the difference never exceeds a magnitude of $4{\cdot}10^{-4}\,\mathrm{K}$, even though the temperature fluctuations reach approximately 1 K. Linearizing the model is equivalent to underestimating the heat radiated by each element. Thus, the linear model results in slightly higher temperatures than the nonlinear model, as illustrated by Figure 6.20.

The magnitude of the difference between the linear and the nonlinear case does not depend only on the amplitude of the fluctuations but also on the relative weight of the radiation links between the different nodes in the structure. Therefore, it depends also on the thermo-optical properties of the surfaces and their geometry. This analysis proves that the linearization is a valid assumption in the baseline studied case. However, the analysis should be repeated in case there appear changes in the magnitude of the perturbations, the geometry of the structure or its thermo-optical properties.

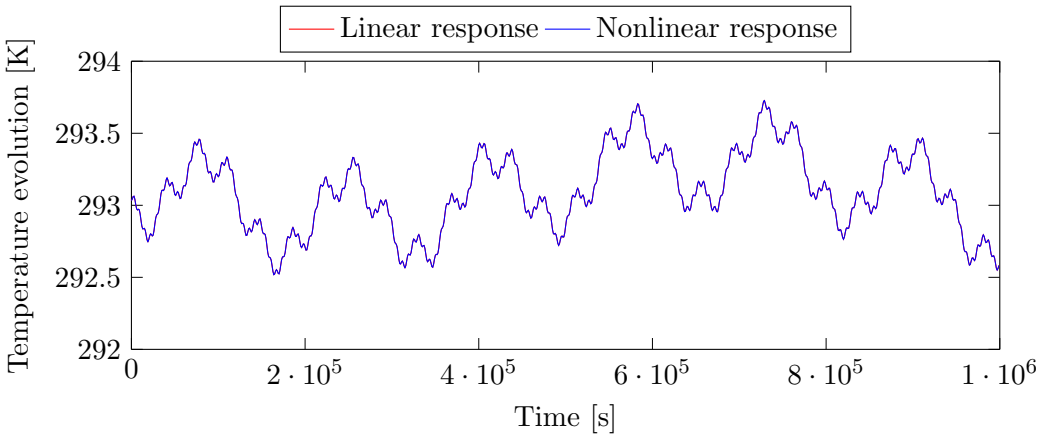

Figure 6.19: Temperature evolution comparison between the linear and the nonlinear model.

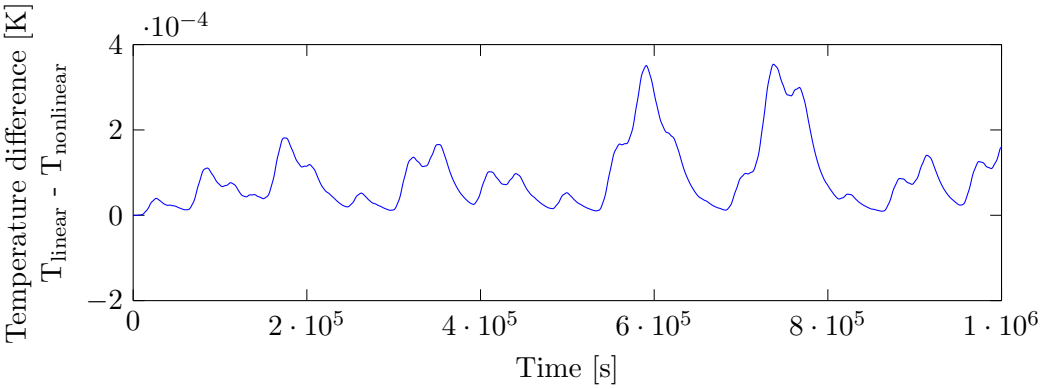

Figure 6.20: Temperature difference between the linear and the nonlinear model.

6.3.2 Quasi-static assumption

A significant difference between the estimated displacement and the actual displacement could potentially arise due to the inertial and damping effects of the structure. The control framework has been developed based on the assumption that these effects are negligible. If it turns out that they are not, the control framework would be calculating the necessary control inputs based on a flawed estimation of the real displacements taking place. As a result, the achieved stability performance would decrease.

Section 4.2.2 has shown that the mechanical transfer functions are mostly flat throughout the frequency range of interest. Therefore, from a pre-simulation point of view, it is expected that the quasi-static assumption is valid. Here, the assumption is validated based on the obtained results from the presented simulations. The thermal field evolution of the structure is considered to be the input and the displacement field is the output. This is first calculated based on the quasi-static assumption, which is expressed as

$$[K_u]\{u\} = [F_T]\{T\} + \{F_d\} \tag{6.2}$$

as explained in Section 4.2.2 and as it is done in the control loop. The results from this approximation are compared to the more accurate results that would be

obtained if the inertial and damping effects were considered. These are obtained from the expression

$$[M_u]\{\ddot{u}\} + [C_u]\{\dot{u}\} + [K_u]\{u\} = [F_T]\{T\} + \{F_d\} \tag{6.3}$$

as outlined in Section 4.1.

The displacement change around the equilibrium condition is represented for these two cases in Figure 6.21. As in the assessment of the linearization effect in the previous section, there is an almost perfect overlap between the two results. A detailed view of the difference between both cases is illustrated in Figure 6.22. This shows that the magnitude of the difference is more than 4 orders of magnitude below the magnitude of the fluctuation amplitude and never exceeds $1{\cdot}10^{-4}$ µm. Thus, it is considered that in the baseline case it is a valid assumption to consider the problem as quasi-static since the performance decrease it introduces is negligible for any practical purposes.

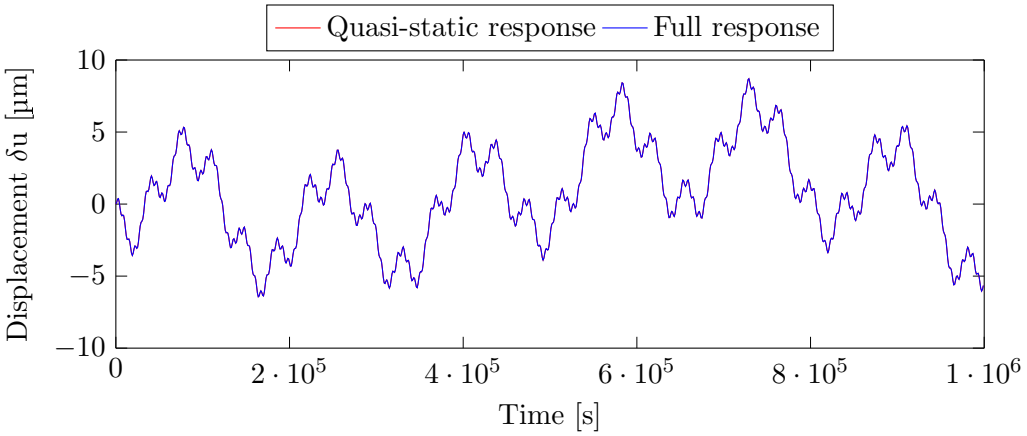

Figure 6.21: Comparison in terms of the displacement evolution at one representative node according to the quasi-static model and to the full model that includes inertial and damping effects.

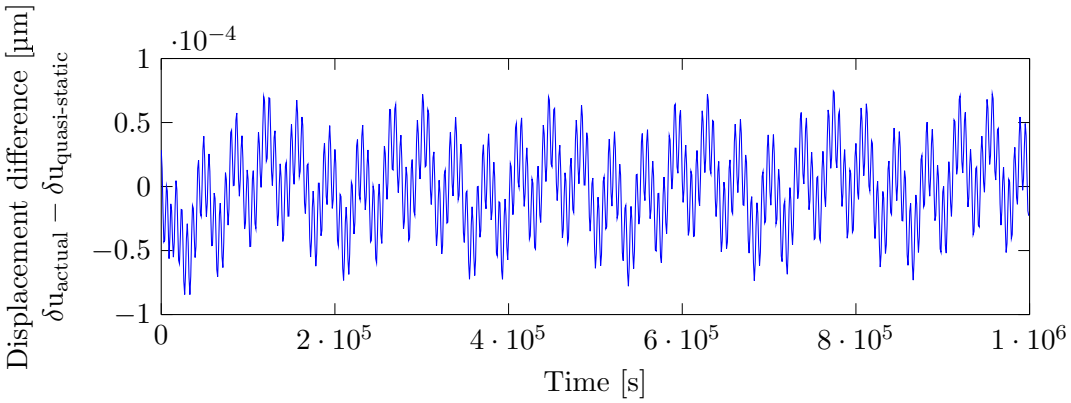

Figure 6.22: Displacement difference between the actual case and the quasi-static approximation.

6.4 Absolute and relative stabilization

The goal of the simulation examples presented in the previous sections is to stabilize the displacement at point A in the structure with respect to an external reference frame, as represented in Figure 6.1. In physical terms, this baseline case consists in stabilizing three degrees of freedom of the structure and thus, three heaters are required. Based on the same presented approach it is also possible to stabilize specific points in the structure with respect to other reference frames. One sensible option consists in stabilizing one point with respect to another. In this scenario, both points are experiencing a displacement with respect to an external reference frame but their relative motion is stabilized.

An example to illustrate this strategy is presented in this section. In this case, the relative motion between points A and B, as represented in Figure 6.1, is stabilized. Technically, this consists in the stabilization of three degrees of freedom and thus, only three heaters are required. The same previous heater configuration, as represented in Figure 6.2, is assumed.

Hence, the control setup is assumed to be exactly the same as in the previously presented cases. The noise in the sensors is assumed to be characterized by a constant bias with $\sigma = 0.05$ K and an error at each measurement with also $\sigma = 0.05$ K. The actuators are assumed to behave as expressed by Equation 6.1. The presented results are obtained under the assumption that the structure is equipped with 20 sensors. It is important to keep in mind that the achieved performance can always be improved by increasing the number of sensors, as has been shown in Section 6.2.1. However, more sensors also entail more complexity and, therefore, a compromise has to be found between performance and complexity. The marginal improvement that each added sensor provides must be evaluated on a case-by-case basis.

The comparison between the uncontrolled and the controlled response for this case is illustrated in Figure 6.23. This figure shows that, even in the uncontrolled case, the relative displacement between points A and B does not exceed 1 µm in any direction. This low magnitude of the displacement can be attributed to a partially synchronized movement at these two points. The largest stabilization is achieved in the y and z directions, which are also the directions in which the largest displacements appear. The numerical comparison between both cases is included in Tables 6.8 and 6.9, which show the maximum amplitude and the standard deviation in each case.

It is also interesting to analyze this scenario in terms of the control effort it requires understood as heat power. Figure 6.24 shows a comparison of the control signals between an ideal case and the actual case. The ideal case assumes that the thermal perturbation is known beforehand and thus the exact control input can be calculated. The actual applied heat is obtained through the feedback loop with 20 noisy sensors and non-ideal heaters. Figure 6.24 shows that the required input power is significantly higher than in the previous cases where only point A is controlled, as represented in Figure 6.16. This could be minimized by identifying more optimal locations for the heaters. Also, there is a higher level of noise in the control signals, which can become a problem depending on the latency in the actuators. This could be reduced by adding temperature sensors, which would allow to consider more thermal modes in the model, providing a better estimation of the temperature field.

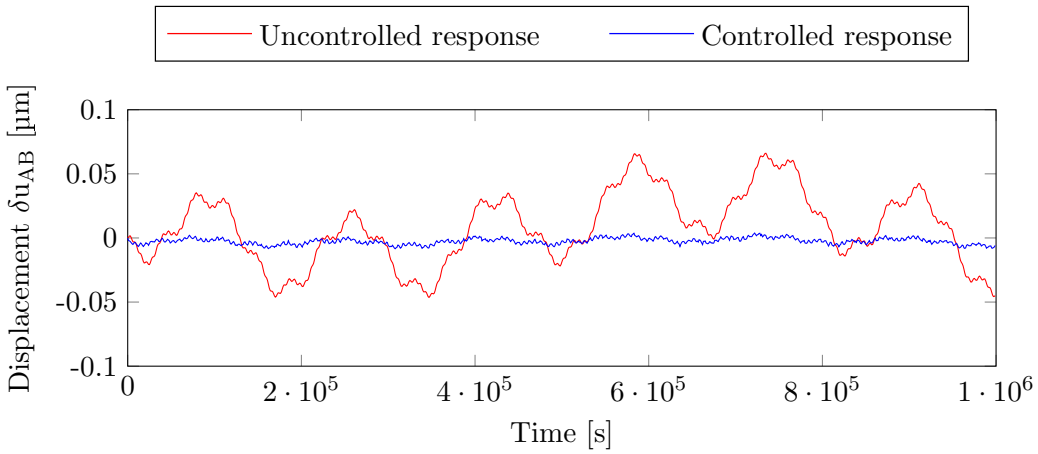

(a) Displacement in the x-direction.

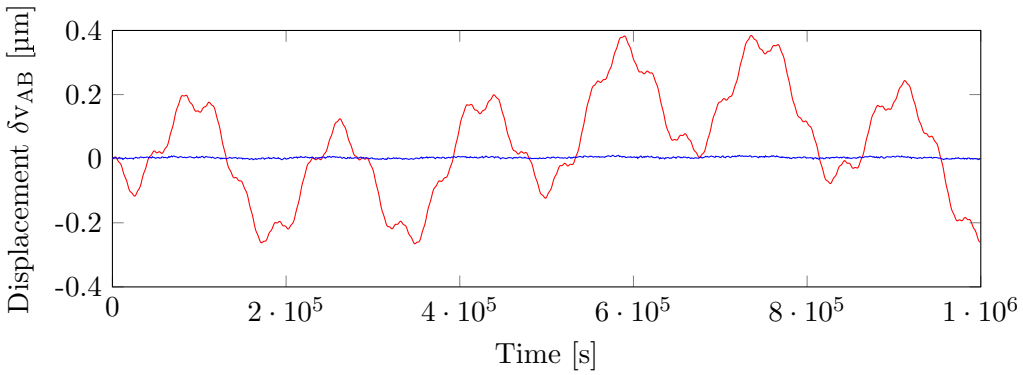

(b) Displacement in the y-direction.

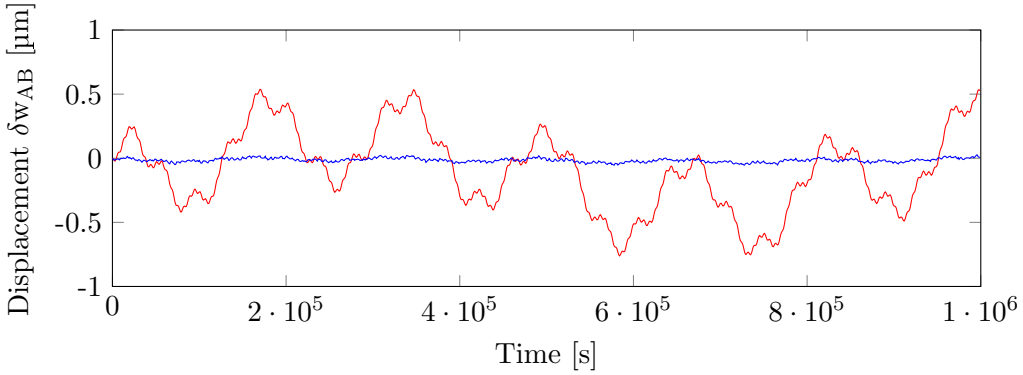

(c) Displacement in the z-direction.

Figure 6.23: Comparison between the controlled and uncontrolled distance changes between points A and B.

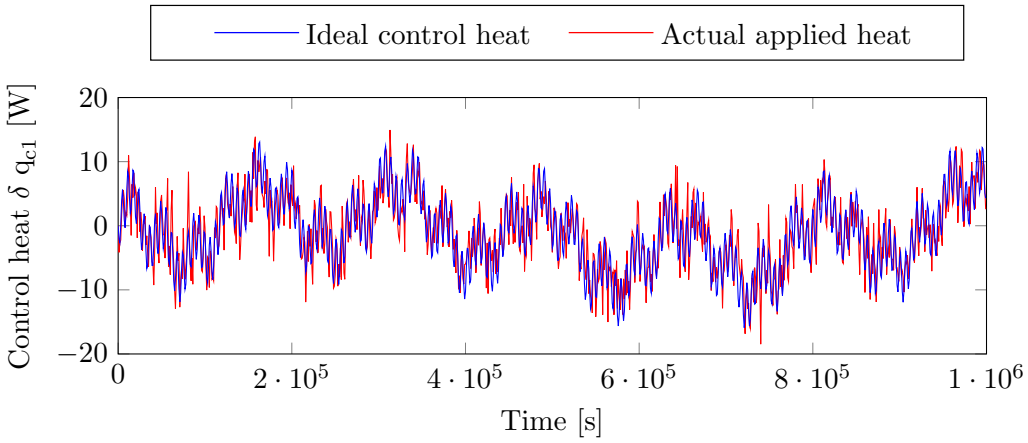

(a) Applied control heat at source 1.

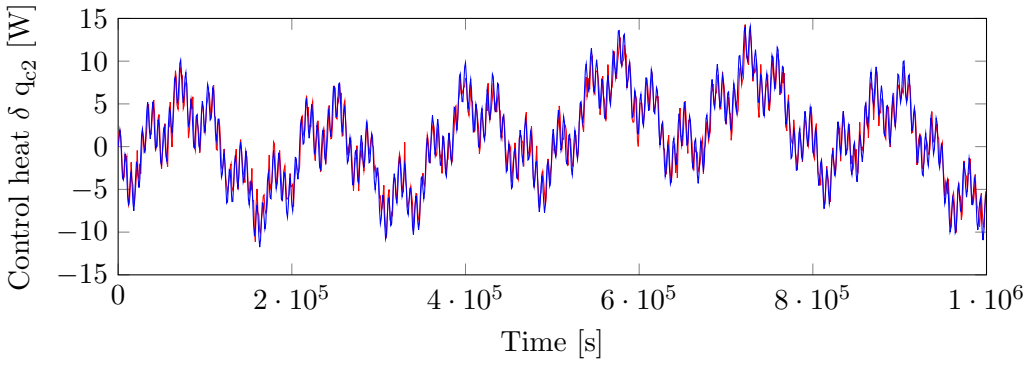

(b) Applied control heat at source 2.

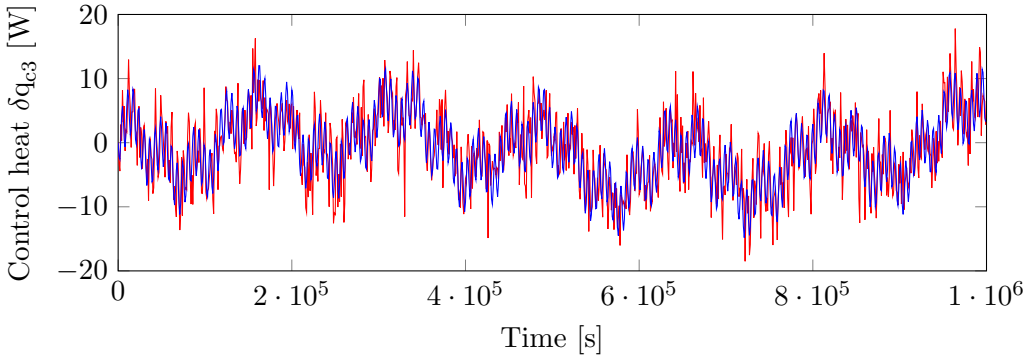

(c) Applied control heat at source 3.

Figure 6.24: Comparison in terms of the applied control heat to stabilize the distance between points A and B considering the ideal case under no uncertainties and the non-ideal case with sensor and actuator uncertainties.

Maximum amplitude			
Direction	Uncontrolled response	Controlled response	Reduction factor
x	0.066 µm	$6.370{\cdot}10^{-3}$ µm	10.4
y	0.384 µm	$6.827{\cdot}10^{-3}$ µm	56.2
z	0.761 µm	$3.945{\cdot}10^{-2}$ µm	19.3

Table 6.8: Maximum amplitude of displacements between points A and B for the uncontrolled and controlled cases.

Standard deviation			
Direction	Uncontrolled response	Controlled response	Reduction factor
x	$2.756{\cdot}10^{-2}$ µm	$2.397{\cdot}10^{-3}$ µm	11.5
y	0.162 µm	$2.335{\cdot}10^{-3}$ µm	69.4
z	0.313 µm	$1.448{\cdot}10^{-3}$ µm	216.2

Table 6.9: Standard deviation of displacements between points A and B for the uncontrolled and controlled cases.

6.5 Material sensitivity analysis

The presented simulations have been conducted under the assumption that the material properties that characterize the structure behavior are perfectly known. Although it is true that the relevant properties can be measured at high levels of accuracy and also that it is possible to manufacture high quality materials within stringent tolerances of some specific properties, it may be also common to apply the presented method on structures for which the material properties are only known within some margin of accuracy. For instance, in an otherwise passively stabilized structure for which measuring all the material properties at high accuracies would require excessive costs. The consequence of having some uncertainty in the knowledge of the material properties translates directly into an inaccuracy in the thermomechanical model, which to a certain extent can affect the achieved performance.

This potential change in performance is assessed here in terms of the main material properties that define the structure. The analysis is divided between those properties affecting the thermal behavior of the structure, presented in Subsection 6.5.1, and those affecting the mechanical behavior, presented in Subsection 6.5.2.

The effect of each property is assessed separately assuming that there is no uncertainty in the other properties. Thus, it is possible to identify which properties can have a larger influence on the achieved performance. The baseline example presented in the previous section is also considered for this study. In particular, only the uncertainty in the structural plate is analyzed. The properties of the remaining parts of the structure, i.e. the bipods and the instruments, are assumed to be known. The achieved performance is calculated considering that the actual value of the property under evaluation differs from the value assumed in the thermomechanical model. This is performed for six values of this difference distributed between ±5%.

6.5.1 Thermal properties

The material properties that directly determine the thermal behavior of the structure are the thermal conductivity λ, the heat capacity c_p, the emissivity ε and the density ρ. From these, only the density is a variable that also has a direct influence on the mechanical behavior. However, if the quasi-static assumption is made, this influence is neglected and thus, it is here assumed that the material density only influences the thermal response. For the sake of consistency, the effects of density uncertainties are analyzed in this section.

First, the analysis related to the uncertainty in the thermal conductivity is presented. As with the rest of the variables, six different cases are considered. In all of them the assumed conductivity value corresponds to the one expressed in Table 3.1 on page 40 but the actual value that describes the real behavior differs from it by -5%, -3%, -1%, 1%, 3% and 5%. The controlled response is simulated in each case and it is quantified in terms of the maximum amplitude and standard deviation of the displacement in each direction. The obtained values are illustrated in Figure 6.25.

The uncertainty in the conductivity value directly results in an inaccurate calculation of the conductivity matrix, calculated according to Equation 3.37 on page 39. As a result, the actual thermal equilibrium state achieved by the structure will differ from the assumed state around which the thermal equations are linearized to calculate the transfer functions. Also, the heat will flow through the structure in slightly different ways than those predicted by the model. As a consequence, the calculation of the control gains used in the feedback loop is not based on a completely accurate model. Thus, the final achieved performance in each direction will slightly differ from the obtained in the ideal case in which the conductivity value is exactly known, as seen in Figure 6.25.

The first important conclusion that can be drawn from Figure 6.25 is that the performance does not necessarily decrease when there is uncertainty in the model. This can seem contradictory at first sight but it must be taken into account that the change in performance is eventually induced by two factors, which might have opposing effects. On the one hand, the uncertainty in the material properties decreases the accuracy of the models. On the other hand, it may be the case that the actual material properties are in reality more beneficial for the structural stability than in the case of the assumed values. Thus, when the structure is in reality more stable than the implemented model assumes, the final net effect can be an improvement of performance, even when uncertainty is present. Depending on which of these aspects has a higher weight, the achieved performance will increase or decrease. This behavior is always case-by-case dependent and, therefore, no general conclusions can be extracted. Whether a change in a particular material property is beneficial or detrimental to the performance will always depends on the geometry of the structure and on the particular displacements that are being stabilized. Even at the same point the behavior can differ depending on the direction.

This behavior can be seen for the conductivity case represented in Figure 6.25. In this case, both for the x and z directions the amplitude of the distortions decreases when the actual conductivity is lower than the assumed conductivity. This indicates that in these two directions, a lower conductivity value results in higher stability,

which is reached even if there is uncertainty in the assumed conductivity value. This behavior is not observed in the y-direction, in which an uncertainty in the conductivity value always decreases the achieved performance.

The second important conclusion, also observable for the conductivity case in Figure 6.25, is that in absolute terms the performance changes have very low magnitudes. Even though it is possible to identify positive and negative trends depending on the direction of the uncertainty, the absolute value of the amplitude change between the two extreme cases only exceeds 0.01 µm in the z-direction, which is also the direction in which the uncontrolled amplitude is larger. In the other directions, the maximum performance changes are in the range of nanometers. As it has been mentioned in Section 6.1, it is questionable whether the assumed finite element models are still valid at these magnitudes. Additionally, when such low values are involved it has not been discarded whether some of the observed effects could be a result of numerical rounding errors at some step in the simulation process.

The changes in performance expressed in percentage for each specific case are included in Table 6.10 on page 134 and in Table 6.11 on page 135, for the maximum amplitude and the standard deviation, respectively. These tables include also the changes introduced by the uncertainty in the other properties. It can be seen from these values that, relative to the other properties, the uncertainties in conductivity are the ones that can result in the largest changes in the achieved performance. Thus, to minimize these possible variations in the obtained performance, a strong effort should be put in obtaining an accurate measurement of the actual conductivity in the materials of the structure.

The second variable that is analyzed is the heat capacity. This physical property appears in the calculation of the thermal capacity matrix, calculated according to Equation 3.36 on page 39. The thermal capacity of the structure does not influence the temperature field that is reached under equilibrium. In fact, it only affects the transient behavior of the structure. Thus, if there is uncertainty in the actual value of the heat capacity, the transfer functions obtained from the thermomechanical model will not exactly describe the actual behavior but they will still be linearized around the correct value.

The resulting performance, in terms of maximum amplitude and standard deviation, is illustrated for the different considered cases in Figure 6.26. This figure illustrates that within the considered range of uncertainty, the relation between maximum amplitude and uncertainty follows approximately a linear relation. In the x and y directions this relation is negative, whereas in the z-direction it is positive. A very similar behavior can be observed in terms of the standard deviation. An exception takes place in the x-direction case, which appears to follow a parabolic relation. However, the expected changes are at such low magnitudes that become irrelevant for any practical purposes and, as aforementioned, could be the result of numerical rounding errors. In terms of the maximum amplitude, the introduced changes do not exceed 0.001 µm in any case. The same data expressed as percentage changes is included in Tables 6.10 and 6.11. These show that both in terms of amplitude and standard deviation, the uncertainty in heat capacity has one of the lowest impacts on the achieved performance. Particularly in the case of the standard deviation, the expected changes can be considered negligible within the studied range.

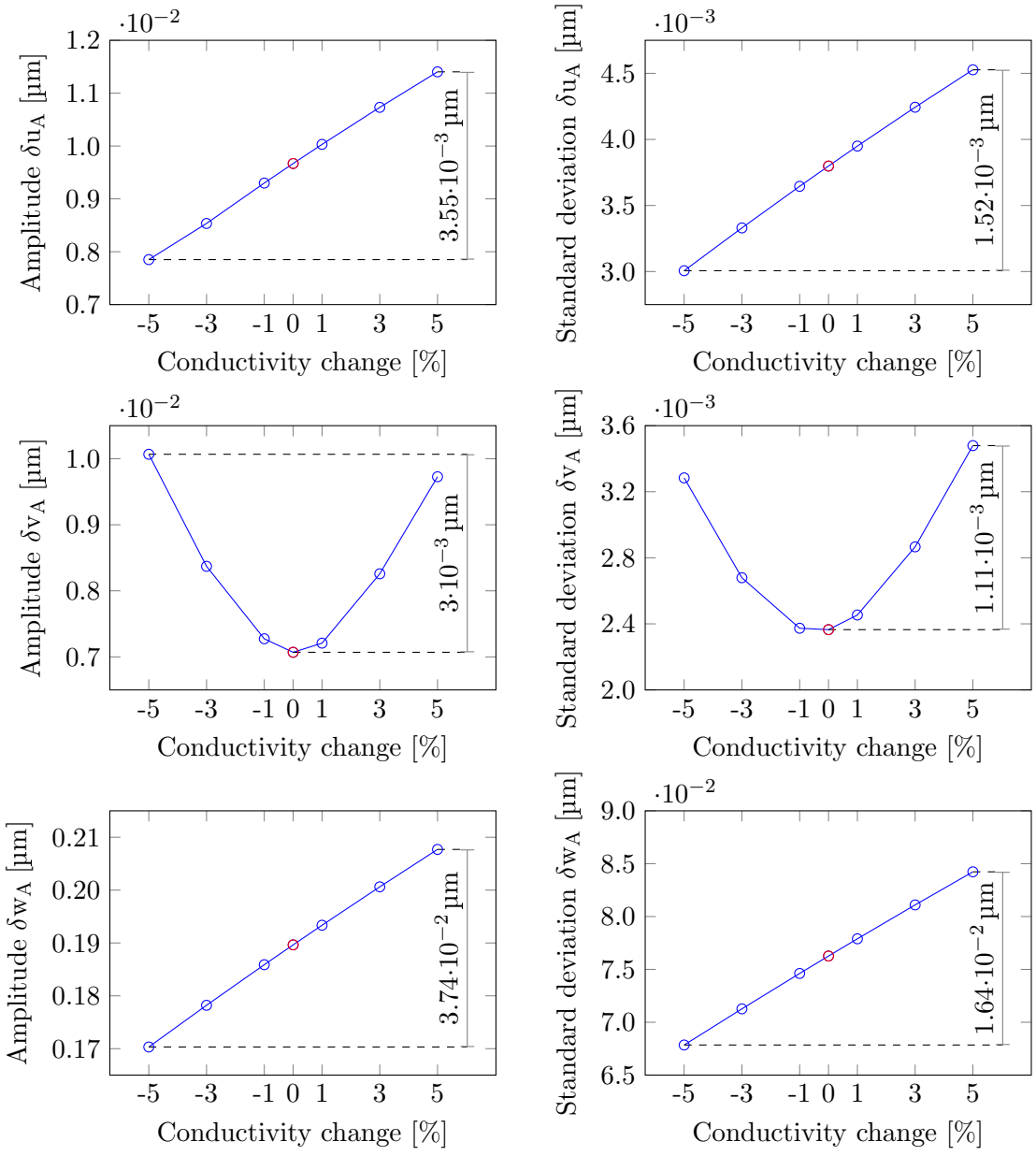

Figure 6.25: Maximum amplitude and standard deviation of the displacement at point A in each direction under different levels of uncertainty in the conductivity value.

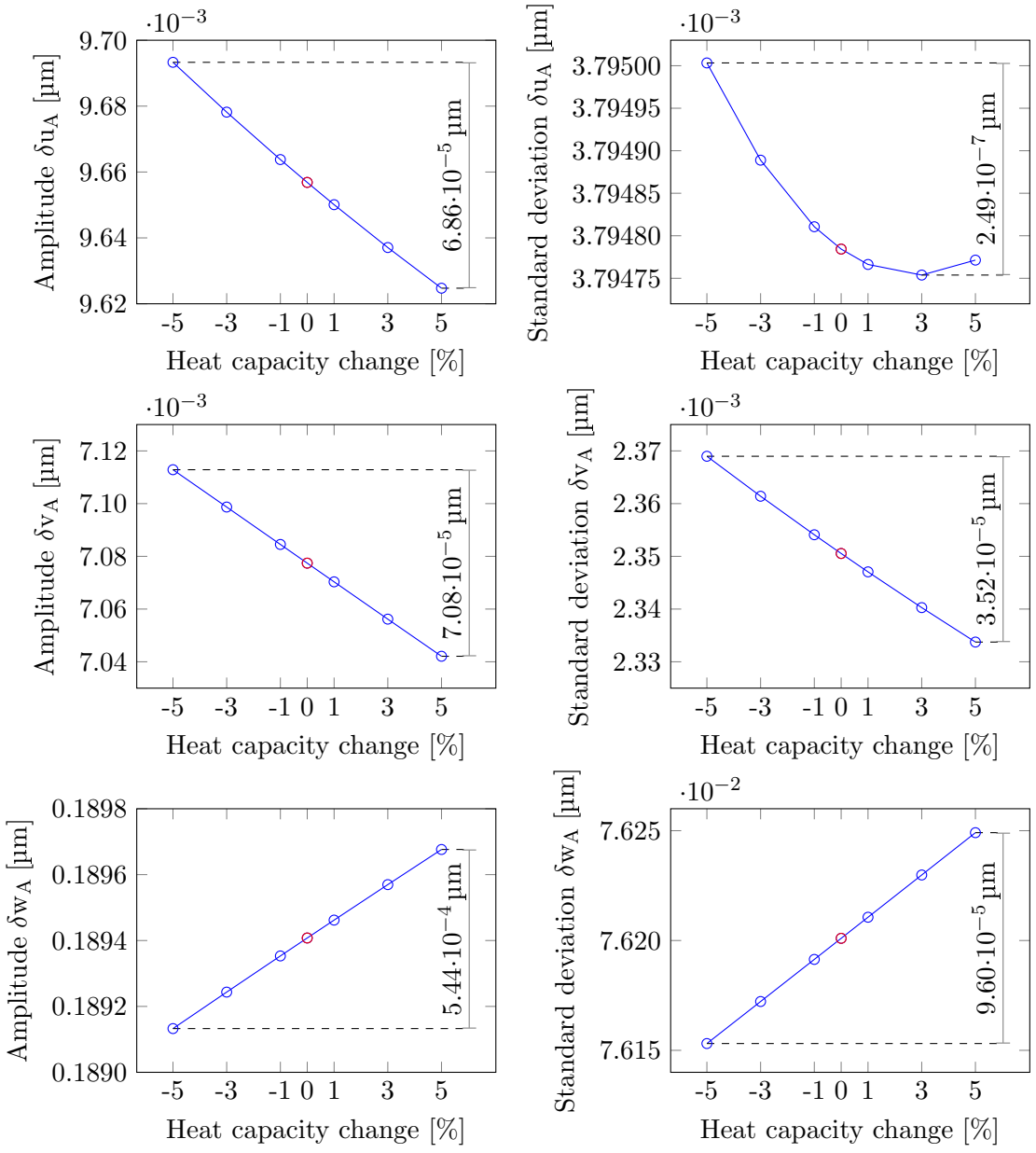

Figure 6.26: Maximum amplitude and standard deviation of the displacement at point A in each direction under different levels of uncertainty in the heat capacity value.

Another variable that determines the thermal behavior of the structure is the emissivity of its surfaces. This property plays a direct role in the characterization of the radiation exchange with the environment and with the other surfaces. Thus, if there is a difference between the assumed and the actual value, the equilibrium state estimated by the thermomechanical model will slightly differ from the actual one. As a result, the transfer functions will be linearized around a slightly biased value which, in turn, affects the gains in the control loop. Also, the expected radiation exchange will be underestimated or overestimated depending on the direction of the uncertainty.

The performance results obtained for the six considered cases are represented in Figure 6.27. The first important fact, regardless of the specific relation between uncertainty and performance, is that the expected changes in performance induced by emissivity uncertainty have also very low magnitudes and only exceed 0.001 µm in the z-direction. As it is the case for the heat capacity uncertainties, in this particular case the performance changes introduced by emissivity uncertainties could also be neglected for any practical purposes. As can be observed in Figure 6.27, the relations in all directions can be approximated as linear within the considered range. The relation is positive in the x and z direction and negative in the y-direction, both in the amplitude and in the standard deviation case. The percentage values included in Tables 6.10 and 6.11 show that the influence of the emissivity is slightly higher than the influence of the heat capacity, but much lower than the thermal conductivity.

The last property studied in this subsection is the density. As aforementioned, this variable has also an influence on the mechanical behavior of the structure. However, when the structural behavior can be approximated as quasi-static this influence becomes negligible. In terms of the thermal behavior, the material density affects the thermal capacity matrix in the same way as the heat capacity does. This can be deduced from the expression of the thermal capacity matrix, expressed in Equation 3.36 on page 39. This equation contains the product between density and heat capacity. Thus, whether there is a percentage change in the density or in the heat capacity, the final result is the same. As a consequence, it can be expected that any uncertainty in material density will have exactly the same final effect that the same uncertainty in terms of the heat capacity would have.

The simulations have been conducted to prove that an uncertainty in density is equivalent to an uncertainty in heat capacity. The results are illustrated in Figure 6.28 and, as expected, exactly the same behavior represented in Figure 6.26, i.e. for the heat capacity case, is obtained. Thus, it can also be concluded that any uncertainty in the actual density value contained within ±5% can be considered negligible for the baseline case. For the sake of consistency, the percentage changes for this case have also been included in Tables 6.10 and 6.11 even though they are essentially the same as for the heat capacity case.

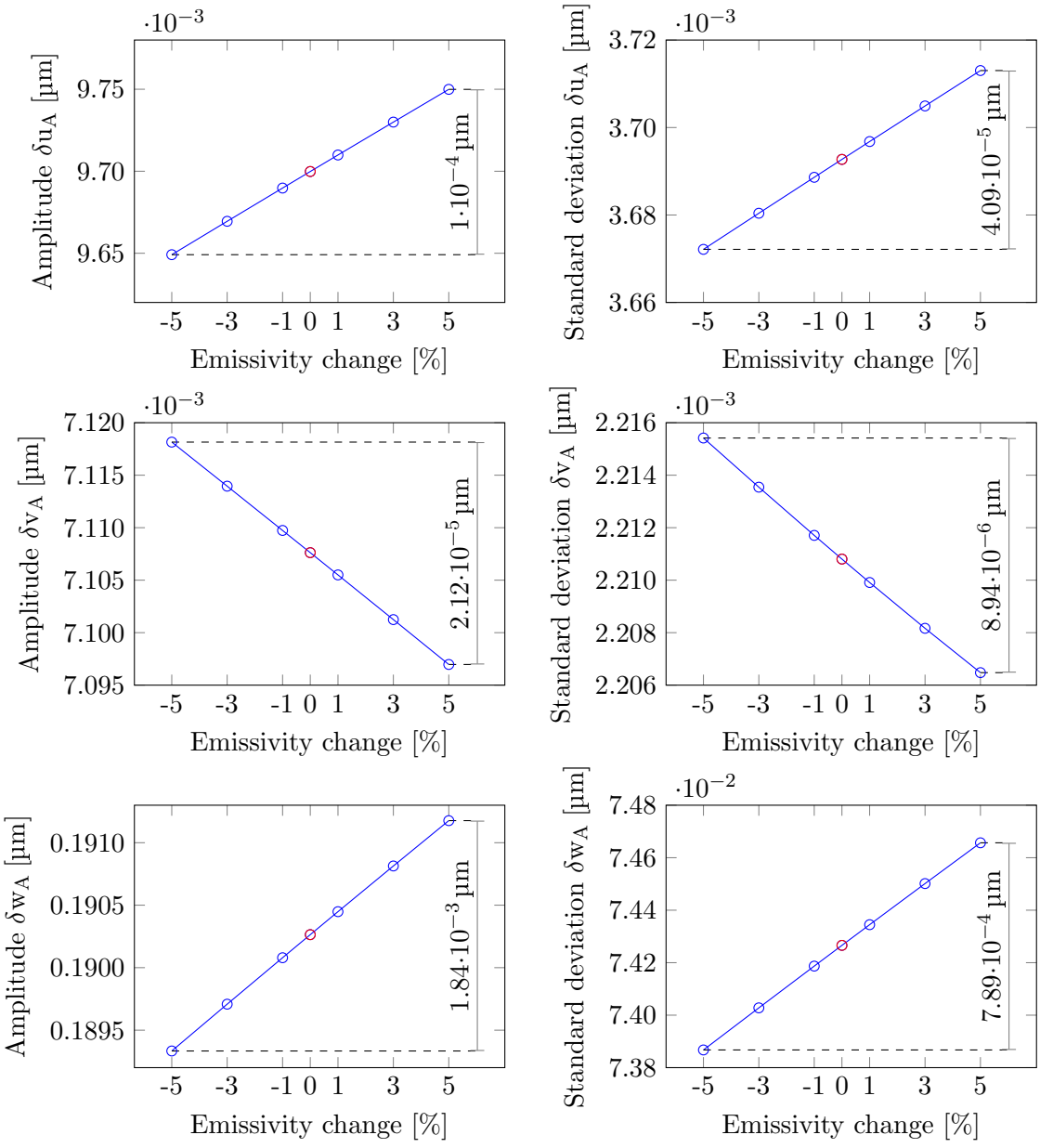

Figure 6.27: Maximum amplitude and standard deviation of the displacement at point A in each direction under different levels of uncertainty in the emissivity value.

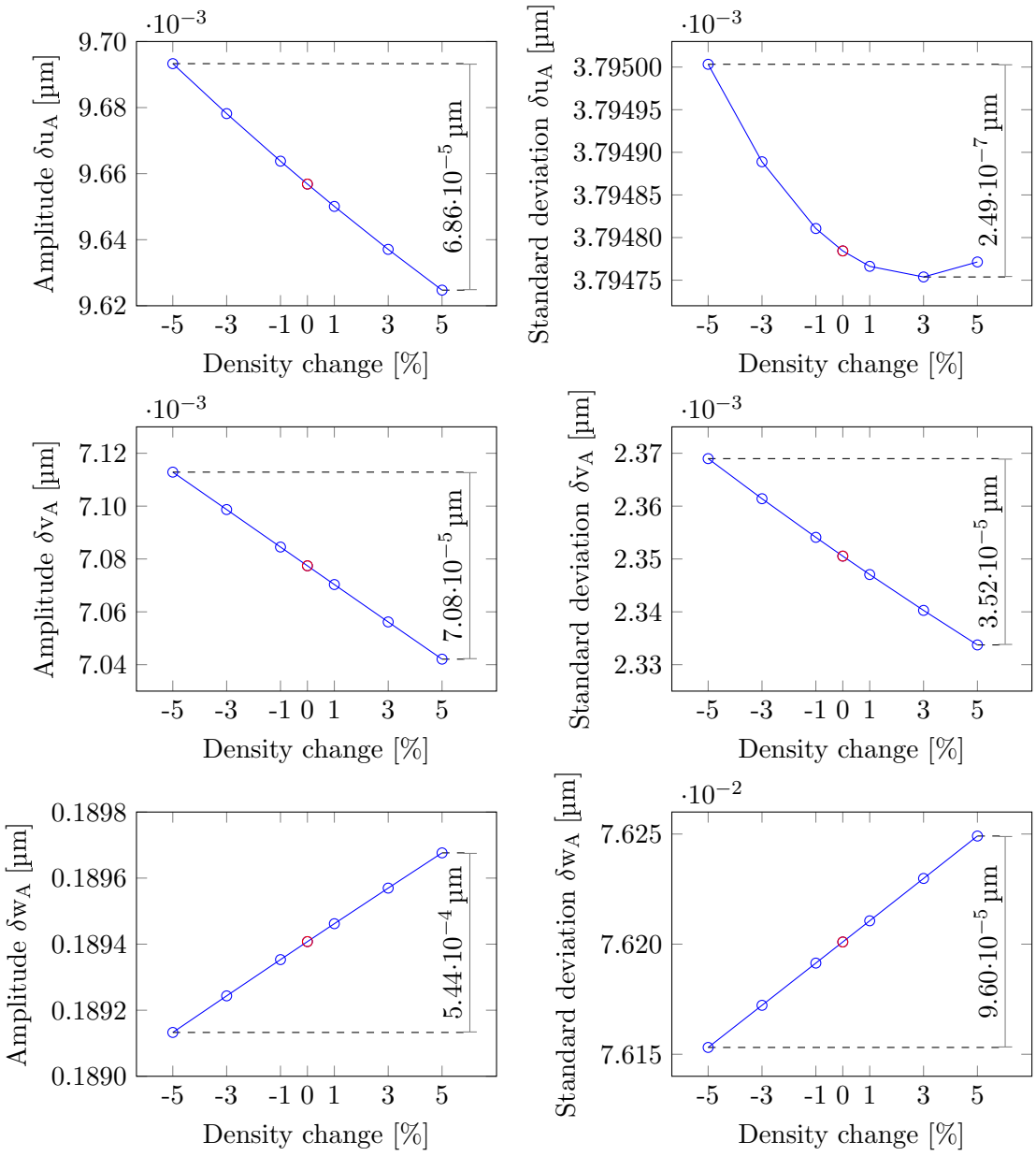

Figure 6.28: Maximum amplitude and standard deviation of the displacement at point A in each direction under different levels of uncertainty in the density value.

6.5.2 Mechanical properties

The material properties that directly influence the mechanical response of the structure are the Young's modulus E, the Poisson's ratio ν and the coefficient of thermal expansion (CTE) α. Both the Young's modulus and the Poisson's ratio influence the finite element model through the definition of the elasticity matrix. This is calculated according to Equation 4.8 on page 57. The relation between these two variables and the elasticity matrix is different and thus, its influence on the achieved performance will also differ.

First, the influence of the uncertainty in the Young's modulus is assessed. The performance under the six considered levels of uncertainty between ±5% is calculated. The results, presented in Figure 6.29 show that the relation between the uncertainty and the performance change is strongly linear, at least in the considered range. The relation is negative in the x and y directions and positive for the z-direction case. In absolute terms, the expected changes introduced due to this uncertainty are very small, always significantly below 0.01 µm. The maximum change in amplitude takes place in the z-direction, where the difference between the two extreme cases reaches approximately 0.003 µm. In comparison to the previously analyzed material properties, the uncertainty in the Young's modulus can introduce some of the largest changes in the achieved performance, reaching levels similar to those introduced by the uncertainty in the thermal conductivity, particularly in the x-direction. This can be corroborated by the percentage changes included in Tables 6.10 and 6.11. In the extreme cases of uncertainties of ±5% the change in the maximum amplitude in the x-direction reaches approximately 12%. As aforementioned, in absolute terms these changes are within the nanometer range.

The same analysis is performed for the uncertainty in the Poisson's ratio and the results are presented in Figure 6.30. In terms of the maximum amplitude, the relation between uncertainty and performance is observed to be also strongly linear. The magnitude of the introduced changes is smaller than for the Young's modulus case. Only in the z-direction the expected changes in amplitude reach a similar magnitude as in the Young's modulus case, with a difference between the extreme cases around 0.003 µm. Performance changes are also observed in the standard deviation values but they never exceed 0.001 µm between the nominal and an extreme case. A curious behavior is observed in the y-direction, in which the amplitude change has a linear relation to the uncertainty, but the standard deviation changes evolve parabolically. Given the extremely low magnitude of the changes in the standard deviation (i.e. below 10^{-10} m) it cannot be discarded that this result is just a consequence of rounding errors in the simulation process. Considering the negligible relevance of this result for any practictal purposes, the reason for this behavior has not been further analyzed.

The last property that influences the mechanical response is the CTE. This variable is introduced in the mechanical model through the mechanical load vector, as expressed by Equation 4.11 on page 57. The CTE is essential to estimate the strain introduced in the structure due to thermal fluctuations. Thus, an uncertainty in its value can result in an overestimation or underestimation of the introduced strains and, in turn, in the displacements. The obtained results for the six considered cases are presented in Figure 6.31. The induced amplitude changes between the extreme

cases only exceed 0.001 µm in the x and z directions. Considering the difference between the nominal condition, i.e. no uncertainty, and the extreme cases of ±5%, the 0.001 µm value is never exceeded. In terms of the standard deviation, the changes are even lower and negligible for any practical purposes. It can be seen from the percentage values in Tables 6.10 and 6.11 on pages 134 and 135 that the uncertainty in the CTE value never introduces changes in the performance above 10%. Its influence appears to be generally lower than the one introduced by the uncertainty in the Young's modulus and slightly higher than the introduced by the Poisson's ratio.

Overall, it can be concluded from the presented analyses that uncertainty in the material properties has a very limited effect on the achieved performance. Only in the case of large uncertainties in the thermal conductivity there could be some relevant changes in the achieved performance, particularly in terms of the amplitude of the response. In any case, the introduced changes in absolute terms would be in the nanometer range.

It could be argued that largest deviations would be seen in reality when all these uncertainties act simultaneously. However, it is also true that different properties affect the performance in different ways and thus, uncertainties in one property may be partially compensated by uncertainties in another. If in some particular cases a strong discrepancy is observed between the modeled behavior and the actual behavior, it would be possible to calibrate the thermomechanical model to partially reduce this difference and provide a better characterization.

Even though the influence of the material uncertainty has been proved to be very limited, this sensitivity analysis provides also some insight into possible optimization approaches that could improve the achieved stability level. A crucial step in achieving high mechanical stability consists in selecting materials that have the adequate physical properties for the considered application. This selection must be performed on a case-by-case basis and it always depends on the geometry of the structure and the expected perturbations. Considering that this first selection step has been performed, the procedure conducted in this section indicates in which direction the properties should vary to further improve the stability in some particular metrics. However, it is important to note that the displacements in each direction can be affected differently by a change in a particular material property. Thus, changing the material can improve the stability in one metric and decrease it in another. Additionally, the material properties are not distributed in a continuous space and introducing changes in materials to modify one particular property may result also in a modification on another property. Despite these potential setbacks, this sensitivity analysis can still be a starting point to further optimize the achieved stability.

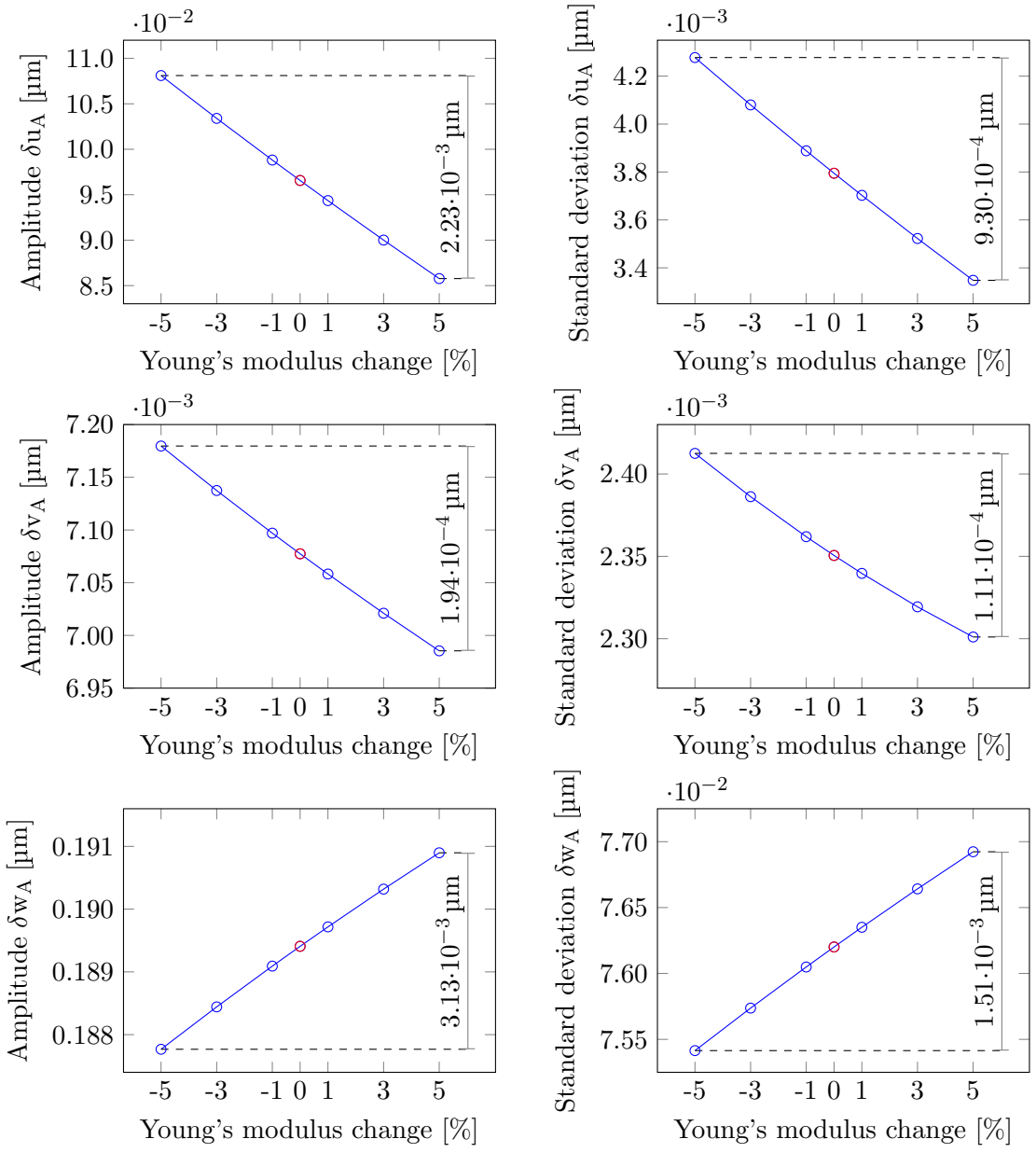

Figure 6.29: Maximum amplitude and standard deviation of the displacement at point A in each direction under different levels of uncertainty in the Young's modulus value.

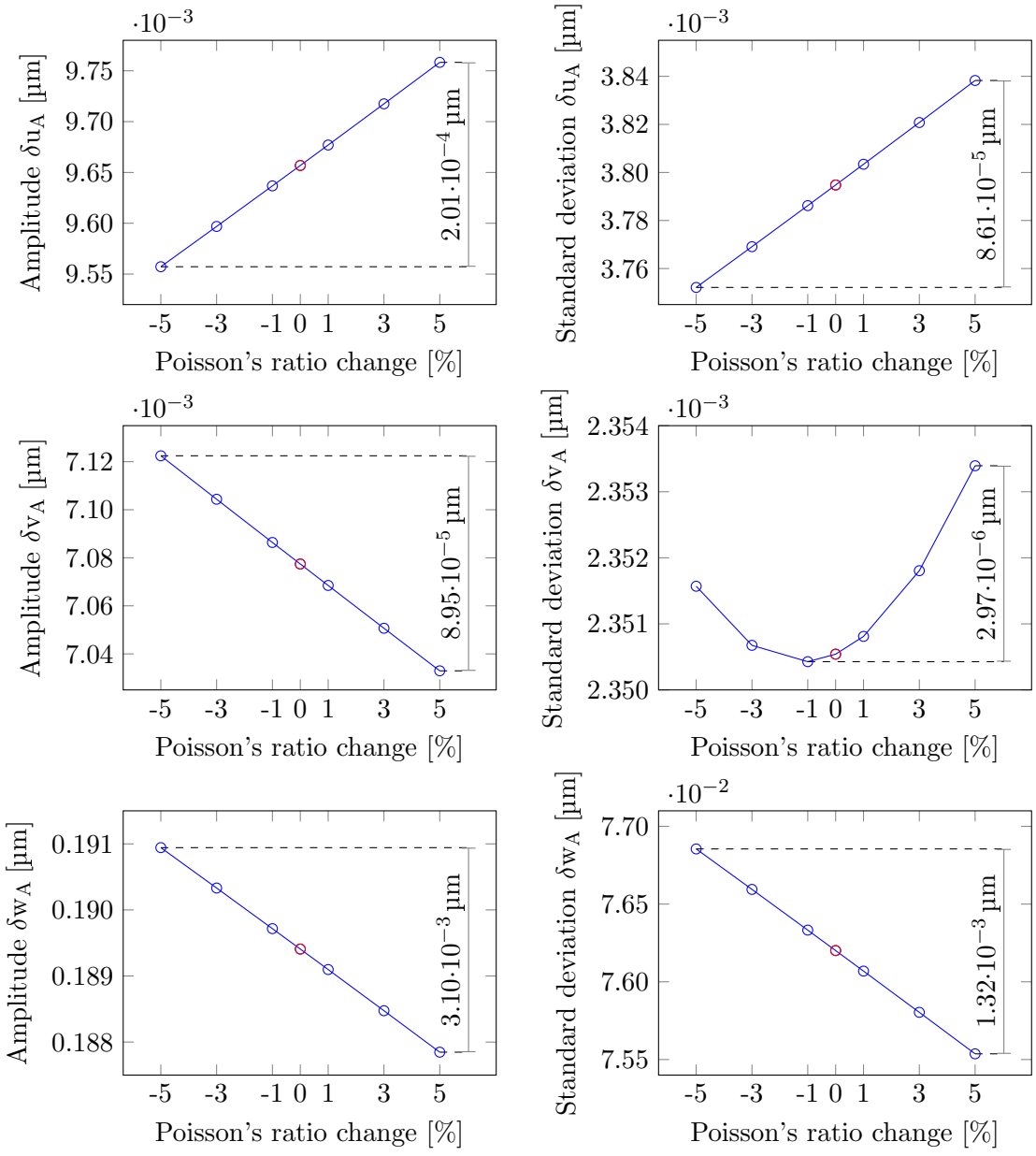

Figure 6.30: Maximum amplitude and standard deviation of the displacement at point A in each direction under different levels of uncertainty in the Poisson's ratio value.

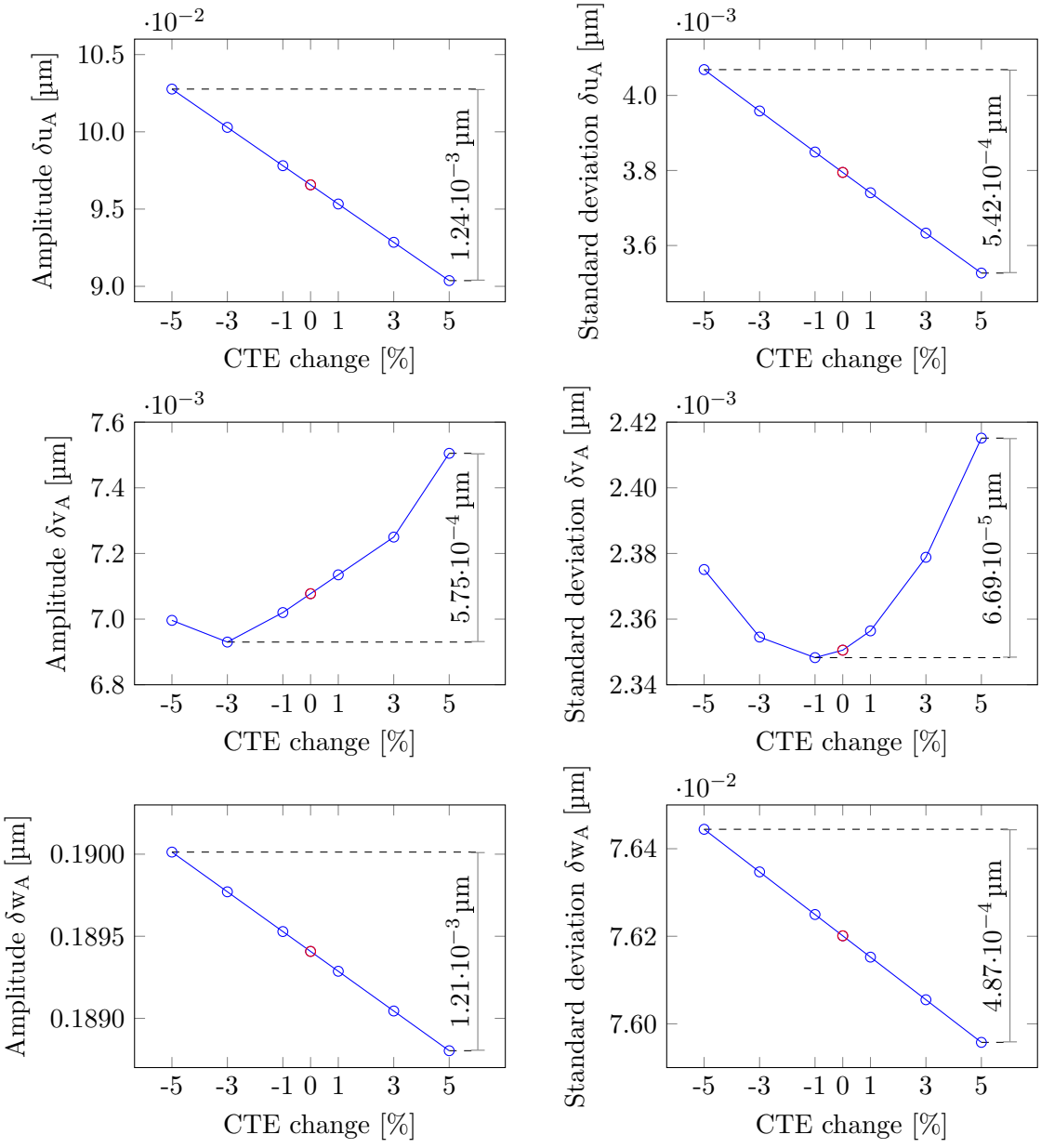

Figure 6.31: Maximum amplitude and standard deviation of the displacement at point A in each direction under different levels of uncertainty in the coefficient of thermal expansion value.

Maximum amplitude							
Direction	Property	-5%	-3%	-1%	1%	3%	5%
x	λ	-18.80%	-11.72%	-3.82%	3.74%	10.99%	17.94%
	c_p	0.38%	0.22%	0.07%	-0.07%	-0.20%	-0.33%
	ε	-0.52%	-0.31%	-0.10%	0.10%	0.31%	0.52%
	ρ	0.38%	0.22%	0.07%	-0.07%	-0.20%	0.33%
	E	11.95%	7.07%	2.33%	-2.29%	-6.79%	-11.18%
	ν	1.03%	-0.62%	-0.21%	0.21%	0.63%	1.05%
	α	6.42%	3.85%	1.28%	-1.28%	-3.85%	-6.42%
y	λ	42.40%	18.41%	2.89%	1.96%	16.81%	37.59%
	c_p	0.50%	0.30%	0.10%	-0.10%	-0.30%	-0.50%
	ε	0.15%	0.09%	0.03%	-0.03%	-0.09%	-0.15%
	ρ	0.50%	0.30%	0.10%	-0.10%	-0.30%	-0.50%
	E	1.44%	0.85%	0.28%	-0.27%	-0.80%	-1.30%
	ν	0.64%	0.38%	0.13%	-0.13%	-0.37%	-0.63%
	α	-1.15%	-2.08%	-0.81%	0.81%	2.44%	6.04%
z	λ	-10.19%	-6.02%	-1.98%	1.96%	5.79%	9.52%
	c_p	-0.15%	-0.09%	-0.03%	0.03%	0.09%	0.14%
	ε	-0.49%	-0.29%	-0.10%	0.10%	0.29%	0.48%
	ρ	-0.15%	-0.09%	-0.03%	0.03%	0.09%	0.14%
	E	-0.87%	-0.51%	-0.17%	0.16%	0.48%	0.79%
	ν	0.81%	0.49%	0.16%	-0.16%	-0.49%	-0.82%
	α	0.32%	0.19%	0.06%	-0.06%	-0.19%	-0.32%

Table 6.10: Percentage change in terms of the maximum amplitude of displacements at point A under different levels of uncertainty in the material properties.

Standard deviation							
Direction	Property	-5%	-3%	-1%	1%	3%	5%
x	λ	-20.86%	-12.33%	-4.04%	3.98%	11.72%	19.18%
	c_p	0.01%	<0.01%	<0.01%	<0.01%	<0.01%	<0.01%
	ε	-0.55%	-0.33%	-0.11%	0.11%	0.33%	0.55%
	ρ	0.01%	<0.01%	<0.01%	<0.01%	<0.01%	<0.01%
	E	12.73%	7.52%	2.47%	-2.43%	-7.18%	-11.78%
	ν	-1.12%	-0.68%	-0.23%	0.23%	0.68%	1.15%
	α	7.22%	4.32%	1.43%	-1.43%	-4.26%	-7.07%
y	λ	38.85%	13.29%	0.36%	3.75%	21.20%	47.12%
	c_p	0.78%	0.46%	0.15%	-0.15%	-0.44%	-0.71%
	ε	-0.16%	-0.10%	-0.03%	0.03%	0.10%	0.18%
	ρ	0.78%	0.46%	0.15%	-0.15%	-0.43%	-0.71%
	E	2.64%	1.52%	0.48%	-0.46%	-1.33%	-2.11%
	ν	0.04%	0.01%	<0.01%	0.01%	0.05%	0.12%
	α	1.04%	0.17%	-0.10%	0.25%	1.20%	2.75%
z	λ	-11.03%	-6.55%	-2.16%	2.14%	6.34%	10.45%
	c_p	-0.06%	-0.04%	-0.01%	0.01%	0.04%	0.06%
	ε	-0.54%	-0.32%	-0.11%	0.11%	0.32%	0.53%
	ρ	-0.06%	-0.04%	-0.01%	0.01%	0.04%	0.06%
	E	-1.03%	-0.61%	-0.20%	0.20%	0.58%	0.95%
	ν	0.86%	0.52%	0.17%	-0.17%	-0.52%	-0.87%
	α	0.32%	0.19%	0.06%	-0.06%	-0.19%	-0.32%

Table 6.11: Percentage change in terms of the standard deviation of displacements at point A under different levels of uncertainty in the material properties.

Chapter 7

Conclusions

This final chapter presents the main conclusions that can be extracted from the presented control framework in combination with the simulated results. Subsequently, the chapter ends with an evaluation of those aspects that could be further investigated and that conform the possibilities and recommendations for future work.

7.1 Thesis Summary and Conclusions

As presented in the introduction of this thesis, the main goal of the present work has been to develop a novel active control framework to compensate distortions that may arise in space structures due to low-frequency thermal perturbations. Based on the obtained simulated results it can be concluded that the fundamentals for a promising control technique to compensate this type of distortions have been established.

The first part of the thesis is centered on the development of a proper thermomechanical model on top of which the control framework can be built. In this regard, it has been concluded that the best option is to base this model on the finite element method (FEM) because, at this stage, this facilitates the interface between the thermal and the mechanical model.

One important condition that determines the thermal behavior of any structure is the heat exchange through radiation. This is especially important in the case of space structures because they are not affected by heat exchange through convection, and thus the radiation exchange becomes more significant in relative terms. The radiation exchange makes the thermal problem nonlinear and, therefore, a linearization approach has been implemented to enable the calculation of linear transfer functions between heat and temperature. This linearization can become a source of errors if the experienced thermal fluctuations are large enough. The effect of this linearization has been assessed for a baseline case in which thermal fluctuations up to 1 K take place. This has shown that the contribution of the linearization to an eventual performance decrease is negligible. Generally, structures that are used for high precision applications are already designed to operate in a relatively quiet environment. Thus, it is expected that large thermal fluctuations are not present and that the linear approximation is valid. As presented in this thesis, this assump-

tion can be checked on a case-by-case basis to ensure that no significant errors are introduced in the control process.

The linearization of the radiation terms enables the calculation of transfer functions between heat and temperature as a function of the frequency. This approach has been shown to be an alternative to the traditional time-integration procedure to solve transient thermal problems. With this novel approach, based on a frequency-domain transformation, it is possible to calculate the time evolution of the displacement field in a more computationally efficient way given that it only requires the multiplication of the input function, i.e. defining the heat evolution, by the corresponding transfer function. The limitation of this approach is that it does not directly provide the solution of the transient terms that define the response, which correspond to exponential terms that converge to zero. The multiplication between transfer function and input function provides only the stationary evolution of the problem expressed as complex numbers, which represents the thermal fluctuation at each node in the finite element mesh.

Based also on the FEM, the mechanical analysis framework has been presented. The mechanical problem can also be solved in the frequency-domain, as it is normally done in the field of structural dynamics to analyze, for instance, the impact of vibrational loads. This approach enables the calculation of transfer functions, which in this case provide the relation between temperature fluctuations and displacements. By combining these functions with those obtained from the thermal problem it is finally possible to obtain thermomechanical transfer functions that directly relate heat input and displacement.

The mechanical analysis in the frequency domain has also illustrated that the inertial and damping terms that generally influence the mechanical response are only relevant at high-frequencies, understood as those above approximately 1 Hz. Thus, below this threshold it is generally acceptable to treat the problem as quasi-static. A similar behavior can be observed in the thermal problem, which behaves as a low-pass filter with a quasi-static behavior at low-frequencies and a turning point between 10^{-5} Hz and 10^{-3} Hz, depending on the specific conditions of the problem. It is concluded from the combination between the thermal and the mechanical problem that, generally, the inertial and damping effects are negligible as long as the perturbation has a thermal origin. These terms would not be negligible only if there were relevant heat perturbations at frequencies around or above 1 Hz. This is generally not possible because it would imply high-amplitude perturbations at unrealistic levels given the low transfer gain of the thermal problem at these frequencies. The validity of the quasi-static assumption has been checked for the baseline case presented throughout this thesis, proving that the inertial and damping terms have by a wide margin a negligible contribution to the mechanical response.

The calculation of transfer functions between heat and displacement based on the finite element thermomechanical model is one of the key aspects to develop the control framework. The strategy followed in the presented method consists in applying the appropriate heat to the structure that compensates some particular displacement measure induced by acting perturbations. This appropriate heat is in turn calculated through the transfer functions and applied by heaters mounted in the structure.

The most favorable case is that in which acting perturbations can be fully characterized and thus, can be predicted before they act on the structure. Under these circumstances it has been concluded that a virtually perfect compensation can be achieved. In other words, the displacement at one point induced by a heat perturbation acting in any point of the structure can be theoretically fully compensated by a control heater installed at any other point of the structure. Generally, heat perturbations are to a certain extent random and, as a consequence, cannot be known before they appear. Thus, a strategy to estimate the distortions induced by random perturbations has been developed, which is a requirement to subsequently calculate control inputs that compensate them.

The approach followed in this thesis has been to estimate the displacement field in real-time based on the thermomechanical model that relates displacement and temperatures. This requires, in turn, an estimation of the temperature field which is obtained based on the combination of the thermal model with sensor measurements. The followed strategy to estimate the thermal field is analogous to that followed in the structural dynamics field to measure the displacement response of structures. This consists in the assumption of a simplified thermal model that describes the temperature field only in terms of the most important linearized thermal modes, which correspond to the eigenvectors of the linearized conductivity matrix. This process is known as modal truncation and, at the expense of introducing an estimation error, enables the estimation of the thermal field based on a limited number of temperature sensors. In the presented example, the thermal field described by 1063 thermal nodes has been estimated based only on the measurements of 20 sensors. The analysis of the modal representation shows that this estimation is always more accurate at lower frequencies and thus, the temperature fluctuations induced by high-frequency perturbations are estimated with larger errors.

A critical factor to properly implement the modal truncation process is to know the origin of the expected perturbations. This does not mean that it is required to know how the perturbations evolve temporally, but it is necessary to know where in the structure they are applied. This is essential because it allows the identification of the thermal modes that carry the largest weight in describing the thermal response and that should, therefore, be included in the truncated model. Hence, a strong effort should be put during the development phase of the structure to thoroughly identify all the possible heat perturbation sources that may act on the structure. This will enable the selection of the relevant thermal modes and, as a consequence, the identification of optimal positions where temperature sensors should be placed.

The estimation of the displacement field is essential to assess whether the applied control is successfully counteracting distortions. The objective of the control strategy is to control some specific measures of the displacement field, which are expressed in terms of the displacement in some specific directions at some specific nodes. The controller used in this thesis applies a proportional control based on the linear quadratic regulator theory. In mathematical terms, this results in a control input calculated from the multiplication of a gain matrix by the temperature vector. In order to enable the displacement control through this strategy it is necessary to equip the structure with one heater for each degree of freedom that is controlled. The control input can be theoretically applied at any point in the structure. However, this is not the case in practice because the control from some particular regions

would result in an unrealistic required amount of heat. Additionally, there will exist limitations due to the presence of other equipment and design requirements. Thus, only some areas in the structure will be available to allocate the heaters. A selection of the exact locations to place the heaters can be based on an optimization of the transfer gains calculated from the thermomechanical transfer functions. Based on this procedure, it is possible to identify the locations that under some assumed conditions minimize the required input power. Optimizations in terms of other variables aside from control power are also possible.

The control performance that can be achieved based on the presented sensor and heater strategies has been simulated for a highly stable structure. This structure has been assumed to be made out of silicon carbide, which with a very low coefficient of thermal expansion can provide passively a highly stable behavior. The simulated results show that the control framework significantly improves the level of dimensional stability with respect to the passive response. This result has two important implications. Firstly, it is concluded that the presented framework enables levels of stability beyond what is passively possible. Secondly, the same control framework can also be implemented in structures that do not have a particularly stable passive behavior to attain a high level of dimensional stability. Thus, the presented technology has the potential to significantly simplify the current development efforts that are required to produce highly stable structures.

This higher level of stability, in relation to the passive approach, is achieved despite the fact that several non-ideal conditions exist. The most important factors defining these conditions are the uncertainties in the behavior of sensors and actuators. Different cases have been simulated to assess the impact of these uncertainties.

There are two aspects related to the sensor characteristics that decrease the achieved level of stability. One is the fact that only a limited number of sensor measurements is available given that it is unfeasible to equip the structure with as many sensors as nodes in the model, which would easily result in thousands of sensors. The other aspect is related to the uncertainty in the measurements. Temperature sensors are inherently inaccurate and can only provide measurements within a given range of accuracy.

The thermal field reconstruction based on the modal representation has been proved to provide highly accurate estimations, which means that the fact that only a few measurements are available does not significantly decrease the achieved performance. Conversely, from the simulated cases it is concluded that the largest contributor to the performance decrease is the noise in the measurements. If a different bias exists at each sensor, an offset in the control output appears, which means that the displacement is not stabilized exactly around the initial equilibrium point. The remaining fluctuations in the stabilized displacements are concluded to be mostly a result of the noise in the sensors. Thus, it is expected that if higher-performance temperature sensors are developed it will be possible to achieve higher levels of stability with exactly the same method.

The decrease in performance that appears due to the sensor noise is partially attenuated by implementing a Kalman filter. This provides a more smooth estimation of the temperature fluctuations and a higher level of stabilization in the displacement output.

The uncertainty in the actuator behavior is assumed to be characterized by a linear relation between the commanded signals and the applied signals. The factors relating both signals are assumed to be random following a known normal distribution. Based on this assumption, the applied control heat is slightly different from the required heat input provided by the controller. The performance decrease arising from this disparity has been shown to be smaller than that induced by the noise in the sensors, which is identified as the largest contributor to the performance decrease.

An additional factor that can impact the achieved performance is the thermal and mechanical coupling between the stabilized structure and the rest of the spacecraft structure. If both structures are strongly coupled, any thermal fluctuation at some point in the spacecraft can translate into a distortion in the stabilized structure. If this fluctuation is measured at the vicinity of its origin it is feasible to compensate it through the implemented control setup. However, if it is only measured through sensors mounted in the stabilized structure, there will be a higher level of uncertainty introduced in the estimation and thus, a suboptimal level of achieved stability. To attenuate these effects there are two options. One is to mount temperature sensors outside of the stabilized structure to accurately measure the fluctuations induced by external perturbations. The other is to minimize the thermomechanical coupling between the stabilized structure and the spacecraft structure. A combination of both strategies is also possible and the adequate compromise should be found depending on the particularities of each case.

It has also been assessed whether the uncertainty in the material properties can affect the achieved performance at a relevant level. It has been concluded from this study that, at least in the baseline case, any uncertainty in the material properties at a reasonable level does not introduce relevant changes in the achieved performance. Among all the physical properties that determine the thermomechanical response of the structure, the uncertainties in thermal conductivity appear to be the ones with the largest potential to influence the achieved performance.

The results achieved by the presented control framework have been presented for a scenario in which a particular point of the structure is stabilized with respect to an external reference frame. The option of stabilizing two different points of the structure with respect to one another has also been evaluated resulting also in a high level of dimensional stability. More complex cases can be implemented following the same steps, with the only requirement of installing the necessary number of heaters.

It is also possible to expand the presented framework to take into account other effects such as heat exchange through convection. With the appropriate changes it would also be possible to develop a fully non-intrusive control setup which would require estimating the thermal field through external sources, such as infrared cameras, and applied heat through external radiation sources. A discussion on these two aspects is presented in more detail in the next section which presents recommendations for future work.

7.2 Recommendations for Future Work

The presented work has tackled the main theoretical aspects that enable structural stabilization based on the application of heat. The main conclusions of the work have been that this control framework is theoretically feasible, which implies that no insurmountable technical difficulties have been identified. Nevertheless, considering that the next logical step consists in developing a physical demonstration of this control framework that fully proves the feasibility of this approach, it is important to make some comments on some theoretical aspects that could be further investigated and some recommendations for the work ahead.

One of the first steps that will have to be conducted when implementing this control framework will be the development of the thermomechanical model of the structure to be controlled. This includes not only the finite element representation, as done in this work, but also a proper validation of the model with respect to the real structure. This requires the definition of correlation procedures and the introduction of correction factors to ensure that the finite element model represents within an acceptable tolerance the behavior of the real structure.

Additionally, given that the implementation will be tested on ground, it will be necessary to expand the current thermal model to include the boundary condition related to the heat exchange through convection. The simplest option would consist in performing the tests under an environment of forced convection, which could be modeled using a linear model. Consequently, no further linearization would be required and only a slight modification of the heat exchange equation would be necessary. It is also important to mention that this step could be avoided if said tests were performed in a vacuum chamber.

The controller presented in this thesis is based on the linear quadratic regulator theory which provides a systematic approach to calculate a matrix of proportional gains. This controller has been implemented in combination with a Kalman filter and a thermal modal expansion. The results obtained from simulations illustrate that a significant improvement in the achieved dimensional stability can be achieved through this method. However, it should not be discarded that even better performances could potentially be achieved with other control approaches. Several aspects in the presented framework could be investigated in more detail to assess whether better strategies exist.

One first aspect is related to the locations of the control heaters. In the presented thesis, their locations have been identified based only on the gain of the transfer functions. This approach is straightforward when only one degree of freedom in the structure needs to be controlled. As the number of degrees of freedom to be controlled increases, and also perturbations from different sources are present, the locations identified by this approach become suboptimal. A more general procedure should be developed to identify optimal heater locations based on the knowledge of some perturbation characteristics and the degrees of freedom that are to be controlled. One possibility is to base this identification on a set of numerical simulations that test different possible configurations to find the most favorable heater locations that optimize specific variables.

Another theoretical aspect that could be investigated is the derivation of the control laws. As aforementioned, the presented controller is based on the linear quadratic regulator procedure and considering applied heat as the input variable. The control is based in modifying the temperature field in such a way that distortions are minimized at some particular points. There exist alternatives to this approach that would modify the obtained results, potentially for the better. One option is to derive the controller based on another multi-input multi-output approach (e.g. PID or H_∞). Also, according to the presented approach it is necessary to equip the structure with as many heaters as controlled degrees of freedom. It could also be interesting to develop a control framework based on a lower number of heaters. Instead of controlling each degree of freedom individually, this could be based on minimizing a global metric defined from the displacements at the controlled nodes. The stability achieved at each controlled node individually would, in principle, be lower than the one presented in this work. However, it is possible that it could still meet some predefined stability requirements and, more importantly, it would result in a simpler setup given that it would require less heaters.

Another aspect around which there is potentially margin for improvement is in the noise filtering process. The implemented Kalman filter has proved essential to filter the noise in the sensors and to provide an accurate estimation of the thermal field, which is required to derive the control inputs. However, under some circumstances part of the noise in the sensors is not fully filtered and it is transmitted to the control signals. This can be problematic above a certain level of noise because it results in a noisy control signal that the actuators may not be able to reproduce. Some investigations should be conducted to minimize this effect. A possible option is to implement more advanced filters or to introduce an additional filter layer at the control signal level.

It is also worth mentioning that the presented control framework could be expanded to compensate distortions that have a purely mechanical origin, i.e. those that do not originate from thermal fluctuations. In the presented strategy, the displacement field is estimated from the thermal field, which in turn is estimated from temperature measurements. This has as a consequence that distortions induced by mechanical loads are not captured because they do not introduce temperature fluctuations. However, if they were measured using another mechanism it would still be possible to compensate them through controlled heat. The measurement of these purely mechanical distortions would require equipping the structures with additional sensors, such as displacement or strain sensors at some specific locations. Even in those cases where distortions had purely a thermal origin, the presence of these additional sensors could be helpful to refine the displacement estimation obtained from the thermal field. This expanded approach would be useful to counteract distortions introduced by low-frequency mechanical perturbations or even permanent deformations to a certain extent. However, it would not be a valid approach to compensate high-frequency perturbations. This ultimately depends on the transfer functions between displacement and temperature fluctuations, which have very low gain at high frequencies.

Considering that the practical feasibility of this concept is proved through experimental tests, it could subsequently be investigated whether the fully non-intrusive option is also practically feasible. This strategy has been shortly described in Chap-

ter 5 and it consists in using an infrared camera as a temperature sensor and radiation sources to apply the control heat. As a result, no direct contact with the structure is required to control its distortions. The implementation of this approach would first require a reassessment of the radiation linearization. Given that in this case the radiation exchange would play a central role in the control strategy it is expected that a more accurate approach to model its nonlinearity would be necessary in order to achieve an acceptable level of performance.

References

[1] Preumont, A. *Vibration control of active structures. An Introduction.* Springer International Publishing, 2018. ISBN: 978-3-319-72295-5. DOI: 10.1007/978-3-319-72296-2.

[2] Laskin, R. A. and Sirlin, S. W. "Future payload isolation and pointing system technology." In: *Journal of Guidance, Control, and Dynamics* 9.4 (1986), pp. 469–477. DOI: 10.2514/3.20134.

[3] Ferrer, E., Buinhas, L. and Förstner, R. "System Design and Thermal Stability Analysis for the IRASSI Infrared Space Interferometer." In: *AIAA SPACE Forum 2016*. 2016. DOI: 10.2514/6.2016-5496.

[4] Bely, P. *The design and construction of large optical telescopes*. Springer-Verlag New York, 2003. ISBN: 978-0-387-95512-4. DOI: 10.1007/b97612.

[5] Spanos, J., Rahman, Z. and Blackwood, G. "A soft 6-axis active vibration isolator." In: *American Control Conference, Proceedings of the 1995, Seattle, Washington (USA), June 21-23, 1995*. Vol. 1. IEEE. 1995, pp. 412–416. DOI: 10.1109/ACC.1995.529280.

[6] Kamesh, D., Pandiyan, R. and Ghosal, A. "Modeling, design and analysis of low frequency platform for attenuating micro-vibration in spacecraft." In: *Journal of Sound and Vibration* 329.17 (Aug. 2010), pp. 3431–3450. DOI: 10.1016/j.jsv.2010.03.008.

[7] Tzou, H. S., Lee, H.-J. and Arnold, S. M. "Smart materials, precision sensors/actuators, smart structures, and structronic systems." In: *Mechanics of Advanced Materials and Structures* 11.4-5 (2004), pp. 367–393. DOI: 10.1080/15376490490451552.

[8] Irschik, H. "A review on static and dynamic shape control of structures by piezoelectric actuation." In: *Engineering Structures* 24.1 (Jan. 2002). Elsevier, pp. 5–11. DOI: 10.1016/S0141-0296(01)00081-5.

[9] Recktenwald, G. W. *Finite-Difference Approximations to the Heat Equation. Lecture Notes on Applied Computational Fluid Dynamics (ME 448)*. Portland State University. 2011. URL: http://web.cecs.pdx.edu/~gerry/class/ME448/code/docs/FDheat.pdf.

[10] Nikishkov, G. P. *Introduction to the finite element method. Lecture Notes.* University of Aizu, Japan. 2009.

[11] Barbagallo, G. and Stramaccioni, D. "Use of Spectral Analysis in Thermal Stability Verification." In: *32nd International Conference on Environmental Systems (ICES), San Antonio, Texas (USA), July 15-18, 2002. SAE Technical Paper*. SAE International, July 2002. DOI: 10.4271/2002-01-2373.

[12] Buinhas, L., Ferrer, E. and Förstner, R. "IRASSI InfraRed Space Interferometer: Mission Analysis, Spacecraft Design and Formation Flying Overview." In: *68th International Astronautical Congress (IAC), Adelaide, Australia , September 25-29, 2017*. International Astronautical Federation (IAF), Sept. 2017.

[13] Gaia Collaboration. "The Gaia mission." In: *Astronomy & Astrophysics* 595.A1 (2016). DOI: 10.1051/0004-6361/201629272.

[14] Lindegren, L., Babusiaux, C., Bailer-Jones, C., Bastian, U., Brown, A. G. A. et al. "The Gaia mission: science, organization and present status." In: *Proceedings of the International Astronomical Union* 3.S248 (2007). Cambridge University Press, pp. 217–223. DOI: 10.1017/S1743921308019133.

[15] Pilbratt, G. L., Riedinger, J. R., Passvogel, T., Crone, G., Doyle, D. et al. "Herschel Space Observatory - An ESA facility for far-infrared and submillimetre astronomy." In: *Astronomy & Astrophysics* 518.L1 (2010). EDP Sciences. DOI: 10.1051/0004-6361/201014759.

[16] Sánchez-Portal, M., Marston, A., Altieri, B., Aussel, H., Feuchtgruber, H. et al. "The pointing system of the Herschel space observatory." In: *Experimental Astronomy* 37.2 (2014). Springer, pp. 453–479. DOI: 10.1007/s10686-014-9396-z.

[17] European Space Agency. *ESA pointing error engineering handbook*. ESSB-HB-E-003. 2011. URL: http://peet.estec.esa.int/handbook/.

[18] Gardner, J. P., Mather, J. C., Clampin, M., Doyon, R., Greenhouse, M. A. et al. "The James Webb Space Telescope." In: *Space Science Reviews* 123.4 (2006). Springer, pp. 485–606. DOI: 10.1007/s11214-006-8315-7.

[19] National Aeronautics and Space Administration. *James Webb Space Telescope Project - Mission Requirements Document*. JWST-RQMT-000634. 2007.

[20] Meza, L., Tung, F., Anandakrishnan, S., Spector, V. and Hyde, T. "Line of sight stabilization of James Webb space telescope." In: *27th Annual AAS Guidance and Control Conference, Breckenridge (Colorado), February 5-9, 2005*. AAS Publications, 2005.

[21] Laureijs, R. J., Duvet, L., Sanz, I. E., Gondoin, P., Lumb, D. H. et al. "The Euclid Mission." In: *Proceedings of SPIE. Space Telescopes and Instrumentation 2010: Optical, Infared, and Millimeter Wave*. Vol. 7731, 77311H. 2010. DOI: 10.1117/12.857123.

[22] Racca, G. D., Laureijs, R., Stagnaro, L., Salvignol, J. C., Alvarez, J. L. et al. "The Euclid mission design." In: *Proceedings of SPIE. Space Telescopes and Instrumentation 2016: Optical, Infrared, and Millimeter Wave*. Vol. 99040O. 2016. DOI: 10.1117/12.2230762.

[23] Rauer, H., Catala, C., Aerts, C., Appourchaux, T., Benz, W. et al. "The PLATO 2.0 mission." In: *Experimental Astronomy* 38.1-2 (2014). Springer, pp. 249–330. DOI: 10.1007/s10686-014-9383-4.

[24] Lindberg, R., Lumb, D., den Hartog, R., Gondoin, P., Rando, N. and Fridlund, M. "Preliminary results on the internal assessment study of the ESA Cosmic Vision mission PLATO." In: *Proceedings of SPIE. Instruments, Methods, and Missions for Astrobiology XI*. Vol. 7097, 70970F. 2008. DOI: 10.1117/12.793353.

[25] European Space Agency. *SPICA Revealing the origins of planets and galaxies*. ESA/SRE(2009)6. 2009. URL: http://sci.esa.int/science-e/www/object/doc.cfm?fobjectid=46023.

[26] European Space Agency. *CDF Study Report NG-CryoIRTel Assessment of Next Generation Cryogenic Infra Red Telecope*. CDF-152(A). 2014. URL: http://sci.esa.int/future-missions-office/56046-cdf-study-report-next-generation-cryogenic-infra-red-telescope-ng-cryoirtel/.

[27] Antonucci, F., Armano, M., Audley, H., Auger, G., Benedetti, M. et al. "LISA Pathfinder: mission and status." In: *Classical and Quantum Gravity* 28.9 (Apr. 2011). IOP Publishing Ltd. DOI: 10.1088/0264-9381/28/9/094001.

[28] LISA Consortium. *LISA Laser Interferometer Space Antenna: A proposal in response to the ESA call for L3 mission concepts*. Jan. 2017. URL: https://www.lisamission.org/proposal/LISA.pdf.

[29] McNamara, P., Vitale, S. and Danzmann, K. "LISA Pathfinder." In: *Classical and Quantum Gravity* 25.11 (2008). Publishing Ltd. DOI: 10.1088/0264-9381/25/11/114034.

[30] Tapley, B. D., Bettadpur, S., Watkins, M. and Reigber, C. "The gravity recovery and climate experiment: Mission overview and early results." In: *Geophysical Research Letters* 31.9 (2004). Wiley Online Library. ISSN: 1944-8007. DOI: 10.1029/2004GL019920.

[31] National Aeronautics and Space Administration. *GRACE Launch - Press Kit*. Mar. 2002. URL: https://www.jpl.nasa.gov/news/press_kits/gracelaunch.pdf.

[32] Wang, F., Bettadpur, S., Save, H. and Kruizinga, G. "Determination of Center-of-Mass of Gravity Recovery and Climate Experiment Satellites." In: *Journal of Spacecraft and Rockets* 47.2 (2010), pp. 371–379. DOI: 10.2514/1.46086.

[33] Schütze, D. et al. "Measuring Earth: Current status of the GRACE Follow-On Laser Ranging Interferometer." In: *Journal of Physics: Conference Series*. Vol. 716. 1. IOP Publishing. 2016. DOI: 10.1088/1742-6596/716/1/012005.

[34] Dehne, M., Cervantes, F. G., Sheard, B., Heinzel, G. and Danzmann, K. "Laser interferometer for spaceborne mapping of the Earth's gravity field." In: *Journal of Physics: Conference Series*. Vol. 154. 1. IOP Publishing Ltd. 2009. DOI: 10.1088/1742-6596/154/1/012023.

[35] Kessler, M. F., Steinz, J. A., Anderegg, M. E., Clavel, J., Drechsel, G. et al. "The Infrared Space Observatory (ISO) mission." In: *Astronomy and Astrophysics* 315 (1996), pp. L27–L31.

[36] Werner, M. W., Roellig, T. L., Low, F. J., Rieke, G. H., Rieke, M. et al. "The Spitzer space telescope mission." In: *The Astrophysical Journal Supplement Series* 154.1 (2004). DOI: 10.1086/422992.

[37] Sauvage, M. et al. "Sub-arcsecond far-infrared space observatory: a science imperative." In: *Submission to ESA Science Programme M-class Mission Call* (2013).

[38] Leisawitz, D., Baker, C., Barger, A., Benford, D., Blain, A. et al. "The Space Infrared Interferometric Telescope (SPIRIT): High-resolution imaging and spectroscopy in the far-infrared." In: *Advances in Space research* 40.5 (2007). Elsevier, pp. 689–703. DOI: 10.1016/j.asr.2007.05.081.

[39] Leisawitz, D., Abel, T., Allen, R., Benford, D., Blain, A. et al. "SPECS: the kilometer-baseline far-IR interferometer in NASA's space science roadmap." In: *Proceedings of SPIE. Optical, Infared, and Millimeter Space Telescopes*. Vol. 5487. 2004. DOI: 10.1117/12.552150.

[40] Beichman, C. A., Coulter, D. R., Lindensmith, C. A. and Lawson, P. R. *Summary Report on Architecture Studies for the Terrestrial Planet Finder*. National Aeronautics and Space Administration. Jet Propulsion Laboratory. June 2002.

[41] European Space Agency. *CDF Study Report FIRI Far Infrared Interferometer*. CDF-49(A). 2006. URL: http://sci.esa.int/future-missions-office/40738-firi-cdf-study-report/.

[42] Lawson, P. R. and Jennifer, A. D. *Technology plan for the terrestrial planet finder interferometer*. National Aeronautics and Space Administration. Jet Propulsion Laboratory. 2005.

[43] Helmich, F. P. and Ivison, R. J. "FIRI - A far-infrared interferometer." In: *Experimental Astronomy* 23.1 (2009), pp. 245–276. DOI: 10.1007/s10686-008-9100-2.

[44] Léger, A., Herbst, T. et al. "DARWIN mission proposal to ESA." In: *[astro-ph] arXiv:0707.3385* (2007). URL: https://arxiv.org/ftp/arxiv/papers/0707/0707.3385.pdf.

[45] Wild, W., de Graauw, Th., Helmich, F., Cernicharo, J., Gunst, A., Bos, A. et al. "ESPRIT: a space interferometer concept for the far-infrared." In: *Proceedings of SPIE. Space Telescopes and Instrumentation I: Optical, Infrared, and Millimeter*. Vol. 6265. 2006, 62651Z. DOI: 10.1117/12.672012.

[46] Ollivier, M., Le Duigou, J.-M., Mourard, D., Absil, O., Cassaing, F. et al. "PEGASE: a DARWIN/TPF pathfinder." In: *Proceedings of the International Astronomical Union* 1.C200 (Oct. 2005). Cambridge University Press, pp. 241–246. DOI: 10.1017/S1743921306009380.

[47] Ladurée, G., Fransen, S., Baldesi, G. and Pflieger, I. "Rigid Body Modes Influence On Microvibration Analysis-Application To Swarm." In: *12th European Conference on Spacecraft Structures, Materials and Environmental Testing, ESTEC, the Netherlands, March 20-23, 2012*. Vol. 691. July 2012, p. 54. ISBN: 978-92-9092-255-1.

[48] Aglietti, G. S., Gabriel, S. B., Langley, R. S. and Rogers, E. "A modeling technique for active control design studies with application to spacecraft microvibrations." In: *The Journal of the Acoustical Society of America* 102.4 (1997). Acoustical Society of America, pp. 2158–2166. DOI: 10.1121/1.419631.

[49] Haftka, R. T. and Adelman, H. M. "An analytical investigation of shape control of large space structures by applied temperatures." In: *AIAA journal* 23.3 (1985), pp. 450–457. DOI: 10.2514/3.8934.

[50] Rittweger, A., Albus, J., Hornung, E., Öry, H. and Mourey, P. "Passive damping devices for aerospace structures." In: *Acta Astronautica* 50.10 (2002). Elsevier, pp. 597–608. DOI: 10.1016/S0094-5765(01)00220-X.

[51] Liu, C., Jing, X., Daley, S. and Li, F. "Recent advances in micro-vibration isolation." In: *Mechanical Systems and Signal Processing* 56 (2015). Elsevier, pp. 55–80. DOI: 10.1016/j.ymssp.2014.10.007.

[52] Cobb, R. G., Sullivan, J. M., Das, A., Davis, L. P., Hyde, T. T. et al. "Vibration isolation and suppression system for precision payloads in space." In: *Smart Materials and Structures* 8.6 (1999). IOP Publishing Ltd, pp. 798–812. DOI: 10.1088/0964-1726/8/6/309.

[53] Allegri, G., Ivagnes, M. M., Marchetti, M. and Poscente, F. "Analysis of the thermo-elastic response of space reflectors exposed to simulated space environment." In: *53rd International Astronautical Congress (IAC), Houston, Texas, October 10-19, 2002.* International Astronautical Federation (IAF), Oct. 2002.

[54] Giesen, P. and Folgering, E. "Design guidelines for thermal stability in optomechanical instruments." In: *Proceedings of SPIE. Optomechanics.* Vol. 5176. 2003, pp. 126–134. DOI: 10.1117/12.510285.

[55] Layton, C. H. and Slocum, A. H. "Optimal design techniques for kinematic couplings." In: *Precision Engineering* 25.2 (2001), pp. 114–127. ISSN: 0141-6359. DOI: 10.1016/S0141-6359(00)00066-0.

[56] Gilmore, D. G. *Spacecraft Thermal Control Handbook. Volume I: Fundamental Technologies.* 2nd ed. The Aerospace Corporation, 2002. ISBN: 1-884989-11-X.

[57] Wada, B. K., Fanson, J. L. and Crawley, E. F. "Adaptive Structures." In: *Journal of Intelligent Material Systems and Structures* 1.2 (Apr. 1990), pp. 157–174. DOI: 10.1177/1045389X9000100202.

[58] Balas, G. J. and Doyle, J. C. "Robustness and performance trade-offs in control design for flexible structures." In: *IEEE Transactions on control systems technology* 2.4 (1994). IEEE, pp. 352–361. DOI: 10.1109/87.338656.

[59] Symans, M. D. and Constantinou, M. C. "Semi-active control systems for seismic protection of structures: a state-of-the-art review." In: *Engineering structures* 21.6 (1999). Elsevier, pp. 469–487. DOI: 10.1016/S0141-0296(97)00225-3.

[60] Lillie, C. F. and Bronowicki, A. J. "Adaptation in space telescopes." In: *45th AIAA/ASME/ASCE/AHS/ASC Structures, Structural Dynamics & Materials Conference, Palm Springs, California (USA), April 19-22, 2004.* Vol. 2064. 2004. DOI: 10.2514/6.2004-2064.

[61] Bushnell, D. "Control of surface configuration by application of concentrated loads." In: *AIAA Journal* 17.1 (1979), pp. 71–77. DOI: 10.2514/3.61064.

[62] Robertshaw, H. H., Wynn, R. H., Kung, H. F., Hendricks, S. L. and Clark, W. W. "Dynamics and control of a spatial active truss actuator." In: *30th Structures, Structural Dynamics and Materials Conference. Mobile, Alabama (USA), AIAA.* 1989. DOI: 10.2514/6.1989-1328.

[63] Zhang, J., Xiang, Z. and Liu, Y. "Quasi-Static Shape Control of Flexible Space Structures by Using Heaters." In: *AIAA journal* 51.4 (2013), pp. 1003–1007. DOI: 10.2514/1.J052155.

[64] Morishima, T., van Ostayen, R., van Eijk, J. and Schmidt, R.-H. M. "Thermal displacement error compensation in temperature domain." In: *Precision Engineering* 42 (Oct. 2015). Elsevier, pp. 66–72. DOI: 10.1016/j.precisioneng.2015.03.012.

[65] Dosch, J. J., Inman, D. J. and Garcia, E. "A self-sensing piezoelectric actuator for collocated control." In: *Journal of Intelligent material systems and Structures* 3.1 (Jan. 1992). Sage Publications Sage CA: Thousand Oaks, CA, pp. 166–185. DOI: 10.1177/1045389X9200300109.

[66] Friebele, E. J., Askins, C. G., Bosse, A. B., Kersey, A. D., Patrick, H. J. et al. "Optical fiber sensors for spacecraft applications." In: *Smart materials and structures* 8.6 (1999). IOP Publishing Ltd, pp. 813–838. DOI: 10.1088/0964-1726/8/6/310.

[67] Chapman, A. J. *Heat Transfer*. Macmillan Publishing Company, 1984. ISBN: 0-02-321470-8.

[68] Altenburg, M. and Burkhardt, J. "Application of Linear Control Methods to Satellite Thermal Analysis." In: *38th International Conference on Environmental Systems (ICES), San Francisco, California (USA), June 29-July 2, 2008*. American Institute of Aeronautics and Astronautics (AIAA), July 2008. DOI: 10.4271/2008-01-2076.

[69] Liszka, T. and Orkisz, J. "The finite difference method at arbitrary irregular grids and its application in applied mechanics." In: *Computers & Structures* 11.1 (1980). Special Issue-Computational Methods in Nonlinear Mechanics, pp. 83–95. ISSN: 0045-7949. DOI: 10.1016/0045-7949(80)90149-2.

[70] Altenburg, M. and Burkhardt, J. "Methods for Solving Linearized Thermal Networks in the Frequency Domain." In: *40th International Conference on Environmental Systems (ICES), Barcelona (Spain), July 11-15, 2010*. American Institute of Aeronautics and Astronautics (AIAA), July 2010. DOI: 10.2514/6.2010-6141.

[71] Gebhart, B. "Surface temperature calculations in radiant surroundings of arbitrary complexity-for gray, diffuse radiation." In: *International Journal of Heat and Mass Transfer* 3.4 (1961), pp. 341–3460. ISSN: 0017-9310. DOI: 10.1016/0017-9310(61)90048-5.

[72] Boglietti, A., Cavagnino, A., Staton, D., Shanel, M., Mueller, M. and Mejuto, C. "Evolution and Modern Approaches for Thermal Analysis of Electrical Machines." In: *IEEE Transactions on Industrial Electronics* 56.3 (Mar. 2009), pp. 871–882. ISSN: 0278-0046. DOI: 10.1109/TIE.2008.2011622.

[73] Panczak, T. D. "The Failure of Finite Element Codes for Spacecraft Thermal Analysis." In: *SAE Technical Paper*. SAE International, July 1996. DOI: 10.4271/961450.

[74] Vujičić, M. R., Lavery, N. P. and Brown, S. G. R. "View factor calculation using the Monte Carlo method and numerical sensitivity." In: *Communications in Numerical Methods in Engineering* 22.3 (2006), pp. 197–203. ISSN: 1099-0887. DOI: 10.1002/cnm.805.

[75] Jacques, L., Béchet, E. and Kerschen, G. "Finite element model reduction for space thermal analysis." In: *Finite Elements in Analysis and Design* 127 (2017), pp. 6–15. ISSN: 0168-874X. DOI: 10.1016/j.finel.2017.01.001.

[76] Logan, D. L. *A first course in the finite element method*. 2nd ed. PWS Publishing Company, 1993. ISBN: 0-534-92964-8.

[77] Hogan, R. E. and Gartling, D. K. "Solution strategies for coupled conduction/radiation problems." In: *Communications in Numerical Methods in Engineering* 24.6 (2008), pp. 523–542. ISSN: 1099-0887. DOI: 10.1002/cnm.1063.

[78] Molina, M., Franzoso, A. and Giacomazzo, M. "Thermal Analysis for Systems Perturbed in the Linear Domain Method Development and Numerical Validation." In: *35th International Conference on Environmental Systems (ICES), Rome (Italy), July 11-14, 2005. SAE Technical Paper*. SAE International, July 2005. DOI: 10.4271/2005-01-3056.

[79] Altenburg, M. and Burkhardt, J. "Advances in Application of Linear Control Methods for Satellite Thermal Analysis." In: *41st International Conference on Environmental Systems (ICES), Portland, Oregon (USA), July 17-21, 2011.* American Institute of Aeronautics and Astronautics (AIAA), July 2011. DOI: 10.2514/6.2011-5160.

[80] Craig, R. R. and Kurdila, A. J. *Fundamentals of structural dynamics*. John Wiley & Sons, 2006. ISBN: 978-0-471-43044-5.

[81] Felippa, C. *Introduction to Aerospace Structures (ASEN 3112). Modal Analysis of Damped Forced MDOF Systems. Lecture Notes.* Department of Aerospace Engineering Sciences. University of Colorado at Boulder. 2016. URL: http://www.colorado.edu/engineering/CAS/courses.d/Structures.d/.

[82] Trindade, M. A., Benjeddou, A. and Ohayon, R. "Piezoelectric active vibration control of damped sandwich beams." In: *Journal of Sound and Vibration* 246.4 (2001), pp. 653–677. DOI: 10.1006/jsvi.2001.3712.

[83] Ang, K. K., Wang, S. Y. and Quek, S. T. "Weighted energy linear quadratic regulator vibration control of piezoelectric composite plates." In: *Smart materials and structures* 11.1 (2002), pp. 98–106. DOI: 10.1088/0964-1726/11/1/311.

[84] Lavretsky, E. and Wise, K. A. *Robust and Adaptive Control - with Aerospace Applications*. Springer, 2013. ISBN: 978-1-4471-4395-6.

[85] Morishima, T. *Novel thermal error reduction techniques in temperature domain*. Doctoral Thesis. Delft University of Technology, 2016. ISBN: 978-94-028-0423-2. DOI: doi:10.4233/uuid:ffdfd697-640c-419a-b39a-539d57b17d60.

[86] Arnold, W. F. and Laub, A. J. "Generalized eigenproblem algorithms and software for algebraic Riccati equations." In: *Proceedings of the IEEE* 72.12 (Dec. 1984), pp. 1746–1754. DOI: 10.1109/PROC.1984.13083.

[87] Bogert, P. B., Haugse, E. and Gehrki, R. E. "Structural shape identification from experimental strains using a modal transformation technique." In: *44th AIAA/ASME/ASCE/AHS Structures, Structural Dynamics and Materials Conference, Norfolk, Virginia (USA), April 7-10, 2003.* American Institute of Aeronautics and Astronautics (AIAA), Apr. 2003. DOI: 10.2514/6.2003-1626.

[88] Koevoets, M., van der Sanden, J. and Ruijl, T. "Thermal-elastic compensation models for position control." In: *Proceedings of the ASPE Annual Meeting.* 2009.

[89] McMurchy, R. R., Payne, R. G. and Dotts, R. L. *Thermal Network Modeling Handbook.* Tech. rep. National Aeronautics and Space Administration, Jan. 1972.

[90] Rasid, M. A. H., Lanfranchi, V., Benkara, K. E. K. and Vargas, L. A. O. "Simple lumped parameter thermal model with practical experimental fitting method for synchronous reluctance machine." In: *15th European Conference on Power Electronics and Applications (EPE), Lille (France), September 2-6, 2013.* IEEE. DOI: 10.1109/EPE.2013.6631995.

[91] Gebhart, B. *Heat transfer.* McGraw-Hill, 1971. ISBN: 9780070231276.

[92] Felippa, C. *Introduction to Finite Element Methods (ASEN 5007). The Isoparametric Representation. Lecture Notes.* Department of Aerospace Engineering Sciences. University of Colorado at Boulder. 2017. URL: https://www.colorado.edu/engineering/CAS/courses.d/IFEM.d/.

[93] Felippa, C. *Introduction to Finite Element Methods (ASEN 5007). Isoparametric Quadrilaterals. Lecture Notes.* Department of Aerospace Engineering Sciences. University of Colorado at Boulder. 2017. URL: https://www.colorado.edu/engineering/CAS/courses.d/IFEM.d/.

Appendix A

Link parameter derivation in the LPM

The Lumped Parameter Method (LPM) presented in Section 3.1.2 requires the calculation of the link parameters that characterize the heat exchange between nodes [89]. This derivation can be based on experimental fitting methods [90] as well as analytical procedures [89]. This appendix presents an analytical procedure based on the finite difference method (FDM) [9] to calculate the conductive and radiative link parameters.

Starting with the conductive link parameters, the FDM can approximate the heat exchange Equation 3.5 in terms of finite differences, as outlined in Section 3.1.1, as

$$\begin{aligned}\rho c_p \left(\frac{T_{i,j,k}^{t+\Delta t} - T_{i,j,k}^{t}}{\Delta t}\right) = \; & \lambda \left(\frac{T_{i+1,j,k} + T_{i-1,j,k} - 2T_{i,j,k}}{\Delta x^2}\right) \\ & + \lambda \left(\frac{T_{i,j+1,k} + T_{i,j-1,k} - 2T_{i,j,k}}{\Delta y^2}\right) \\ & + \lambda \left(\frac{T_{i,j,k+1} + T_{i,j,k-1} - 2T_{i,j,k}}{\Delta z^2}\right) + Q_{i,j,k}.\end{aligned} \tag{A.1}$$

The procedure to calculate the conductive link parameters consists in equating the previous expression with the heat exchange equation in LPM form, i.e.,

$$C_n \left(\frac{T_n^{t+\Delta t} - T_n^{t}}{\Delta t}\right) = \sum_{m=1}^{N} K_{nm}(T_m - T_n) + Q_n. \tag{A.2}$$

First, Equation A.1 can be rewritten into

$$\begin{aligned}\rho c_p \left(\frac{T_{i,j,k}^{t+\Delta t} - T_{i,j,k}^{t}}{\Delta t}\right) = \; & \lambda \left(\frac{T_{i+1,j,k} - T_{i,j,k}}{\Delta x^2}\right) + \lambda \left(\frac{T_{i-1,j,k} - T_{i,j,k}}{\Delta x^2}\right) \\ & + \lambda \left(\frac{T_{i,j+1,k} - T_{i,j,k}}{\Delta y^2}\right) + \lambda \left(\frac{T_{i,j-1,k} - T_{i,j,k}}{\Delta y^2}\right) \\ & + \lambda \left(\frac{T_{i,j,k+1} - T_{i,j,k}}{\Delta z^2}\right) + \lambda \left(\frac{T_{i,j,k-1} - T_{i,j,k}}{\Delta z^2}\right) + Q_{i,j,k}.\end{aligned} \tag{A.3}$$

In the LPM, each node represents an isothermal volume. If the discretization of the domain is performed using a rectangular grid, then the volume of one node is a rectangular hexahedron with side lengths equal to Δx, Δy and Δz. A representation of this volume is included in Figure A.1. The next step consists in multiplying the previous equation by the nodal volume, this yields

$$\begin{aligned}\rho c_p \left(\frac{T_{i,j,k}^{t+\Delta t} - T_{i,j,k}^{t}}{\Delta t}\right) \Delta x \Delta y \Delta z = \; & \lambda \left(\frac{T_{i+1,j,k} - T_{i,j,k}}{\Delta x}\right) \Delta y \Delta z \\ & + \lambda \left(\frac{T_{i-1,j,k} - T_{i,j,k}}{\Delta x}\right) \Delta y \Delta z \\ & + \lambda \left(\frac{T_{i,j+1,k} - T_{i,j,k}}{\Delta y}\right) \Delta x \Delta z \\ & + \lambda \left(\frac{T_{i,j-1,k} - T_{i,j,k}}{\Delta y}\right) \Delta x \Delta z \\ & + \lambda \left(\frac{T_{i,j,k+1} - T_{i,j,k}}{\Delta z}\right) \Delta x \Delta y \\ & + \lambda \left(\frac{T_{i,j,k-1} - T_{i,j,k}}{\Delta z}\right) \Delta x \Delta y + Q_{i,j,k}.\end{aligned} \tag{A.4}$$

The product $\rho c_p \Delta x \Delta y \Delta z$ at the left-hand side of Equation A.4 can be abbreviated by the total heat capacity of the node represented by $C_{i,j,k}$. At the right-hand side, the increments at the denominator are equivalent to distances between nodes, which can be represented by l. The multiplication between increments is equivalent to the cross-sectional area between nodes that can be represented by A. Therefore, Equation A.4 can also be written as

$$\begin{aligned}C_{i,j,k} \left(\frac{T_{i,j,k}^{t+\Delta t} - T_{i,j,k}^{t}}{\Delta t}\right) = \; & \frac{\lambda A_i}{l_i} \left(T_{i+1,j,k} - T_{i,j,k}\right) \\ & + \frac{\lambda A_i}{l_i} \left(T_{i-1,j,k} - T_{i,j,k}\right) \\ & + \frac{\lambda A_j}{l_j} \left(T_{i,j+1,k} - T_{i,j,k}\right) \\ & + \frac{\lambda A_j}{l_j} \left(T_{i,j-1,k} - T_{i,j,k}\right) \\ & + \frac{\lambda A_k}{l_k} \left(T_{i,j,k+1} - T_{i,j,k}\right) \\ & + \frac{\lambda A_k}{l_k} \left(T_{i,j,k-1} - T_{i,j,k}\right) + Q_{i,j,k}.\end{aligned} \tag{A.5}$$

Considering now only the heat exchange equation centered at node n (equivalent to node i, j, k) Equation A.5 can be written as

$$C_n \left(\frac{T_n^{t+\Delta t} - T_n^{t}}{\Delta t}\right) = \sum_{m=1}^{N} \frac{\lambda A_{nm}}{l_{nm}} (T_m - T_n) + Q_n. \tag{A.6}$$

Comparing Equation A.6 to Equation A.2 it can be concluded that the conductive link parameters can be calculated using

$$K_{nm} = \frac{\lambda A_{nm}}{l_{nm}}. \tag{A.7}$$

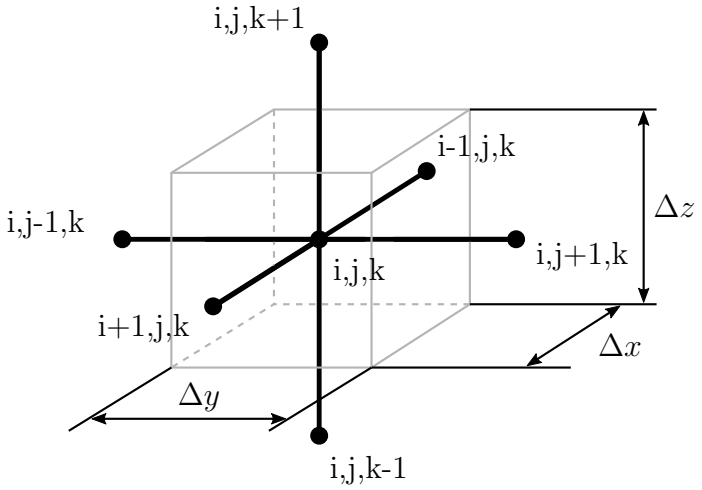

Figure A.1: Representation of one node in the LPM.

Since this derivation is based on the FDM, the error introduced in Equation A.6 is minimized when the discretization scheme resembles the one required for the FDM, i.e., a rectangular grid. If the domain is meshed using an irregular grid the error introduced in the estimation of the conductive link parameters might increase and another approach for the estimation might be more appropriate.

Equation A.6 is a lumped parameter expression of the thermal problem considering only heat exchange through conduction and internal heat sources. The contribution of the radiation exchange between nodes is traditionally introduced into this equation based on the approach described by Gebhart in [71]. This method is based on the definition of the absorption factors. For every pair of nodes i and j there is an absorption factor B_{ij} that represents the fraction of energy emitted by the area A_i that is absorbed in A_j. This must not be confused with the view factor, commonly represented by F_{ij}, which is the fraction of radiation leaving from A_i that reaches A_j.

The absorption factors are related to the view factors according to [91],

$$B_{ij} = F_{ij}\varepsilon_j + \sum_{k=1}^{N} F_{ik}(1-\varepsilon_k)B_{kj}. \tag{A.8}$$

Writing Equation A.8 for each absorption factor results in a system of linear equations that can be solved to calculate the absorption factors as a function of the view factors. One important difference between F_{ij} and B_{ij} is that the view factors depend only on the geometry of the domain whereas the absorption factors are also a function of the surface emissivities.

The heat exchange between nodes i and j is the difference between the heat emitted by A_i that is absorbed by A_j and the heat emitted by A_j that is absorbed by A_i. This can be expressed through the absorption factors as

$$Q_{ij} = \sigma\varepsilon_i A_i B_{ij} T_i^4 - \sigma\varepsilon_j A_j B_{ji} T_j^4. \tag{A.9}$$

This same expression can be rewritten introducing the reciprocity of the absorption factors [71],

$$\varepsilon_i B_{ij} A_i = \varepsilon_j B_{ji} A_j, \tag{A.10}$$

which results in

$$Q_{ij} = \sigma \varepsilon_i A_i B_{ij} \left(T_i^4 - T_j^4 \right). \tag{A.11}$$

Equation A.11 can now be introduced into Equation A.6 to account for the radiation exchange between nodes. Finally, this results in the equation that has been presented in Section 3.1.2 which written for node n is

$$C_n \frac{T_n^{t+\Delta t} - T_n^t}{\Delta t} = \sum_{n=1}^{N} \left(\frac{\lambda_{nm} A_{nm}}{l_{nm}} (T_m - T_n) \right) + \sum_{m=1}^{N} \left(\sigma \varepsilon_n A_n B_{nm} (T_m^4 - T_n^4) \right) + Q_n. \tag{A.12}$$

Therefore, the radiative link parameters for each pair of nodes can be calculated as

$$R_{nm} = \sigma \varepsilon_n A_n B_{nm}. \tag{A.13}$$

Calculating the conduction links at each node based on Equation A.7 and the radiation links based on Equation A.13 it is possible to fully characterize a lumped parameter model that describes the thermal behavior of a structure in space, i.e. under the absence of convection.

Appendix B

FEM thermal formulation

The FEM approach implemented in this work is based on the Galerkin method [76], which in turn is a particular case of the weighted residual method. The goal of this appendix is to present in detail the assumptions and mathematical formulation that are followed in this approach and to clarify the notation that is used throughout the thesis. The presented formulation is particularized for the thermal problem.

First, the equation describing the thermal field in the domain of study is expressed in form of the PDE

$$\rho c_p \frac{\partial T}{\partial t} = \lambda \nabla^2 T + Q. \tag{B.1}$$

The FEM provides a numerical approximation to the solution of this PDE expressed inside each finite element as

$$\overline{T}(x, y, z, t) = \sum_{i=1}^{n_e} T_i(t) N_i(x, y, z) = [N]\{T\}, \tag{B.2}$$

with $\overline{T}$ being the approximated thermal field, n_e the number of nodes in one finite element, T_i the nodal temperatures for each node in the element and N_i the assumed shape functions that interpolate the thermal field between nodes. If expressed in matrix form $[N]$ is a row vector containing the shape function values and $\{T\}$ is the column vector of the nodal temperatures. This approximation does not give an exact solution of Equation B.1 and, therefore, a residual will remain. This residual can be identified by R and is defined as

$$R = \rho c_p \frac{\partial \overline{T}}{\partial t} - \lambda \nabla^2 \overline{T} - Q. \tag{B.3}$$

The weighted residual method calculates the solution of the nodal temperatures T_i by minimizing a weighted form of this residual, integrated over the whole domain. This is expressed as

$$\int_\Omega w_i R d\Omega = \int_\Omega w_i \left(\rho c_p \frac{\partial \overline{T}}{\partial t} - \lambda \nabla^2 \overline{T} - Q \right) d\Omega = 0 \quad \text{for} \quad i = 1, 2, \ldots, n_e \tag{B.4}$$

The choice of the weight function w_i results in different methods. A common approach is the Galerkin method, which uses as weight functions the same shape

functions that are used to define the thermal field in Equation B.2. Therefore, the Galerkin method consists in solving

$$\int_\Omega N_i \left(\rho c_p \frac{\partial \overline{T}}{\partial t} - \lambda \nabla^2 \overline{T} - Q \right) d\Omega = 0 \quad \text{for} \quad i = 1, 2, \ldots, n_e \tag{B.5}$$

Introducing now the identity B.2 and rearranging the terms in B.5 results in

$$\int_\Omega N_i \left(\rho c_p [N] \{\dot{T}\} \right) d\Omega = \int_\Omega N_i \left(\lambda \nabla^2 \overline{T} \right) d\Omega + \int_\Omega N_i Q d\Omega \quad \text{for} \quad i = 1, 2, \ldots, n_e \tag{B.6}$$

The first term at the right-hand side can be integrated by parts, which yields

$$\int_\Omega N_i \left(\lambda \nabla^2 \overline{T} \right) d\Omega = - \int_\Omega \nabla N_i \lambda \nabla \overline{T} d\Omega + \int_S N_i \left(\lambda \nabla \overline{T} \right) d\vec{s}. \tag{B.7}$$

At this point it is useful to define the derivative matrix $[B]$, which is a matrix built with the gradient of the shape functions. For a generic case with n_e nodes in each element, the $[B]$ matrix is defined as

$$[B] = \nabla [N] = \begin{bmatrix} \dfrac{\partial N_1}{\partial x} & \dfrac{\partial N_2}{\partial x} & \cdots & \dfrac{\partial N_{n_e}}{\partial x} \\ \dfrac{\partial N_1}{\partial y} & \dfrac{\partial N_2}{\partial y} & \cdots & \dfrac{\partial N_{n_e}}{\partial y} \\ \dfrac{\partial N_1}{\partial z} & \dfrac{\partial N_2}{\partial z} & \cdots & \dfrac{\partial N_{n_e}}{\partial z} \end{bmatrix} \tag{B.8}$$

Using this matrix it is now possible to calculate the temperature gradient as

$$\nabla \overline{T} = [B] \{T\}. \tag{B.9}$$

Introducing also the equivalences

$$\{q\} = -\lambda \nabla \overline{T} \tag{B.10}$$

$$\text{and} \quad d\vec{s} = \{n\} ds \tag{B.11}$$

with $\{n\}$ being the normal vector to the surface, it is now possible to combine equations B.6 and B.7 resulting in

$$\begin{aligned} \int_\Omega N_i \left(\rho c_p [N] \{\dot{T}\} \right) d\Omega = & - \int_\Omega \left(\nabla N_i \lambda [B] \{T\} \right) d\Omega \\ & - \int_S N_i \{q\}^T \{n\} ds \\ & + \int_\Omega N_i Q d\Omega \quad \text{for} \quad i = 1, 2, \ldots, n_e \end{aligned} \tag{B.12}$$

Writing Equation B.12 for all the nodes in the element results in

$$\begin{aligned} \left(\int_\Omega \rho c_p [N]^T [N] d\Omega \right) \{\dot{T}\} = & - \left(\int_\Omega \lambda [B]^T [B] d\Omega \right) \{T\} \\ & - \int_S [N]^T \{q\}^T \{n\} ds \\ & + \int_\Omega [N]^T Q d\Omega. \end{aligned} \tag{B.13}$$

Introducing the definitions

$$\text{Thermal capacity matrix :} \qquad [C] = \int_{\Omega} \rho c_p [N]^T [N] d\Omega \tag{B.14}$$

$$\text{Thermal conductivity matrix :} \qquad [K] = \int_{\Omega} \lambda [B]^T [B] d\Omega \tag{B.15}$$

$$\text{Heat flux vector :} \qquad \{R_q\} = -\int_{S} [N]^T \{q\}^T \{n\} ds \tag{B.16}$$

$$\text{Heat source vector :} \qquad \{R_Q\} = \int_{\Omega} [N]^T Q d\Omega \tag{B.17}$$

the matrix form of the thermal problem in finite elements is finally obtained

$$[C]\{\dot{T}\} + [K]\{T\} = \{R_q\} + \{R_Q\}. \tag{B.18}$$

One of the crucial steps in applying the FEM is to define the shape functions to interpolate the thermal field within one finite element, as expressed in B.2. These shape functions can be defined using polynomial expressions and their exact definition depends both on the geometrical shape and the coordinate system of the finite elements.

There exists a wide variety of finite elements that can be used to mesh a three-dimensional domain: tetrahedrons, hexahedrons, prisms, pyramids, etc. It is also possible to use more than one type of element to create a mesh. In the examples presented in this work the domain of study has been meshed using uniquely hexahedron elements built with 8 nodes. The fact that the domain is meshed using the same type of element gives some uniformity to the employed equations and simplifies the radiation exchange equations. However, the presented method in this work is fully applicable using also other types of elements.

The hexahedron element with 8 nodes is represented in Figure B.1. Each of these elements in the mesh requires the definition of 8 shape functions in the xyz coordinate frame. This can become unpractical given that each element might have a slightly different geometry, and thus, each shape function at each element requires different components if expressed in this frame. A very practical approach to simplify this process is known as the isoparametric representation [92]. Based on this approach, the shape functions are defined using a set of coordinates known as natural coordinates (ξ, η, μ) and subsequently transformed to the global system of coordinates (x, y, z). Using the isoparameteric representation, the hexahedron shape functions that are used in this work are expressed as

$$\begin{aligned}
N_1 &= \frac{1}{8}(1-\xi)(1-\eta)(1-\mu) & N_2 &= \frac{1}{8}(1+\xi)(1-\eta)(1-\mu) \\
N_3 &= \frac{1}{8}(1+\xi)(1+\eta)(1-\mu) & N_4 &= \frac{1}{8}(1-\xi)(1+\eta)(1-\mu) \\
N_5 &= \frac{1}{8}(1-\xi)(1-\eta)(1+\mu) & N_6 &= \frac{1}{8}(1+\xi)(1-\eta)(1+\mu) \\
N_7 &= \frac{1}{8}(1+\xi)(1+\eta)(1+\mu) & N_8 &= \frac{1}{8}(1-\xi)(1+\eta)(1+\mu)
\end{aligned} \tag{B.19}$$

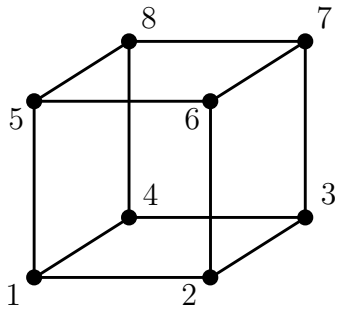

Figure B.1: Finite element using a hexahedral shape.

The transformation between coordinates (ξ, η, μ) and (x, y, z) can be performed using

$$x = \sum_{i=1}^{8} x_i N_i(\xi, \eta, \mu) \qquad y = \sum_{i=1}^{8} y_i N_i(\xi, \eta, \mu) \qquad z = \sum_{i=1}^{8} z_i N_i(\xi, \eta, \mu) \tag{B.20}$$

where x_i, y_i and z_i are the coordinates of each node in the element.

Using the natural coordinates (ξ, η, μ) each hexahedron element is represented by a cube with each coordinate ranging from -1 to 1.

Finally, the isoparametric representation is also useful to simplify the numerical integration of the FEM matrices B.14, B.15 and B.17. For each of these matrices it is necessary to perform a volume integral. This integral can be calculated in the domain of the natural coordinates introducing the Jacobian determinant, i.e.

$$d\Omega = dxdydz = |J| d\xi d\eta d\mu. \tag{B.21}$$

The Jacobian determinant can be calculated from the Jacobian matrix, equal to

$$[J] = \begin{bmatrix} \dfrac{\partial x}{\partial \xi} & \dfrac{\partial y}{\partial \xi} & \dfrac{\partial z}{\partial \xi} \\ \dfrac{\partial x}{\partial \eta} & \dfrac{\partial y}{\partial \eta} & \dfrac{\partial z}{\partial \eta} \\ \dfrac{\partial x}{\partial \mu} & \dfrac{\partial y}{\partial \mu} & \dfrac{\partial z}{\partial \mu} \end{bmatrix}. \tag{B.22}$$

The components of this matrix can in turn be calculated using

$$\begin{aligned} \frac{\partial x}{\partial \xi} &= \sum_{i=1}^{8} \frac{\partial N_i}{\partial \xi} x_i & \frac{\partial y}{\partial \xi} &= \sum_{i=1}^{8} \frac{\partial N_i}{\partial \xi} y_i & \frac{\partial z}{\partial \xi} &= \sum_{i=1}^{8} \frac{\partial N_i}{\partial \xi} z_i \\ \frac{\partial x}{\partial \eta} &= \sum_{i=1}^{8} \frac{\partial N_i}{\partial \eta} x_i & \frac{\partial y}{\partial \eta} &= \sum_{i=1}^{8} \frac{\partial N_i}{\partial \eta} y_i & \frac{\partial z}{\partial \eta} &= \sum_{i=1}^{8} \frac{\partial N_i}{\partial \eta} z_i \\ \frac{\partial x}{\partial \mu} &= \sum_{i=1}^{8} \frac{\partial N_i}{\partial \mu} x_i & \frac{\partial y}{\partial \mu} &= \sum_{i=1}^{8} \frac{\partial N_i}{\partial \mu} y_i & \frac{\partial z}{\partial \mu} &= \sum_{i=1}^{8} \frac{\partial N_i}{\partial \mu} z_i \end{aligned} \tag{B.23}$$

To increase the speed in the integration of expressions B.14, B.15 and B.17, Gaussian quadrature rules are frequently implemented [93]. The approach followed in this work has been to use the Gaussian quadrature rule with 6 points.

Appendix C

Stabilization analysis for the aluminum case

The results presented in Chapter 6 have been obtained assuming that the structural plate represented in Figure 3.4 is made of silicon carbide, according to the properties presented in Table 3.1 on page 40. The thermomechanical properties of silicon carbide, among which there is a very low coefficient of thermal expansion, result in a structural configuration that exhibits a highly stable passive behavior. As presented thoroughly in Chapter 6, this passive level of stabilization can be further increased through the presented framework.

As illustrated through the examples in Chapter 6, the highest levels of structural stability can be attained by combining an already passively stable structure with an active control technique. However, it is also possible to achieve high levels of stability by applying an active control technique to a structure that is not particularly stable in passive terms. In some cases, applying the active method of stabilization may already provide the required level of stability and, therefore, could spare the design efforts related to developing a passively highly-stable structure, which often entails using high-performance materials.

To exemplify this approach, this appendix analyzes the distortion reduction that could be achieved if the structural plate represented in Figure 3.4 were made of aluminum. The assumed mechanical properties in this case are those included in Table 3.1 for the aluminum alloy.

First, the uncontrolled and controlled distortions are simulated assuming that a known sinusoidal perturbation arising from instrument 1 is applied to the structure. This is equivalent to the case presented in Section 6.1. If it is known that the thermal perturbation follows a sinusoidal function with an amplitude of 10 W, as represented in Figure 6.3 on page 95, then it is possible to calculate the exact heat inputs that are necessary to compensate the arising distortions at point A. Under this ideal condition where the perturbation is known it is possible to achieve an almost perfect distortion cancellation reaching controlled distortions in the order of magnitude of 10^{-22} m. This result is represented in Figure C.1, where both the uncontrolled and controlled responses are presented. This figure can be compared to the results for the silicon carbide case in Figure 6.5 on page 96. The comparison shows that the distortions

in the uncontrolled case are significantly larger for the aluminum case. Nonetheless, the figure also proves that it is possible to virtually cancel completely the distortion effects of known perturbations, even when the structure is not particularly passively stable.

To analyze the scenario in which the perturbation is unknown, the achieved response considering the feedback loop presented in Chapter 6 is also simulated for the aluminum case. The same setup presented in Chapter 6 and represented in Figures 6.1 and 6.2 is assumed. Based on the assumption that the structure is equipped with 20 noisy sensors and 3 control heaters, the achieved controlled response in each direction at point A is represented in Figure C.2.

It can be observed in Figure C.2 that under the absence of active control the distortions can achieve significantly higher values than in the silicon carbide case. The maximum amplitude appears in the y-direction, where an amplitude of 22.3 µm is reached. When the active control is applied, the distortions in each direction are reduced by a factor of approximately 20. The exact maximum amplitudes in each direction, both for the uncontrolled and the controlled cases, are included in Table C.1. Also, the stabilization improvement in terms of the standard deviation for each direction is presented in Table C.2.

It can be concluded from this example that high levels of stabilization can be achieved for cases in which the structure has not been designed to be particularly stable in passive terms. In this case, a structure that under no active stabilization would experience distortions in the range above 10 µm, can be dimensionally stabilized at levels below 1 µm. Provided that this level of stabilization satisfies some predefined stability requirements, this strategy could result in some cases in a significant decrease of costs associated with the development of stable structures.

Maximum amplitude			
Direction	Uncontrolled response	Controlled response	Reduction factor
x	5.529 µm	0.261 µm	21.2
y	22.322 µm	0.897 µm	24.9
z	2.900 µm	0.149 µm	19.5

Table C.1: Maximum amplitude of displacements at point A for the uncontrolled and controlled cases in a plate made of aluminum.

Standard deviation			
Direction	Uncontrolled response	Controlled response	Reduction factor
x	2.153 µm	$6.837{\cdot}10^{-2}$ µm	31.5
y	8.692 µm	$1.403{\cdot}10^{-1}$ µm	61.9
z	1.135 µm	$4.229{\cdot}10^{-2}$ µm	26.8

Table C.2: Standard deviation of displacements at point A for the uncontrolled and controlled cases in a plate made of aluminum.

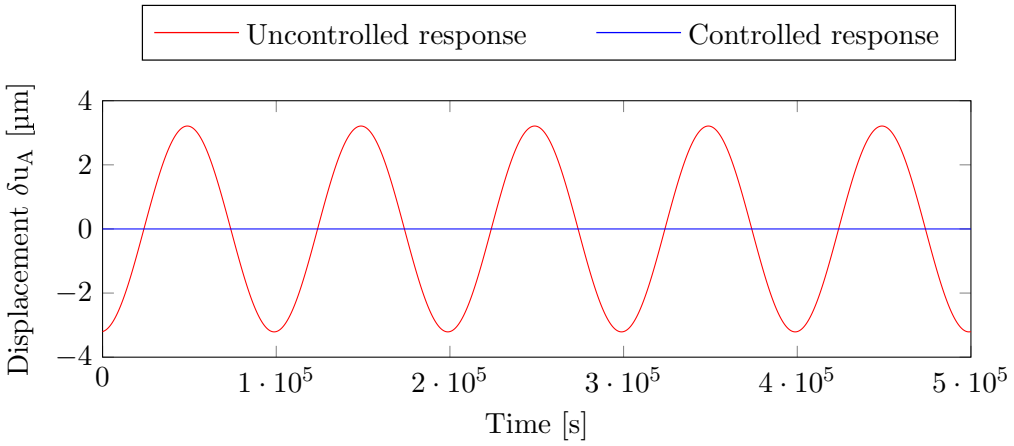

(a) Displacement in the x-direction.

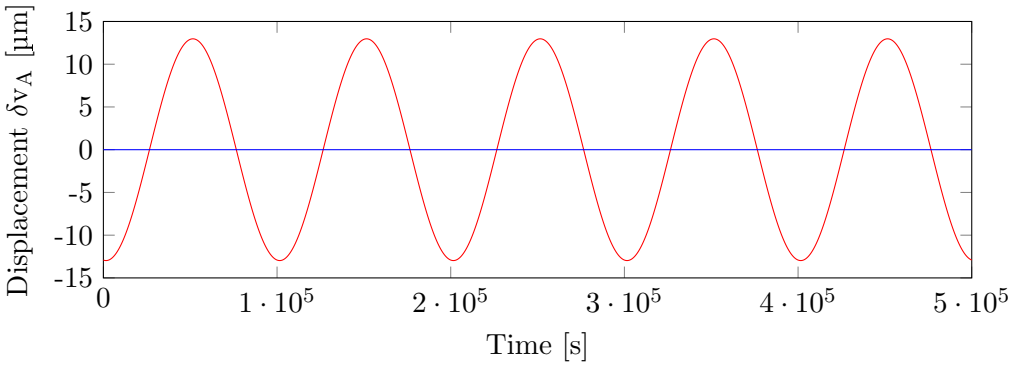

(b) Displacement in the y-direction.

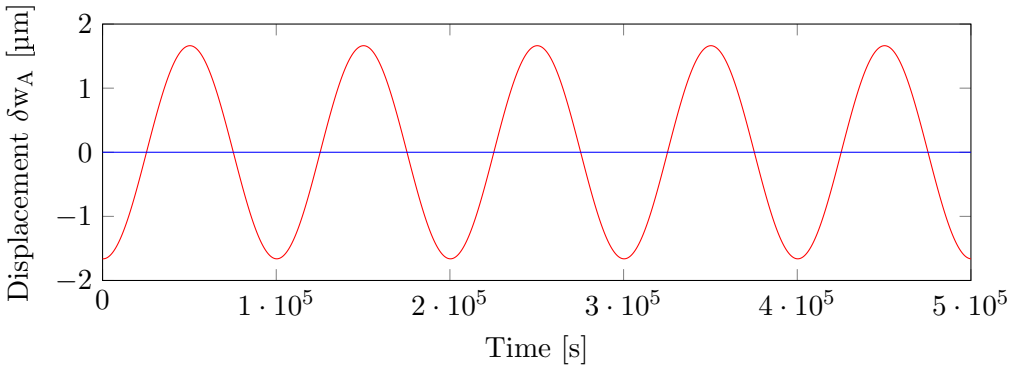

(c) Displacement in the z-direction.

Figure C.1: Displacements at point A induced by known perturbations in Instrument 1 considering a plate made of aluminum.

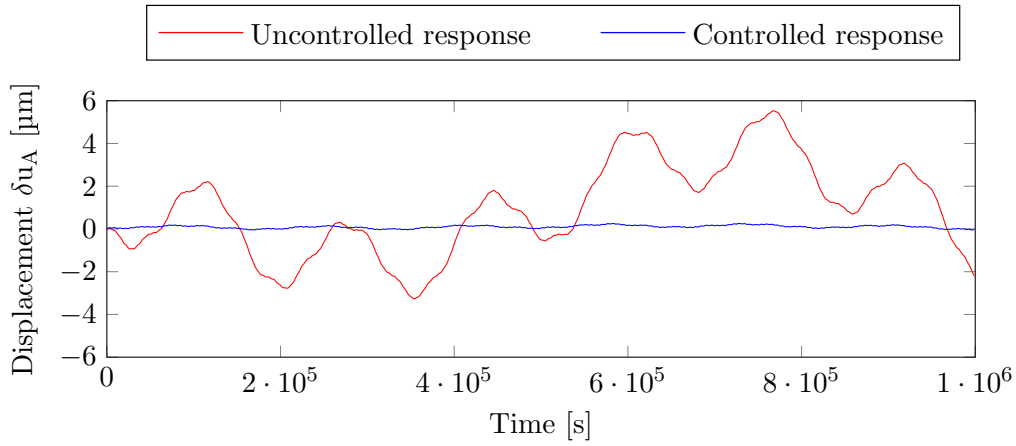

(a) Displacement in the x-direction.

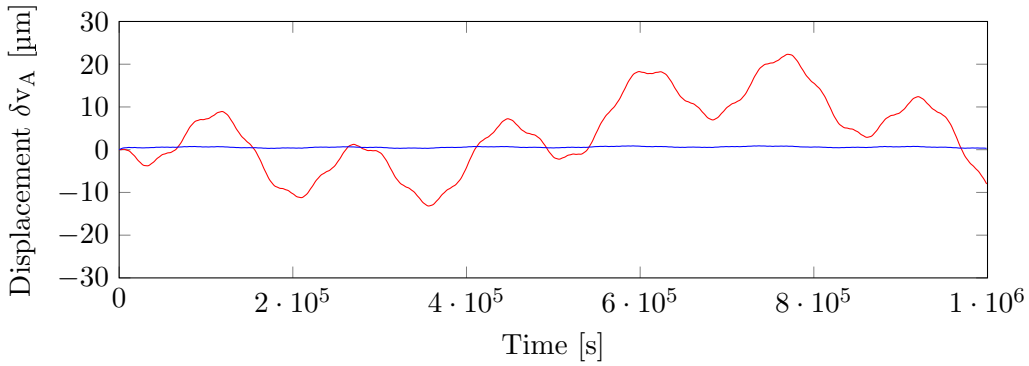

(b) Displacement in the y-direction.

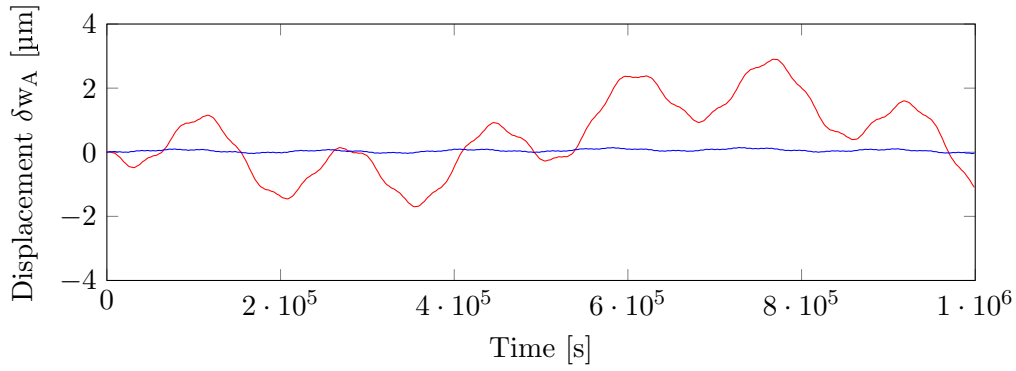

(c) Displacement in the z-direction.

Figure C.2: Displacements at point A induced by random perturbations in Instrument 1 considering a plate made of aluminum.